

# **Searches for New Physics using Pairs of Jets Containing $b$ -quarks at the ATLAS Detector**

*Laurie M<sup>c</sup>Clymont*

A dissertation submitted in partial fulfillment  
of the requirements for the degree of  
**Doctor of Philosophy**  
of  
**University College London.**

Department of Physics and Astronomy,  
University College London

7th December 2017

I, Laurie McClymont, confirm that the work presented in this thesis is my own. Where information has been derived from other sources, I confirm that this has been indicated in the work.

# Abstract

Two searches for Beyond Standard Model resonances are performed in 13 TeV proton–proton collision data collected by the ATLAS detector in 2015 and 2016 using the invariant mass distribution of pairs of jets, where at least one or both jets are identified as containing a  $b$ -quark. The searches are sensitive to resonances decaying to a pair of  $b$ -quarks or a  $b$ -quark and a gluon. A high-mass search probes the mass region 1.4 – 6 TeV using a data-set corresponding to an integrated luminosity of  $13.3\text{ fb}^{-1}$ . A low-mass search utilises real-time  $b$ -jet identification to probe the mass region 0.6 – 1.5 TeV using a data-set corresponding to an integrated luminosity of  $24.3\text{ fb}^{-1}$ . No evidence of a resonance is found. Excited  $b^*$  quarks with masses from 1.4 to 2.3 TeV and a set of  $Z'$  boson models with masses from 0.6 to 1.25 TeV or at 1.5 TeV are excluded at the 95% credibility-level. In addition 95% credibility-level upper limits are set on generic Gaussian signals in the mass range 0.65 – 6 TeV.

# **Acknowledgements**

Wasssupppp!

# Contents

<b>1</b>	<b>Introduction</b>	<b>25</b>
1.1	Structure of Thesis . . . . .	26
1.2	Personal Contributions . . . . .	27
<b>2</b>	<b>An Incomplete Theory</b>	<b>29</b>
2.1	The Standard Model . . . . .	29
2.1.1	Particles . . . . .	29
2.1.2	Forces . . . . .	31
2.2	QCD: Hadronic Jet Formation and Dijet Production . . . . .	32
2.2.1	Renormalisation and the Running of $\alpha_S$ . . . . .	32
2.2.2	Hadronic Jet Formation . . . . .	34
2.2.3	Dijet Production in $p p$ Collisions . . . . .	35
2.2.4	A Special Case: $t\bar{t}$ . . . . .	39
2.3	Beyond Standard Model Physics . . . . .	40
2.3.1	Motivations . . . . .	40
2.3.2	Beyond Standard Model Theories . . . . .	42
<b>3</b>	<b>The LHC and the ATLAS Detector</b>	<b>45</b>
3.1	The Large Hadron Collider (LHC) . . . . .	45
3.1.1	LHC running conditions in 2015 and 2016 . . . . .	45
3.2	ATLAS Detector Description . . . . .	46
3.2.1	ATLAS Co-ordinate System . . . . .	47
3.2.2	Inner Detector . . . . .	49
3.2.3	Calorimeters . . . . .	52
3.2.4	Muon Spectrometer . . . . .	56
3.2.5	Magnets . . . . .	58

<b>4 Object Definition and Reconstruction</b>	<b>59</b>
4.1 Tracks . . . . .	59
4.2 Jets . . . . .	60
4.2.1 Hadronic Topocluster Reconstruction . . . . .	61
4.2.2 Jet Reconstruction . . . . .	63
4.2.3 Jet Calibration . . . . .	65
4.2.4 Jet Energy Uncertainties . . . . .	68
4.3 $b$ -Jets . . . . .	70
4.3.1 Assigning a Flavour Label . . . . .	70
4.3.2 Baseline $b$ -tagging Algorithms . . . . .	70
4.3.3 Multi-Variate $b$ -tagging Algorithm . . . . .	72
4.3.4 Calibration and Uncertainties . . . . .	74
4.3.5 $b$ -Jet Energy Scale . . . . .	76
4.4 Electrons and Muons . . . . .	78
4.5 Further objects . . . . .	79
<b>5 Triggering in the di-<math>b</math>-jet analysis</b>	<b>80</b>
5.1 Jet-Triggers . . . . .	80
5.1.1 Level 1 . . . . .	80
5.1.2 HLT . . . . .	81
5.1.3 High-mass trigger selection . . . . .	81
5.2 $b$ -Jet Triggers . . . . .	82
5.2.1 General description . . . . .	82
5.3 Efficiency Measurement of the $b$ -Jet Trigger . . . . .	84
5.3.1 Strategy . . . . .	84
5.3.2 Datasets . . . . .	85
5.3.3 Event Selection . . . . .	86
5.3.4 The Initial Problem . . . . .	87
5.3.5 Investigation . . . . .	87
5.3.6 Solution: $b$ -Jet Trigger GRL . . . . .	93
5.3.7 Efficiency Measurement and Systematic Derivation . . . . .	95
5.3.8 Cross-checks . . . . .	105
5.4 To Do . . . . .	106
<b>6 Di-<math>b</math>-jet Search: Outline and Event Selection</b>	<b>107</b>
6.1 Analysis Outline . . . . .	107

6.2	List of Data Sets Used . . . . .	108
6.3	Backgrounds and Signal . . . . .	110
6.4	Event Selection . . . . .	112
6.4.1	Jet Selection . . . . .	113
6.4.2	Event-Level Cuts . . . . .	114
6.4.3	<i>b</i> -Tagging . . . . .	118
6.4.4	Effect of <i>b</i> -Jet Trigger Matching in the <i>Full16_LowMass</i> Data-set .	122
6.4.5	Event Selection Summary . . . . .	125
<b>7</b>	<b>Di-<i>b</i>-jet Search: Search Phase</b>	<b>130</b>
7.1	Dijet Mass Spectrum . . . . .	130
7.2	Background Estimation . . . . .	131
7.2.1	Functional Form . . . . .	132
7.2.2	Wilks' Test Statistic . . . . .	133
7.3	Resonance Search Strategy . . . . .	134
7.4	<i>Summer16_HighMass</i> Search Phase . . . . .	136
7.4.1	Background Modelling Strategy . . . . .	136
7.4.2	Validation Studies: Background-Only Data-set . . . . .	137
7.4.3	Validation Studies: Dijet Mass Range Studies . . . . .	138
7.4.4	Validation Studies: Spurious Signal . . . . .	141
7.4.5	Validation Studies: Signal Injection . . . . .	143
7.4.6	Search Phase Results . . . . .	146
7.5	<i>Full16_LowMass</i> Search Phase . . . . .	147
7.5.1	Background-Only Samples . . . . .	147
7.5.2	Global Fit Strategy . . . . .	150
7.5.3	Sliding window background estimation (SWiFT) . . . . .	152
7.5.4	Window Selection Strategy . . . . .	153
7.5.5	SWiFT Validation Studies: Window Width Selection Procedure . .	155
7.5.6	SWiFT Validation Studies: Spurious Signal . . . . .	157
7.5.7	SWiFT Validation Studies: Signal Injection . . . . .	162
7.5.8	Results of Window Width Selection Procedure . . . . .	167
7.5.9	Search Phase Results . . . . .	169
<b>8</b>	<b>Di-<i>b</i>-jet Search: Limit Setting Phase</b>	<b>170</b>
8.1	Limit Setting Methodology . . . . .	170
8.2	Description of Systematic Uncertainties . . . . .	173

<i>Contents</i>	8
8.3 <i>Summer16_HighMass</i> Data-set Limits . . . . .	175
8.4 <i>Full16_LowMass</i> Data-set Limits . . . . .	178
8.4.1 Signal Morphing . . . . .	178
8.4.2 Summary of Systematic Uncertainties . . . . .	179
8.4.3 Signal Subtracted Background Estimation . . . . .	180
8.4.4 Results . . . . .	182
<b>9 Future Prospects of Di-<i>b</i>-Jet Searches</b>	<b>185</b>
9.1 Di- <i>b</i> -Jet Searches at Higher Luminosities . . . . .	185
9.2 Combination of <i>b</i> -Tagging Categories . . . . .	186
9.3 Improvement of <i>b</i> -Jet Trigger Efficiency Measurement . . . . .	187
9.4 Signal Plus Background Fit in the Search Phase . . . . .	188
<b>10 Conclusions</b>	<b>189</b>
<b>Appendices</b>	<b>191</b>
<b>A Dijet Binning</b>	<b>191</b>
<b>B Single Jet Trigger Threshold <math>p_T</math> Fit</b>	<b>192</b>
<b>C All Configurations for Low Mass Fit Studies</b>	<b>194</b>
<b>D Colophon</b>	<b>198</b>
<b>E Contents Plan</b>	<b>199</b>
<b>Bibliography</b>	<b>201</b>

# List of Figures

2.1	A schematic showing the gluon propagator with the additional first order loops. . . . .	33
2.2	Summary of measurements of $\alpha_S$ as a function of the energy scale, $Q$ . . . . .	33
2.3	A Feynman diagram showing dijet production in a proton–proton collision through the $qg \rightarrow qg$ channel. . . . .	35
2.4	MMHT2014 NNLO PDFs at $Q^2 = 10 \text{ GeV}^2$ and $Q^2 = 10^4 \text{ GeV}^2$ , with associated 68% confidence-level uncertainty bands. . . . .	37
2.5	A Feynman diagram showing an example of a di-lepton $t\bar{t}$ event. . . . .	39
2.6	The leading-order Feynman diagram of the process $q\bar{q} \rightarrow Z' \rightarrow b\bar{b}$ . . . . .	43
2.7	The leading-order Feynman diagram of the process $bg \rightarrow b^* \rightarrow bg$ . . . . .	44
3.1	Integrated luminosity versus time delivered to and recorded by ATLAS during 2015 and 2016 . . . . .	46
3.2	A cut-away schematic of the ATLAS detector. . . . .	47
3.3	A visualisation of the ATLAS detector and the various sub-detectors with simplified illustrations of how various types of particles interact with the ATLAS detector overlaid. . . . .	48
3.4	A schematic showing a slice of the barrel of the ATLAS Inner Detector including the Insertable <i>B</i> -Layer. . . . .	50
3.5	A schematic showing the barrel and end-cap components of the ATLAS Inner Detector. . . . .	50
3.6	A cut-away schematic of the ATLAS calorimeter system. . . . .	52
3.7	A cut-away of the ATLAS muon spectrometer. . . . .	57
3.8	The layout of the ATLAS magnets. . . . .	58
4.1	A schematic illustrating the formation of hadronic jets and the resulting observed energy deposits in the calorimeter system. . . . .	61

4.2	A schematic illustrating the algorithm used to form a topocluster. The numbers on the grid represent $ S_{\text{cell}} $ and the colours represent the cell label. . . . .	63
4.3	A comparison of the jets formed using the (a) Cambridge-Aachen, (b) $k_T$ and (c) anti- $k_T$ algorithm from the same simulated event. The constituent clusters of each of the jets formed is indicated using various colours. . . . .	66
4.4	Calibration stages for the EM+JES calibration scheme. . . . .	67
4.5	The fractional jet energy resolution uncertainty as a function of jet- $p_T$ and $\eta$ . The total uncertainty is shown as are the contributions from the various sources of uncertainty. . . . .	69
4.6	The fractional jet energy scale uncertainty as a function of jet- $p_T$ and $\eta$ . The total uncertainty is shown as are the contributions from the various sources of uncertainty. . . . .	69
4.7	A diagram to illustrate the key features of a $b$ -jet that are utilised by the base $b$ -tagging algorithms. . . . .	71
4.8	A diagram illustrating how three base flavour tagging algorithms are combined in the MV2 algorithm. . . . .	73
4.9	The expected $b$ -jet efficiency of $b$ -tagging algorithm, MV2, with respect to (a) light-jet and (b) $c$ -jet rejection in simulated $t\bar{t}$ events. The various lines show the performance of the algorithm for different configurations and training setups. . . . .	74
4.10	Ratio of $b$ -tagging efficiency in data and Monte Carlo for the MV2c10 $b$ -tagging algorithm at the 77% working point as a function of jet- $p_T$ , extracted using di-lepton $t\bar{t}$ events. Statistical uncertainties (black lines) and total uncertainties (green shaded region) are shown. . . . .	75
4.11	The total fractional $b$ JES uncertainty shown with the various contributions. . . . .	77
4.12	The validation of the $b$ JES uncertainty in data using the double-ratio $R'_{trk}$ . . . . .	78
5.1	The expected $b$ -jet efficiency of $b$ -jet triggers with respect to (a) light-jet and (b) $c$ -jet rejection in the case where the $b$ -tagging algorithm used is MV2c20 (Black), IP3D+SV1 (Blue) and for the set-up used in Run-1 (red stars) . . . . .	83
5.2	The 60% $b$ -jet trigger efficiency with respect to an offline 70% operating point tag for Data (black) and simulation (red) against jet- $p_T$ (a) and jet- $\eta$ (b). The $b$ -trigger aware GRL is not applied and trigger matching is not required. . . . .	87

5.3	The 60% $b$ -jet trigger efficiency with respect to an offline 70% operating point tag for data from Epoch 1 (black) and simulation (red) against jet- $p_T$ (a) and online beamspot $z$ -position (b). The $b$ -jet trigger aware GRL has not been applied.	89
5.4	(a) The 60% $b$ -jet trigger efficiency with respect to an offline 70% operating point tag and (b) the number of offline jets passing 70% operating point tag and matching a HLT trigger jet against vertex class for data from Epoch 1 (black) and simulation (red). The $b$ -jet trigger aware GRL has not been applied.	89
5.5	The 60% $b$ -jet trigger efficiency with respect to an offline 70% operating point tag for data from epoch 2 (black) and simulation (red) against jet- $p_T$ (a), jet- $\eta$ (b) and online beamspot $z$ -position (c).	91
5.6	$b$ -perf efficiency, $\varepsilon_{bPerf}$ , for data from Epoch 2 (black) and simulation (red) against leading-jet $p_T$ (a), online beamspot $z$ -position (b) and leading jet- $\eta$ (c).	91
5.7	The 60% $b$ -jet trigger efficiency with respect to an offline 70% operating point tag for data from Epoch 3 (black) and simulation (red) against (a) jet- $p_T$ , (b) jet- $\eta$ , (c) online beamspot $z$ -position and (d) vertex class.	92
5.8	The 60% $b$ -jet trigger efficiency with respect to an offline 70% operating point tag for data from Region 1 (black) and simulation (red) against jet- $p_T$ (a) and jet- $\eta$ (b). The $b$ -jet trigger aware GRL has been applied.	94
5.9	$b$ -perf efficiency, $\varepsilon_{bPerf}$ , for data from Region 2 (black) and simulation (red) against leading (a) jet- $p_T$ and (b) jet- $\eta$ . The $b$ -jet trigger aware GRL has been applied.	94
5.10	The 60% $b$ -jet trigger efficiency with respect to an offline 70% operating point tag for the full 2016 data-set (black) and simulation (red) against jet- $p_T$ (a), jet- $\eta$ (b), online beamspot $z$ -position (c) and vertex class (d).	95
5.11	$b$ -perf efficiency, $\varepsilon_{bPerf}$ , for the full 2016 data-set (black) and simulation (red) against (a) leading jet- $p_T$ and (b) jet- $\eta$ . The $b$ -jet trigger aware GRL has been applied.	95
5.12	A comparison of offline jets tagged at the 70% operating point for inclusive jets (red) and truth-matched $b$ -jets (blue) against jet- $p_T$ (a) and jet- $\eta$ (b) in a simulated $t\bar{t}$ sample.	97

5.13 The 60% $b$ -jet trigger efficiency with respect to an offline 70% operating point tag for inclusive jets (black) compared to truth matched $b$ -jets and non $b$ -jets (a) and the case where non $b$ -jet content has been doubled (b) for a simulated $t\bar{t}$ sample. The lower panel in both plots show the ratio to the inclusive efficiency. . . . .	97
5.14 The 60% $b$ -jet trigger efficiency with respect to an offline 70% operating point tag for nominal inclusive case (black) compared to varied inclusive case (red) and just non $b$ -jets (blue) in the case where non $b$ -jet efficiency has been halved (a) and doubled (b) for a simulated $t\bar{t}$ sample. The lower panel in both plots show the ratio of the varied inclusive efficiency to the nominal inclusive efficiency. . . . .	98
5.15 A figure to demonstrate the high- $p_T$ extrapolation procedure for the 60% $b$ -jet trigger efficiency with respect to an offline 70% operating point tag. Data (black) is compared against simulation (red) after various corrections have been applied as a function of jet- $p_T$ . Panel (a) shows the flat normalisation fit uncorrected simulation, panel (b) shows the linear correction fit to normalised simulation, panel (c) shows the linear correction fit errors to the corrected simulation and panel (d) shows the quadratic fit to the corrected simulation. . . . .	100
5.16 The measured 60% $b$ -jet trigger efficiency with respect to an offline 70% operating point tag as measured in data as a function of offline jet- $p_T$ . The central values are shown in black with the statistical error and the green bands represent the total error including systematic errors. . . . .	102
5.17 Data/simulation scale factors for the 60% $b$ -jet trigger efficiency with respect to an offline 70% operating point tag as a function of offline jet- $p_T$ . The central values are shown in black with the statistical error and the green bands represent the total error including systematic errors. . . . .	102
5.18 The measured 60% $b$ -jet trigger efficiency with respect to an offline 70% operating point tag as measured in data (black) and from the corrected simulation (red) as a function of offline jet- $p_T$ . In the ratio plot on the lower panel the extrapolation errors is represented by the red band, whilst the total error is overlaid in green. . . . .	103
5.19 The measured $\varepsilon_{bPerf}$ as measured in data as a function of offline leading jet- $\eta$ . The central values are shown in black with the statistical error and the green bands represent the total error including systematic errors. . . . .	105

6.1	A cartoon illustrating the use of the dijet mass ( $m_{jj}$ ) distribution in the search phase of the di- $b$ -jet analysis. Shown is the smoothly falling distribution from QCD dijet production (SM) and a resonance shape caused by a Beyond Standard Model particle (BSM) . . . . .	108
6.2	The comparisons of the (a) leading jet- $p_T$ ( $p_T^{\text{lead}}$ ) and (b) dijet mass ( $m_{jj}$ ) using events that pass an unprescaled L1_J75 trigger (black) compared to events that pass a range of single-jet triggers (coloured) in one run of 2016 data. As shown in the legend, the single-jet triggers considered are HLT_j380, HLT_j400 and HLT_j360. In plot (b) the <i>Summer16+15</i> event selection (excluding $b$ -tagging) is applied with a leading jet- $p_T$ cut as described in the legend. The ratio with respect to L1_J75 is shown in the lower panel. . . . .	114
6.3	The comparisons of the dijet mass ( $m_{jj}$ ) spectrum of events that pass an unprescaled L1_J75 trigger (black squares) and events that pass the HLT_j380 trigger and the <i>Full16_HighMass</i> event selection jet- $p_T$ requirements (red dots) in one run of 2016 data where L1_J75 is unprescaled. The <i>Full16_HighMass</i> event selection requires that leading jet $p_T$ ( $p_T^{\text{lead}}$ ) $> 430$ GeV and subleading jet- $p_T > 80$ GeV. The jet- $ \eta $ and $ y^* $ of the <i>Full16_HighMass</i> event selection have been applied. The ratio with respect to L1_J75 is shown in the lower panel. . . . .	116
6.4	Comparisons of the dijet mass ( $m_{jj}$ ) of events that pass the analysis jet- $p_T$ cuts of leading (subleading) jet- $p_T > 200$ (80) GeV (black) compared to events that pass a set of low jet- $p_T$ cuts of leading (subleading) jet- $p_T > 200$ (80) GeV (red). The events are required to pass the L1_J75 trigger and are taken from one run of 2016 data where the trigger L1_J75 is unprescaled. In addition the events are required to have (a) $ y^*  < 0.6$ and (b) $ y^*  < 0.8$ . No $b$ -tagging cuts have been applied. . . . .	117
6.5	The dijet flavour composition of the simulated dijet background as a function of dijet mass ( $m_{jj}$ ) for the <i>Summer16+15</i> data-set shown without applying $b$ -tagging (inclusive) and for $\geq 1$ $b$ -tag and 2 $b$ -tag categories. In the legend b, c and l refer to a truth matched $b$ -jet, $c$ -jet and light jet respectively. The <i>Summer16+15</i> data-set event selection has been applied. . . . .	120
6.6	The dijet flavour composition of the simulated dijet background as a function of dijet mass ( $m_{jj}$ ) for the <i>Full16_LowMass</i> data-set shown after the application of online and offline $b$ -tagging requirements. In the legend b, c and l refer to a truth matched $b$ -jet, $c$ -jet and light jet respectively. The <i>Full16_LowMass</i> data-set event selection has been applied. . . . .	121

- 6.7 (a) A comparison of the dijet mass ( $m_{jj}$ ) spectra created using the *EXOT2* derivation and the *FTAG1* derivation. (b) A comparison of the dijet mass spectra of all events and  $b$ -jet trigger matched events using the *FTAG1* derivation. For both plots the full *Full16\_LowMass* event selection is applied. Details of the derivation containers is given in the text. . . . . 123
- 6.8 Event displays showing high dijet mass ( $m_{jj}$ ) events that pass the (a) 2 and (b)  $\geq 1$   $b$ -tag di- $b$ -jet event selection. The left section of the figures show a cut-away of the ATLAS detector; the inner detector is shown in purple, the hadronic calorimeter is shown in blue and the toroid magnet and supporting structure is shown in black and grey. The upper right section of the figures show a close-up view of the inner tracker in the  $r - z$  plane. In both sections tracks inside the inner detector are shown in orange and energy deposits in the EM and hadronic calorimeter are shown in green and yellow respectively. The two leading jets formed are indicated by the cones, a blue cone indicates that the jet has been  $b$ -tagged and a yellow cone indicates that it has not. In the upper right panel the yellow spheres show the primary vertex candidates and the red spheres show the secondary vertex candidates. . . . 126
- 6.9 Plots to show the acceptance of the *Summer16+15* data-set event selection for the  $b^*$  quark and SSM  $Z'$  boson signal models. Panel (a) shows the signal acceptance multiplied by trigger efficiency as a function of the simulated mass of the signal model, in the case where  $b$ -tagging has been applied and not. Panel (b) shows the event tagging efficiency as a function of the dijet mass ( $m_{jj}$ ) for a range of simulated masses,  $m$ , as indicated on the plot. In both figures the  $b$ -tagging categories used are indicated in the legend. Details of the *Summer16+15* data-set event selection are described in the text. 127
- 6.10 Plots to show the acceptance of the *Full16\_HighMass* data-set event selection for the  $b^*$  quark, Sequential Standard Model (SSM)  $Z'$  boson and Dark Matter mediator (DM)  $Z'$  boson signal models. Panel (a) shows the signal acceptance multiplied by trigger efficiency as a function of the simulated mass of the signal model, before and after the dijet mass and  $b$ -tagging requirements are applied. Panel (b) shows the event tagging efficiency as a function of the dijet mass ( $m_{jj}$ ), for the  $b^*$  quark and SSM  $Z'$  boson models for a range of simulated masses,  $m$ , as indicated in the legend. In both figures the  $b$ -tagging categories used are indicated in the legend. Details of the *Full16\_HighMass* data-set event selection are described in the text. . . . 128

6.11 Plots to show the acceptance of the <i>Full16_LowMass</i> data-set event selection for the Sequential Standard Model (SSM) $Z'$ boson and Dark Matter mediator (DM) $Z'$ boson signal models. Panel (a) shows the signal acceptance multiplied by trigger efficiency as a function of the simulated mass of the signal model, before and after the dijet mass and offline $b$ -tagging requirements are applied. Panel (b) shows the event tagging efficiency of just online $b$ -tagging and the combination of online and offline $b$ -tagging as a function of the dijet mass, $m_{jj}$ , for the SSM $Z'$ boson at a range of simulated masses, $m$ , as indicated in the legend. Details of the <i>Full16_LowMass</i> data-set event selection are described in the text. . . . .	128
7.1 The Wilks' $p$ -value as a function of luminosity for a $8.8 \text{ fb}^{-1}$ subset of <i>Summer16_HighMass</i> data-set in the (a) 2 $b$ -tag and (b) $\geq 1$ $b$ -tag category. . . . .	137
7.2 The scaled dijet mass distribution (red) compared to the effective entries dijet mass distribution (green) of Monte-Carlo simulation of QCD dijet production for the (a) 2 $b$ -tag and (b) $\geq 1$ $b$ -tag category. The <i>Summer16_HighMass</i> data-set event selection has been applied. . . . .	138
7.3 The dijet mass distribution taken from multi-jet simulation for the (a) 2 $b$ -tag and (b) $\geq 1$ $b$ -tag, category, fitted to using the 4 parameter dijet fit function, with the lower edge of the dijet mass spectrum at $m_{jj} = 1100 \text{ GeV}$ . The BumpHunter algorithm is run to identify the most discrepant excess, as indicated by the blue lines. Pseudo-experiments are used to assign the excess a $p$ -value, which is shown on the plot. The <i>Summer16_HighMass</i> data-set event selection has been applied. . . . .	139
7.4 The BumpHunter (top row), DeficitHunter (middle row) and $\chi^2$ (bottom row) $p$ -values for the search phases using the 4 parameter dijet fit function performed to the dijet mass spectrum taken from the simulation of QCD dijet production for the 2 $b$ -tag category (left column) and $\geq 1$ $b$ -tag category (right column) as a function lower edge of the dijet mass ( $m_{jj}$ ) spectrum used in search phase. The <i>Summer16_HighMass</i> data-set event selection has been applied to the simulation. . . . .	140

7.5	The dijet mass spectrum taken from multi-jet simulation for the (a) 2 $b$ -tag and (b) $\geq 1$ $b$ -tag, category, fitted to using the 4 parameter dijet fit function, with lower mass bound of the fit range $m_{jj} = 1378$ GeV. The BumpHunter algorithm is run to identify the most discrepant excess, as indicated by the blue lines. Pseudo-experiments are used to assign the excess a $p$ -value, which is shown on the plot. The <i>Summer16_HighMass</i> data-set event selection has been applied. . . . .	141
7.6	The scaled dijet mass distribution (red) compared to the effective entries of the dijet mass distribution (green) for the 2 $b$ -tag category, for the (a) 2 $b$ -tag and (b) $\geq 1$ $b$ -tag case. Overlaid is a data-like distribution (blue) created by applying Poisson fluctuations to the scaled distribution. The <i>Summer16_HighMass</i> data-set event selection has been applied. . . . .	142
7.7	A data-like distribution taken from multi-jet simulation for the (a) 2 $b$ -tag and (b) $\geq 1$ $b$ -tag, category, fitted to using the 3 parameter dijet fit function. The BumpHunter algorithm is run to identify the most discrepant excess, as indicated by the blue lines. Pseudo-experiments are used to assign the excess a $p$ -value, which is shown on the plot. The <i>Summer16_HighMass</i> data-set event selection has been applied. . . . .	142
7.8	The BumpHunter test statistic observed when the search phase is applied to a data-like distribution from a simulated QCD dijet sample compared to the distributions of the BumpHunter test statistic for 10,000 pseudo-experiments applied to the background estimation for the (a) 2 $b$ -tag and (b) $\geq 1$ $b$ -tag categories. The fraction of pseudo-experiments with a BumpHunter test statistic greater than the observed value is the BumpHunter $p$ -value. . . . .	143
7.9	The distribution of BumpHunter (top row), DeficitHunter (middle row) and $\chi^2$ (bottom row) $p$ -values for the search phase using the 3 parameter dijet fit function performed on 200 data-like dijet mass spectra taken from the simulation of QCD dijet production for the 2 $b$ -tag category (left column) and $\geq 1$ $b$ -tag category (right column). The <i>Summer16_HighMass</i> data-set event selection has been applied to the simulated sample. . . . .	144
7.10	The dijet mass ( $m_{jj}$ ) spectrum of the <i>Summer16_HighMass</i> data-set in the (a) 2 $b$ -tag and the (b) $\geq 1$ $b$ -tag category compared to the background estimation created using the 3 parameter dijet fit function. The most discrepant excess as found by the BumpHunter algorithm and associated the $p$ -value are shown. . . . .	146

7.11 The dijet mass ( $m_{jj}$ ) spectra of the full <i>Full16_LowMass</i> data-set and a $3 \text{ fb}^{-1}$ subset of <i>Full16_LowMass</i> data. The lower panel shows a ratio. . . . .	148
7.12 A figure showing the process of obtaining the <i>Full16_LowMass</i> fitting control region dijet mass ( $m_{jj}$ ) spectrum used for the <i>Full16_LowMass</i> data-set fit studies. Panel (a) shows the dijet mass spectrum of events before $b$ -tagging is applied (0-tag) and of a $3 \text{ fb}^{-1}$ subset of <i>Full16_LowMass</i> data. Panel (b) shows the offline $b$ -tagging efficiency with respect to online tagging estimated using the luminosity adjusted ratio of the two spectra in plot (a), the lower panel shows the significance of difference between the luminosity adjusted ratio and the fit. Panel (c) shows the dijet mass spectrum of the fitting control region and the full <i>Full16_LowMass</i> data-set. Panel (d) shows the smooth and data-like dijet mass spectra from the fitting control region. . . . .	149
7.13 The smooth dijet mass spectrum from the <i>Full16_LowMass</i> fitting control region fitted to using the 3, 4 and 5 parameter global fits. The lower panel shows the significance of the difference between the data and the background fits. . . . .	151
7.14 The global fit and BumpHunter algorithm procedure run on the smooth dijet mass spectrum from the <i>Full16_LowMass</i> fitting control region using the global 4 and 5 parameter dijet fit functions. The upper panel shows the data compared to the background estimate and the lower panel shows the significance of the difference between the two. The most discrepant excess as found by the BumpHunter algorithm is indicated by the vertical blue lines and the $p$ -value of this excess is printed on the plot. . . . .	151
7.15 The windows used by the SWiFt background estimate in the <i>Full16_LowMass</i> data-set analysis for a range of window half-widths. The bin centre is indicated by the black mark and the corresponding window is indicated by the coloured squares. . . . .	153
7.16 The cumulative probability of the global $\chi^2$ $p$ -value, and number of window fits with Wilks' $p$ -value $< 0.1$ of the SWiFt background estimation for 100 data-like distributions taken from the <i>Full16_LowMass</i> fitting control region. The SWiFt procedure has been performed using the 5 parameter dijet fit function for the range of window half-widths ( $wHW$ ) of 10 to 16. The fraction of seeds that pass the fit quality requirements for each swift configuration is shown in the bottom right of the plot. . . . .	156

- 7.17 An illustration of the window selection procedure for a  $3 \text{ fb}^{-1}$  subset of *Full16\_LowMass* data. It shows the global  $\chi^2$   $p$ -value, and number of window fits with Wilks'  $p$ -value  $< 0.1$  for the SWiFt background estimate using a range of window half-widths ( $wHW$ ) and number of parameters (nPars) of the dijet fit function. The dotted lines indicate thresholds that are used in the window selection procedure. . . . . 156
- 7.18 The SWiFt search phase run on a  $3 \text{ fb}^{-1}$  subset of the *Full16\_LowMass* data-set. The SWiFt procedure has been run for the 4 and 5 parameter dijet fit function for a window half-width ( $wHW$ ) of 16. The upper panel shows the data compared to the background estimate and the lower panel shows the significance of the difference between the two. The most discrepant excess as found by the BumpHunter algorithm is indicated by the vertical blue lines and the  $p$ -value of this excess is printed on the plot. . . . . 157
- 7.19 The SWiFt search phase run on the smooth distribution from the *Full16\_LowMass* fitting control region. The SWiFt procedure has been run for the 4 and 5 parameter dijet fit function for a window half-width ( $wHW$ ) 10 and 16. The upper panel shows the data compared to the background estimate and the lower panel shows the significance of the difference between the two. The most discrepant excess as found by the BumpHunter algorithm is indicated by the vertical blue lines and the  $p$ -value of this excess is printed on the plot. . . . . 158
- 7.20 The SWiFt search phase run on a data-like dijet mass spectrum of the *Full16\_LowMass* fitting control region. The SWiFt procedure has been run for the 4 and 5 parameter dijet fit function for a window half-width ( $wHW$ ) of 16. The upper panel shows the data compared to the background estimate and the lower panel shows the significance of the difference between the two. The most discrepant excess as found by the BumpHunter algorithm is indicated by the vertical blue lines and the  $p$ -value of this excess is printed on the plot. . . . . 159
- 7.21 This figure shows the normalised distribution of BumpHunter  $p$ -values from performing the SWiFt background estimate to an ensemble of data-like distributions taken from the *Full16\_LowMass* fitting control region. This is repeated for the 4 and 5 parameter dijet fit function for a symmetric window with window half-width ( $wHW$ ) range of 10 to 16, giving the 8 different window width and fit function combinations. The number of data-like distributions or seeds is given on the plot. . . . . 161

7.22 The SWiFt search phase run on a data-like distribution from the fitting control region with a simulated SSM $Z'$ boson of mass 800 GeV injected. The SWiFt procedure has been run for the 5 parameter dijet fit function for a window half-width ( $wHW$ ) range of 10 to 16. . . . .	164
7.23 The SWiFt search phase run on a data-like distribution from the fitting control region with a simulated SSM $Z'$ boson of mass 800 GeV and the nominal cross-section injected. The SWiFt search phase is run for the 5 parameter dijet fit function for a window half-width ( $wHW$ ) of (a) 16 and (b) 14 with an exclusion region of 705-834 GeV. . . . .	165
7.24 An illustration of the window selection procedure a data-like distribution when a simulated SSM $Z'$ boson has been injected of mass 800 GeV with the nominal cross-section, and a region 705-834 GeV of has been excluded from the SWiFt background estimation. It shows the global $\chi^2$ $p$ -value and number of window fits with Wilks' $p$ -value $< 0.1$ for SWiFt background estimate, for a range of window half-widths ( $wHW$ ) and the 5 parameter dijet fit function. The procedure would have selected the 5 parameter dijet fit function with a window half-width of 14. . . . .	165
7.25 An illustration of the window selection procedure for the full <i>Full16_LowMass</i> data-set. It shows the global $\chi^2$ $p$ -value and number of window fits with Wilks' $p$ -value $< 0.1$ for the SWiFt background estimate using a range of window half-widths ( $wHW$ ) and the 5 parameter dijet fit function. The dotted lines indicate the requirements used in the window selection procedure. A window half-width of 16 is selected. . . . .	168
7.26 The $\chi^2$ $p$ -value and Wilks' $p$ -value for each window fit in the SWiFt background estimate performed on the full <i>Full16_LowMass</i> data-set, shown as a function of the window centre. The 5 parameter dijet fit function with a window half-width of 16 is used as the SWiFt configuration. The dotted lines indicate thresholds that are used in the window selection procedure. . . . .	168
7.27 The dijet mass spectrum ( $m_{jj}$ ) of the <i>Full16_LowMass</i> data-set and the SWiFt background estimation created using the 5 parameter dijet fit function and a window half-width ( $wHW$ ) of 16. The most discrepant excess found by the BumpHunter algorithm and the $p$ -value of this excess are indicated on the plot. . . . .	169
8.1 The background systematic uncertainties as a function of dijet mass in the <i>Summer16+15</i> data-set analysis. . . . .	175

8.2	95% credibility level upper limits on cross-section times acceptance times tagging efficiency for the $Z'$ boson and $b^*$ quark as a function of simulated mass using the <i>Summer16+15</i> data-set. . . . .	176
8.3	95% credibility observed upper limits on the product of cross-section, detector acceptance, tagging efficiency and branching ratio ( $\sigma \times A \times \epsilon \times BR$ ) for Gaussian signals using the <i>Summer16+15</i> data-set. . . . .	177
8.4	Simulated SSM $Z'$ boson dijet mass signal templates and the intermediate dijet mass signal templates created using the signal morphing technique used in the <i>Full16_LowMass</i> data-set limit setting phase. . . . .	178
8.5	The $b$ -jet trigger and background systematic uncertainties for the <i>Full16_LowMass</i> data-set as a function of dijet mass ( $m_{jj}$ ). . . . .	179
8.6	The nominal SWiFt background and signal subtracted background (SSB) estimations for a data-like dijet mass spectrum from the fitting control region with a SSM $Z'$ boson injected as a ratio to the nominal SWiFt background estimation performed on the same data-like dijet mass spectrum when no signal is injected. . . . .	181
8.7	The ratio of signal subtracted background estimations and the SWiFt background estimate performed on the full <i>Full16_LowMass</i> data-set. . . . .	182
8.8	95% credibility level upper limits on cross-section times acceptance times tagging efficiency ( $\sigma \times A \times \epsilon$ ) for the $Z'$ boson and as a function of simulated mass using the <i>Full16_LowMass</i> data-set. . . . .	183
8.9	95% credibility upper limits on the product of cross-section, detector acceptance, tagging efficiency and branching ratio, $\sigma \times A \times \epsilon \times BR$ , for Gaussian signals using the <i>Full16_LowMass</i> data-set. . . . .	184
B.1	A plot showing the threshold jet- $p_T$ at which a trigger is 99% efficient with respect to a lower- $p_T$ benchmark trigger as a function of the trigger-level $p_T$ requirements of the single jet trigger. A linear fit is performed, as shown by the red line. The $1\sigma$ error band on the fit slope is shown by the dotted lines. . . . .	193
C.1	The SWiFt search phase procedure run on the smooth distribution from the fitting control region in the low-mass category. The SWiFt configurations are 4 and 5 parameter fit function for a window-half-width (wHW) range of 10 to 16. . . . .	194
C.2	The SWiFt search phase procedure run on a data-like distribution from the fitting control region in the low-mass category. The SWiFt configurations are 4 and 5 parameter fit function for a window-half-width (wHW) range of 10 to 16. . . . .	195

C.3 This figure shows the normalised distribution of BUMPHUNTER $p$ -values from performing the SWiFt background estimate to an ensemble of data-like distributions taken from the fitting control region in the low-mass category. The SWiFt configurations are 4 and 5 parameter fit function for a window-half-width (wHW) range of 10 to 16.	196
C.4 The SWiFt search phase procedure run on a data-like distribution from the fitting control region with a Pythia8 SSM $Z'$ of mass 800 GeV injected. The SWiFt procedure has been run for the 4 and 5 parameter fit function for a window-half-width (wHW) range of 10 to 16.	197

# List of Tables

2.1	The key properties of the particles of the Standard Model . . . . .	30
3.1	Summary of the main characteristics of the components of the ATLAS Inner Detector. . . . .	51
3.2	A summary of the stochastic and constant terms of the intrinsic energy resolution of components of the ATLAS calorimeter. . . . .	56
4.1	The Mv2c10 b-tagging algorithm operating points; with the corresponding $b$ -jet efficiency, $c$ -jet rejection, light-jet rejection and $\tau$ rejection. . . . .	74
5.1	A table describing the effect of not finding a valid xPrmVtx primary vertex on different epochs of data. . . . .	88
5.2	A table showing the systematic assigned for the high- $p_T$ extrapolation. . . .	99
5.3	A table showing the jet-level Data/simulation scale factor (SF) as a function of jet- $p_T$ with total error and the contributions of the different systematics considered; specifically statistical, high- $p_T$ extrapolation, non- $b$ -jet purity and non- $b$ -jet trigger efficiency. . . . .	101
5.4	A comparison of the systematic uncertainty on the $b$ -jet trigger jet-level efficiency for various offline operating points (OP) w.r.t. the 60% online operating point. The increase in systematic looser offline operating points is driven by non $b$ -jet impurities. . . . .	103
5.5	A table showing the event-level Data/MC scale factor (SF) as a function of leading jet- $\eta$ with total error and the contributions of the different systematics considered. . . . .	104

6.1	The estimated $S/\sqrt{B}$ at $18.9 \text{ fb}^{-1}$ for 4 different MV2c10 operating points (OP). $S$ is estimated using a simulated SSM $Z'$ boson sample and $B$ is estimated using a $18.9 \text{ fb}^{-1}$ subset of 2 $b$ -tag category data. The <i>Full16_HighMass</i> data-set event selection has been applied. Three different simulated mass points are considered and the mass windows used to estimate $S$ and $B$ for each mass point are shown in the table. . . . .	119
6.2	The estimated $S/\sqrt{B}$ at $3 \text{ fb}^{-1}$ for 3 different MV2c10 operating points (OP). $S$ is estimated using a simulated SSM $Z'$ boson sample and $B$ is estimated using a $3 \text{ fb}^{-1}$ subset of data. The <i>Full16_LowMass</i> data-set event selection has been applied. Three different simulated mass points are considered and the mass windows used to estimate $S$ and $B$ for each mass point are shown in the table. . . . .	119
6.3	A summary of the key details of the di- $b$ -jet event selections applied for each of the data-sets considered. For full details refer to the text. . . . .	125
7.1	The functional form of the dijet fit functions. The fit functions are named by the number of free parameters used. $p_i$ are the free parameters of the fit function. $\sqrt{s}$ is the centre-of-mass energy of the collisions. . . . .	132
7.2	The fraction of data-like distributions (seeds) with a BumpHunter $p$ -value less 0.1 and 0.05, for the SWiFt search phase performed to an ensemble of data-like distributions taken from the <i>Full16_LowMass</i> fitting control region. 161	
7.3	The BumpHunter $p$ -value when performing the SWiFt search phase with no region exclusion applied on a data-like spectrum that has been injected with a sequential standard model $Z'$ with a variety of simulated masses when the cross-section has been multiplied by a normalisation factor 1, 2 or 3 (Signal Norm.). The SWiFt search phase has been performed using a window half-width range of 10 to 16 and the number of parameters used in the dijet fit function (nPars) are 4 or 5. A dash indicates that the largest excess found by BumpHunter algorithm is not consistent with the simulated mass of the injected signal. Bold text indicates that the SWiFt configuration has a BumpHunter $p$ -value $< 0.01$ and is selected by the window selection procedure after the region exclusion procedure has been applied. . . . .	166
8.1	A table summarising the signal systematic uncertainties used in the <i>Summer16+15</i> data-set. . . . .	175
8.2	A table summarising the signal systematic uncertainties used in the <i>Full16_LowMass</i> data-set. . . . .	179

9.1	A summary of the integrated luminosity of data-sets used by the di- <i>b</i> -jet analyses performed at ATLAS and the expected integrated luminosities at key points in the LHC schedule . . . . .	186
9.2	A comparison of the observed 95% credibility level upper mass limits set by the <i>Summer16_HighMass</i> data-set analysis and a di- <i>b</i> -jet search performed by the CMS collaboration . . . . .	187

## Chapter 1

# Introduction

The Standard Model is the current best description of the fundamental particles of the universe and their interactions. However, inconsistencies within the Standard Model indicates that there must be Beyond Standard Model (BSM) physics. Many proposed BSM models predict the existence of new particles which preferentially decay to a pair or  $b$ -quarks or a  $b$ -quark and a gluon. The observation of such a particle would provide crucial experimental evidence in the development of a more complete theory of particle physics.

Many searches for BSM resonances decaying to a pair of quarks or gluons have been performed using the invariant mass distribution of pairs of hadronic jets created by high-energy hadron collisions [1], such searches are known as inclusive dijet searches. Inclusive dijet searches have been performed in 13 TeV proton–proton collisions at the LHC in the mass range 1.1 – 8 TeV [2, 3, 4] and 0.1 – 1.5 TeV [5, 6, 7]; no evidence of a BSM resonance has yet been found.

The sensitivity of dijet searches to BSM models decaying to one or more  $b$ -quarks can be increased using hadronic jets containing  $b$ -quarks, which leads to a significant reduction of Standard Model backgrounds. Such searches are known as di- $b$ -jet searches. Di- $b$ -jet searches have previously been performed by the CDF collaboration using 1.8 TeV  $p\bar{p}$  collisions at the Tevatron [8] and the CMS collaboration using 8 TeV  $pp$  collisions at the LHC [9], no evidence of a BSM resonance was found.

Di- $b$ -jet searches have been performed using the ATLAS experiment with higher-energy proton–proton collisions than any previous di- $b$ -jet search, representing an unprecedented opportunity to search for BSM resonances decaying to  $b$ -quarks. This thesis presents two di- $b$ -jet searches performed by using 13 TeV  $pp$  collision data collected in 2015 and 2016 by the ATLAS detector. A high-mass di- $b$ -jet search probes the mass region 1.4 – 6 TeV using an integrated luminosity of  $13.3 \text{ fb}^{-1}$ ; the analysis has been published as

a conference note [10]. A low-mass di-*b*-jet search probes the mass region  $0.6 - 1.5$  TeV using an integrated luminosity of  $24.3 \text{ fb}^{-1}$ ; the analysis is soon to be published.

For the low-mass di-*b*-jet search real-time identification of *b*-jets is used to collect data, this data-acquisition tool is known as the ATLAS *b*-jet trigger. Therefore, for the low mass di-*b*-jet search a detailed understanding of the performance of the ATLAS *b*-jet trigger is required. The measurement of the ATLAS *b*-jet trigger efficiency in 2016 data is also presented in this thesis.

## 1.1 Structure of Thesis

The thesis presents the di-*b*-jet searches in the following structure.

Firstly, the theoretical and experimental background to the di-*b*-jet searches is discussed.

- **Chapter 2** presents a description of the Standard Model, a summary of the motivations for BSM physics and an outline of some BSM models that predict resonances decaying to one or more *b*-quarks.
- **Chapter 3** presents a description of the LHC accelerator and the ATLAS detector.
- **Chapter 4** presents the reconstructed physics objects used in di-*b*-jet searches.
- **Chapter 5** presents a description of the triggers used in di-*b*-jet searches and the measurement of the ATLAS *b*-jet trigger efficiency in 2016 data.

Then, the two di-*b*-jet searches presented in this thesis are described in consecutive chapters.

- **Chapter 5** presents an outline of the analysis strategy and the event selection used in the di-*b*-jet searches.
- **Chapter 6** presents the search phase of the di-*b*-jet searches; which is a search for evidence of resonances in the di-*b*-jet events selected. The strategy and results from the search phase for both di-*b*-jet searches are shown.
- **Chapter 7** presents the limit setting phase of the di-*b*-jet searches. The strategy and results of the limit setting phase for both di-*b*-jet searches are shown.

Finally, the work presented in this thesis is summarised.

- **Chapter 8** presents an outlook of the future prospects of the di-*b*-jet searches.
- **Chapter 9** presents the conclusions of the research presented in this thesis

## 1.2 Personal Contributions

In modern experimental particle physics most research is performed as part of large collaborations, such that the technical complications of building, running and analysing the experiments can be shared amongst many. One such of these collaborations is the ATLAS experiment at the LHC, comprised of over 3,000 physicists and engineers.

This thesis presents research performed between September 2014 and December 2017 carried out as part of the ATLAS collaboration. To present the research in a complete form, the work must be presented within the context of the research carried out by the the ATLAS collaboration. Furthermore, only the most significant contributions of the work are presented, such that this thesis forms a coherent and consistent document without repetition or outdated studies.

For clarity, this section summarises my personal contributions to the research activities of the ATLAS collaboration and highlights where these are presented in the thesis. In addition, all figures and tables that I did not produce are indicated using a citation in the caption, only figures that I produced do not have a citation.

- ***b*-Tagging:**

I was an active member of the *b*-tagging group between September 2014 and September 2015. I investigated improvements to *b*-tagging at high jet- $p_T$  and performed the first data/simulation comparisons of *b*-tagging performance in 13 TeV data using dijet events collected between May and July 2015 by the ATLAS detector.

- **Di-*b*-jet Search with *Full15\_HighMass* data-set:**

Between September 2015 and February 2016 I was a member of the analysis team that performed the first ever di-*b*-jet search at ATLAS. This analysis searched the mass range 1.2 – 5 TeV using  $3.2 \text{ fb}^{-1}$  of 13 TeV  $pp$  collision data collected in 2015 by the ATLAS detector. The analysis has been published here [11]. I performed validated studies for the background estimation procedure.

- **Di-*b*-Jet Search with *Full15\_LowMass* data-set:**

Between February 2015 and June 2016 I was a member of the analysis team that performed the first ever di-*b*-jet search at ATLAS using a *b*-jet trigger. This analysis searched the mass range 0.6 – 1.2 TeV using  $3.2 \text{ fb}^{-1}$  of 13 TeV  $pp$  collision data collected in 2015 by the ATLAS detector. This analysis has been published as a conference note [12]. I performed validated studies for the background estimation procedure.

- **Di-*b*-Jet Search with *Summer16\_HighMass* data-set:**

Between June 2015 and September 2016 I was a member of the analysis team for the *Summer16\_HighMass* data-set analysis. This analysis is presented in Chapters 6-8. The analysis has been published as a conference note [10]. I was responsible for:

- Validating the background estimation and search phase (presented in Section 7.4)
- Selection of the mass range of the analysis (Section 6.4)
- Creation of event displays (Section 6.4)

- ***b*-Jet Trigger Efficiency Measurement with *Full16\_LowMass*:**

Between September 2016 and December 2017 as part of the *b*-jet trigger group, I was the lead analyser of the *b*-jet trigger efficiency measurement in 2016 data which is presented in Section 5.3. I was responsible for all aspects of the analysis, using a framework and strategy developed by John Alison.

- **Di-*b*-Jet Analysis with *Full16\_LowMass* data-set:**

Between September 2016 and December 2017 I was a member of the analysis team for the *Full16\_LowMass* data-set analysis. The analysis is presented in Chapters 6-8. This analysis is soon to be published; therefore internal ATLAS documentation [13] is cited to indicate work performed by other members of the analysis team. I was responsible for:

- All aspects of event selection, except *b*-tagging optimisation (Section 6.4)
- Validation and results of the search phase (Section 7.5)
- Adapting the data processing framework for the use of the *b*-jet trigger.
- Derivation of *b*-jet trigger and background systematic uncertainties,

  - Creation of background templates used in limit-setting phase (both Section 8.4).

- Representing the analysis to ATLAS collaboration as analysis contact.

- **Di-*b*-jet Analysis with *Full16\_HighMass* data-set:**

Between September 2016 and December 2017 I was a member of the analysis team for the *Full16\_HighMass* data-set analysis. This analysis is soon to be published together with the *Full16\_LowMass* data-set analysis. The analysis is not presented in this thesis. I contributed towards the validation of the background estimation and search phase.

- **Event Display:**

Between July 2015 and December 2016 I carried out maintenance of the ATLANTIS Event Display used in the ATLAS control room and performed shifts as on-call ‘expert’.

## Chapter 2

# An Incomplete Theory

One of the great questions that humans have always tried to answer is what are the fundamental building blocks of the universe and what are the rules that govern them? The current best answer to this question is the ‘*Standard Model of Particle Physics*’, a mathematical description of a finite set of fundamental particles and their interactions. The Standard Model has been found to agree with experimental data at great precision [14] and as a result is the foundation of the field of particle physics. However, it is known that this is not a complete theory and there must be a deeper underlying theory that lies beyond the Standard Model.

This chapter firstly aims to describe the Standard Model and possible Beyond Standard Model physics in the context of di- $b$ -jet searches. Section 2.1 briefly describes the particles and forces of the Standard Model. Section 2.2 describes hadronic jet formation and the production of the dominant Standard Model background to di- $b$ -jet searches. Section 2.3 will discuss Beyond Standard Model (BSM) physics; specifically the problems in the Standard Model that require BSM physics and proposed BSM models that predict resonances preferentially decaying to one or two  $b$ -quarks.

## 2.1 The Standard Model

The Standard Model is a quantum field theory, meaning that the theory describes a finite set of particles and their interactions in terms of a set of fields.

### 2.1.1 Particles

There are 18 fundamental matter particles in the Standard Model, where fundamental means that they are not composed of other constituent particles. Full details of the Standard Model particles are found in [15].

These particles form three groups of particles with similar properties, which are:

- **Quarks:** There are 6 different types of quarks, known as flavours, arranged in 3 generations. For each quark there is also an anti-quark, which has identical mass and spin, but opposite charge and quantum numbers.
- **Leptons:** There are 6 different types of leptons, arranged into 3 generations, each containing a charge  $-1$  particle and a charge 0 neutrino. For each lepton there is also an anti-lepton.
- **Bosons:** There are a set of integer-spin particles known as bosons. The bosons act as the mediators of the forces that will be described below.

Table 2.1 summarises the key properties of the matter particles.

Particle Group	Particle Name	Symbol	Charge	Spin	Mass [GeV]
Quark	Up	$u$	$+2/3$	$1/2$	0.002
	Down	$d$	$-1/3$	$1/2$	0.005
	Charm	$c$	$+2/3$	$1/2$	1.3
	Strange	$s$	$-1/3$	$1/2$	0.096
	Top	$t$	$+2/3$	$1/2$	173
	Bottom	$b$	$-1/3$	$1/2$	4.2
Lepton	Electron	$e$	$-1$	$1/2$	$5.1 \times 10^{-4}$
	Electron Neutrino	$\nu_e$	0	$1/2$	$<2 \times 10^{-9}$
	Muon	$\mu$	$-1$	$1/2$	0.11
	Muon Neutrino	$\nu_\mu$	0	$1/2$	$<1.9 \times 10^{-4}$
	Tau	$\tau$	$-1$	$1/2$	1.8
	Tau Neutrino	$\nu_\tau$	0	$1/2$	$<1.8 \times 10^{-2}$
Boson	Photon	$\gamma$	0	1	0
	W-boson	$W^\pm$	$\pm 1$	1	80
	Z-boson	$Z_0$	0	1	91
	Gluon	$g$	0	1	0
	Higgs Boson	$H$	0	0	125

**Table 2.1:** The key properties of the particles of the Standard Model, organised by particle group and then by generation. Values taken from [15].

## 2.1.2 Forces

The Standard Model combines three key quantum field theories. The first is the electro-weak theory [16] which describes three interactions grouped into two forces: the electromagnetic and weak forces. The second is Quantum Chromodynamics (QCD) [17] which describes the strong force. Finally, the Brout-Englert-Higgs Mechanism [18, 19] describes the origin of mass in the Standard Model<sup>1</sup>. Each of the forces is discussed below.

- **Electro-magnetic (EM) Force:**

The EM force is an interaction between electrically charged particles and is mediated by the photon. The strength of the EM coupling is proportional to the EM coupling constant,  $\alpha_{EM}$ , multiplied by the product of the charges of the two particles, where  $\alpha_{EM} \sim 1/137$ .

- **Weak Force:**

The weak force is composed of the two remaining interactions from electro-weak theory; the neutral current interaction and the charged current interaction.

- The ‘*neutral current interaction*’ is mediated by the  $Z_0$  boson, interacts with all fermions, and does not allow flavour changing interactions.
- The ‘*charged current interaction*’ is mediated by the  $W^+$  and  $W^-$  bosons, has a universal interaction with all fermions, and flavour changing interactions are allowed. In the quark sector, the charged current interaction couples with weak eigenstates of fermions rather than their flavour eigenstates, allowing for interactions that change the generation of the quark’s flavour. The relative amplitudes of each flavour changing interaction is described by the CKM matrix; the values of this matrix highly suppresses generational changing interactions involving the 3rd generation of quarks.

At low energies ( $Q < m_W$ ) the weak force is less strong than the EM force due to the large mass of the  $W/Z$  boson (Weak/EM  $\sim 10^{-4}$ ) and at larger energies ( $Q \geq m_W$ ) the EM force and weak force become comparable in strength.

- **Strong Force:**

Quantum Chromodynamics (QCD) describes the strong force. The strong force is mediated by the gluon and interacts with particles that have colour charge; which are quarks and gluons. QCD has 3 colour charges: known as red, green and blue. A quark has a colour charge, an anti-quark has an anti colour charge and a gluon has a colour charge and an anti-colour charge, leading to 8 independent colour states of a gluon. A colour neutral object can be formed if all three colour charges are present (i.e. in a baryon containing three quarks) or if a colour and the corresponding anti-colour is present (i.e. in a meson that contains  $q\bar{q}$ ). QCD describes hadronic jet formation and the largest background in a

---

<sup>1</sup>With the exception of the neutrinos, whose mass is not described by the Standard Model.

di- $b$ -jet search, so is discussed further in Section 2.2.

- **Higgs Mechanism:**

The Higgs mechanism <sup>2</sup> introduces an extra scalar field to the Standard Model with a Higgs potential given by the so-called ‘Mexican-hat potential’. This allows for spontaneous symmetry breaking which gives mass to the bosons of the Standard Model. In addition, a Yukawa coupling term between the scalar field and the fermions gives rise to the mass of the fermions <sup>3</sup>. A final prediction of the Higgs mechanism is the existence of the Higgs boson. The first observation the Higgs boson by the ATLAS [20] and CMS [21] experiments in 2012 confirms the Higgs mechanism, a great triumph of the Standard Model.

## 2.2 QCD: Hadronic Jet Formation and Dijet Production

As described above Quantum Chromodynamics (QCD) is a theory that describes the strong interaction between quarks and gluons. This section will firstly describe renormalisation of QCD, which is important for understanding how QCD works. Then I will describe two elements of QCD that are critical to the analyses being presented in this thesis; the formation of hadronic jets and the production of dijet events through QCD in proton–proton collisions, the dominant background in di- $b$ -jet searches. Quarks and gluons can often fill similar roles in hadronic jet formation and dijet production, hence I will refer to them collectively as ‘partons’ in this section.

### 2.2.1 Renormalisation and the Running of $\alpha_S$

For any calculation in QCD, or indeed any quantum field theory, one must consider the higher-order loop diagrams; for example a simple gluon propagator has additional first-order loops as shown in Figure 2.1. The summation over all higher-order loops leads to divergences in calculations of scattering events in QCD.

To avoid these divergences, there is a well accepted mathematical tool, known as renormalisation, where one effectively re-scales the fields in the Lagrangian [17]. Renormalisation is done such that the divergences are removed when performing perturbative calculations of QCD. This leads to a dependence of the strong coupling constant,  $\alpha_S$ , on the renormalisation scale used,  $\mu_R$ , an effect known as the running of  $\alpha_S$ . To get an effective strength of the strong interaction in any given process, the value of  $\mu_R$  is set as the scale of the momentum transfer,  $Q$ , of the process. The running of  $\alpha_S$  can be measured through

---

<sup>2</sup>Also known as the Higgs-Englert-Brout mechanism

<sup>3</sup>With the exception of the neutrinos, whose mass is not described by the Standard Model

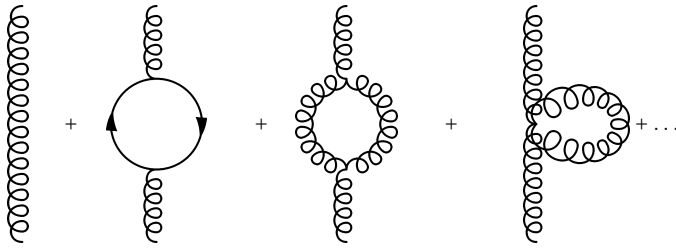


**Figure 2.1:** A schematic showing the gluon propagator with the additional first order loops [22].

experimental observation; Figure 2.2 shows the measured values of  $\alpha_s$  as a function of the energy scale,  $Q$ , in a range of experiments.

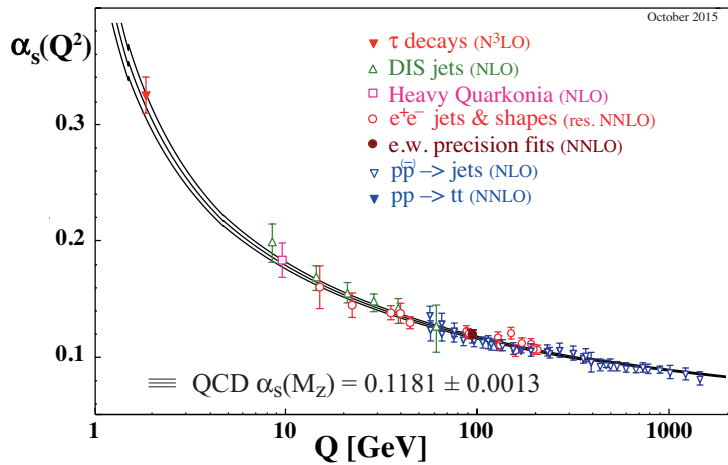


**Figure 2.2:** Summary of measurements of  $\alpha_s$  as a function of the energy scale,  $Q$ . The respective degree of QCD perturbation theory used in the extraction of  $\alpha_s$  is indicated in brackets (NLO: next-to-leading order; NNLO: next-to-next-to leading order; res. NNLO: NNLO matched with resummed next-to-leading logs; N3LO: next-to-NNLO) [17].

There are three features of Figure 2.2 that should be noted. Firstly, the size of  $\alpha_s$  is generally large compared to  $\alpha_{EM}$ ; this means that, depending on the energy scale, the strong force is typically stronger than the EM force by one or two orders of magnitude. Secondly, at high energies/small distances the strong force becomes relatively weak, this phenomenon is known as ‘asymptotic freedom’. At these energy scales, perturbative expansions of QCD are possible. Finally, at low energies/large distances the strong force is exceptionally strong. As a result, if two interacting quarks become separated by a large distance then it becomes energetically favourable to pair-produce  $q\bar{q}$  pairs from the vacuum until a colour neutral object can be formed. Therefore quarks are not observed in isolation, but instead quarks form colour neutral hadrons; this feature of QCD is known as ‘confinement’. At low-energy scales perturbative expansions of QCD are not possible.

## 2.2.2 Hadronic Jet Formation

It is common in hadronic colliders that a high-momentum quark or gluon will be produced in the final-state<sup>4</sup>. However, due to the effect of quark confinement described above, an isolated quark or gluon will not be observed. Instead a stream of energetic, collimated hadrons will be formed, known as a hadronic jet. Hadronic jet formation occurs through two distinct processes; parton-shower and hadronisation.

- **Parton Shower:**

The high-energy final-state quark or gluon will split into a  $qg$  or  $q\bar{q}$  pair respectively. The resulting quarks and gluons will also undergo splitting to form more partons, which in turn can split. This process continues to form the parton shower. Due to relativistic effects, each splitting will generally be at a small opening angle in the lab-frame and as such the partons will be highly collimated in the direction of the initial parton. The parton shower process occurs at high energy such that the value of  $\alpha_S$  is small and thus perturbative expansions of QCD can be used to perform calculations. However, at each step of the splitting the energy of the partons decreases and thus the value of  $\alpha_S$  increases.

- **Hadronisation:**

When the energy scale becomes small<sup>5</sup>,  $\alpha_S$  becomes large such that the dominant QCD effect is quark confinement. Therefore, the quarks and anti-quarks produced in the parton shower form hadrons. The hadrons are colour neutral objects, meaning that stable hadrons that do not interact through QCD will be formed<sup>6</sup>. The hadronisation process occurs at large values of  $\alpha_S$  so cannot be calculated using perturbative expansions; models such as the string model [23] and the cluster model [24] are used to simulate hadronisation.

The end result of the hadronisation process is a set of collimated stable hadrons, known as a hadronic jet, which can be observed in an experiment. Note that our understanding of how one goes from an initial parton to a hadronic jet is model dependant, for example there is a choice of hadronisation model. Hence, in experiment this dependence is removed by defining a jet in terms of observables, such that the experimental results are model-independent and results can be reinterpreted when improved models become available<sup>7</sup>. The details of the experimental definition of a hadronic jet is discussed in Section 4.2.

<sup>4</sup>An example of this is dijet production, as will be described in Section 2.2.3.

<sup>5</sup>This is generally defined as small relative to the hadronic scale,  $\Lambda$ , which is typically a few hundred MeV

<sup>6</sup>Some unstable hadrons, such as a  $\Delta^{++}$ , may be initially formed in the process but these will decay rapidly through the strong interaction. In addition, some hadrons might not be stable under the weak interaction, such as a Kaon, but the time-scale of their decays will be much larger.

<sup>7</sup>A good explanation of why model-independent jets is desirable is found here [25]

### 2.2.3 Dijet Production in $pp$ Collisions

QCD dijet production is one of the most common process that occurs in proton–proton colliders. QCD dijet production occurs when the two protons interact through QCD to give two quarks or gluons in the final state; the frequency of this interaction is described by the hadronic cross-section,  $\sigma_{had}$ . The free partons will then form hadronic jets through the processes described in Section 2.2.2. Figure 2.3 shows the Feynman diagram of dijet production in a proton–proton collision through the  $qg \rightarrow qg$  channel.

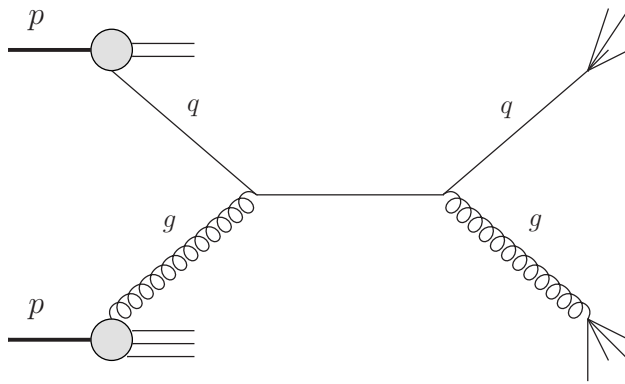


**Figure 2.3:** A Feynman diagram showing dijet production in a proton–proton collision through the  $qg \rightarrow qg$  channel. Adapted from [26].

To calculate the hadronic cross-section,  $\sigma_{had}$ , in a proton–proton collision, two elements are separated out in a process called ‘*factorisation*’.

The first element is the ‘*parton-level cross-section*’,  $\hat{\sigma}$ , which is the cross-section of two partons from the proton ( $p_i$  and  $p_j$ ) scattering to give two final state partons ( $p_k$  and  $p_l$ ). In Figure 2.3,  $p_i$  and  $p_j$  represent the incoming  $q$  and  $g$  and  $p_k$  and  $p_l$  represent the the outgoing  $q$  and  $g$ . The parton-level cross section is discussed further in Section 2.2.3.1.

The second element is the *Parton Distribution Function* (PDF),  $F_i(x_i)$ , which gives the number density of a specific parton,  $p_i$ , with momentum fraction,  $x_i$ , in a proton. Momentum fraction is defined as the fraction of the proton’s total momentum that the parton is carrying,  $x = p_{\text{parton}}/p_{\text{proton}}$ . This part of the interaction is indicated by the circles on the left of the Feynman diagram in Figure 2.3. Further details on PDFs is found in Section 2.2.3.2.

The elements are combined to calculate  $\sigma_{had}$ :

$$\sigma_{had} = \sum_{i,j,k,l} \int dx_i dx_j F_i(x_i, Q^2) F_j(x_j, Q^2) \hat{\sigma}(p_i, p_j \rightarrow p_k p_l) \quad (2.1)$$

where there is an integral over all possible values of momentum fractions  $x_i$  and  $x_j$ , a sum

over all possible initial partons from the two protons labelled  $i$  and  $j$ , and a sum over all possible final-state partons labelled by  $k$  and  $l$ <sup>8</sup>.  $Q^2$  is the energy scale of the collision.

With the two elements separated we can discuss each separately.

### 2.2.3.1 Parton-level Cross-Section

To describe the parton-level cross-section, some useful variables must first be defined. The first is the invariant mass of the outgoing partons,  $m_{kl}$ , which is given in terms of the four-momentum of the two partons;

$$m_{kl}^2 = (p_k^\mu + p_l^\mu)^2 \quad (2.2)$$

Then there are two related angular variables,  $y^*$  and  $\theta^*$ , defined in terms of the rapidities of the outgoing partons,  $y_k$  and  $y_l$ ;

$$y^* = \left( \frac{y_k - y_l}{2} \right) \quad (2.3)$$

$$\cos(\theta^*) = \tanh(y^*) \quad (2.4)$$

Finally the Mandelstam variables are defined as,

$$\hat{s} = m_{kl}^2, \quad \hat{t} = -\hat{s}(1 - \cos \theta^*), \quad \hat{u} = -\hat{s}(1 + \cos \theta^*) \quad (2.5)$$

The Mandelstam variables represent the square of the 4-momentum of the propagator in a 2→2 particle scatter event for an s, t or u-channel Feynman diagram respectively.

The parton-level differential cross-section of incoming partons  $i$  and  $j$  scattering to give outgoing partons  $k$  and  $l$  is given in terms of the variables  $\theta^*$  and  $m_{kl}$  [27];

$$\frac{d^2\hat{\sigma}(p_i, p_j \rightarrow p_k p_l)}{dm_{kl}^2 d\cos \theta^*} = \frac{\pi \alpha_s^2}{2 m_{kl}^2} \delta(x_i x_j s - m_{kl}^2) S(ij \rightarrow kl) \frac{1}{1 + \delta_{kl}} \quad (2.6)$$

where  $\sqrt{s}$  is the centre-of-mass energy and  $S(ij \rightarrow kl)$  is the process dependant kinematics of a  $ij \rightarrow kl$  parton scatter. The  $\delta(x_i x_j s - m_{kl}^2)$  term requires that the invariant mass of the incoming partons is same as the invariant mass of the propagator.

The  $S(ij \rightarrow kl)$  for each process is given in Table 1 in [1]. All but one process can occur through a t-channel diagram and therefore the  $S(ij \rightarrow kl)$  for those processes contains a  $1/\hat{t}$  or  $(1/\hat{t})^2$  term. The importance of this will be discussed in Section 2.2.3.3.

---

<sup>8</sup>The final state sums do not include top-quarks because, as will be discussed in Section 2.2.4, they do not form regular jets. In addition, due to its heavy mass, the top-quark is heavily suppressed in the PDFs so can be ignored in the sum over initial partons.

### 2.2.3.2 Parton Distribution Functions

The proton contains two  $u$ -quarks and a  $d$ -quark, known as valence quarks, and a sea of quarks and gluons created through QCD interactions, such as gluons being emitted from the valence quarks and  $q\bar{q}$  pairs being produced from the emitted gluons.

Parton Distribution Functions (PDFs) give the number density of a specific parton  $p_i$  in a proton  $P_i$  for a given momentum fraction  $x_i$  and energy scale,  $Q$ . Due to the large value of  $\alpha_S$  in the proton, QCD cannot be considered in perturbative expansions and as such the PDFs cannot be calculated directly. Instead the PDFs can be measured by combining a range of experimental scattering results. In particular, strong constraints on the PDFs come from deep inelastic scattering using  $ep$  colliders, such as HERA [28]; the strong constraints are due, in part, to there only being one parton in the collision allowing direct access to the PDFs in a cross-section measurement.

Figure 2.4 shows the  $xF(x, Q^2)$  for a  $Q^2$  of 10 and  $10^4$   $\text{GeV}^2$  from the MMHT2014 PDF set [29]. The various coloured lines represent the PDF for each of the different partons. It shows that as  $x$  increases the values of the PDF for the sea quarks and gluons will fall smoothly; this is because it is energetically unfavourable to produce high momentum gluons or  $q\bar{q}$  pairs. The fall in the PDFs with respect to  $x$  is particularly notable for the gluon which is the dominant contribution at large  $Q^2$  and at low  $x$ . The PDFs of the valence quarks,  $u_v$  and  $d_v$ , have a peak value around  $x \sim \frac{1}{3}$ , and then fall off rapidly at higher  $x$ . This shape is caused as at leading-order the quarks share the momentum equally, but higher-order QCD effects smear this distribution.

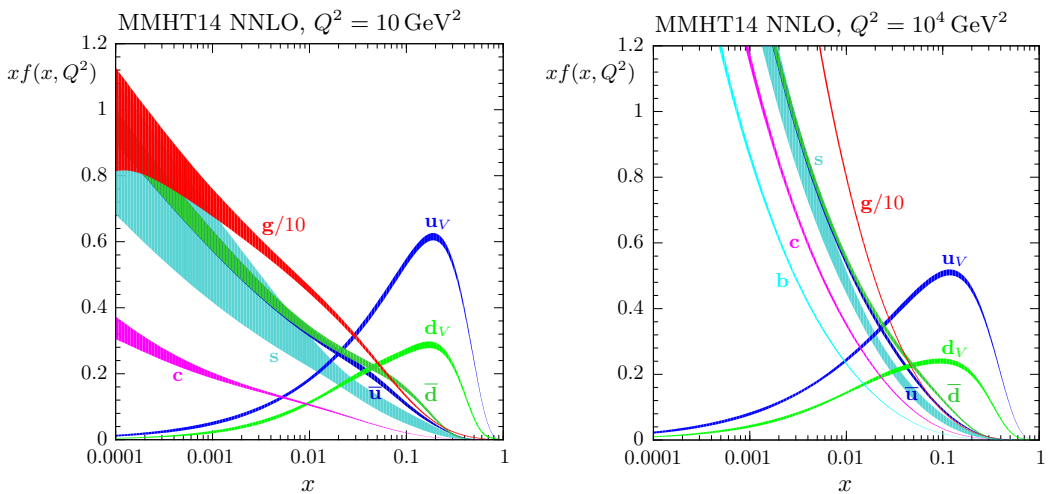


**Figure 2.4:** MMHT2014 NNLO PDFs at  $Q^2 = 10 \text{ GeV}^2$  and  $Q^2 = 10^4 \text{ GeV}^2$ , with associated 68% confidence-level uncertainty bands [29].

### 2.2.3.3 Features of the QCD Dijet Production

From the two factorised elements discussed above, there are four important features of the dijet hadronic cross-section that are significant when forming the di-*b*-jet search strategy.

- **Large cross-section :**

The strong coupling constant  $\alpha_s$  is large meaning that the dijet cross-section is large. Therefore QCD dijet production is the dominant background in di-*b*-jet searches.

- **Smoothly falling with respect to  $m_{kl}$  :**

QCD dijet production will be smooth and monotonically decreasing with respect to  $m_{kl}$  as a result of three factors. Firstly, the cross section has a  $1/m_{kl}^2$  term. Secondly, as shown in Section 2.2.1,  $\alpha_s$  will smoothly decrease with increasing  $Q$ , which in this case is correlated with  $m_{kl}$ . Finally, as  $m_{kl}$  increases then the momentum fraction of the proton,  $x$ , required to create the dijet event will also increase. As shown in Figure 2.4, the parton distribution functions are generally falling with respect to  $x$ , which will lead to falling behaviour in the hadronic cross-section.

- **Increased production at large values of  $|y^*|$  :**

As discussed in Section 2.2.3.1, all but one of the  $S(ij \rightarrow kl)$  terms contains a  $1/\hat{t}$  or  $(1/\hat{t})^2$  contribution from t-channel Feynman diagrams. These terms will become large when  $\hat{t} \rightarrow 0$  which, from the definition of  $\hat{t}$  in Equation 2.5, occurs when  $\cos \theta^* \rightarrow 1$ . This means that QCD dijet production is increased large values of  $|y^*|$ .

- **Preference of light-flavour quarks:**

Most  $ij \rightarrow kl$  processes that produce heavy flavour quarks (*c* or *b*), with the exception of  $q\bar{q} \rightarrow b\bar{b}$  (or  $c\bar{c}$ ) and  $gg \rightarrow b\bar{b}$  (or  $c\bar{c}$ ), require a heavy flavour quark to be one of the initial partons. Figure 2.4 shows the heavy flavour quarks are suppressed in the PDFs relative to the other partons. Therefore, dijet events will be dominated by jets initiated by gluons or light-quarks (*u*, *d* or *s*).

Finally, it should be noted that the above description of the QCD dijet production is not complete; only considered tree-level diagrams have been considered, but there also exists higher-orders diagrams. Related to that issue is the occurrence of initial state and final state radiation, known as ISR and FSR respectively. ISR is when an additional parton is radiated off the incoming parton and FSR is when an additional parton is radiated off an outgoing parton. ISR and FSR can lead to additional jets in an event, creating a multi-jet event.

In addition, there is also the Underlying Event (UE) which effectively comprises of the remnants of the proton not used in the hard-scatter. The UE will mostly be hadronic activity and as a result can lead to additional jets in the event, again creating a multi-jet event.

### 2.2.4 A Special Case: $t\bar{t}$

The top-quark is a special case when discussing the formation of jets from quarks, due to two properties of the top quark which are distinctive. Firstly, due to the large suppression of decays from the 3rd generation in the CKM matrix, the top quark decays to a  $b$ -quark and a  $W$ -boson with a branching ratio of close to 1. Secondly, the top quark is much heavier than the bottom quark meaning that the decay to a  $b$ -quark is very energetically favourable. Therefore, the top-quark decays on a shorter time-scale than parton shower process resulting in two separate objects; the  $W$ -boson and the hadronic jet.

As in dijet production,  $t\bar{t}$  pairs can be pair-produced in proton–proton collisions through QCD interactions. The two top quarks will decay into two  $W$ -bosons and two jets containing  $b$ -quarks. One mode of  $t\bar{t}$  decay is when one  $W$ -boson decays into a  $l^+ \nu_l$  pair and the other into a  $l^- \bar{\nu}_l$  pair. This is known as a di-lepton  $t\bar{t}$  event, a Feynman diagram showing an example of a di-lepton  $t\bar{t}$  event is shown in Figure 2.5<sup>9</sup>.

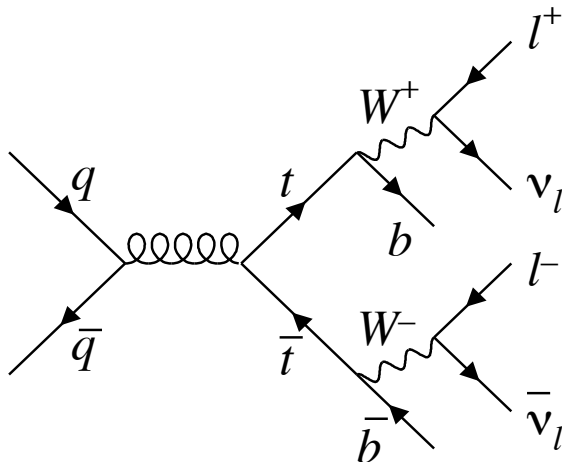


**Figure 2.5:** A Feynman diagram showing an example of a di-lepton  $t\bar{t}$  event [30].

Di-lepton  $t\bar{t}$  forms a distinct experimental signature. In particular, the case of opposite flavour di-lepton  $t\bar{t}$ , where the two leptons have different flavours, is very distinct as this can only be caused by two separate weak-decays. In addition we have two jets formed from  $b$ -quarks, which can be observed. The distinct signature of di-lepton  $t\bar{t}$  events and the fact that the top-quark nearly always decays to a  $b$ -quark means that this decay topology is often used to obtain a pure sample of jets containing  $b$ -quarks, as will be done in Section 4.3.4 and 5.3.

---

<sup>9</sup>This figure shows the  $q\bar{q}$  mode of  $t\bar{t}$  production. The  $gg$  mode is the dominant at the LHC

## 2.3 Beyond Standard Model Physics

The preceding sections of this chapter described the Standard Model and some of its successes. However, the Standard Model is known to be an incomplete picture of the universe. This section will present some of the key deficiencies of the Standard Model demonstrating that Beyond Standard Model (BSM) physics is required and discuss some proposed BSM models that motivate the analyses shown in this thesis.

### 2.3.1 Motivations

The motivations for BSM physics listed in this section describe only a subset of deficiencies of the Standard Model, with a focus on the most important missing parts and those that motivate models searched for in this thesis.

#### 2.3.1.1 Gravity

When listing forces in Section 2.1.2, we made no reference to gravity. This is because our description of gravity, Einstein’s General Theory of Relativity, has not been successfully merged with the Standard Model in a so-called ‘Quantum Theory of Gravity’. It is a clear inadequacy of the Standard Model that there is no explanation of gravity

#### 2.3.1.2 Dark Matter

Astronomers have been able to make the remarkable observation that  $\sim 80\%$  of the universe’s matter must be so-called ‘Dark Matter’ [31]. Dark Matter are particles not described by the Standard Model, so is clear evidence of Beyond Standard Model physics. It is known that Dark Matter interacts through gravity and can only interact weakly, if at all, with the Standard Model, otherwise we would have already observed it through interactions with Standard Model particles .

The evidence for Dark Matter comes from many separate astronomical observations: such as studies of galaxy rotation curves, the cosmic microwave background and a collision of two clusters of galaxies known as the bullet cluster, A wider summary of the evidence for Dark Matter can be found here [32].

Furthermore, it is believed the Dark Matter couples to the Standard Model. This is required in many models of Dark Matter [33] to explain the observed relative abundance of Dark Matter particles in the universe. As a result this means that there may be some yet unknown mechanism that couples to both Dark Matter and Standard Model particles; this mechanism is referred to as a Dark Matter mediator.

### 2.3.1.3 Hierarchy Problem

The Hierarchy problem [34] is the fact that the energy scale of the Higgs mechanism, ( $M_H = 125$  GeV), is much smaller than the energy scale of gravity, known as the Planck scale ( $M_{Planck} \sim 10^{19}$  GeV) [15]. This means that the energy scale of the Standard Model is very far from the energy scale of the next known interaction, gravity.

The Hierarchy problem leads to complications in theoretical calculations, such as the that of the Higgs boson mass [34]. When calculating the Higgs boson mass one must consider radiative contributions from additional loop diagrams, similar to the corrections considered for a gluon propagator shown in Figure 2.1. However, these contributions are found to be of the order  $\delta m_H^2 \sim \frac{1}{16\pi^2} M_{Planck}^2$ , orders of magnitude larger than the observed mass of the Higgs boson. This means that some mechanism must either cancel the contributions or reduce their size. Whilst the free parameters of the Standard Model can be chosen such that these different contributions approximately cancel out, such fine-tuning of the parameters is hard to believe without some underlying explanation.

Instead, there are two solutions typically proposed to stabilise the effect of the loop corrections. Firstly, one can introduce BSM physics that has loop contributions that cancel the Standard Model contributions. For example this occurs in theories of supersymmetry [35]. Secondly, one can introduce some BSM physics at a new energy scale such that the loop diagram contributions are cut off at  $\delta m_H^2 \sim \frac{1}{16\pi^2} M_{BSM}^2$ . If the BSM physics is on the TeV scale then this would reduce the size of the loop corrections to the scale of the Higgs boson's mass, giving some prior belief that new physics could be found at this energy scale.

### 2.3.1.4 Generational Structure of Quarks

The quarks of the Standard Model have a well ordered generational symmetry. However the generational symmetry is not perfect; each generation is heavier than the previous one and within the generations quarks have different masses. In particular, the third generation of quarks is somewhat special; the top quark is much heavier than the bottom quark and is the heaviest particle of the Standard Model. Furthermore, as the mass of the top quark is close to the mass of the Higgs boson, the 3rd generation of quarks have a role symmetry breaking within the Higgs mechanism for some BSM models [36].

There is no good explanation of why there is generational structure in the Standard Model, why the mass hierarchy is unsymmetric or why the third generation has one quark with such a large mass. The generational structure could be a result of some underlying broken symmetry which forms a part of a deeper theory of particle physics. Any deeper

theory explaining the generational structure could contain observable BSM particles, and, given the special nature of the third generation, the BSM particles could couple strongest with the third generation of quarks.

Unlike the case of Dark Matter, the generational structure of quarks and the special nature of the third generation is not concrete evidence of BSM physics. But it does mean that there are motivations to be particularly interested in searches for resonances decaying to the third generation of quarks.

### 2.3.2 Beyond Standard Model Theories

The previous section discussed a list of deficiencies of the Standard Model, which makes us confident that Beyond Standard Model physics must exist. This leads us to ask what the new theory of physics could be and how can one obtain evidence of such a theory.

Many proposed theories of BSM physics include the addition of a new particle and, in particular, the special nature of the third generation<sup>10</sup> means that some models of BSM predict new particles that preferentially decay to two  $b$ -quarks or a  $b$ -quark and a gluon. Furthermore, the Hierarchy Problem suggests that BSM physics may exist at the TeV energy-scale. The observation of such a resonance would be evidence of BSM physics.

Two such models that predict resonances with preferential decays to  $b$ -quarks are discussed below. These are used as ‘benchmark models’ in the analyses presented in this thesis, where a benchmark model is a plausible signal model that is used to form and optimise a search strategy. Furthermore the benchmark models are used to represent many models that decay to one or more  $b$ -quarks.

#### 2.3.2.1 $Z'$ Boson

One of the most simple additions to the Standard model is that of a  $U(1)'$  gauge symmetry which would result in an additional spin-1 boson, known as the  $Z'$  boson. An additional  $U(1)'$  symmetry appears in many different BSM models and is therefore a well motivated BSM extension [37]. The  $Z'$  boson can decay to a pair of  $b$ -quarks, as shown in Figure 2.6.

Three different  $Z'$  boson models are considered. The first is known as the ‘*Sequential Standard Model*’ (SSM)  $Z'$  in which the couplings of the new  $Z'$  boson are the same as the Standard Model. The strongest limits on the SSM  $Z'$  boson at the TeV scale are set by searching for a  $Z'$  boson decaying to lepton pairs [38]<sup>11</sup>. The second model is a ‘*lepto-*

---

<sup>10</sup>Discussed in Section 2.3.1.4

<sup>11</sup>Because a di-lepton signature is distinct to the large QCD dijet backgrounds produced in  $pp$  collisions

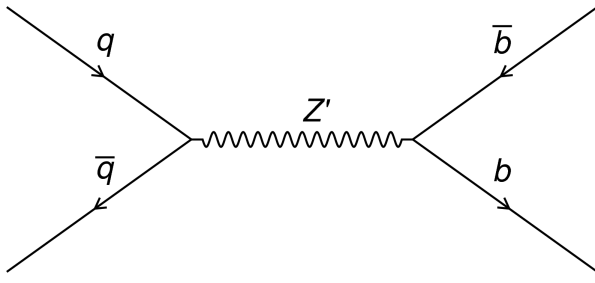


**Figure 2.6:** The leading-order Feynman diagram of the process  $q\bar{q} \rightarrow Z' \rightarrow b\bar{b}$ .

*phobic*'  $Z'$  boson that does couple to the lepton sector but has the same coupling to each of the quarks as the Standard Model [39], this model is therefore not strongly constrained by di-lepton searches.

The final model is a '*Dark Matter inspired*' (DM)  $Z'$  model; in which the DM  $Z'$  boson acts as a Dark Matter mediator which can couple to both the Dark Matter sector and the Standard Model quark sector [40]. The motivation for a Dark Matter mediator was discussed in Section 2.3.1.2. This model introduces an additional  $U(1)'$  symmetry and a Dirac fermion Dark Matter particle that only interacts through the new gauge group. The resulting DM  $Z'$  boson does not couple with the lepton sector and couples with the DM fermion and the Standard Model quark sector with couplings  $g_\chi$  and  $g_{SM}$ , respectively.

It is worth noting in the models considered the  $Z'$  boson does not preferentially decay to  $b$ -quarks but rather with similar branching ratio as the other quarks. However, this can still be considered as preferential decay to  $b$ -quarks with respect to the dijet background, which is dominated by gluons and quarks from the first two generations, as discussed in Section 2.2.3. Furthermore, there exists  $Z'$  models that do not couple to all generations equally [41], such that a  $Z'$  boson preferentially decaying to  $b$ -quarks is possible.

### 2.3.2.2 Excited Third-Generation Quark

To explain the generational and mass structure of the quark sector, discussed in Section 2.3.1.4, quark compositeness models describe quarks, not as fundamental particles, but instead constructed of other fundamental particles. One consequence of quark compositeness models is the prediction of excited quarks,  $q^*$ , which can be observed as heavy resonances.

In particular we consider an excited 3rd generation quark, the  $b^*$  quark. The dominant decay mode of a  $b^*$  quark is to  $bg$  with a branching ratio of 85% while the remaining decay

modes are to  $Wt$ ,  $bZ$  and  $b\gamma$  with branching ratios of 10%, 4.5% and 0.5% respectively<sup>12</sup>. A Feynman diagram showing the dominant production and decay mode of a  $b^*$  quark is shown in Figure 2.7.

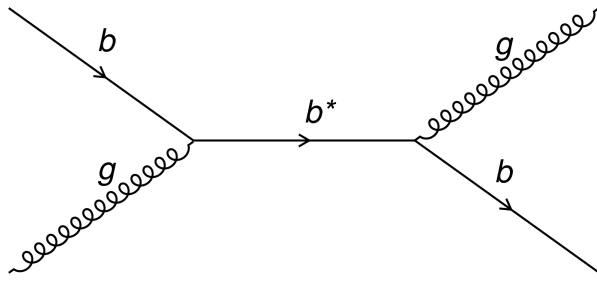


**Figure 2.7:** The leading-order Feynman diagram of the process  $bg \rightarrow b^* \rightarrow bg$

### 2.3.2.3 Model Independence

The two benchmark models demonstrate that searching for particles decaying to one or two  $b$ -quarks is well motivated. However, it is important to note that the prior belief in any specific model of BSM is small. This is because there are many BSM theories proposed and there is little evidence to prefer one model over another. In addition, one must also consider that the true theory may not have been anticipated, such that experiments might be able to see evidence of something truly unexpected.

This means that the di- $b$ -jet searches should be constructed to be sensitive to as many BSM models as possible and allow for the unexpected gifts that nature might throw up.

---

<sup>12</sup>Using the assumptions outlined in [42].

## Chapter 3

# The LHC and the ATLAS Detector

### 3.1 The Large Hadron Collider (LHC)

High-energy particle colliders have been an essential tool in high-energy physics research for over 50 years, with a rich history of discovering new particles as each generation of collider pushes the energy frontier; including the discovery of the Z and W bosons using the Super Proton Synchotron at CERN in 1983 [43, 44, 45, 46] and the discovery of the top-quark at the Tevatron in 1995 [47, 48].

The Large Hadron Collider (LHC) is the highest energy collider ever built, operated by the *Conseil Européen pour la Recherche Nucléaire (CERN)*. Lying in a tunnel 100 m beneath the Swiss/French border near Geneva, the LHC is a 27 km circumference ring of superconducting magnets and accelerating structures, which accelerate beams of protons to a maximum energy of 6.5 TeV. These proton beams are collided in four different locations on the LHC ring and around each collision point a different detector is constructed to observe these collisions; one such of these detectors is the ATLAS detector.

#### 3.1.1 LHC running conditions in 2015 and 2016

Since May 2015 the LHC has been colliding bunches of protons at a center-of-mass energy of 13 TeV, the highest energy collisions ever obtained by a particle collider<sup>1</sup>. In 2015 and 2016 the LHC produced  $pp$  collisions with a bunch spacing of 25 ns<sup>2</sup>

*Integrated luminosity*,  $L$ , is the quantity used to describe the size of a data-set from a collider experiment. Integrated luminosity is defined is defined using  $N_{evt} = \sigma * L$ , where  $\sigma$  is the cross-section of a particular process occuring at that collider experiment and  $N_{evt}$  is the

---

<sup>1</sup>The period of data-taking from 2015 is known as Run-2.

<sup>2</sup>A small amount of data in 2015 was collected with a bunch spacing of 50 ns

number of events that occur through that process in the data-set. Instantaneous luminosity is the measure used to define the rate of data-collecting by the ATLAS detector and is defined as  $\frac{dL}{dt}$ .

Figure 3.1 shows the integrated luminosity delivered by the LHC and recorded by ATLAS in 2015 and 2016; an integrated luminosity of  $3.9 \text{ fb}^{-1}$  and  $35.6 \text{ fb}^{-1}$  was recorded by ATLAS in 2015 and 2016 respectively [49].

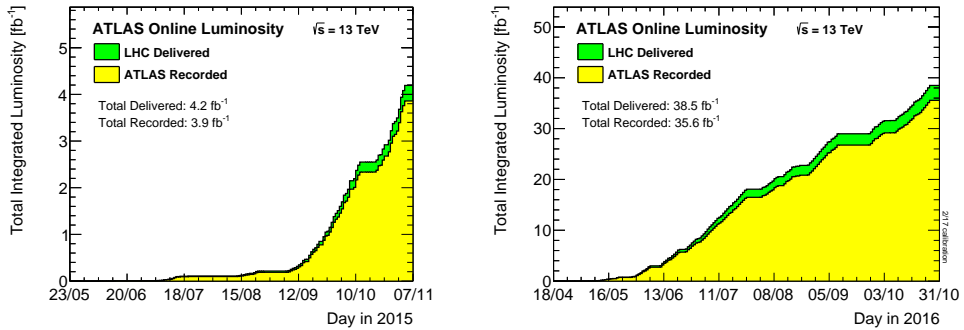


**Figure 3.1:** Integrated luminosity versus time delivered to (green) and recorded by ATLAS (yellow) during stable beams for  $pp$  collisions at 13 TeV centre-of-mass energy in (a) 2015 and (b) 2016 [49].

To be able to produce a high instantaneous luminosity bunches of protons are collided meaning that there is more than one collision per bunch-crossing. This causes ‘pile-up’ to occur; which is physics objects caused by collisions other than the hard-scatter collision<sup>3</sup> of interest. The average number of collisions per bunch-crossing ( $\langle\mu\rangle$ ) is 23.7 in 2015 and 2016 data taken by ATLAS.

## 3.2 ATLAS Detector Description

The ATLAS (**A** Toroidal **L**arge **H**adron **C**ollider **A**pparatuS) detector design, construction and performance has been described in detail in [50, 51, 52]. Therefore this chapter provides a general description of the detector with a focus on the needs of di-*b*-jet searches.

The ATLAS detector is effectively a large closed cylindrical detector, made up of four key components which sit in concentric rings around the interaction point, where the proton bunches collide. These components are the inner detector, calorimeters, muon spectrometer and the magnets; each of which are described in further detail below. This design is used as each sub-detector measures different quantities and interacts differently to the various

---

<sup>3</sup>Hard-scatter refers a collision that produced a high- $p_{\text{T}}$  object

range of particles that ATLAS is required to observe, such that the ATLAS detector is able to identify and measure the key properties<sup>4</sup> of particles that pass through its volume. Figure 3.2 shows a cut-away schematic of the detector and Figure 3.3 shows a slice of the detector in the plane perpendicular to the beam-pipe, overlaid are simplified illustrations how the detector responds to a range of particles [53].

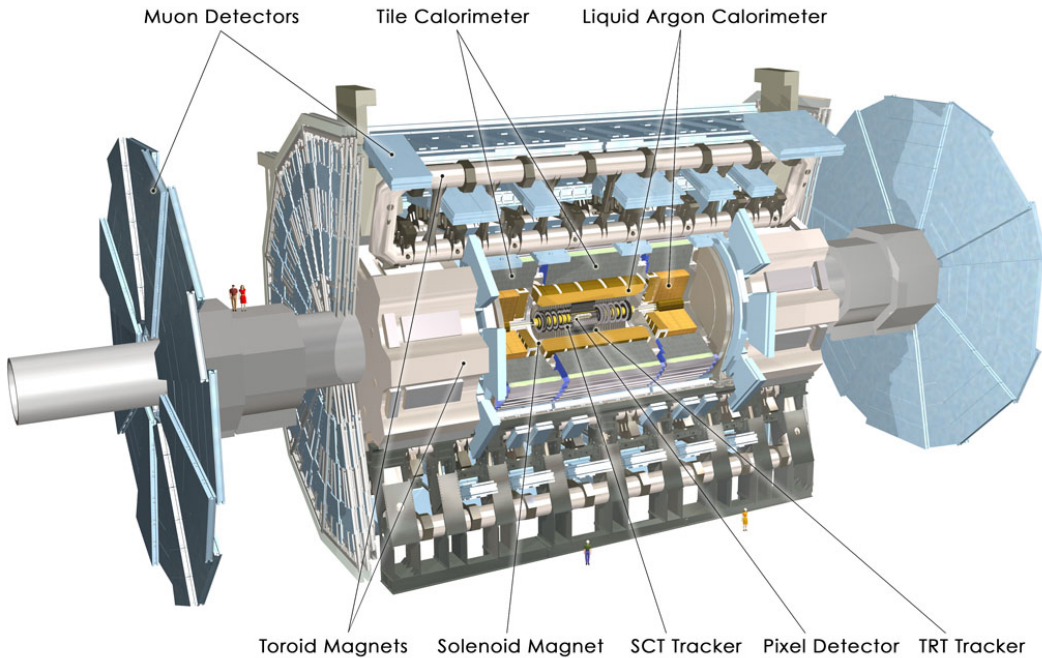


**Figure 3.2:** A cut-away schematic of the ATLAS detector [50].

### 3.2.1 ATLAS Co-ordinate System

Firstly, to describe the detail of the ATLAS detector there must be a description of the co-ordinate system that is used. ATLAS uses a right-handed coordinate system, in which the origin lies at the interaction point. The  $x$ -axis points towards the centre of the LHC ring parallel to the surface of the earth, the  $y$ -axis points upwards towards the surface of the earth and the  $z$ -axis runs along the beam-pipe, pointing anti-clockwise along the LHC beam-pipe. The azimuthal angle,  $\phi$ , is defined right-handedly around the  $z$ -axis starting at the  $x$ -axis.

The polar angle,  $\theta$ , is defined as the angle measured from the  $z$ -axis, such that along the  $z$ -axis corresponds to  $\theta = 0$  and anti-aligned with the  $z$ -axis corresponds to  $\theta = \pi$ . However, to define the angular direction with respect to the  $z$ -axis the ATLAS co-ordinate system uses pseudo-rapidity,  $\eta$ , instead of using  $\theta$ , for reasons that will be outlined below.  $\eta$  is defined

---

<sup>4</sup> For example four-momentum and charge.

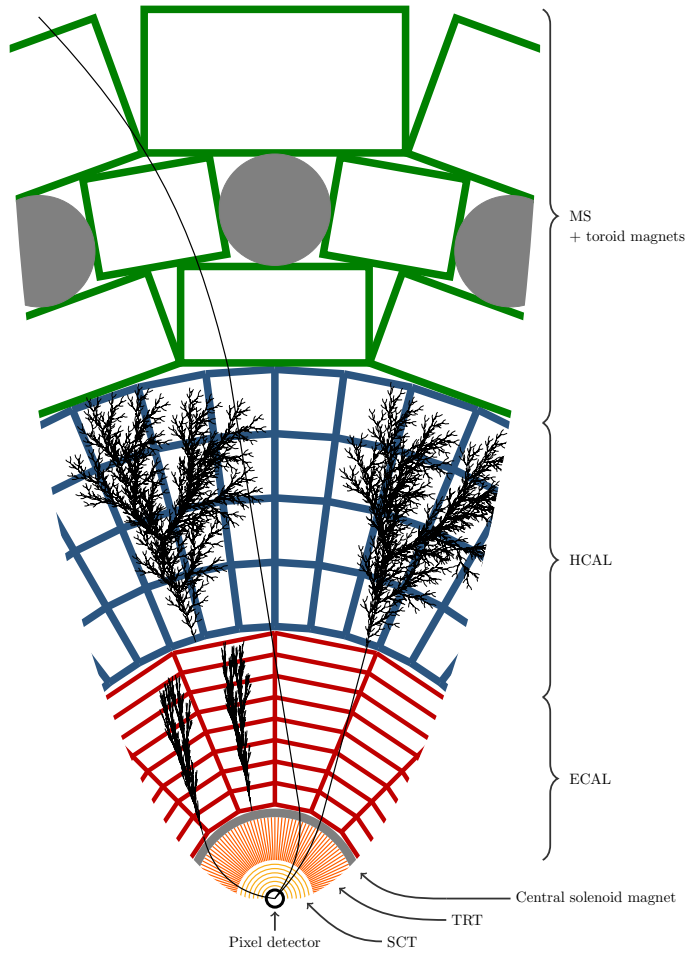


**Figure 3.3:** A visualisation of the ATLAS detector and the various sub-detectors. The view is taken as a slice in a plane perpendicular to the beam-pipe, showing the radial range from the beam-pipe to the edge of the detector. Overlaid are simplified illustrations of how various types of particles interact with the ATLAS detector; specifically from left to right the particles are an electron, a chargeless hadron (e.g. a neutron), a photon, a muon and a charged hadron (e.g. proton). The sub-detector components are not to scale [53].

as a function of  $\theta$ :

$$\eta = -\ln \left[ \tan \left( \frac{\theta}{2} \right) \right] \quad (3.1)$$

Thus,  $\eta = 0$  corresponds to a particle travelling perpendicular to the beam-pipe, where a positive value of  $\eta$  corresponds to a particle travelling with a tilt towards the positive  $z$ -axis. The quantity is called pseudo-rapidity as in the massless limit ( $\lim_{E \rightarrow |\vec{p}|}$ ) it can be shown that  $\eta$  converges to rapidity,  $y$ , where rapidity is defined as,

$$y = \frac{1}{2} \ln \left( \frac{E + p_z}{E - p_z} \right) \quad (3.2)$$

A key property of rapidity is that differences in rapidity,  $\Delta y$ , are invariant against Lorentz boosts along the  $z$ -axis; This is important as collisions in  $pp$  colliders have different Lorentz boosts along the  $z$ -axis caused by the effects of the Parton Distribution Functions described in Section 2.2.3.2. Thus,  $\eta$  is the final variable chosen in the ATLAS co-ordinate system due to the relation of  $\eta$  with both  $\theta$  and  $y$  and the above mentioned property of  $\Delta y$ .

The final important quantity of the ATLAS co-ordinate system is  $\Delta R$ , which is defined as

$$\Delta R = \sqrt{\Delta\eta^2 + \Delta\phi^2} \quad (3.3)$$

$\Delta R$  represents the angular separation between two vectors in the ATLAS co-ordinate system.

### 3.2.2 Inner Detector

The Inner Detector (ID), the innermost sub-detector on ATLAS, measures the trajectory of charged particles passing through the detector. The ID is constructed from many concentric layers of detector, and as a charged particle passes through the detector each of the layers provides a position measurement, known as a hit. Typically a particle passing through the whole Inner Detector at  $\eta = 0$  will provide 44 hits. Using the hits from the many layers the trajectory of the particle is determined; the measured trajectory is known as a track<sup>5</sup>. The ID is immersed in a 2 T magnetic field which bends the particle's trajectories; the sign of the charge and momentum of the particle is inferred from the sign and magnitude of the track's curvature.

The ID is made of three main component parts; the Insertable B-Layer (IBL), the pixel detector<sup>6</sup>, the Semi-Conductor Tracker (SCT) and the Transition Radiation Tracker (TRT), as visualised in Figure 3.4. The figure also shows the radial positions of each of they layers. The ID provides hits for tracking in the range  $\eta < 2.5$ ; to achieve this ID components are organised into the barrel, which are cylinders around the beam-pipe in the central region of the detector and the end-caps, which are disks that lie perpendicular to beam-pipe on either end of the barrel. Figure 3.7 shows the layout of the barrel and end-cap components for the pixel, SCT and TRT detectors in one half of the detector. Table 3.1 summarises the key properties of the components of the ID in both the barrel and the end cap.

The inner most part of the detector is the Insertable B-Layer (IBL) and the silicon pixel detector, which are both made out silicon based pixel modules. The high-granularity of the IBL and pixel detector allow for high precision position measurements (see Table 3.1),

---

<sup>5</sup>The procedure used for track reconstruction will be discussed in Section 4.1

<sup>6</sup>Often the IBL is considered as part of the pixel detector

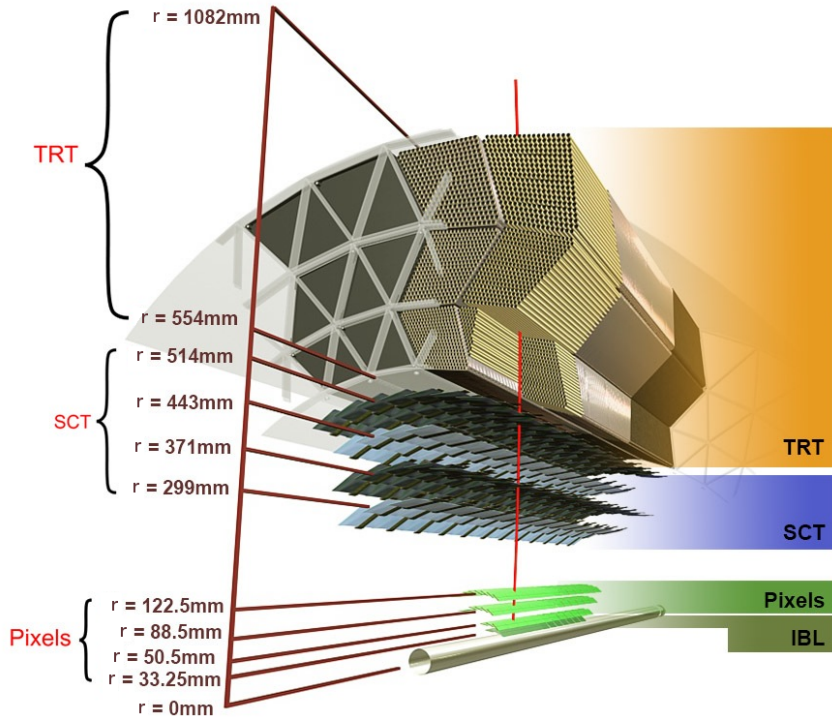


**Figure 3.4:** A schematic showing a slice of the barrel of the ATLAS Inner Detector (ID) including the Insertable B-Layer (IBL). Each component of the ID is labelled and the radial distances from the beam-pipe ( $r$ ) are shown [54].

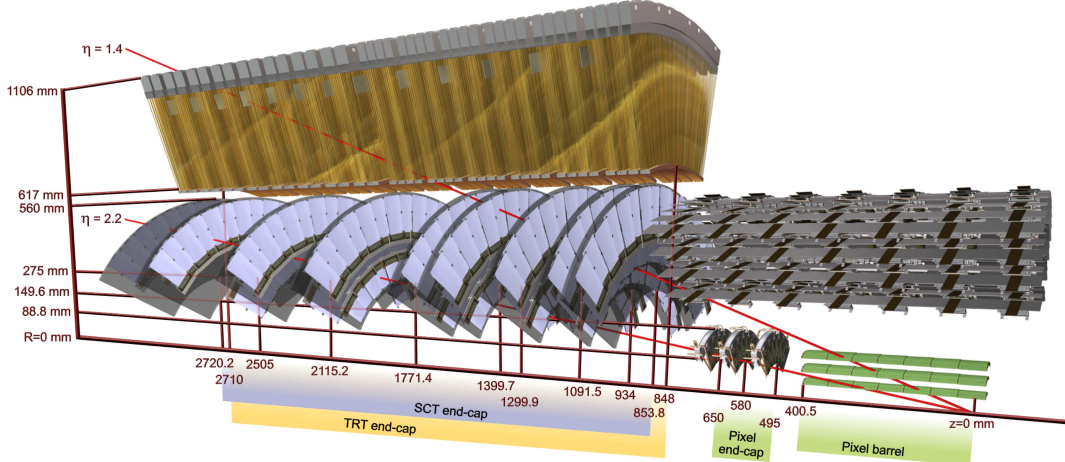


**Figure 3.5:** A schematic showing the barrel and end-cap components of the ATLAS Inner Detector (ID), the Insertable B-Layer is not shown. Each component of the ID is labelled and the axial distance from the beam-pipe ( $z$ ) is shown. The red lines indicate the trajectory of a particle at  $\eta = 1.4$  and  $2.2$  with  $p_T = 10\text{ GeV}$ . [50].

close to the beam pipe, which is important for vertex reconstruction<sup>7</sup>. The pixel detector is made out of 3 layers in the barrel and 3 end-caps at either end. The IBL was added to

<sup>7</sup>A vertex is defined as the point at which one or more tracks cross

Component of ID	$\eta$ Coverage	Element Size ( $\mu\text{m}$ )	Intrinsic Resolution ( $\mu\text{m}$ )		# Layers or Disks
<b>IBL</b>	$ \eta  < 2.5$	50 x 250	8 ( $R\text{-}\phi$ )    40 ( $z$ )		1
<b>Pixel</b>	Barrel $ \eta  < 1.7$	50 x 400	10 ( $R\text{-}\phi$ )	115 ( $z$ )	3
	$1.7 <  \eta  < 2.5$		10 ( $R\text{-}\phi$ )	115 ( $R$ )	3 (both ends)
<b>SCT</b>	Barrel $ \eta  < 1.4$	80	17 ( $R\text{-}\phi$ )	580 ( $z$ )	4
	$1.4 <  \eta  < 2.5$		17 ( $R\text{-}\phi$ )	580 ( $R$ )	9 (both ends)
<b>TRT</b>	Barrel $ \eta  < 0.7$	4000	130 ( $R\text{-}\phi$ )		$\sim 36$ hits per track
End-cap	$0.7 <  \eta  < 2.0$				

**Table 3.1:** Summary of the main characteristics of the components of the ATLAS Inner Detector (ID). For the SCT and TRT the element sizes refer to the spacing of the readout strips and the diameter of the straw tubes respectively [50, 55].

the ID in 2014 to improve tracking efficiency, which had been degraded by damage to the other layers of the pixel detector caused by data-taking before 2014, and to provide an extra measurement close to the beam-pipe for improved vertex reconstruction. The IBL is made out of 1 layer of pixel modules in the barrel only, as this can provide an angular coverage of  $\eta < 2.5$ .

Moving radial outwards the next component of the ID is the Semi-Conductor Tracker. SCT modules are made from pairs of semi-conducting strips; the strips are  $\sim 120$  mm in length<sup>8</sup>, have a strip (spacial separation between strips) is  $80 \mu\text{m}$  and the strips in the pairs have a stereo angle of 40 mrad between them.

The outermost component of the ID is the Transition Radiation Tracker (TRT) constructed of many 4 mm radius cylindrical tubes filled with a xenon based gas mixture<sup>9</sup> with an anode wire through the central axis. A charged particle passing through the gas causes ionisation allowing a measurement of its position using drift-time. Furthermore, the space between straws is filled with polymer fibres (barrel) and foils (endcaps) to create transition radiation, which is emitted by relativistic charged particles as they pass a boundary between materials with different refractive indices. The intensity of the transition radiation is inversely proportional to mass, providing additional information for particle identification.

The trajectory, momentum and charge measurements provided by the Inner Detector are essential for particle identification in ATLAS. In particular, the high precision measurements close to the beam-line allow for vertex reconstruction, which is essential for identification of tracks coming from  $B$  or  $C$  hadrons, and hence the identification of  $b$ -jets. The

---

<sup>8</sup>This number varies for the various parts of the SCT

<sup>9</sup>70% Xe, 27% CO<sub>2</sub> and 3% O<sub>2</sub> [56].

identification of  $b$ -jets is important for di- $b$ -jet searches and so is discussed further in Section 4.3.

### 3.2.3 Calorimeters

The ATLAS calorimeter, located on the outside of the solenoid magnet surrounding the ID, is designed to provide an energy measurement of the traversing particles. The ATLAS calorimeter measures the energy of hadronic jets which is used to calculate the invariant mass of jet pairs, which is important in the context of di- $b$ -jet searches.

The ATLAS calorimeter consists of two different systems built in concentric rings; the inner-most is the ‘Electromagnetic Calorimeter system (ECAL)’ used to measure electromagnetic objects such as photons and electrons. Outside of that is the ‘Hadronic Calorimeter system (HCAL)’ that provides an energy measurement of hadronic objects, such as hadronic jets. The HCAL consists of the Tile and Hadronic Endcap calorimeters. Both the ECAL and HCAL have barrel and end-cap components to make energy measurements at a large range of  $\eta$  values. Figure 3.6 shows a cut-away of the ATLAS calorimeter.

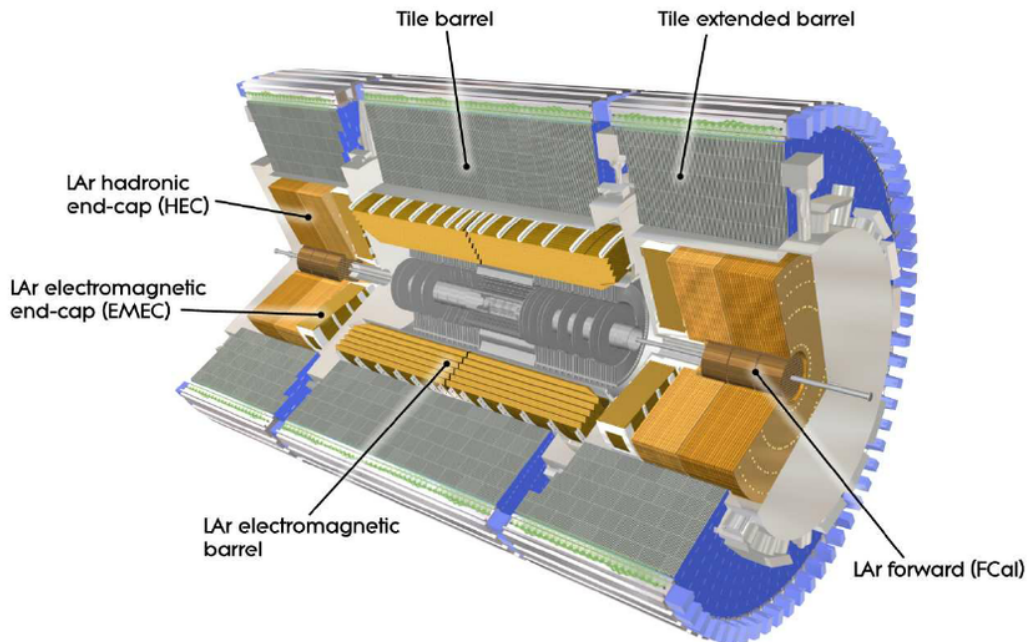


**Figure 3.6:** A cut-away schematic of the ATLAS calorimeter system [50].

A more detailed description of each of the calorimeter components will follow; however, the principle behind each detector is common so is described first. The calorimeters at ATLAS are sampling calorimeters, which means they consist of alternating layers of ab-

sorber and active material. The role of the ‘*absorber layer*’ is to force the particle, whose energy we want to measure, to emit secondary particles. These secondary particles will again emit further particles and so on meaning a ‘*particle cascade*’ is formed, the many resulting particles from the cascade are known as the cascade particles. The role of the ‘*active material layer*’ is to measure the energy of the many resulting particles from the cascade, the techniques used by active layers in the ECAL and HCAL are different so will be described below. The ATLAS detector is built such that the initial particle will fully cascade within the volume of the calorimeter system and then, from the sum of the energy of the cascade particles, the energy of the initial particle is inferred.

### 3.2.3.1 Electromagnetic Calorimeter (ECAL)

For the electromagnetic interaction, at energies above the critical energy of a material ( $\sim 7 \text{ MeV}$  for Lead [15]) the particle cascade process is dominated by two processes; bremsstrahlung, ( $e^\pm \rightarrow e^\pm + \gamma$ ) and pair production ( $\gamma \rightarrow e^+ + e^-$ ). The electromagnetic calorimeter at ATLAS is known as the ‘Liquid Argon (LAr) calorimeter’. The absorber material used in the LAr calorimeter is lead, due to its large density of charged particles (high  $Z$ ) which increases the rate of the cascade processes. The active material is liquid argon (LAr); when a cascade particle passes through the liquid argon it causes ionisation, and the released electrons are captured and counted using an electric field. Ionisation dominates the cascade process when the cascade particles are below the critical energy of a material ( $\sim 30 \text{ MeV}$  for LAr) so the released electrons by ionisation will approximately have a constant mean energy (roughly the critical energy of the material minus the energy required to ionise). Therefore, the number of released electrons is proportional to the energy of the cascade particle, meaning that the energy of the cascade particle can be measured.

As discussed above the LAr calorimeter is split up into two sections; the barrel section covers a region of  $|\eta| < 1.475$  and two end-cap components cover  $1.375 < |\eta| < 3.2$ . The depth of an electromagnetic calorimeter is often expressed in units of radiation length,  $X_0$ , which is both the mean distance that an electron loses all but  $1/e$  of its energy through bremsstrahlung and  $7/9$  of the mean free path for a photon to produce an  $e^+e^-$  pair. High-Z materials have a shorter radiation length; in lead  $X_0 = 0.56 \text{ cm}$ . The LAr calorimeter has a depth of  $> 22 X_0$  in the barrel and  $> 24 X_0$  in the end-caps, meaning that almost all of the particle shower from a high-energy photon or electron is contained within electromagnetic calorimeter. The maximum granularity of the LAr calorimeter in the  $\eta-\phi$  plane is  $0.025 \times 0.025$  for the Barrel and  $0.025 \times 0.1$  for the end-cap<sup>10</sup>.

---

<sup>10</sup>Full details on the granularity of all components of the ATLAS calorimeter is found in Table 1.3 of [50].

### 3.2.3.2 Hadronic Calorimeter (HCAL)

For particles that interact through the strong force, such as the components of a hadronic jet, the particle cascade is a more complicated process. A hadronic cascade is dominated by processes such as ionisation, nuclear spallation and neutron generation [57, 22]. For a chargeless hadron, for example a neutron, strong processes, such as spallation, are the only processes that contribute to its cascade. During these hadronic cascade processes many  $\pi_0$  mesons are created, which can decay to a pair of photons and thus form electromagnetic cascade, as described above.

For hadronic interactions, the depth of detector is given in units of the interaction length,  $\lambda$ , defined as the distance required to reduce the number of relativistic hadrons by  $1/e$ .

By the end of the LAr calorimeter there is  $2.3 \lambda$  of active material in the barrel. This means that hadronic shower depth is larger than the depth of the LAr calorimeter, therefore for a full measurement of the hadronic energy, the Hadronic Calorimeter system (HCAL) is required.

The Tile Calorimeter is constructed from absorber layers of steel and active material layers of scintillating tiles. The cascade particles produced by the absorber will excite atoms in the scintillating tiles which will then produce photons at a constant mean energy, therefore by measuring the intensity of the scintillating light (number of photons produced) the energy of the cascade particle can be determined. The Tile Calorimeter has a depth of  $7.4 \lambda$ , meaning the majority of the hadronic shower is captured by the LAr and Tile calorimeter. The Tile Calorimeter is split up into the barrel and the extended barrel components; the barrel covers the region  $|\eta| < 1.0$  and the extended barrel covers the region  $0.8 < |\eta| < 1.7$ . The maximum granularity of the Tile calorimeter in the  $\eta-\phi$  plane is  $0.1 \times 0.1$  for both the barrel and the extended barrel<sup>11</sup>.

To cover the more forward regions there are two more calorimeter detectors. The Hadronic Endcap Calorimeter (HEC) is housed in two large wheels at either end of the ATLAS detector and covers a region of  $1.5 < \eta < 3.2$ . The HEC is a sampling calorimeter built using copper as the absorber layers and liquid argon as the active material and has a depth of  $\sim 12 \lambda$ . The maximum granularity of the HEC calorimeter in the  $\eta-\phi$  plane is  $0.1 \times 0.1$ .

In addition the Forward Calorimeter (FCAL) covers the very forward region  $3.1 <$

---

<sup>11</sup>Full details on the granularity of all components of the ATLAS calorimeter is found in Table 1.3 of [50].

$\eta < 4.9$ , which is outside the range considered within this analysis. It is constructed from absorber layers of copper (for EM interactions) and tungsten (for hadronic interactions) with liquid argon for the active material layers. The maximum granularity of the LAr calorimeter in the  $\eta$ - $\phi$  plane is  $3.0 \times 2.5$ .

Another important point about the ATLAS calorimeter is that it is a non-compensating calorimeter; that is to say that the response of the detector to an electromagnetic particle (such as an electron) is larger than the response of a hadronic particle (for example a pion). This is because some energy is lost in hadronic cascade process; mainly due to the energy required to release nucleons from calorimeter nuclei during spallation, but also from the recoil energy given to the calorimeter nuclei and neutrinos created during strong processes that can escape the calorimeter [58, 59]. The ATLAS calorimeter is initially calibrated to the EM-scale, meaning that the initial energy measurement of a calorimeter assumes that the particle is only EM-interacting. To account for the fact that the ATLAS calorimeter is non-compensation, a jet energy scale correction is applied to a hadronic jet in the calibration process, which is described further in Section 4.2.3.

### 3.2.3.3 Energy Resolution of a Calorimeter

The energy resolution of a calorimeter is given by three terms:

$$\left(\frac{\Delta E}{E}\right)^2 = \left(\frac{c_s}{\sqrt{E}}\right)^2 + \left(\frac{c_n}{\sqrt{E}}\right)^2 + c_c^2 \quad (3.4)$$

The three terms are:

- **Stochastic Term ( $c_s$ ):** This term represents random fluctuations in the cascade shower process. This uncertainty is Poisson-like meaning that  $\Delta E_s$  proportional to the square root of the number of photons/electrons, which gives us that  $\Delta E_s \propto \sqrt{E}$ .
- **Noise Term ( $c_n$ ):** This term represents effects that are independent of the energy measurement, such that  $\Delta E_n = c_n$ . Contributions to the noise term include electronic noise or radioactivity.
- **Constant Term ( $c_c$ ):** This term represents effects that affect all energy measurements equally, such that  $\Delta E_c/E = c_c$ . Contributions to the constant term include regions of inactive material such as detector cracks and dead modules.

Approximate values of  $c_s$  and  $c_c$  for different components of the ATLAS calorimeter are given in Table 3.2. The noise term depends strongly on  $\eta$  and pile-up conditions so is not given. For high- $p_T$  objects ( $>\sim 100$  GeV), such as the jets used in the di- $b$ -jet searches,

the constant term will become the dominant term, as the other terms are suppressed by the large values of  $E$ .

Calorimeter Component	Stochastic ( $c_s$ ) [ $\sqrt{\text{GeV}}$ ]	Constant ( $c_c$ )
EM Barrel	10%	0.7%
EM End-cap	10%	0.7%
Tile	50%	3%
HEC	50%	3%
FCAL	100%	10%

**Table 3.2:** A summary of the stochastic and constant terms of the intrinsic energy resolution of components of the ATLAS calorimeter [50]

### 3.2.4 Muon Spectrometer

The Muon Spectrometer (MS) is the outermost part of the ATLAS detector and is designed to detect charged particles pass through the calorimeters. As the muon is the only particle detectable by the ATLAS detector that are not stopped by the calorimeter, measurements in the Muon Spectrometer are used to identify muons. The Muon Spectrometer consists of layers of detector providing positional measurements of 'hits' in the presence of a magnetic field, similar to the concept used for the Inner Detector (ID). Furthermore, the position measurements from both the Muon Spectrometer and the ID are used to calculate the trajectory of the muon, known as muon tracks, and from that the  $p_T$  of the muon can be inferred. By using position measurements from both the Muon Spectrometer and the ID, muon tracks have a long lever arm which improves momentum resolution. Muon track reconstruction is further discussed in Section 4.4.

In the barrel region ( $|\eta| < 1.4$ ) the large barrel toroid provides the magnetic field, in the end-cap region ( $1.6 < |\eta| < 2.7$ ) the two smaller end-cap magnets provide the magnetic field and finally in the transition region ( $1.4 < |\eta| < 1.6$ ) both sets of magnets contribute to the magnetic field. A further description of the magnets used in ATLAS is found in the next section.

Muon chambers are the detectors tasked with providing the muon position measurements required to reconstruct muon tracks. In the barrel region, muon chambers are arranged in three concentric cylindrical layers of chambers formed around the beam-pipe, whilst in the transition and end-cap regions there are three layers of chambers either side of the barrel lying in disks perpendicular to the beam-pipe.

The muon chambers come in two types; trigger and precision. The '*trigger muon*

*chambers*' provide a position measurement in 3-dimensions within 15–25 ns which is used to identify muons tracks in the trigger. The trigger muon chambers comprise of Resistive Plate Chambers (RPCs) in the barrel and Thin Gap Chambers (TGCs) in the end-cap regions. Only measurements for  $|\eta| < 2.0$  are used for triggering due to the high flux of muons close to the beam-pipe. The '*precision muon chambers*' provide a precise measurement of the muon position co-ordinates in the  $R$ - $z$  plane, the plane in which track curvature occurs in the muon spectrometer, allowing for precise measurements of the muon track- $p_T$ . In the region  $|\eta| < 2.0$ , the precision muon chambers are Monitored Drift Tubes (MDTs), whilst at large pseudo-rapidities ( $2.0 < |\eta| < 2.7$ ), Cathode Strip Chambers (CSCs) are used. A schematic of the Muon Spectrometer is shown in Figure ??, the types of chambers used in each part is labelled.

There is an additional use of the muon spectrometer that relates to high-energy jets. Whilst for most jets their shower is fully contained within the calorimeter there are some jets, particularly at high- $p_T$ , where a non-negligible fraction of energy from the shower goes beyond the calorimeter. This effect, known as ‘punch-through’, is estimated using energy deposits in the muon spectrometer.

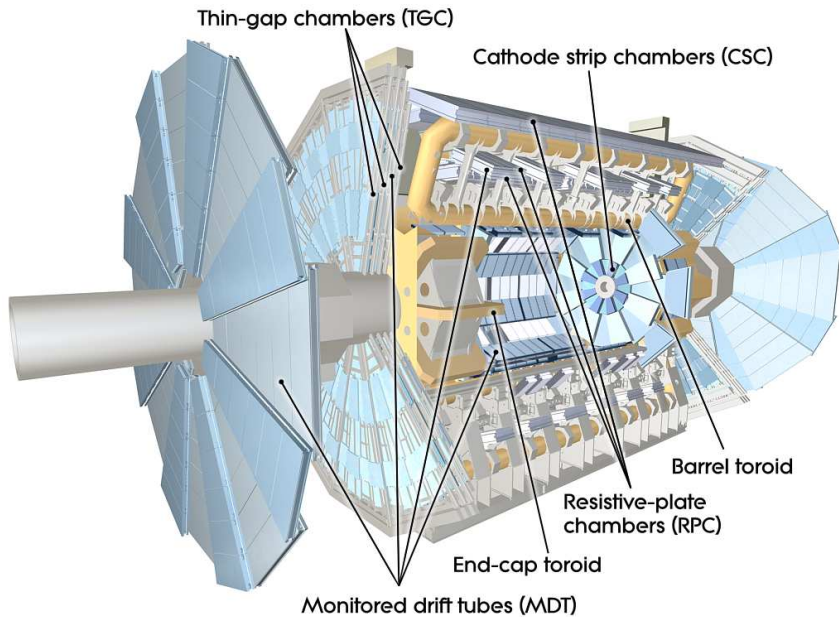


**Figure 3.7:** A cut-away of the ATLAS muon spectrometer (MS). The types of muon chamber used in each part of the MS are labelled on the figure. [50].

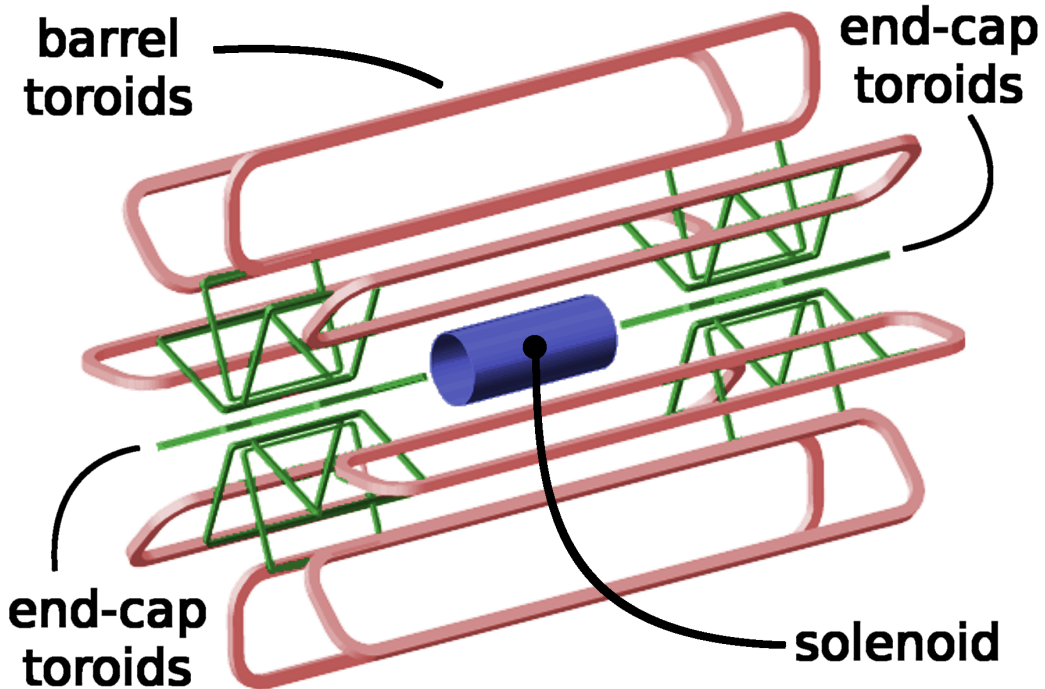


**Figure 3.8:** The layout of the ATLAS magnets [60].

### 3.2.5 Magnets

In ATLAS magnetic fields are important for obtaining the momentum and charge of particles from their observed trajectories in the ID and Muon Spectrometer. ATLAS is made up of four large superconducting magnets; the inner solenoid which surrounds the inner detector and provides a 2 T magnetic field within the ID. The barrel toroid magnet provides a magnetic field of up to  $\sim 0.5$  T in the central regions of the muon spectrometer and the two end-cap toroid magnets which produce a magnetic field of  $\sim 1$  T in the forward regions of the Muon Spectrometer. Figure 3.8 shows the layout of the magnets in ATLAS [60].

**Note for AK:** Trigger to be moved entirely to trigger chapter, reduces need for repetition.

## Chapter 4

# Object Definition and Reconstruction

The previous chapter described how the ATLAS detector collects information on final state particles produced in  $pp$  collisions in the form of, for example, hits in the Inner Detector and Muon Spectrometer or energy deposits in the calorimeter. This chapter defines physics objects, which are observables that allow us to study the hard-scatter processes and form the basis of the analyses in future chapters. This chapter will describe how, using the information provided by the ATLAS detector, each physics object is identified and their 4-momentums and trajectories reconstructed.

Specifically this chapter will focus on physics objects important to the analyses in this thesis: tracks are described in Section 4.1, jets in Section 4.2,  $b$ -jets in Section 4.3, and electrons and muons in Section 4.4. Finally, Section 4.5 will briefly describe some further physics objects widely used in the ATLAS physics program outside of the analyses being presented here.

### 4.1 Tracks

The ATLAS detector is able to reconstruct the trajectory of charged particles produced in the proton-proton collision as they pass through the Inner Detector; the reconstructed trajectories are known as tracks. Track reconstruction is essential in a number of important areas of ATLAS analyses: for example; primary vertex reconstruction, identification of  $b$ -jets (Section 4.3) and the identification and reconstruction of electrons and muons (Section 4.4).

Track reconstruction uses hits from the Pixel detector, SCT and TRT which are described in Section 3.2.2. The track reconstruction is performed using an ‘inside-out’ approach, which entails using the higher precision Pixel and SCT hits initially before adding in the TRT hits to improve track quality. The tracking reconstruction procedure [54] follows

these steps:

- **Clustering:**<sup>1</sup> Neighbouring hits in a layer of the Pixel or SCT detector are converted into a 3D ‘space-point’ that represents the point where the charged particle traversed the active material of the ID. In the Pixel detector one cluster of hits can form a space-point, whilst in the SCT hits from both sides of a strip layer are required to create a 3D space-point.
- **Track Seeding:** Track seeds are formed from three space-points in consecutive layers of the Inner Detector that are consistent with the trajectory of a particle with  $p_T > 500$  MeV.
- **Track Candidates:** From the track seeds, track candidates are built by iteratively adding space-points from the remaining Pixel and SCT detector layers using an combinatorial Kalman filter [61]. There can be multiple track candidates per seed.
- **Track selection / Ambiguity resolving:** Each track candidate is assigned a ‘track-score’ that is based a number of variables of the track candidate; the  $p_T$ ,  $\eta$ ,  $\chi^2$  fit and the hit pattern. The hit pattern refers to the number of Pixel or SCT hits, the number of holes (missing hits where one was expected) and the quality of the hits. Track candidates must also pass some track quality requirements, that are similarly based on the track candidate’s  $p_T$ ,  $\eta$  and the hit pattern. The self-consistent set of track candidates that have the highest ‘track-score’ and that pass track quality requirements are then selected. Exact details of the track-scoring, track requirements and selection algorithm is described in [54].
- **Add TRT Information:** Track candidates from the previous step are extrapolated into the TRT and all hits within 10 mm are added. The track candidates are then refitted using Pixel, SCT and TRT hits to make use of the full tracking detector.

The outputs of the above track reconstruction process will be referred to as tracks in the remainder of this thesis. Also it is important to note that, as discussed in Section 3.2.2, the tracks are curved by a known magnetic field in the Inner Detector, therefore the tracks contain information on the charge and the momentum of the particles whose trajectory they are describing.

## 4.2 Jets

If a collision results in a free quark or gluon in its final state then a stream of high-energy hadrons is created, which is known as a hadronic jet. The underlying processes in hadronic jet formation can be summarised as follows; firstly the free quark/gluon will radiate additional gluons and quarks in a process known as the parton shower, these gluons and quarks

---

<sup>1</sup>In the associated reference this step is referred to as ‘clusterization’, but here I will use clustering for consistency with the English language.

will then undergo hadronisation to form hadrons which are the constituents of the hadronic jet. A more detailed description of the parton shower and hadronisation process can be found in Section [QCD theory description] Not written yet **LM fix**. The components of the hadronic jet deposit energy in the cells of the ATLAS calorimeter, through the processes described in Section 3.2.3, such that the ATLAS calorimeter has an energy and positional measurement of the components of the hadronic jet. The process of parton shower, hadronisation and energy deposition in the calorimeter, as described above, is illustrated in Figure 4.1.

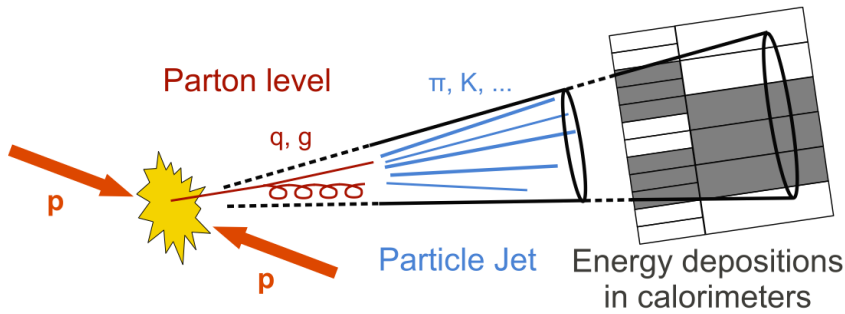


**Figure 4.1:** A schematic illustrating the formation of hadronic jets and the resulting observed energy deposits in the calorimeter system [62].

This section contains a description of the procedure utilised by ATLAS to go from energy deposits in calorimeter cells to well defined and calibrated hadronic jets. This procedure can be split up into three separate steps that are described in the following sections; firstly topoclusters are formed as described in Section 4.2.1, then jets are formed from topoclusters using reclustering algorithms as described in Section 4.2.2 and finally Section 4.2.3 and Section 4.2.4 describes how the jets are calibrated and the relevant jet energy uncertainties are derived.

In this section the formation of hadronic jets constructed from calorimeter cells is described, as this is the only jet object used in the context of the analyses presented in this thesis. However, it is worth noting, that there are other types of jets used at ATLAS; for example hadronic jets can also be constructed from tracks formed in the Inner Detector, a technique that has been useful in dense environments [63].

### 4.2.1 Hadronic Topocluster Reconstruction

The first step of jet building at ATLAS is the formation of 3D clusters, known as topoclusters, from groups of energy deposits in neighbouring calorimeter cells [64]. The calorimeter cells can be from either the EM or hadronic calorimeter systems, which have a gran-

ularity given in Table ???. The algorithm employed makes use of the variable “cell signal significance” defined as,

$$S_{\text{cell}} = \frac{E_{\text{cell}}}{\sigma_{\text{noise,cell}}} \quad (4.1)$$

where  $E_{\text{cell}}$  is the energy deposited in a cell and  $\sigma_{\text{noise,cell}}$  is the uncertainty due to noise in that cell. The sources of noise in a calorimeter cell are described in Section **LM fix, need to have a noise section somewhere....**. A large value of  $S_{\text{cell}}$  ( $> 1$ ) indicates that the energy deposit is likely due to a particle depositing energy in the calorimeter rather than noise within the calorimeter.

Using the value of  $S_{\text{cell}}$ , each calorimeter cell is labelled as follows

- If  $|S_{\text{cell}}| > 4$ : the cell is labelled a **seed** cell.
- If  $|S_{\text{cell}}| > 2$ : the cell is labelled a **growth** cell.
- If  $|S_{\text{cell}}| > 0$ : the cell is labelled a **boundary** cell.

Then the algorithms builds topoclusters as in the following steps,

1. A seed cell forms the centre of a new topocluster.
2. Neighbouring seed cells are added together to form one topocluster seed.
3. Then, growth cells neighbouring the topocluster are added.
4. Finally, boundary cells neighbouring the topocluster are added.

Figure 4.2 illustrates an example of where the algorithm would form a topocluster and an example where it wouldn’t.

The topoclusters are treated as massless objects, such that the four-momentum of each deposit can be calculated using the sum of energy deposited in the topoclusters and the  $\eta - \phi$  position of the topocluster. The constructed topoclusters and their four-momentums are then used as the inputs to the next step of jet reconstruction.

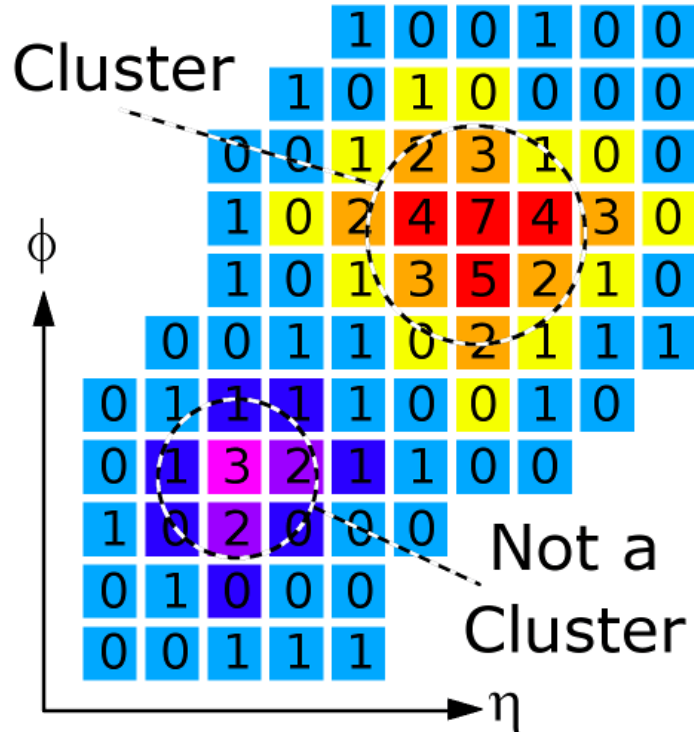


**Figure 4.2:** A schematic illustrating the algorithm used to form a topocluster. The numbers on the grid represent  $|S_{\text{cell}}|$  and the colours represent the cell label [60].

### 4.2.2 Jet Reconstruction

The next step in the process is to form jets from the topoclusters described in the previous section. To do this a jet reconstruction algorithm is defined, that uses the location and energy of the topoclusters in an event to form a set of jets. Each jet formed by the algorithm has a well defined four-momentum and set of constituents. Jet reconstruction algorithms are used to define jets as this means that jets are experimentally well-defined model-independent observables, which is required if measurements using jets are to be re-usable by the wider particle physics community. A detailed discussion of jet reconstruction algorithms and their related issues is found in [65]; as such this section provides a summary relevant to the analyses being presented in this thesis.

ATLAS analyses use a type of jet reconstruction algorithms known as sequential recombination algorithms, which selectively add together the calorimeter topoclusters to form the jet; these are specifically the  $k_t$ , anti- $k_t$  and Cambridge-Aachen (CA) algorithms.

The three algorithms use a set of four-momentums (clusters), which are initially the topoclusters formed in the calorimeter. One then introduces an inter-jet distance between

clusters  $i$  and  $j$  defined as,

$$d_{ij} = \min[(p_{Ti})^a, (p_{Tj})^a] \left( \frac{\Delta R_{ij}}{R} \right)^2, \quad \Delta R_{ij} = \sqrt{(y_i - y_j)^2 + (\phi_i - \phi_j)^2} \quad (4.2)$$

and a particle-beam distance for cluster  $i$  defined as,

$$d_{iB} = (p_{Ti})^a \quad (4.3)$$

where  $y$  is rapidity (as defined in Section 3.2.1),  $\phi$  is azimuthal angle,  $p_T$  is transverse momentum (component of momentum perpendicular to the beam-pipe of colliding particles) and  $p_z$  is the component of momentum that is parallel to the beam-pipe of colliding particles.  $R$  is the jet width parameter, a free parameter of the algorithm. The parameter  $a$  in Eq. (4.2) and (4.3) takes the value  $a = 2$  for the  $k_t$  algorithm,  $a = -2$  for the anti- $k_t$  algorithm and  $a = 0$  for the Cambridge-Aachen algorithm.

The inter-jet and particle-beam distances are not physical distances as such, but can instead be thought of as dimensionful measures of how likely it is that clusters  $i$  and  $j$  represent clusters caused by hadrons from the same jet. If the inter-jet distance for a pair of clusters is smaller than the particle-beam distances for the two clusters ( $d_{ij} < d_{iB}$ ) then it is likely that the two clusters are from the same jet. In contrast, if  $d_{ij} > d_{iB}$  then it is unlikely that the two clusters are from the same jet.

The algorithm then proceeds using the following steps:

1. Calculate  $d_{ij}$  and  $d_{iB}$  for all combinations of clusters.
2. Find the minimum of the  $d_{ij}$  and  $d_{iB}$ .
3. If the minimum is a  $d_{ij}$  combine cluster  $i$  and  $j$  to form a new cluster and return to step 1.
4. If the minimum is a  $d_{iB}$  then call cluster  $i$  a final-state jet, remove it from the set and return to step 1.
5. Stop when all clusters have been declared as jets.

The final jet has a four-momentum equal to the addition of all the topoclusters assigned to that jet. It can now be seen that the jet width parameter,  $R$ , effectively gives the scale of the width of a reconstructed jet. This is because when  $\Delta R_{ij} > R$  for a pair of clusters,  $d_{iB} < d_{ij}$  for the cluster with the smaller value of  $p_T$ , and thus the algorithm will not merge the two clusters.

The sequential reclustering algorithms described above are used as they satisfy two important theoretically motivated criteria: infrared and collinear safety. Infrared safety

requires that the jet reconstruction algorithm result should be invariant against soft gluon emission<sup>2</sup> and collinear safety requires that the jet reconstruction algorithm result should be invariant against a parton splitting into two partons with small angular separation. These conditions are desirable as if the jet reconstruction algorithm is infrared or collinear unsafe, two different sets of jets could be formed from identical hard-scatter processes due to an additional emission process in the parton shower. The sequential reclustering algorithms described above are infrared and collinear safe.<sup>3</sup>.

$\text{Anti-}k_T$  is the jet reconstruction algorithm used for the analyses being presented in this thesis, which is typical of analyses at ATLAS. This is because the anti- $k_T$  algorithm provides regular jet shapes around the centre of the jet, due to the fact that the algorithm reconstructs the high- $p_T$  core of the jets first and then adds in the lower  $p_T$  suburbs in later steps. Figure 4.3 shows the jets formed by the Cambridge-Aachen,  $k_T$  and anti- $k_T$  algorithm using the same set of input clusters; this illustrates that anti- $k_T$  algorithm creates more regular jet shapes than the other sequential-reclustering algorithms. Further to this, the value of the jet width parameter is chosen as  $R=0.4$ , which is consistent with the values suggested for gluon/quark jets in Section 5 of [65] and is the standard value used in ATLAS analyses.

### 4.2.3 Jet Calibration

The jets initially formed by the jet reclustering algorithms from the topoclusters will not represent the energy of the parton that initiated the parton shower (known as the initial parton) and as such will not give an accurate dijet mass reconstruction which is required for the analyses presented in this thesis. As a result, a hadronic jet calibration is required to map the initial reconstructed jet to a more representative calibrated jet that can be used in an analysis.

The key factors for the unrepresentative hadronic jet energy measurement are [22, 68]:

- **Jet energy scale:** As discussed in Section 3.2.3.2, the ATLAS calorimeter is non-compensating which means that the calorimeter response is different for an EM-object and a hadronic object. The calorimeter response is calibrated at the EM-scale such that the energy measurements from a calorimeter cell are correct for an EM-object; as a result the initial energy measurement for a hadronic jet will be incorrect. To account for this a correction is required to take the jet energy measurement from the EM-scale to the

<sup>2</sup>Soft means a low momentum

<sup>3</sup>Cone-based algorithms jet reconstruction algorithms used at some previous collider experiments, such as UA2 [66], do not satisfy this infrared and collinear safety.

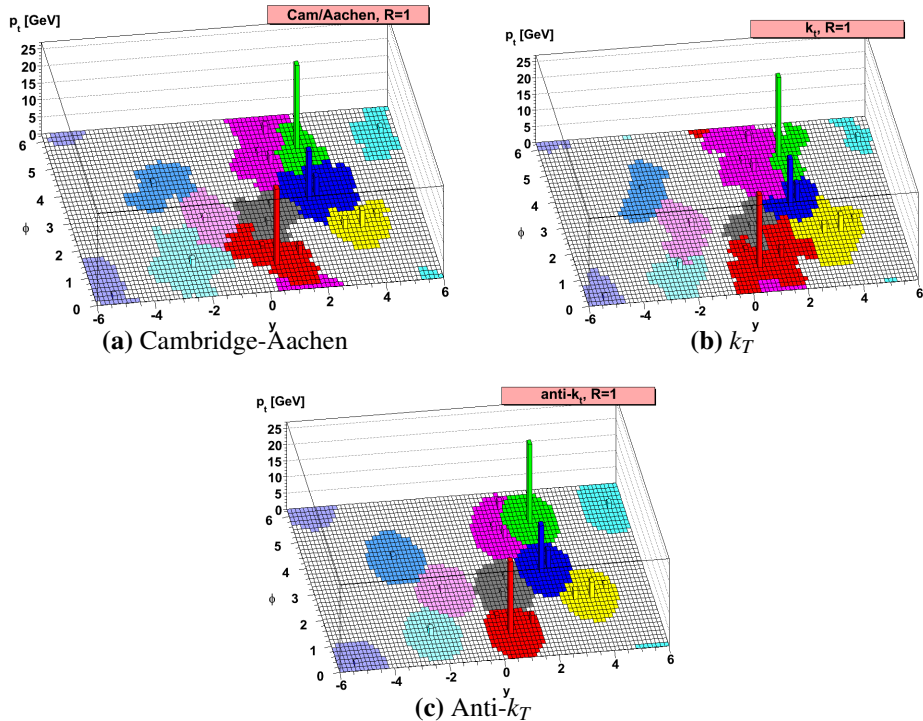


**Figure 4.3:** A comparison of the jets formed using the (a) Cambridge-Aachen, (b)  $k_T$  and (c) anti- $k_T$  algorithm from the same simulated event. The constituent clusters of each of the jets formed is indicated using various colours [67].

hadronic-scale.

- **Dead Material:** The hadronic jet may overlap with an unresponsive region of the detector, resulting in some energy deposits being incorrectly measured.
  - **Leakage:** Some energy from the jet will be distributed outside the angular acceptance of the calorimeter whilst some energy will pass through the calorimeter in a process known as ‘punch-through’, as discussed in Section 3.2.4.
  - **Reconstruction Issues:** There are two issues with jet reconstruction that require correction: firstly, some energy deposits coming from the initial parton may not be constructed as topoclusters due to the cell signal significance thresholds required in topocluster formation. Secondly, some topoclusters that should be clustered to the jet may not be included in the reconstructed jet or included in a different jet instead.
  - **Pile-up:** Energy from collisions other than the hard-scatter collision can also be included by the reclustering algorithm. This includes in-time and out-of-time pile-up. A definition of pile-up can be found in Section []. **LM Fix: Need a description of pile-up, probably in LHC running conditions**

As a result of the factors listed above a correction to the jets must be applied; which is done using the procedure described in [69]. An executive summary of the procedure is found below.

An important input of applying a calibration is deciding what one is correcting with respect to. The truth initial parton seems at first like a good choice, however this correction depends strongly on the theoretical modelling of the parton shower and hadronisation process, hence, this would mean that the calibrated jets are not model-independent. Instead, in ATLAS jets are corrected with respect to a ‘truth jet’; where a truth jet is defined as a jet formed by running the anti- $k_T$  algorithm on the set of stable truth particles in a simulated event. A stable particle is required to have a lifetime  $c\tau > 10$  mm and muons, neutrinos, and particles from pile-up collisions are ignored. Truth jets are well-defined and model-independent objects representing the jets that would have been reconstructed if one had a perfect detector; therefore they are a good choice for jet corrections.

The calibration process uses Monte-Carlo simulation and data to correct reconstructed jets using a number of steps; starting from the jets initially formed from the EM-scale topoclusters. These steps are outlined in Figure 4.4.

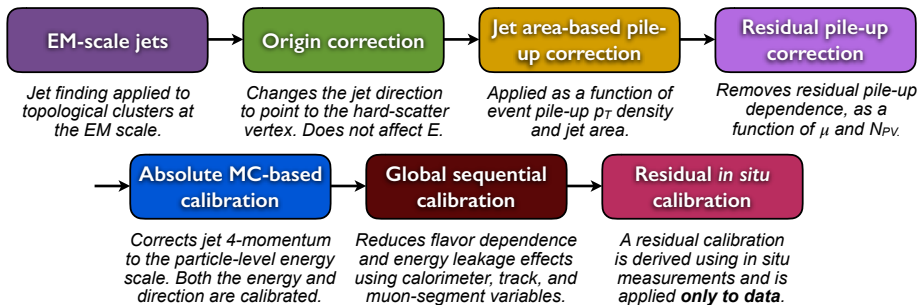


**Figure 4.4:** Calibration stages for the EM+JES calibration scheme [69].

To discuss each step in a little more detail:

- **Origin Correction:** This step changes the direction of the jets such that the four-momentum points to the hard-scatter primary vertex rather than the centre of the detector. This calculation conserves the jet energy.
- **Jet Area-Based Pile-up Correction:** This step removes unwanted energy contributions from pile-up. This correction subtracts the area of the jet,  $A$ , multiplied by the average energy density due to pile-up,  $\rho$ .
- **Residual Pile-up Correction:** This step further reduces effects from pile-up utilising the linear dependence of pile-up effects on the number of primary vertices,  $N_{PV}$  and the mean

number of additional  $pp$  collisions per bunch crossing of the event,  $\mu$ .

- **Absolute JES Correction:** This step corrects the jet four-momentum from the EM-scale, at which they were initially formed, to the hadronic-scale, which is defined in terms of the truth jets in simulation. This correction is derived using truth jets and reconstructed detector-level jets in dijet Monte-Carlo events.
- **Global Sequential Calibration:** This step uses information from the calorimeter, muon spectrometer and track-based variables to refine the reconstructed energy and reduce the overall uncertainties.
- **In-situ calibration:** All previous steps in this calibration have been done using simulation to correct detector-level jets to truth jets. This step accounts for any differences between simulation and data. This step uses events containing a jet to be calibrated and a well-measured reference objects, including photons, Z bosons, and calibrated jets. Then conservation of momentum gives us information on the true  $p_T$  of the jet to be calibrated. One can calculate a double ratio with respect to jet- $p_T$ ;

$$\text{Correction} = \frac{1}{R(p_T, \eta)} = \frac{\langle p_T^{\text{jet}} / p_T^{\text{ref}} \rangle_{\text{MC}}}{\langle p_T^{\text{jet}} / p_T^{\text{ref}} \rangle_{\text{Data}}} \quad (4.4)$$

which is applied as a correction to jet  $p_T$  in data; this correction is not applied in simulation.

This calibration scheme is known as an EM+JES, as the topoclusters are at the EM-scale. Here, I should note that there are other schemes used for calibrating jets at ATLAS, for example some analyses [70] correct each topocluster to the hadronic scale before clustering the jet, in a scheme called Local Cluster Weighted (LCW) [64]. EM+JES is generally used in ATLAS analyses as it is a simpler calibration scheme than LCW, but provides similar results.

The end result of the processes described in this section is a jet, reconstructed from EM-scale topoclusters using an anti- $k_T$  algorithm with a jet width parameter  $R=0.4$ , which has been calibrated using simulation and a data-driven in-situ step. The result of this process is what is known as an anti- $k_T$   $R=0.4$  EM+JES jet, and is the definition for a jet in this thesis.

#### 4.2.4 Jet Energy Uncertainties

All measurements have uncertainties, and this section investigates the uncertainties of jet energy measurement. Jet energy measurements separate the associated uncertainties into two components; jet energy resolution and jet energy scale.

Jet energy resolution (JER) is defined as  $\sigma(E)/E$ , and JER uncertainties come from an imperfect simulation of detector resolution in Monte-Carlo simulation. This uncertainty is measured using an in-situ technique from the balancing of jets in 8 TeV collision data which is extrapolated for 13 TeV data; the final uncertainty accounts for this extrapolation. Figure 4.5 shows the fractional JER uncertainty as a function of jet- $p_T$  and jet- $\eta$ . Full details on the derivation of this uncertainty can be found in [68] and [71].

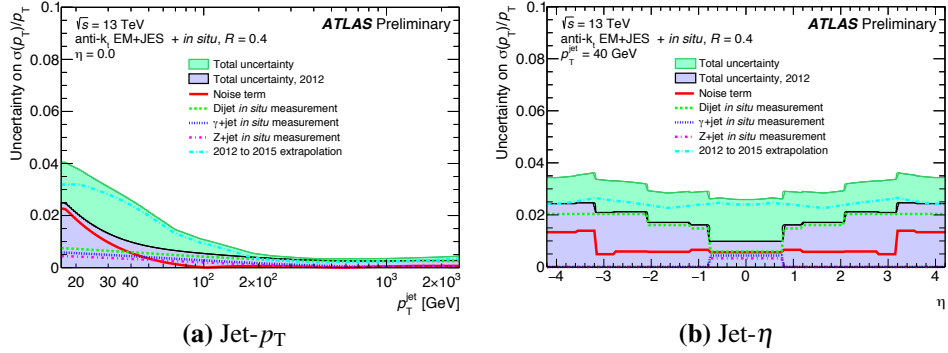


**Figure 4.5:** The fractional jet energy resolution uncertainty as a function of jet- $p_T$  and  $\eta$ . The total uncertainty is shown as are the contributions from the various sources of uncertainty [68].

Jet energy scale (JES) uncertainties arise from the calibration procedure to correct jets from the EM-scale to the hadronic-scale, outline above. 80 separate uncertainties are derived to cover each step of the calibration, the dominant uncertainties arise from the data-driven in-situ step [69]. Figure 4.6 shows the fractional JES uncertainty as a function of jet- $p_T$  and jet- $\eta$ .

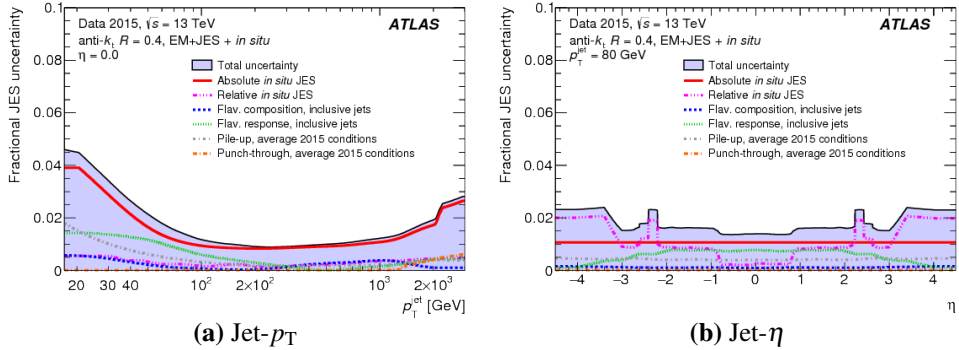


**Figure 4.6:** The fractional jet energy scale uncertainty as a function of jet- $p_T$  and  $\eta$ . The total uncertainty is shown as are the contributions from the various sources of uncertainty [69].

## 4.3 *b*-Jets

Hadronic jets, described in Section 4.2, can be further categorised into three separate categories based on the flavour of the constituent quarks. *b*-jets are defined as jets containing one or more *b*-hadrons, *c*-jets are defined as jets containing one or more *c*-hadrons but no *b*-hadrons and finally light-flavoured jets comprise of only light hadrons (formed of *u*, *d* and *s* quarks). A description of how this definition is practically used in simulation is given in Section 4.3.1.

The identification of *b*-jets, known as *b*-tagging, is an essential tool in a range of ATLAS collaboration results; for example analyses studying the  $t\bar{t}$  final state [72]<sup>4</sup> and the first direct evidence of the Higgs boson coupling to the quark-sector [63]. In the same sense, identification of *b*-jets is an essential part of the analysis being presented here; by selecting *b*-jets we increase our sensitivity to BSM models that decay to 1 or 2 *b*-jets in their final state. **LM Fix, link to where I explain why this is good, maybe Intro.**

The process of *b*-tagging at ATLAS in Run-2 has been previously described in great detail [73, 74], so what follows is a summary of the key features of the process.

### 4.3.1 Assigning a Flavour Label

In simulation, the particle-level truth information is known, and hence a truth flavour label of a jet can be defined. Flavour is assigned to jets by matching truth-level heavy-hadrons with  $p_T > 5$  GeV and  $\Delta R < 0.3$  between the hadron and the jet. If a *b*-hadron is matched to a jet, the jet is then declared a *b*-jet; this process is then repeated for *c*-hadrons and then  $\tau$  leptons. If no match between *b*, *c* or  $\tau$  is achieved then the jet is assigned as a light-flavour jet. The matching is exclusive, which means that each particle is only assigned to one jet. This definition of truth flavour in simulation is used generally within this thesis.

### 4.3.2 Baseline *b*-tagging Algorithms

To identify *b*-jets, *b*-tagging algorithms utilise the long lifetimes of the heavy-hadrons that decay through the flavour changing weak interaction. A hadron containing a *b*-quark has a lifetime  $\sim 1.6$  ps [15]. A *b*-jet decay chain will typically contain two of these flavour changing interactions, as at the quark level, the *b*-quark contained in the jet will decay to a *c*-quark, which will then decay into a *u* or *d* quark. The lifetimes of the heavy flavour hadrons means that they will decay a measurable distance from the primary vertex, the point where the hard-scatter collision occurs; for example a  $B_0$  meson with a  $p_T$  of  $x$  GeV

---

<sup>4</sup>Section 5.3 contains an analysis utilising *b*-tagging in the  $t\bar{t}$  final state.

will travel approximately  $x/10$  mm. Hence, the flavour of a jet can be inferred from the presence of particles that originate from a point offset from the primary vertex.

In practice this is performed using the topology of tracks and properties of the jets, which have been described in Section 4.1 and 4.2 respectively. To utilise tracks and jets in tandem one must associate the tracks to the jets, which is performed by requiring small angular separation  $\Delta R$  between the two objects. The maximum value of  $\Delta R$  for association varies as a function of the jet- $p_T$ , resulting in a narrower cone for high- $p_T$  jets which are more collimated. At 20 GeV, it is 0.45 while for more energetic jets with a pT of 150 GeV the cut is 0.26. Tracks are exclusively matched, meaning each track is only associated with one jet, chosen using the smallest value of  $\Delta R$ .

There are three base *b*-tagging algorithms utilised to produce discriminating variables [74], which are described in the next three sections. The variables are then combined in a multi-variate algorithm which is described in Section 4.3.3. Figure 4.7 shows a schematic illustrating how tracks are used by the three *b*-tagging algorithms to identify a *b*-jet, the details of this figure are referred to in the following three sections.

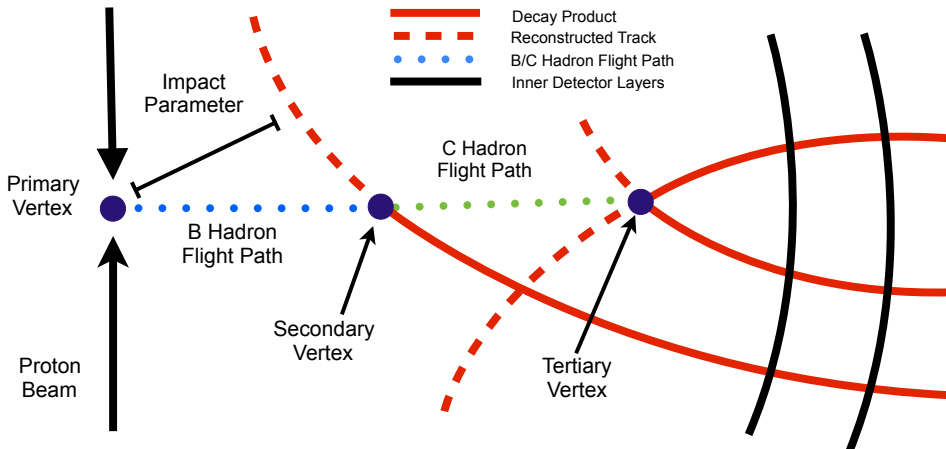


**Figure 4.7:** A diagram to illustrate the key features of a *b*-jet that are utilised by the base *b*-tagging algorithms.

#### 4.3.2.1 Impact parameter based

The IP3D algorithm is utilises the impact parameter, which is defined as the shortest distance between a specific track and the primary vertex. A track corresponding to a particle coming from the offset decay vertex of a heavy-hadron is likely to have a large impact parameter, meaning that the distribution of track impact parameter is different for each of the jet-flavours. The impact parameter of a track coming from the decay of a heavy hadron is indicated in Figure 4.7. In this algorithm, for all tracks associated to a jet, the impact

parameter is calculated in both the transverse (perpendicular to beam-line) and longitudinal (parallel to beam-line) direction, which are referred to as  $d_0$  and  $z_0$ . Then the IP3D algorithm calculates a likelihood of the jet having a specific flavour, based on the distributions of the impact parameters ( $d_0, z_0$ ) and their significances ( $d_0/\sigma_{d0}$  and  $z_0/\sigma_{z0}$ ) for tracks within the jet. Another similar algorithm, IP2D, also calculates the jet flavour likelihood from just the transverse distributions, ( $d_0$  and  $d_0$  significance), which is more robust to pile-up, as tracks from pile-up jets are likely to have a large  $z_0$  significance value.

#### 4.3.2.2 Secondary vertex

The SV1 algorithm aims to reconstruct a secondary vertex of two or more intersecting tracks, corresponding to the decay of a heavy-flavour hadron; the secondary vertex within a *b*-jet's decay chain is illustrated in Figure 4.7. The SV1 algorithm then calculates many variables that are associated with properties of the reconstructed secondary vertex that show flavour discrimination; some example variables are the vertex invariant mass, which will be larger for *b*-jets due to the heavy mass of the *b*-hadron<sup>5</sup>, the distance in the transverse plane between the primary vertex and the secondary vertex, which will be larger for *b*-jets due to the long lifetime of the *b*-hadron, and the number of tracks at the secondary vertex, which will be larger for reliable secondary vertices.

#### 4.3.2.3 Jet Fitter

The JetFitter algorithm (JF) attempts to reconstruct the full decay chain of the *b*-hadron into a charmed-hadron and then into light-hadrons. This is done by assuming that all vertices lie on a common *b*-flight axis, and then constructing vertices from the intersection of one or more tracks and the flight axis. The aim of this is to reconstruct the secondary and tertiary vertices which correspond to the decays of the *b*-hadron and charmed-hadron, as illustrated in Figure 4.7. Similar to SV1, the JetFitter algorithm then calculates a number of flavour discriminating variables: for example vertex mass and number of vertices with two or more tracks.

#### 4.3.3 Multi-Variate *b*-tagging Algorithm

The three base algorithms are combined in a boosted decision tree (BDT), a machine-learning technique for combining the many flavour-discriminating variables, resulting in an algorithm that is known as MV2. As shown in Figure 4.8, MV2 combines the likelihood output of IP3D and IP2D with the discriminating variables of SV1 and JF discussed in the preceding sections, resulting in an output between -1 and 1, where 1 indicates that the jet is

---

<sup>5</sup>Mass of a  $B_0$ -meson  $\sim 5$  GeV which is the most common *B*-hadron in a *b*-jet [15].

very likely to be a *b*-jet and -1 indicates the inverse.

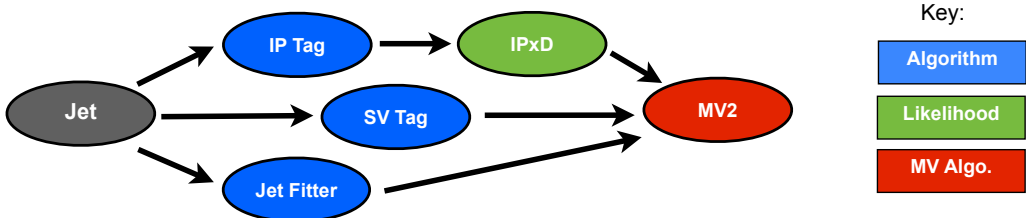


**Figure 4.8:** A diagram illustrating how three base flavour tagging algorithms are combined in the MV2 algorithm.

The BDT is trained using a simulated sample of  $t\bar{t}$  events that will contain a mix of *b*-, *c*- and light-jets as well as a sample containing a  $Z'$  boson decaying to *b*-quarks to increase statistics in the high jet- $p_T$  region. The training makes use of the truth flavour labels assigned to jets using the process described in Section 4.3.1. A training sample with known truth labels is required as this allows the BDT to be optimised such that it uses the complex correlations between the input variables to allow for high *b*-jet efficiencies whilst still obtaining a large *c*- and light-jet rejection. Subtly different algorithms can be obtained using samples containing different fractions of light and *c*-jets, the fraction of *c*-jets used is labelled in the algorithm name; for example the MV2c10 algorithm has been trained on a sample containing 10% charm-jets, which gives strong light- and *c*-rejection.

A cut is then applied to this MV2 output in order to select jets that are likely to *b*-jets. The choice of cut will vary the *b*-jet efficiency, light-jet rejection and *c*-jet rejection, where *b*-jet efficiency is defined as the probability of accepting a true *b*-jet, light-jet rejection is defined as 1 divided by the probability of accepting a true light-jet, and a similar definition applies for *c*-jet rejection. Figure 4.9 shows the *b*-jet efficiency against (a) light and (b) *c*-jet rejection of the MV2 algorithm for a continuous range of cuts. The different lines show the performance of the algorithm in the 2015 configuration [73] and in the 2016 configuration [74] where a range of different fraction of *c*-jets are used in the training; 2016 MV2c10 is the configuration used generally in this thesis as recommended in [74].

ATLAS has a set of common pre-set cuts used, known as operating points, such that work required to calibrate *b*-tagging in each analysis is shared. Looser operating points have a relatively low cut on MV2 output, meaning that the *b*-jet efficiency is higher at the cost of worse light- and *c*-jet rejections, and the inverse is true for tighter operating points. Table 4.1 shows the list of fixed cut operating points that are used in ATLAS with a given cut on MV2c10 output; shown with the corresponding benchmark *b*-jet efficiency, *c*-jet rejection, light-jet rejection and  $\tau$  rejection.<sup>6</sup>

---

<sup>6</sup>In this thesis only the fixed-cut operating points shown above will be used, however, there also exists a set

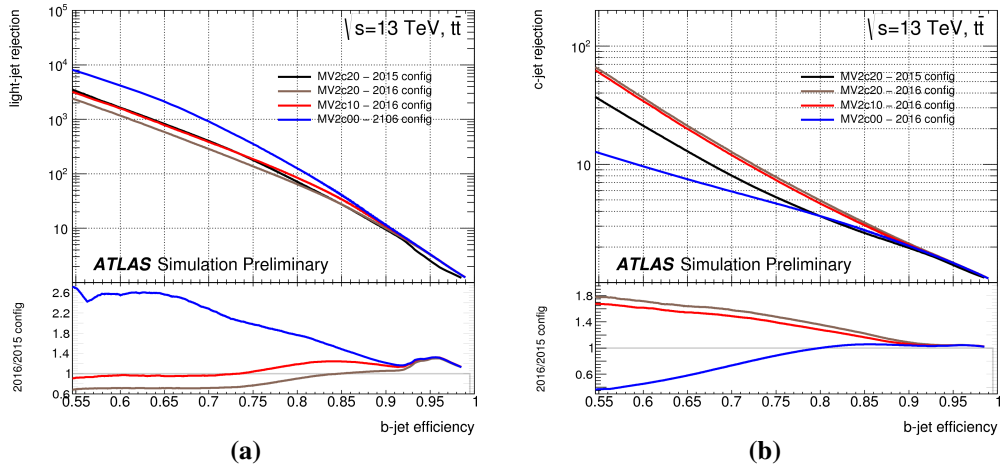


**Figure 4.9:** The expected  $b$ -jet efficiency of  $b$ -tagging algorithm, MV2, with respect to (a) light-jet and (b)  $c$ -jet rejection in simulated  $t\bar{t}$  events. The various lines show the performance of the algorithm for different configurations and training setups [74].

MV2 Cut Value	$b$ -jet efficiency [%]	$c$ -jet rejection	Light-jet rejection	$\tau$ rejection
0.9349	60	34	1538	184
0.8244	70	12	381	55
0.6459	77	6	134	22
0.1758	85	3.1	33	8.2

**Table 4.1:** The Mv2c10 b-tagging algorithm operating points; with the corresponding  $b$ -jet efficiency,  $c$ -jet rejection, light-jet rejection and  $\tau$  rejection. This table is taken from reference [74].

#### 4.3.4 Calibration and Uncertainties

As with any part of a measurement, the process of  $b$ -tagging must be calibrated using data.  $b$ -tagging calibration is performed using a pure sample of  $b$ -jets extracted from di-lepton  $t\bar{t}$  events using the probability distribution function method [75, 76]. With the pure  $b$ -jet sample one can calculate the  $b$ -jet efficiency,  $\epsilon_{b\text{Tag}}$ , defined as:

$$\epsilon_{\text{bTag}} = \frac{N(\text{b-tagged true } b\text{-jets})}{N(\text{True } b\text{-jets})} \quad (4.5)$$

where  $b$ -tagged means above the cut on the MV2 output for a given operating point. By measuring  $\varepsilon_{b\text{Tag}}$  in both data and in Monte-Carlo simulation one can derive a correction to simulation, known as a data/MC scale factor ( $SF_{b\text{Tag}}$ ), defined as:

$$SF_{\text{bTag}} = \epsilon_{\text{bTag}}^{\text{Data}} / \epsilon_{\text{bTag}}^{\text{MC}} \quad (4.6)$$

of flat efficiency operating points where the MV2 cut depends on jet- $p_T$

Uncertainties are derived for the scale factors to account for factors such as uncertainties in the modelling of the backgrounds in simulation and uncertainties in the modelling of the detector response to electrons, muons and jets. The dominant uncertainty comes from modelling of  $t\bar{t}$  in simulation. Figure 4.10 shows the data/MC scale factor measured in 2015 and 2016 data as a function of jet  $p_T$ . The scale factor is consistent with unity within uncertainties everywhere, showing that *b*-tagging is generally well-modelled in simulation.

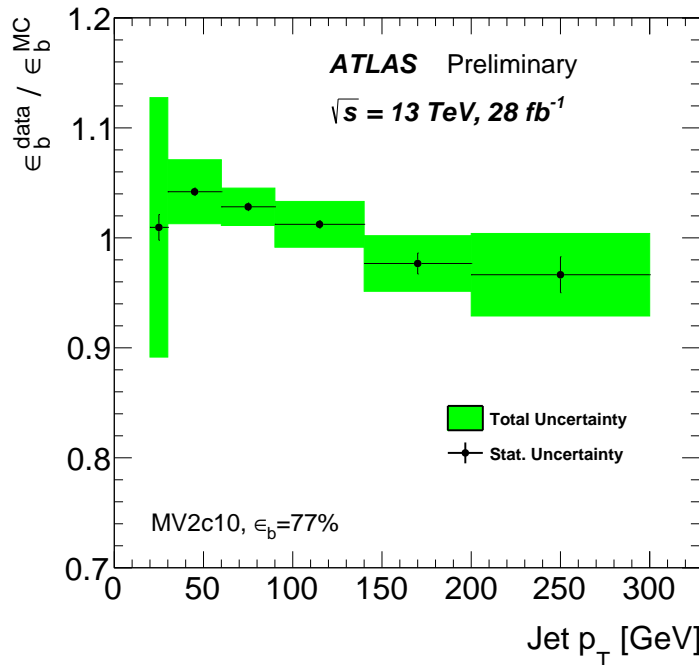


**Figure 4.10:** Ratio of *b*-tagging efficiency in data and Monte Carlo for the MV2c10 *b*-tagging algorithm at the 77% working point as a function of jet- $p_T$ , extracted using di-lepton  $t\bar{t}$  events. Statistical uncertainties (black lines) and total uncertainties (green shaded region) are shown [76].

The *b*-tagging calibration using di-lepton  $t\bar{t}$  events described above is unable to measure a data/MC scale factor for jets with  $p_T$  greater than 300 GeV, due to low data statistics in the high- $p_T$  region. Thus, the measured scale factors are extrapolated to cover the high jet- $p_T$  region, and that this extrapolation procedure introduces additional uncertainties [77]. The extrapolation and uncertainty is calculated from simulated events by considering variations on the quantities affecting the *b*-tagging performance such as the resolution of the impact parameter, quality of reconstructed tracks, description of the detector material, and number of tracks per jet. The dominant effect on the uncertainty when extrapolating to the high jet- $p_T$  region is related to the different tagging efficiencies when varying the track impact parameters. **Question for AK; this paragraph inspired from flag tag recommendation on a twiki; reference is internal. :/**

### 4.3.5 *b*-Jet Energy Scale

In Sections 4.2.3 and 4.2.4 it was described that one must apply a correction to correct the energy of a jet from the detector-level to the true particle-level jet energy and this correction had an associated uncertainty. For *b*-jets this correction may be different to light jets due to differences in the parton shower and hadronisation processes for a *b*-jet; for example during the decay of the *b*-hadron muons and neutrinos are produced which will not deposit all/any of their energy in the calorimeter which could affect the scale of the correction. This effect is known as the *b*-jet energy scale (*b*JES) and is accounted for with an additional uncertainty.

The *b*JES uncertainty is derived and validated in data by comparing the measured jet energy with respect to an independent well calibrated object, in this case tracks, as described in Appendix H of [78]. We perform this comparison for *b*-jets and inclusive jets for a dijet sample in simulation and data, where a *b*-jet means it has been *b*-tagged at the 85% operating point and inclusive means no requirement on *b*-tagging has been applied. To do the track-jet comparison tracks are associated to jets using ghost association. Ghost association re-runs the jet clustering algorithm used to form the jets in an event, using tracks with  $p_T$  manually set to 0 as inputs in addition to the usual calorimeter topoclusters. As the tracks have  $p_T$  set to 0, the jet reconstruction algorithm will form the same jets as before, except that tracks will now be associated to the various jets.

The measured jet- $p_T$  is compared to the sum of the tracks associated to the jet,  $\Sigma p_T^{trk}$  using the observable,  $r_{trk}$ , defined as

$$r_{trk} = \Sigma p_T^{trk} / p_T^{jet} \quad (4.7)$$

One can split up the expected value of the observable  $r_{trk}$  into three components.

$$\langle r_{trk} \rangle = \left\langle \frac{\Sigma p_T^{trk,truth}}{\Sigma p_T^{trk,reco}} \right\rangle \left\langle \frac{p_T^{jet,truth}}{\Sigma p_T^{trk,truth}} \right\rangle \left\langle \frac{p_T^{jet,reco}}{p_T^{jet,truth}} \right\rangle \quad (4.8)$$

The first term describes the track energy response which, as tracks are calibrated, has been measured in data and simulation. The second term is the mean charged fraction of the jet,  $\langle f_{charge} \rangle$ , which will be estimated from simulation. The third term is the jet energy response, which is the jet energy scale correction that we are interested in measuring.

The systematic uncertainties that cover the measurement of  $r_{trk}$  arise from the jet and *b*-jet modelling in simulation (referred to as fragmentation), *b*-tagging calibration, jet resolution and tracking efficiency. In addition, an uncertainty to cover a bias observed in  $\langle f_{charge} \rangle$  for *b*-tagged jets relative to inclusive jets is added to the relative systematic un-

certainty. The uncertainty on the  $r_{trk}$  measurement are used as the *b*JES uncertainty, which varies between 1-4% depending on jet- $p_T$ . Figure 4.11 shows the derived total *b*JES uncertainty with respect to jet- $p_T$ , the components that contribute to the uncertainty are also shown.

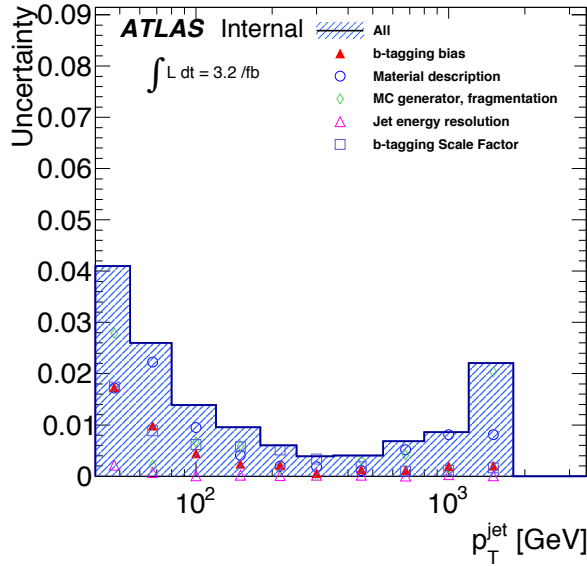


**Figure 4.11:** The total fractional *b*JES uncertainty shown with the various contributions [78].

Then one can test the derived *b*JES uncertainties in data using a double ratio approach. The first ratio compares the observable in data and Monte-Carlo;

$$R_{trk} = r_{trk}^{Data} / r_{trk}^{MC} \quad (4.9)$$

And then the double ratio,  $R'_{trk}$  compares the  $R_{trk}$  for *b*-jets and inclusive jets;

$$R'_{trk} = R_{trk}^{b-jet} / R_{trk}^{inclus.} \quad (4.10)$$

The double-ratio approach means that many of the uncertainties unrelated to *b*JES are cancelled in the ratios.

Figure 4.12 shows the double ratio  $R'_{trk}$  with the *b*JES uncertainty applied. The ratio is almost consistent with unity within uncertainties validating our *b*JES uncertainty in data.

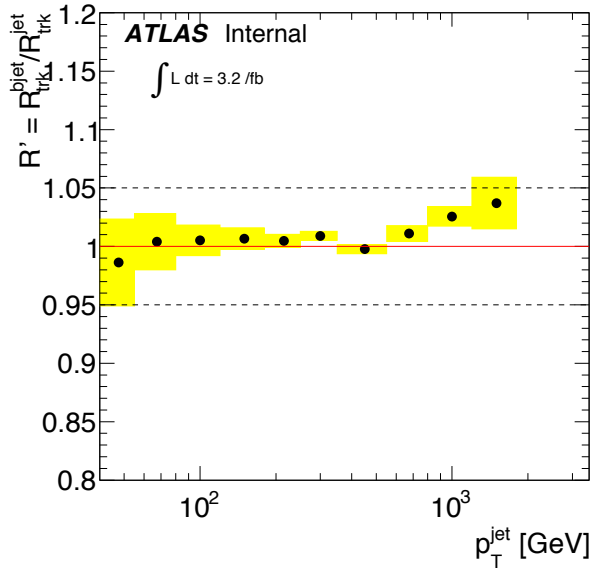


**Figure 4.12:** The validation of the  $b$ JES uncertainty in data using the double-ratio  $R'_{trk}$  [78].

## 4.4 Electrons and Muons

Reconstruction of electrons and muons is important for a number of analyses at ATLAS; including the selection of di-lepton  $t\bar{t}$  events which are used in the calibration of  $b$ -tagging and the  $b$ -jet trigger, described in Sections 4.3.4 and 5.3 respectively. As these objects are not used in the final analysis presented in this thesis, they are described below in less detail than has been given to jets and  $b$ -jets.

Electron<sup>7</sup> reconstruction at ATLAS [79] uses the matching of narrow clusters of energy deposits in the calorimeter to a track from the inner detector, from which the four-momentum of the electron can be determined. Information such as the calorimeter shower shape, properties of the matched track and TRT transition radiation (described in Section 3.2.2) allows for identification of electrons with respect to other physics objects described in this section. Three different operating points are provided for electron identification: which are, in order of increasing background rejection *Loose*, *Medium*, and *Tight*.

Muon<sup>8</sup> reconstruction at ATLAS uses muon tracks reconstructed using the Muon Spectrometer (MS) and tracks constructed by the Inner Detector (ID). There are several types of muon reconstruction techniques and different muon identification working points available [80].

Two of the techniques for reconstruction are combined muons and extrapolated muons.

---

<sup>7</sup>For the purposes of reconstruction positrons are included as a subset of electrons

<sup>8</sup>Similar to positrons, in reconstruction anti-muons are included as a subset of muons

Combined muons are reconstructed by extrapolating muon tracks inwards to match tracks formed by the ID. Extrapolated muons are formed from muon tracks alone, with a loose requirement on the track pointing to the primary vertex; extrapolated muons are important in the range  $2.5 < \eta < 2.7$  for which there is no ID coverage. Again for reconstructed muons the four-momentum can be determined.

Four muon identification working points have been defined *Loose*, *Medium*, *Tight*, and *High- $p_T$* . Medium muons, as used in Section 5.3, are made up of combined and extrapolated muons that pass a quality criteria based on number of MS hits, track fit quality and, where relevant, compatibility between the ID and MS tracks.

## 4.5 Further objects

In the previous sections of this chapter all objects used in the analyses presented in this analysis have been described. However this is not an exhaustive list of the range of objects that ATLAS can reconstruct. In this section I will briefly outline some of the many other objects of interest that are used elsewhere in ATLAS analyses.

- **Photons:** Photons can be identified from using narrow clusters of energy deposits in the calorimeter similar to that of electrons, except with no track associated [81]. Information such as the calorimeter shower shape and TRT transition radiation allows for identification of electrons with respect to other physics objects, notably electrons.
- **Taus:** Taus, in their most common decay mode, can be identified and reconstructed using narrow calorimeter jets associated to a topologies of tracks that match their known decay chain [82].
- **Missing Transverse Momentum:** It is known that the momentum in the transverse plane is conserved, hence from the negative sum of the momentums of all reconstructed physics objects in an event one can determine the presence of missing transverse momentum (MET) [83]. MET can be used to identify the presence of particles that interact weakly with the ATLAS detector, such as neutrinos [63] or even dark matter [84].

## Chapter 5

# Triggering in the di-*b*-jet analysis

As described in Section ??, ATLAS does not have the resources to process and store all the data from the 40 MHz of collisions delivered by the LHC. To solve this problem the ATLAS trigger system performs the vital role of reducing the rate of data-taking to 1 kHz by selecting events containing a high- $p_T$  object.

As a result all analyses must chose a trigger strategy and understand the impact of this trigger on their analysis. In the di-*b*-jet analysis a single jet trigger is used for the high-mass channel and a double *b*-jet trigger for the low-mass channel. This chapter aims to provide a detailed description of the triggers used in this analysis, and as such is organised in the following manner; Section 5.1 provides a brief description of jet triggers as used in the high-mass channel and the limitations of this approach, Section 5.2 contains a description of *b*-jet triggers that are used in the low-mass channel and finally Section 5.3 presents the measurement of the *b*-jet trigger efficiency, an essential input of the low-mass channel.

## 5.1 Jet-Triggers

Jet-triggers are tasked with selecting events with one or more jets from the deposits in the ATLAS calorimeter system, this is one of most challenging triggers in any hadron-hadron collider due to the extremely high cross-sections of hadronic jet production [85]. In Run-2 the jet-triggers are used at both L1 and HLT level; each using different levels of information and different algorithms, so are described separately within this section.

### 5.1.1 Level 1

The L1 trigger is a hardware based trigger which accepts or rejects an event within 2.2  $\mu$ s. The L1 jet-trigger receives trigger towers from the calorimeter; where a trigger tower is the

measured energy deposit in a cell of the ECAL or HCAL of granularity  $0.1 \times 0.1$  in the  $\eta - \phi$  plane. In the L1 trigger hadronic jet algorithms search for a neighbouring group of  $4 \times 4$  trigger towers containing energy deposits above some pre-set threshold. Our analysis uses the L1 trigger known as `L1_J100`, which requires that at least one trigger tower group with an energy deposit of 100 GeV has been found. Other L1 triggers that search for multiple clusters are also possible to reduce the energy thresholds required. The L1 trigger then seeds the HLT trigger. It is also worth noting that at L1 there is no tracking information, meaning that electron and taus are also triggered on using similar techniques as hadronic jet algorithms, except using narrower groups of trigger towers.

### 5.1.2 HLT

The HLT trigger is a software based trigger which, due to the lower input rate and larger time window, is able to use more complex algorithms to reconstruct jets. At the HLT level jets are reconstructed using topoclusters (TCs) constructed from neighbouring cells selected using the cell's energy significance ( $E/\sigma$ ); TCs are seeded from cells with  $E/\sigma > 4$ , then neighbouring cells with  $E/\sigma > 2$  are added and finally all neighbouring cells around are also added. Jets are then reconstructed from the topoclusters; in this analysis jets have been reconstructed using the anti- $k_T$  algorithm with an  $R = 0.4$ <sup>1</sup>.

### 5.1.3 High-mass trigger selection

For the high-mass analysis the trigger `HLT_j380` is used, that is fired when a jet is found with a  $p_T > 380$  GeV. This is chosen as it is the lowest unprescaled single jet-trigger; meaning that of triggers that accept every event passing a single jet criteria, this trigger has the lowest jet- $p_T$  threshold. Due to the exponential increase in jet production cross-section at low jet- $p_T$ , the  $p_T$  threshold is set to keep the acceptance rates low enough such that the HLT trigger is within its output rate budget of 1 kHz.

However, as will be discussed further in Section 6, this  $p_T$  threshold limits the high-mass di- $b$ -jet analysis to only select events with  $m_{jj} > 1.2$  TeV. Otherwise the  $m_{jj}$  range will enter a kinematic region where trigger acceptance is less than 1 in such a way that the QCD background is sculpted in a manner that the background modelling can not adapt to. To reach lower masses a different trigger strategy is required.

---

<sup>1</sup>Section 4.2 (`sec:obj-jets`) defines these terms

## 5.2 *b*-Jet Triggers

This analysis searches for pairs of *b*-jets, which, as described in Section 4.3(*sec:obj-bjets*), can be identified from the topology of tracks in the inner detector indicating that a *B*-hadron was within the jet. The same techniques can be used at the trigger level to reduce rates significantly<sup>2</sup> allowing a lower jet- $p_T$  threshold than was used by the single jet- $p_T$  trigger, and hence lower  $m_{jj}$  values to be accessed. *b*-jet triggers have been used in a range of previous ATLAS analyses including for searches for exotic particle decaying into a pair of Higgs bosons, which then decay to 4 *b*-jets [86].

### 5.2.1 General description

In 2016 data, the *b*-jet trigger configuration contains three steps [87], making use of the regions of interest (RoI) described by the jets found by the jet-trigger. Firstly, a ‘fast’-tracking algorithm is run in a super-RoI which is formed around all jets in the event which have  $E_T > 30$  GeV; these tracks are then used to identify the primary vertex in the event. Secondly, within each jet RoI precision tracking is run, with a constraint on the PV position from the first step. Finally, these tracks are the input to the multi-variate *b*-tagging algorithm described in Section 4.3.3(*sec:obj-bjets\_MV2*) to identify *b*-jets. There are several *b*-jet triggers available in the ATLAS trigger menu; with a variety of requirements on the jet multiplicity, number of tagged jets and *b*-tag operating point used. Figure 5.1 shows ROC curves representing the expected performance of the Run-2 *b*-jet trigger.

There are few subtleties worth commenting on the *b*-jet trigger configuration which affect decisions taken in this analysis. One is that on this figure there are two lines corresponding to different *b*-tagging algorithms used in *b*-jet trigger; IP3D+SV1 was used in 2015 data-taking, whilst the MV2c20 was used in 2016 data-taking. Another difference between 2015 and 2016 is the primary vertex finding algorithm used; 2016 data-taking employed an algorithm based on offline primary vertex finding, known as `xPrmVtx`, whilst in 2015 an algorithm using a simpler histogram based approach was employed, known as `EFHist`.

Finally it is worth noting that there are differences between online and offline *b*-tagging that will have an impact on what is to follow. Firstly, coarser tracking information is available online, notably online tracks are not reconstructed from the whole range of the detector. Secondly, a slightly different training setup is used for the multi-variate algorithm, mainly that a different fraction of *c*-jets were present in the training sample; 10% were used offline and 20% were used online.

---

<sup>2</sup>It is known that the QCD background is dominated by light-jets, see Figure ??*Plot of background flav comp*

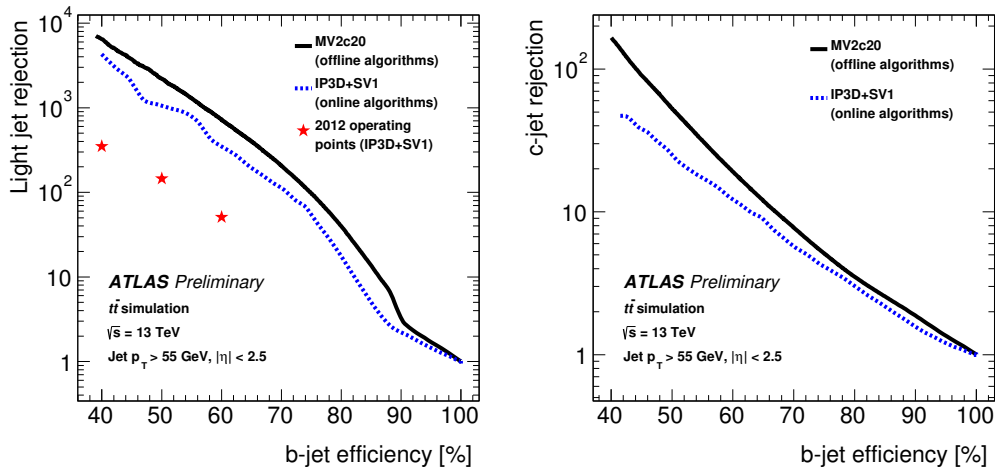


**Figure 5.1:** The expected *b*-jet efficiency of *b*-jet triggers with respect to (a) light-jet and (b) *c*-jet rejection in the case where the *b*-tagging algorithm used is MV2c20 (Black), IP3D+SV1 (Blue) and for the set-up used in Run-1 (red stars) [87].

In this analysis a double *b*-jet trigger is used,

```
HLT_j150_bmv2c2060_split_j50_bmv2c2060_split
```

which triggers on two jets with  $p_T > 150$  and 50 GeV respectively, which have been *b*-tagged at the 60% efficiency working point.

## 5.3 Efficiency Measurement of the $b$ -Jet Trigger

Any part of the ATLAS detector framework needs to be understood and calibrated with data for use in an analysis; and this includes the trigger which can have a large impact on the analysis. In this section I discuss the strategy and results of the  $b$ -jet trigger efficiency measurement in 2016, which is an important input to the low-mass channel of the di- $b$ -jet analysis.

For clarity in this section I would like to make two definitions clear. Online refers to any algorithms run or objects reconstructed at the trigger level, offline refers to algorithms run after events have passed the trigger at the data-processing level.

### 5.3.1 Strategy

The  $b$ -jet trigger is always used in tandem with offline  $b$ -tagging which is calibrated independently of the  $b$ -trigger. As mentioned before, there are many differences between offline and online  $b$ -tagging. Hence, to do this measurement whilst making use of the offline  $b$ -tagging calibrations already available,  $b$ -jet trigger efficiency with respect to offline  $b$ -tagging,  $\epsilon_{bTrig}$ , is measured. This is defined as the number of offline-tagged true  $b$ -jets that match an online-tagged trigger-jet divided by the number of offline tagged  $b$ -jets that match a trigger jet. Or to put this in an equation;

$$\epsilon_{bTrig} = \frac{N(\text{Offline-tagged, online-tagged, true } b\text{-jets})}{N(\text{Offline-tagged, trigger-matched, true } b\text{-jets})} \quad (5.1)$$

This quantity can be interpreted as the probability that a true  $b$ -jet is tagged at the trigger-level, given that it there is a jet at the trigger level and that it would be  $b$ -tagged at the offline stage.

To measure  $\epsilon_{bTrig}$  a sample that has high  $b$ -jet purity is required, such that jets used to calculate this ratio are true  $b$ -jets. It is also necessary to trigger on this sample in such a way that there is no bias from using  $b$ -tagging online; or simply put the  $b$ -jet trigger cannot be used to select events. The sample used to fill these criteria is a di-lepton  $t\bar{t}$  sample containing a muon and an electron. Top-quarks decay to a  $W$ -boson and a  $b$ -quark with almost 100% branching ratio meaning that this sample provides a good source of  $b$ -quarks, but also the electron and muon give a distinct signature which allows us to select this process with good purity and gives a non- $b$ -jet object to trigger on. The exact event selection is described below.

The  $b$ -jet trigger efficiency is determined in data and is compared to the efficiency

found in a simulated  $t\bar{t}$  sample which is used to extrapolate the efficiency to higher jet- $p_T$  where the data-derived efficiency loses statistical precision. The efficiency in data, including the simulation based extrapolation, can then be compared to simulation to derive a Data/Monte-Carlo scale factor, which is used as the input to the analysis.

$\epsilon_{bTrig}$  and Data/Monte-Carlo scale factors are derived for all combinations of offline and online  $b$ -tagging working points. However, only the process for the 70% offline and 60% online working point is shown as this is set of working points used in this analysis, further details will be described in Chapter ??.

### 5.3.2 Datasets

The data used for this analysis is the full 2016 ATLAS data-set. In addition to the usual data-quality requirements applied, as discussed in Section ?? a  $b$ -jet trigger aware Good Run List (GRL)<sup>3</sup> applies the requirement that the online beamspot  $z$ -position is within 2mm of the origin in Periods A-I of the data. This means that the data-set contains  $24.3 \text{ fb}^{-1}$  of data. A discussion of the requirement for this GRL is in Section 5.3.6.

For the simulated  $t\bar{t}$  sample, the generation is performed with a Powheg-Box v2 [88] generator with the CT10 PDF sets in the matrix element calculations. Also considered is a simulated single-top sample; electroweak t-channel, s-channel and  $Wt$ -channel single top-quark events are generated using the Powheg-Box v1 generator. This generator uses the 4-flavour scheme for the NLO matrix elements calculations together with the fixed four-flavour PDF set CT10f4. For both processes the parton shower, fragmentation, and the underlying event are simulated using Pythia6.428 [89] with the CTEQ6L1 [90] PDF sets and the corresponding Perugia 2012 tune (P2012) [91]. The top mass is set to 172.5 GeV. The EvtGen v1.2.0 program [92] is used for properties of the bottom and charm hadron decays.

---

<sup>3</sup>A GRL is effectively a list of lumi-blocks that pass certain data-quality requirements. As mentioned in the text a further discussion is held here in Section ??

### 5.3.3 Event Selection

A high-purity sample of  $b$ -jets is selected using a di-lepton  $t\bar{t}$  selection.

The event selection is summarised as follows:

- The event fired a single lepton bperf trigger which are:
  - HLT\_mu26\_imedium\_2j35\_bperf
  - HLT\_e26\_tight\_iloose\_2j35\_bperf
  - HLT\_e26\_lhtight\_iloose\_2j35\_bperf
- At least 1 medium muon:  $p_T > 25$  GeV, which has no jet within a  $\Delta R$  of 0.4.
- At least 1 medium electron:  $p_T > 25$  GeV.
- 2 offline  $b$ -tagged jets, defined as:
  - Offline  $R=0.4$  anti- $k_T$  jets.
  - $p_T > 35$  GeV and  $|\eta| < 2.5$ .
  - Offline  $b$ -tagged at the 85% operating point.
  - Jet must be matched to a trigger-jet.

Descriptions of the object-definitions of muons, electrons, jets and  $b$ -tagged can be found in Sections ??(sec:obj-muon), ??(sec:obj-elec), 4.2(sec:obj-jet) and 4.3(sec:obj-bjet) respectively. Online trigger jets are matched exclusively to offline jets using  $\Delta R$  matching, requiring for a match the jets must have  $\Delta R < 0.6$ .

The triggers used are bperf trigger, which are special triggers used in data-taking specifically for monitoring the  $b$ -jet trigger performance. They fire if a muon or an electron with  $p_T > 26$  GeV is reconstructed at the trigger level. The bperf triggers then run the online  $b$ -tagging algorithm on all trigger jets with  $|\eta| < 2.5$  and  $p_T > 35$  GeV without performing any cuts on the output of the multi-variate algorithm; ensuring there is no bias in the efficiency measurement.

### 5.3.4 The Initial Problem

To give context to the following section; the first discussion will be what was first observed when measuring the  $b$ -jet efficiency. To show the problems observed clearly, in this section the initial event selection is replicated; hence no  $b$ -jet trigger aware GRL is applied, offline jets are not required to match a trigger jet in the denominator and the triggers required are single lepton triggers without the additional  $b$ -perf functionality<sup>4</sup>. In addition, for this and the following two sections simulation refers to  $t\bar{t}$  only, but it will be shown later that the effect of single-top production is small so the conclusions here are still valid.

Figure 5.2 shows  $\epsilon_{b\text{Trig}}$  against jet- $p_T$  and jet- $\eta$ ; the efficiency in data is substantially below the efficiency expected from simulation and shows a clear shape in jet- $\eta$  distributions. This substantial differences need to be investigated and understood.

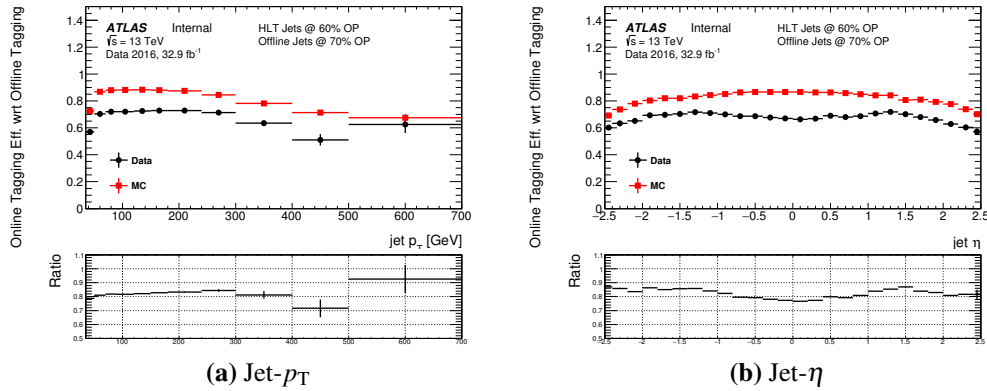


**Figure 5.2:** The 60%  $b$ -jet trigger efficiency with respect to an offline 70% operating point tag for Data (black) and simulation (red) against jet- $p_T$  (a) and jet- $\eta$  (b). The  $b$ -trigger aware GRL is not applied and trigger matching is not required.

### 5.3.5 Investigation

Given the disagreements between data and simulation shown above a number of cross-checks were performed to understand this discrepancy, including checking for performance dependence on period, detector performance, pile-up conditions and online beamspot position. In this section, I summarise the results of the investigation and our understanding of the  $b$ -trigger performance in 2016 data. For this, the set-up as described in 5.3.3 is used with the exception that the  $b$ -jet aware GRL is not applied to allow us to see the problems clearly.

The major problem that was discovered to be causing the large discrepancies was re-

<sup>4</sup>Specifically HLT\_mu26\_imedium, HLT\_e26\_tight\_iloose and HLT\_e26\_lhtight\_iloose.

lated to primary vertex finding. As described above, in 2016 data an algorithm known as `xPrmVtx` was used to find the primary vertex. It has since been uncovered that there was a bug in the code used to implement this algorithm; effectively different co-ordinates were used by different components of the code. Online tracks passed to `xPrmVtx` use position with respect to online beam-spot position, where the `xPrmVtx` algorithm assumed track position with respect to the origin. This means that when the online beamspot  $z$ -position is far from the origin, a dummy vertex with position at the origin is passed to the  $b$ -tagging algorithms. This leads to sub-optimal performance, as will be shown below. For ease of reading online beamspot  $z$ -position is henceforth referred to as  $z_{bs}^{online}$ .

The exact setup for the  $b$ -jet trigger has changed as data has been taken, to respond to performance issues as they are noticed and patches are applied. As such the relevant conditions of the  $b$ -jet trigger can be split into three regions of data-taking, which I will refer to as epochs. The effect of `xPrmVtx` returning a dummy vertex on  $b$ -jet trigger performance is different in each of these epochs, the details are summarised Table 5.1. As a result of these differences in trigger performance, each epoch is now considered independently.

Epoch	Runs	Periods	Effect if no <code>xPrmVtx</code> PV is found
1	296939- 300571, 300655	A,B(part)	An invalid vertex is passed to the online b-tagging
2	300600, 300784-308084	B(part),C,D,E,F,G,I,J	The $b$ -jet trigger is not fired
3	309331-311481	K,L	A back-up primary vertex finding algorithm is used.

**Table 5.1:** A table describing the effect of not finding a valid `xPrmVtx` primary vertex on different epochs of data.

Firstly let us consider Epoch 1; Figure 5.3(a) shows that efficiency against jet- $p_T$  is 80-90% of that in simulation, similar to that shown in the previous section. However, Figure 5.3(b) shows that  $\epsilon_{bTrig}$  in Epoch 1 has a strong dependence of  $z_{bs}^{online}$ ; when  $z_{bs}^{online}$  is close to zero  $\epsilon_{bTrig}$  in data and simulation are comparable<sup>5</sup> but as  $|z_{bs}^{online}|$  increases efficiency falls off steeply. To understand this performance the variable ‘vertex class’ is studied, which is defined as 0 when a valid `xPrmVtx` vertex is found and 1 if not. Figure 5.4(a) shows that when an `xPrmVtx` vertex is found  $\epsilon_{bTrig}$  is reasonably high ( $\sim 0.8$ ) and is comparable between data and simulation (within 5%), whilst if no valid `xPrmVtx` vertex

---

<sup>5</sup>In simulation the  $z_{bs}^{online}$  is always set to zero.

is found then efficiency is very low in both simulation and data. However, Figure 5.4(b) shows that a valid  $\text{xPrmVtx}$  vertex is found in simulation in  $> 99\%$  of the jets, whilst in data there is  $\sim 16\%$  of events where no valid  $\text{xPrmVtx}$  vertex is found. Hence, combining the information in Table 5.1, Figure 5.3 and Figure 5.4 it can be concluded that in Epoch 1 in events where the  $|z_{bs}^{\text{online}}|$  is far from 0 then  $\text{xPrmVx}$  returns a dummy vertex which results in a low  $\varepsilon_{bTrig}$ , explaining the data/simulation differences in Epoch 1.

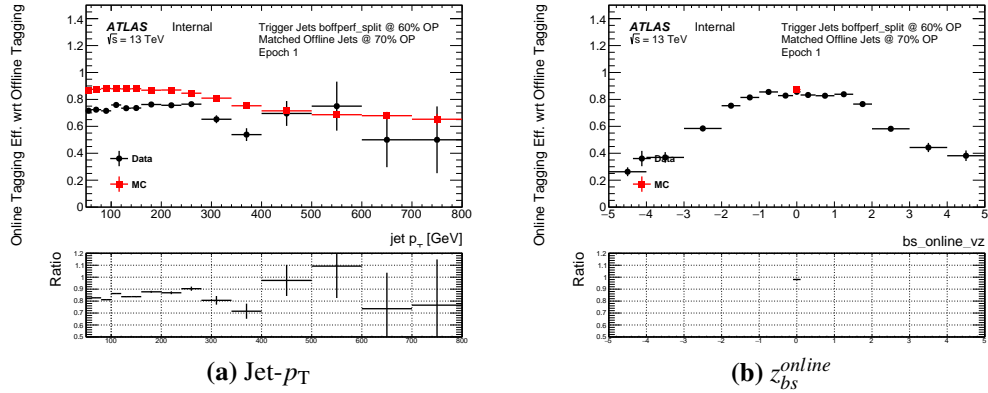


**Figure 5.3:** The 60%  $b$ -jet trigger efficiency with respect to an offline 70% operating point tag for data from Epoch 1 (black) and simulation (red) against jet- $p_T$  (a) and online beamspot  $z$ -position (b). The  $b$ -jet trigger aware GRL has not been applied.

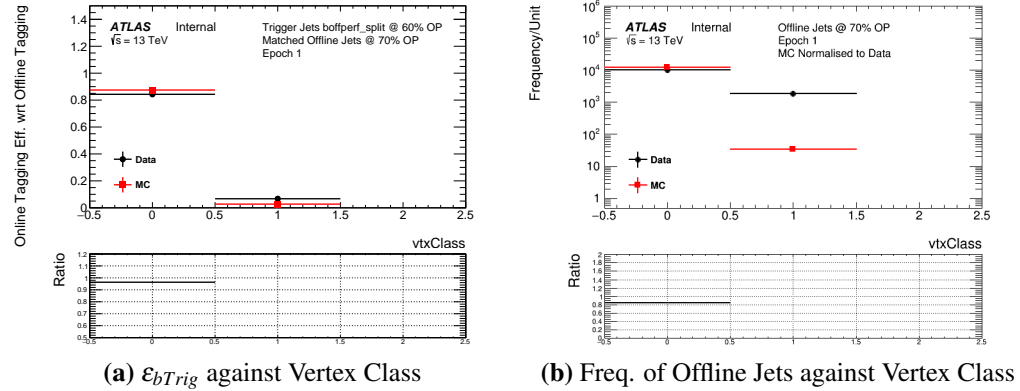


**Figure 5.4:** (a) The 60%  $b$ -jet trigger efficiency with respect to an offline 70% operating point tag and (b) the number of offline jets passing 70% operating point tag and matching a HLT trigger jet against vertex class for data from Epoch 1 (black) and simulation (red). The  $b$ -jet trigger aware GRL has not been applied.

In Epoch 2, there is a similar problem to Epoch 1, but there is a subtle difference which requires us to look at this region in a different way. As in Epoch 1, when  $z_{bs}^{\text{online}}$  is far from zero then a  $\text{xPrmVtx}$  PV is not found. However in Epoch 2 this means that the  $b$ -jet trigger was discovered to falsely terminate whilst processing the event, meaning that there are no online  $b$ -jets available in the event, and therefore the trigger will not

fire. However, the additional complication compared to Epoch 1 is this means that the  $b$ -perf triggers used to measure the efficiency are also not fired when no valid  $\text{xPrmVtx}$  PV is available. Hence, measuring  $\epsilon_{b\text{Trig}}$  using the set-up as described will not capture the cases where a valid  $\text{xPrmVtx}$  PV is found and thus  $\epsilon_{b\text{Trig}}$  should be consistent in data and simulation; Figure 5.5 shows that the  $\epsilon_{b\text{Trig}}$  measured in data to be in agreement with simulation within 5%.

For Epoch 2, in addition to measuring  $\epsilon_{b\text{Trig}}$  it is necessary to also account for the cases when a false  $\text{xPrmVtx}$  PV is found. This is done by measuring the  $b$ -perf efficiency,  $\epsilon_{b\text{Perf}}$ , the efficiency that there is a valid primary vertex in the event.  $\epsilon_{b\text{Perf}}$  is calculated by dividing the number of events that pass the trigger `HLT_mu26_imedium_2j35_bperf` by the number that pass the trigger `HLT_mu26_imedium`, such that the denominator has no  $b$ -trigger dependency so is unaffected by  $\text{xPrmVtx}$  PV. This is an event level quantity and as such is measured with respect to other event level quantities, such as leading jet- $p_T$ . Figure 5.6 shows that:  $\epsilon_{b\text{Perf}}$  has a data/simulation ratio of around 80% which is similar to that in Section 5.3.4 and  $\epsilon_{b\text{Perf}}$  shows similar behaviour with respect to  $z_{bs}^{online}$  as observed in Epoch 1. Finally it is observed that  $\epsilon_{b\text{Perf}}$  has a lower efficiency at smaller values of absolute leading jet- $\eta$ ; this is due to the fact that at high- $\eta$  tracks have a larger error on the longitudinal impact parameter,  $z_0$ , meaning that the mis-match of co-ordinates can in the  $\text{xPrmVtx}$  algorithm is covered by the errors, mitigating this issue. This effect must be accounted for in the final efficiency measurement. **This last two sentances are dodgy**

Epoch 3, when no  $\text{xPrmVtx}$  PV is found then a backup PV finding algorithm is used, known as `EFHist`, which finds the PV through a basic histogramming of the tracks, the simplicity of the algorithm means that a PV can be found as long as 1 track is present. Figure 5.7 shows  $\epsilon_{b\text{Trig}}$  for Epoch 3 for jet- $p_T$ , jet- $\eta$ ,  $z_{bs}^{online}$  and vertex class (as defined above). In Epoch 3  $\epsilon_{b\text{Trig}}$  measured in data is within 5% of simulation and there is no shape difference between the two with respect to jet- $\eta$ . In addition it is shown that in Epoch 3 there is no strong dependence on  $z_{bs}^{online}$ , and that efficiency in data is consistent if a valid  $\text{xPrmVtx}$  vertex or not (vertex class = 0 or 1 respectively). This demonstrates the success of the backup vertex approach.

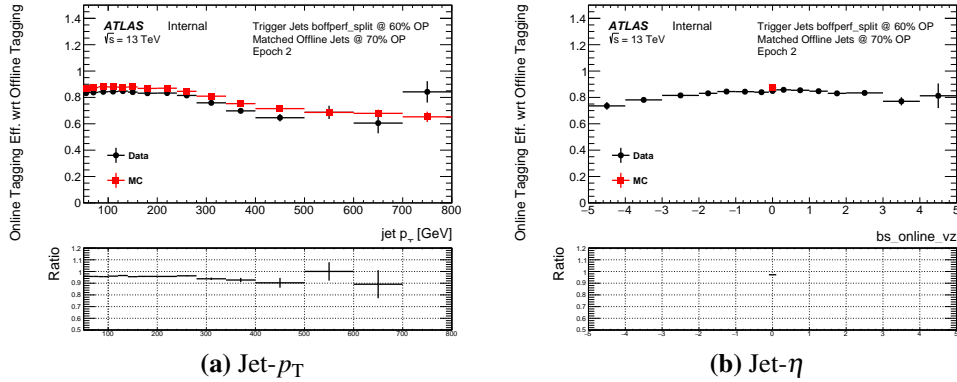


**Figure 5.5:** The 60%  $b$ -jet trigger efficiency with respect to an offline 70% operating point tag for data from epoch 2 (black) and simulation (red) against jet- $p_T$  (a), jet- $\eta$  (b) and online beamspot  $z$ -position (c).

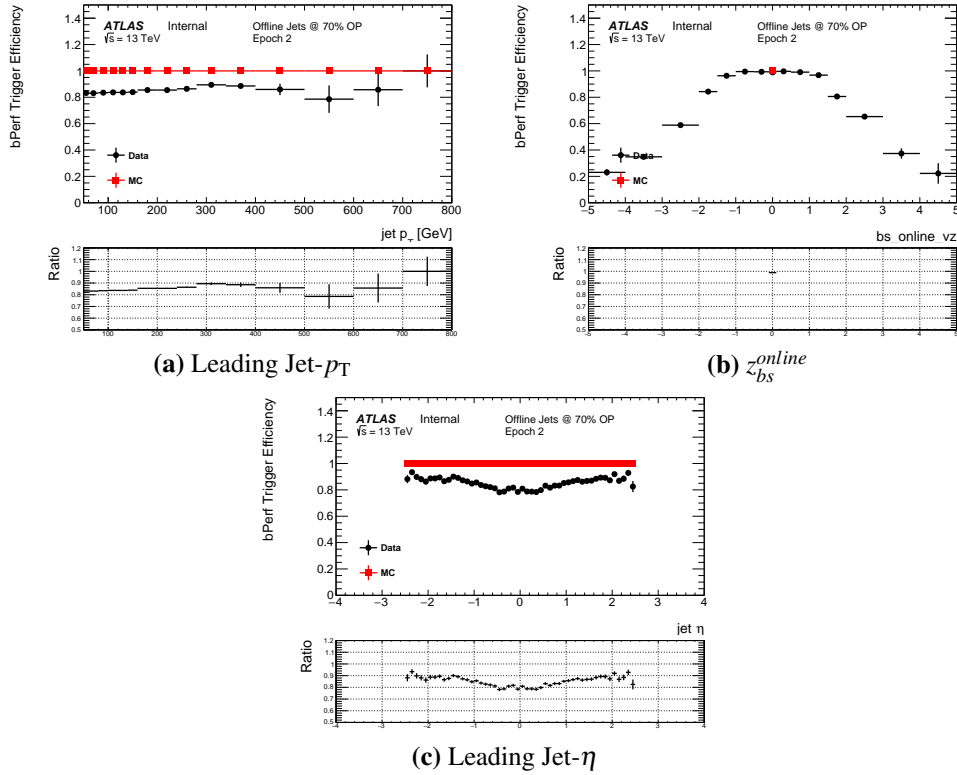


**Figure 5.6:**  $b$ -perf efficiency,  $\varepsilon_{bPerf}$ , for data from Epoch 2 (black) and simulation (red) against leading-jet  $p_T$  (a), online beamspot  $z$ -position (b) and leading jet- $\eta$  (c).

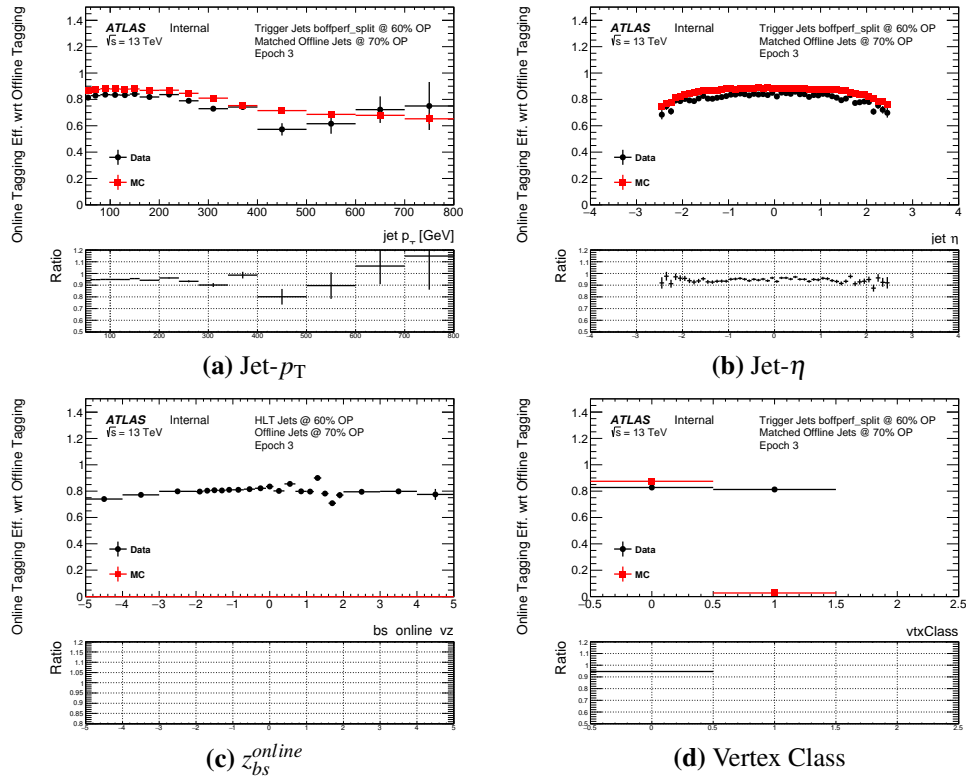


**Figure 5.7:** The 60%  $b$ -jet trigger efficiency with respect to an offline 70% operating point tag for data from Epoch 3 (black) and simulation (red) against (a) jet- $p_T$ , (b) jet- $\eta$ , (c) online beamspot  $z$ -position and (d) vertex class.

### 5.3.6 Solution: $b$ -Jet Trigger GRL

To summarise, in the previous section it is shown that at large values of absolute online beamspot  $z$ -position the measured  $\varepsilon_{b\text{Trig}}$  in Epoch 1 and  $\varepsilon_{b\text{Perf}}$  in Epoch 2 is lower in data than in MC, due to poor  $\text{xPrmVtx}$  PV finding performance. In Epoch 3 there is reasonable data/simulation agreement due to the use of a backup vertex finding algorithm.

The solution employed is to apply a  $b$ -jet trigger aware GRL that removes events with an absolute  $z_{bs}^{\text{online}}$  greater than 2mm in Epoch 1 and 2, such that the events with low efficiency are removed. The cost of this approach is the luminosity of our data-set is reduced, specifically the data-set falls from  $32.9 \text{ fb}^{-1}$  to  $24.3 \text{ fb}^{-1}$ . However there are three key reasons why use of a  $b$ -jet trigger GRL was chosen over simply applying an overall efficiency. Firstly, as there is no beamspot position distribution in simulation it is not clear that kinematics of events at high  $z_{bs}^{\text{online}}$  can be well understood and modelled; the sculpting of the efficiency with respect to jet- $\eta$  is an example of this. Secondly, the efficiencies are quite low at high beamspot  $z$ -position, so the loss in luminosity  $\times$  acceptance is relatively small and finally the use of a GRL means a more realistic estimate of the actual luminosity used in an analysis is used.

For the choice of which value of beamspot  $z$  position to use for in the GRL, it was required to select the widest cut where the efficiency had not significantly declined, such that as much luminosity as possible is retained while removing most of the affected region. This 2 mm cut was chosen from examining Figure 5.3(b) and Figure 5.6(b) and from studying a variety of cuts from 2 mm to 1 mm.

After the GRL is applied,  $\varepsilon_{b\text{Trig}}$  for Region 1 becomes approximately 90-95% of the efficiency measured in simulation, as shown in Figure 5.8, and  $\varepsilon_{b\text{Perf}}$  for Region 2 becomes approximately 95% of the efficiency measured in simulation, as shown in Figure 5.9.

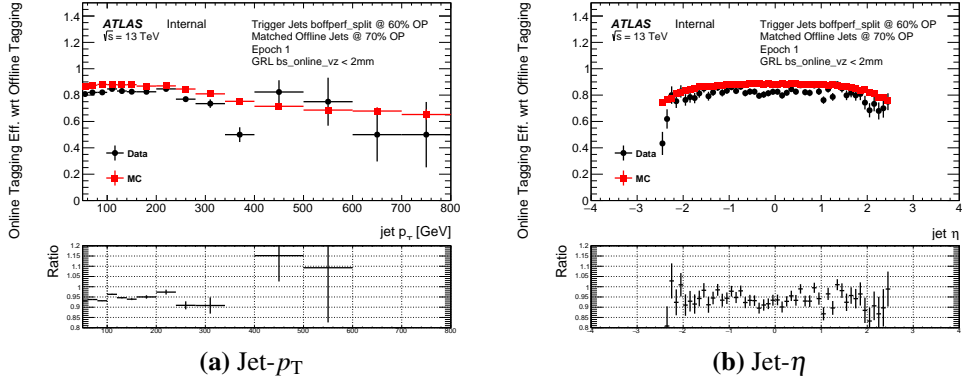


**Figure 5.8:** The 60%  $b$ -jet trigger efficiency with respect to an offline 70% operating point tag for data from Region 1 (black) and simulation (red) against jet- $p_T$  (a) and jet- $\eta$  (b). The  $b$ -jet trigger aware GRL has been applied.

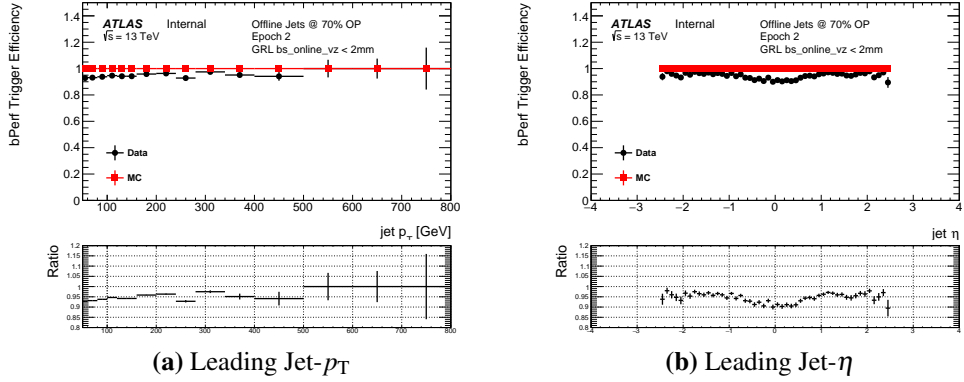


**Figure 5.9:**  $b$ -perf efficiency,  $\varepsilon_{bPerf}$ , for data from Region 2 (black) and simulation (red) against leading (a) jet- $p_T$  and (b) jet- $\eta$ . The  $b$ -jet trigger aware GRL has been applied.

Figures 5.10 and 5.11 shows measured  $\varepsilon_{bPerf}$  and  $\varepsilon_{bTrig}$  for the full 2016 data-set, combining Regions 1, 2 and 3, with the  $b$ -jet trigger aware GRL applied. This represents the raw observed data/simulation efficiencies when the full event selection has been applied.

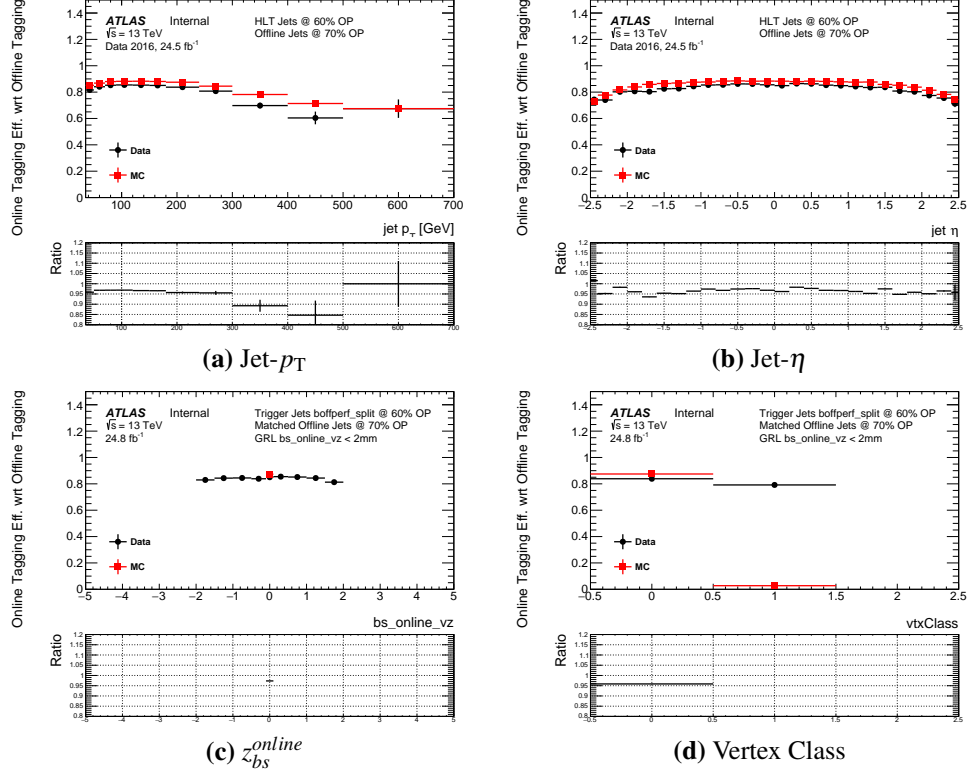


**Figure 5.10:** The 60%  $b$ -jet trigger efficiency with respect to an offline 70% operating point tag for the full 2016 data-set (black) and simulation (red) against jet- $p_T$  (a), jet- $\eta$  (b), online beamspot  $z$ -position (c) and vertex class (d).

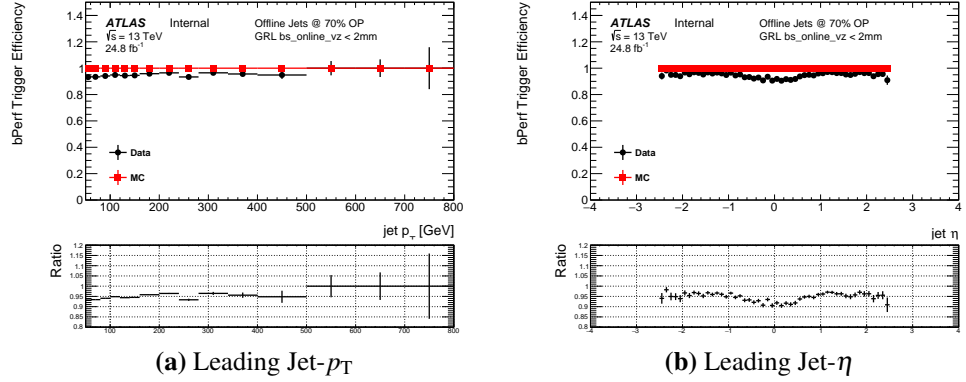


**Figure 5.11:**  $b$ -perf efficiency,  $\epsilon_{bPerf}$ , for the full 2016 data-set (black) and simulation (red) against (a) leading jet- $p_T$  and (b) jet- $\eta$ . The  $b$ -jet trigger aware GRL has been applied.

### 5.3.7 Efficiency Measurement and Systematic Derivation

In the previous two sections it has been shown that when applying a  $b$ -jet aware GRL, the  $b$ -jet trigger performance is understood and the data/simulation agreement is within 5%. In this section the measurement of data efficiency, data/simulation scale factors (SFs) and

associated systematics to account for the 5% are described.

As discussed above, there are two factors considered in this section. Firstly there is the  $\epsilon_{bTrig}$  measurement that accounts for differences in online and offline  $b$ -tagging given that a valid primary vertex has been found. Sections 5.3.7.1 to 5.3.7.3 describes the derivation of a set of systematics and corrections to the raw measurement and Section 5.3.7.4 presents the final measurement, which is applied as a jet-level efficiency in the final analysis. Secondly, in Section 5.3.7.5, is a description the measurement of the  $\epsilon_{bPerf}$  that accounts for the efficiency of finding a valid primary vertex and the relevant systematics, which is applied as an event level efficiency.

In this section describing the final measurement, the full 2016 data set is used, the simulated  $t\bar{t}$  sample includes single-top processes and the full event selection from Section 5.3.3 is applied.

### 5.3.7.1 Purity Error

It is known that despite the strict event selection there will inevitably be non  $b$ -jet contamination in our sample. To estimate the  $b$ -jet purity simulation is used, where the true flavour of the jet is available. Jets are categorised as true  $b$ -jets, meaning that a  $B$ -hadron was found within a cone of  $R = 0.4$ , or true non- $b$ -jets if not. Then distributions for inclusive jets to the truth matched  $b$ -jets in the simulation sample are compared. Figure 5.12 shows the  $b$ -jet purity for jet- $p_T$  and jet- $\eta$ ; showing that the  $b$ -jet purity is  $> 95\%$  up to jet- $p_T \sim 300$  GeV and  $> 90\%$  for higher values of jet- $p_T$ .

To estimate the effect of these impurities on the efficiency measurement simulation is again used. Firstly, the efficiency in our nominal inclusive simulation is compared to the efficiencies if only true- $b$ -jets or true non- $b$ -jets are selected, this is shown in Figure 5.13(a). The ratio is applied as a correction to the final efficiency measurement. Then any mismodelling of the  $b$ -jet fraction in simulation is also considered, to account for this the efficiency for the simulated inclusive sample is compared to the efficiency when the non  $b$ -jet content has been doubled, as shown in Figure 5.13(b). The maximum difference from the efficiency measured in the inclusive simulated sample and the cases where there is only true  $b$ -jets and where the non  $b$ -jet content has been doubled, shown in the two ratio plots in Figure 5.13, is taken as a symmetric systematic.

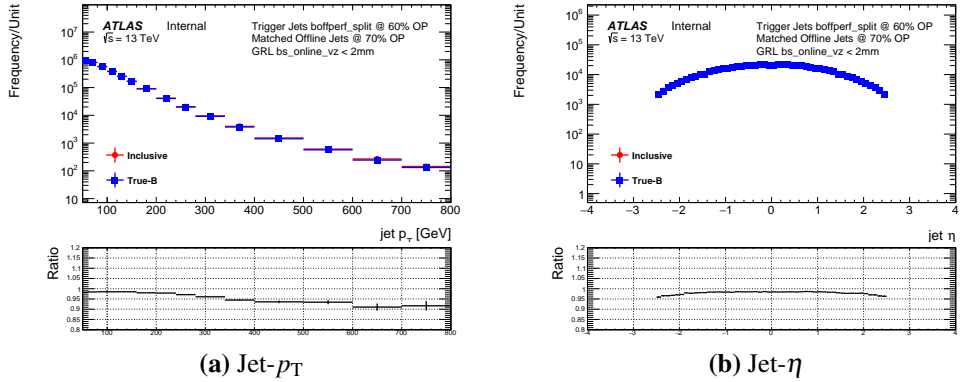


**Figure 5.12:** A comparison of offline jets tagged at the 70% operating point for inclusive jets (red) and truth-matched  $b$ -jets (blue) against jet- $p_T$  (a) and jet- $\eta$  (b) in a simulated  $t\bar{t}$  sample.

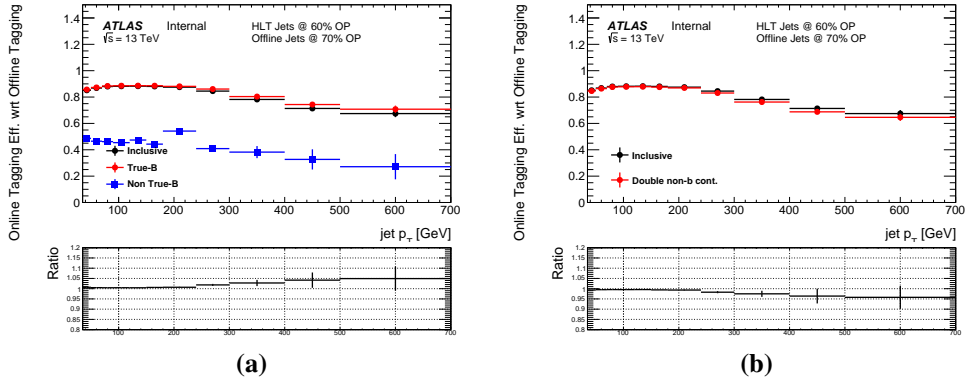


**Figure 5.13:** The 60%  $b$ -jet trigger efficiency with respect to an offline 70% operating point tag for inclusive jets (black) compared to truth matched  $b$ -jets and non  $b$ -jets (a) and the case where non  $b$ -jet content has been doubled (b) for a simulated  $t\bar{t}$  sample. The lower panel in both plots show the ratio to the inclusive efficiency.

### 5.3.7.2 Non- $b$ -jet trigger efficiency error

As one would expect and as shown in left plot of Figure 5.13, non  $b$ -jets (shown in blue) have a different  $b$ -jet trigger efficiency to that of  $b$ -jets. However the exact efficiency is not known well and could be mismodelled in simulation. To account for this uncertainty the nominal efficiency in simulation is compared to the cases where the non- $b$ -jet efficiency has been halved and doubled in simulation, as shown in Figure 5.14. When doubling the non- $b$ -jet trigger efficiency this is limited at the upper end to being no greater than the true  $b$ -jet trigger efficiency. The maximum bin-by-bin difference between the nominal and the two cases, as shown in the two ratio plots, is taken as a systematic.

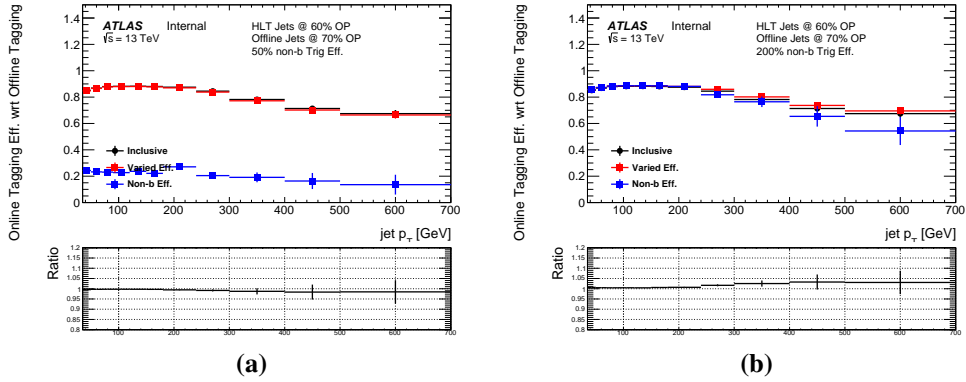


**Figure 5.14:** The 60%  $b$ -jet trigger efficiency with respect to an offline 70% operating point tag for nominal inclusive case (black) compared to varied inclusive case (red) and just non  $b$ -jets (blue) in the case where non  $b$ -jet efficiency has been halved (a) and doubled (b) for a simulated  $t\bar{t}$  sample. The lower panel in both plots show the ratio of the varied inclusive efficiency to the nominal inclusive efficiency.

### 5.3.7.3 High- $p_T$ extrapolation

Measuring  $b$ -jet trigger efficiency for high- $p_T$  jets is limited by the statistics in the simulated  $t\bar{t}$  sample, so the shape from simulation will be used to extrapolate the efficiency for jet- $p_T > 240$  GeV. The point from which to extrapolate from was chosen as this is when data statistic error starts to become large.

The procedure is made of two sequential fits (normalisation and correction) to the data/simulation ratio, which are used to create a “corrected simulation”  $\epsilon_{bTrig}$  distribution. For jet- $pT > 240$  GeV, the corrected  $\epsilon_{bTrig}$  is used in place of data when measuring the data  $\epsilon_{bTrig}$  efficiency and when calculating data/MC scale factors. A final quadratic fit is used to assign a systematic.

In more detail:

- **Flat Normalisation Fit:**

The measured  $\epsilon_{bTrig}$ , in both data and simulation are compared, and a horizontal fit is performed to the ratio of the two. The fit range is set at  $p_T > 50$  GeV to discount the first bin, which has a larger purity uncertainty. This is then used to normalise the simulated efficiency distribution to match data. This fit is shown in the lower plot of panel (a) in Figure 5.15. The error on the one parameter of this fit is taken as a systematic error.

- **Linear Correction Fit:**

The measured  $\epsilon_{bTrig}$ , in both data and the normalised simulation are compared, and

a linear fit is performed to the ratio of the two from jet- $p_T > 240$  GeV. This is then used to correct the simulated efficiency distribution to match data. This fit is shown in the lower plot of panel (b) in Figure 5.15. The simulated  $\epsilon_{bTrig}$ , after both the normalisation and linear correction is referred to as the corrected simulation. To assign a systematic on the fit parameters, the slope of this fit is varied up and down within errors, whilst the point at which the fit crosses 1 is kept constant. The maximum difference between the nominal fit and the varied fits is taken as the error on the linear correction fit. Panel (c) of Figure 5.15 shows the data compared to the corrected simulation. The lower panel shows the ratio of the two, and the blue lines represent the errors on the linear correction fit.

- **Quadratic Systematic Fit:**

Finally to assess an error on the choice of a linear fit as the functional form above, a fit is performed to the data and corrected simulation ratio using a quadratic function. This ratio and the fit is shown in panel (d) of Figure 5.15. The difference of the fit from 1 is considered as the functional form error when assigning as systematic.

The systematic error on the extrapolation is defined as the error from normalisation fit added to the bin-by-bin maximum of the error from the linear correction fit and the error from the quadratic systematic fit. The errors on the high- $p_T$  extrapolation procedure are summarised in Table 5.2

Jet pT [GeV]	MC Extrap. Error (%)	Norm Fit Err. (%)	Lin. Fit (%)	Quad. Fit (%)
240.0-300.0	0.8	0.0	0.8	0.3
300.0-400.0	4.0	0.0	2.9	4.0
400.0-500.0	5.6	0.0	5.6	1.7
500.0-700.0	18.0	0.0	9.6	18.0

**Table 5.2:** A table showing the systematic assigned for the high- $p_T$  extrapolation.

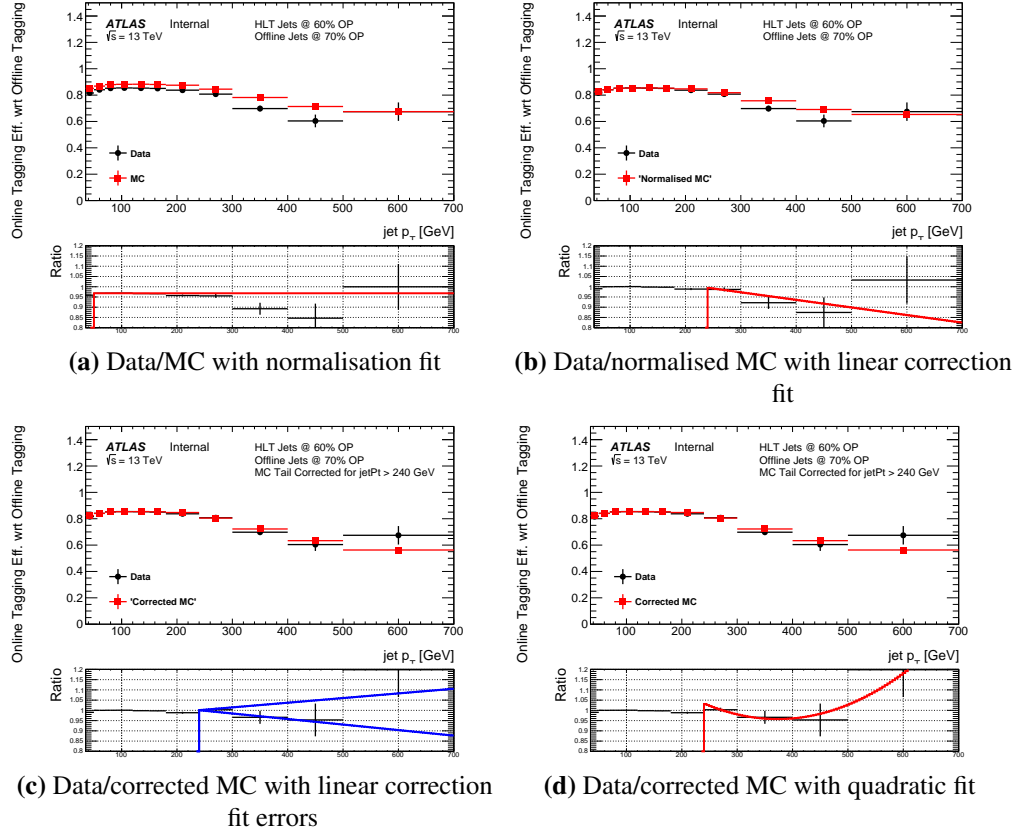


**Figure 5.15:** A figure to demonstrate the high- $p_T$  extrapolation procedure for the 60%  $b$ -jet trigger efficiency with respect to an offline 70% operating point tag. Data (black) is compared against simulation (red) after various corrections have been applied as a function of jet- $p_T$ . Panel (a) shows the flat normalisation fit uncorrected simulation, panel (b) shows the linear correction fit to normalised simulation, panel (c) shows the linear correction fit errors to the corrected simulation and panel (d) shows the quadratic fit to the corrected simulation.

### 5.3.7.4 Jet-Level Efficiency and Scale Factor Measurement

Now the raw measurements of  $\varepsilon_{bTrig}$  from Figure 5.10 and the additional corrections and systematics described above can be brought together. In Figure 5.10 it is shown that, whilst  $\varepsilon_{bTrig}$  does depend on jet- $\eta$ , the data to simulation ratio is flat with respect to jet- $\eta$ . However there is no significant dependence on jet- $p_T$  hence data/simulation scale factors are derived as a function of only jet- $p_T$ .

The full jet-level  $\varepsilon_{bTrig}$  measurement is shown in Figure 5.16. For use in combination with the simulation, a data/simulation scale factor as a function of jet- $p_T$  is also derived and will be applied at the jet-level, which is also shown in Figure 5.17.

The errors considered for the jet-level efficiency account for: mismodelling of the  $b$ -jet

purity in simulation, mismodelling of the  $b$ -jet trigger efficiency for non  $b$ -jets, simulation statistical error, data statistical error ( $\text{jet-}p_T < 240 \text{ GeV}$ ) and simulation based extrapolation ( $\text{jet-}p_T > 240 \text{ GeV}$ ). Table 5.3 summarises the errors on the jet-level scale factor. These errors are taken as a symmetric error in each  $\text{jet-}p_T$  bin and the scale factors are applied to each  $b$ -tagged jet.

As a final sanity check Figure 5.18 shows  $\varepsilon_{b\text{Trig}}$  measured in data to that from the corrected simulation, in the lower panel a ratio of data to corrected simulation is shown and the extrapolation and total errors are overlaid in red and green respectively. The derivation of the corrected simulation and associated extrapolation errors is described in Section 5.3.7.3 This shows that the corrected simulation lies within the total errors for the whole range of  $\text{jet-}p_T$  and at high- $p_T$ , as one might expect, the error is dominated by the extrapolation uncertainties. Note that the corrected simulation is only used to represent data for  $\text{jet-}p_T > 240 \text{ GeV}$ .

Jet $p_T$ [GeV]	SF	Total Err. (%)	Stat. (%)	Extrap. (%)	Pur. (%)	L. Trig. Eff. (%)
35.0-50.0	95.9	1.0	0.1	-	0.7	0.7
50.0-70.0	96.8	0.7	0.1	-	0.5	0.5
70.0-90.0	96.9	0.6	0.1	-	0.5	0.5
90.0-120.0	96.9	0.7	0.1	-	0.5	0.5
120.0-150.0	96.7	0.6	0.2	-	0.4	0.4
150.0-180.0	96.6	0.9	0.2	-	0.6	0.6
180.0-240.0	95.7	1.1	0.5	-	0.7	0.7
240.0-300.0	95.3	2.6	0.4	0.8	1.8	1.7
300.0-400.0	92.4	5.6	1.1	4.0	2.8	2.5
400.0-500.0	88.8	8.1	2.6	5.6	4.2	3.3
500.0-700.0	83.4	19.4	4.0	18.0	4.9	3.1

**Table 5.3:** A table showing the jet-level Data/simulation scale factor (SF) as a function of jet- $p_T$  with total error and the contributions of the different systematics considered; specifically statistical, high- $p_T$  extrapolation, non- $b$ -jet purity and non- $b$ -jet trigger efficiency.

Only the 70% offline working point has been shown as this is offline working points used in the di- $b$ -jet analysis (further details are described in Chapter ??). However, the jet-level efficiencies and uncertainties are also calculated for all other offline working points. Table 5.4 shows a comparison of the jet level uncertainties for the 70%, 77% and 85% operating point. This shows that for looser offline working points the uncertainty becomes larger, due to increased non- $b$ -jet impurities.

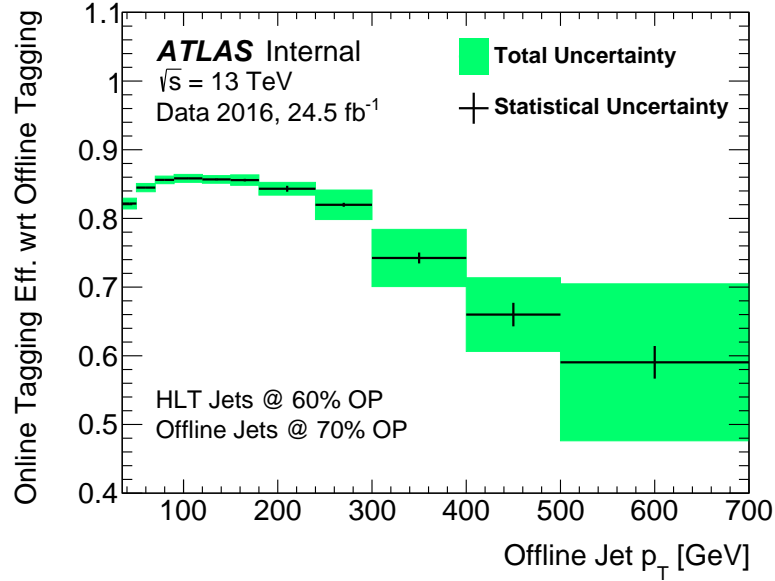


**Figure 5.16:** The measured 60%  $b$ -jet trigger efficiency with respect to an offline 70% operating point tag as measured in data as a function of offline jet- $p_T$ . The central values are shown in black with the statistical error and the green bands represent the total error including systematic errors.

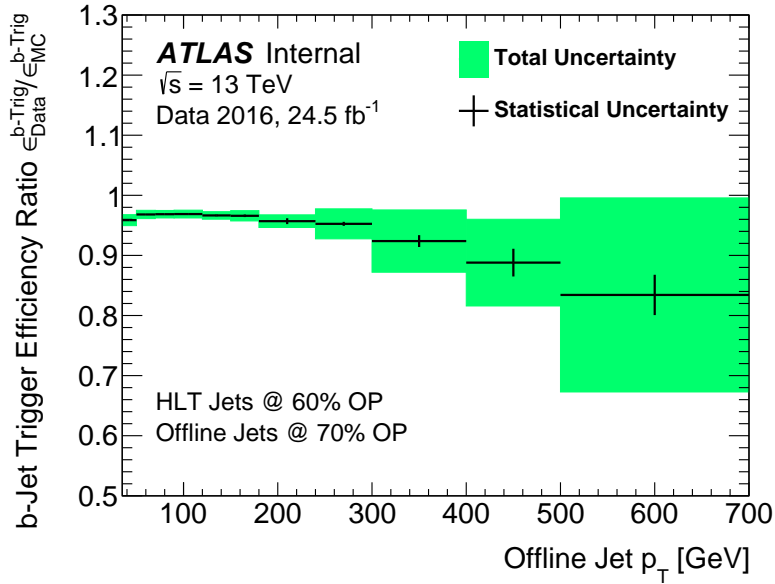


**Figure 5.17:** Data/simulation scale factors for the 60%  $b$ -jet trigger efficiency with respect to an offline 70% operating point tag as a function of offline jet- $p_T$ . The central values are shown in black with the statistical error and the green bands represent the total error including systematic errors.

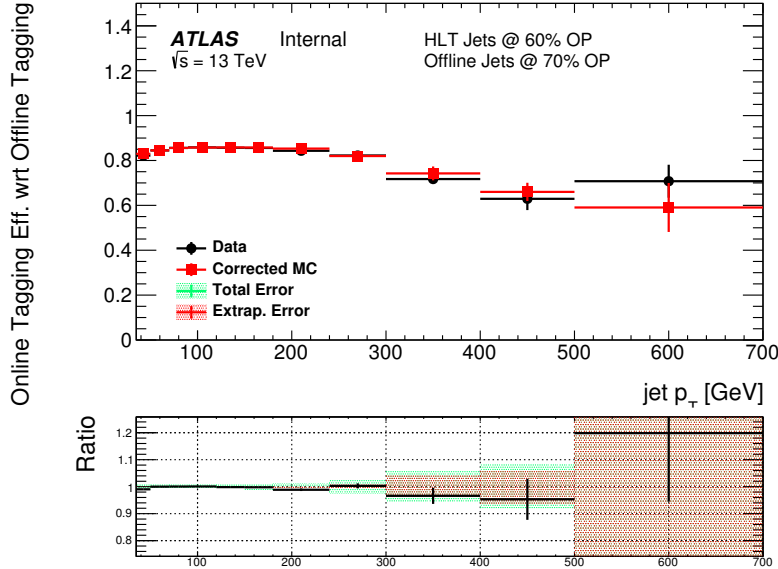


**Figure 5.18:** The measured 60%  $b$ -jet trigger efficiency with respect to an offline 70% operating point tag as measured in data (black) and from the corrected simulation (red) as a function of offline jet- $p_T$ . In the ratio plot on the lower panel the extrapolation errors is represented by the red band, whilst the total error is overlaid in green.

Jet $p_T$ [GeV]	Systematic Uncertainty for Offline OP		
	70% OP	77% OP	85% OP
35.0-50.0	1.0%	2.3%	6.2%
50.0-70.0	0.7%	1.6%	4.6%
70.0-90.0	0.6%	1.3%	3.7%
90.0-120.0	0.7%	1.3%	3.7%
120.0-150.0	0.6%	1.4%	3.7%
150.0-180.0	0.9%	1.8%	4.6%
180.0-240.0	1.1%	2.6%	6.4%
240.0-300.0	2.6%	4.4%	10.2%
300.0-400.0	5.6%	7.5%	17.6%
400.0-500.0	8.1%	10.9%	22.2%
500.0-700.0	19.4%	19.0%	36.6%

**Table 5.4:** A comparison of the systematic uncertainty on the  $b$ -jet trigger jet-level efficiency for various offline operating points (OP) w.r.t. the 60% online operating point. The increase in systematic looser offline operating points is driven by non  $b$ -jet impurities.

### 5.3.7.5 Event-Level Efficiency and Systematic

As already discussed, in some regions of data-taking the performance  $b$ -jet trigger efficiency itself depends on the online beamspot position. Hence, a  $b$ -jet trigger aware GRL is applied to remove a large fraction of events where poor  $b$ -jet trigger performance is observed.

However, even after the application of this GRL, there remains a bias with respect to leading jet- $\eta$  in the probability of finding a valid primary vertex, which is notated as  $\varepsilon_{bPerf}$ . This bias is shown in Figure 5.11. This efficiency is measured differently in each epoch, in Epoch 1 it can be found as the number of events with vertex class = 0 divided by the number of events, in Epoch 2 it is defined as the dividing the number of events that pass the trigger `HLT_mu26_imedium_2j35_bperf` by the number that pass the trigger `HLT_mu26_imedium` and in Epoch 3, due to the back-up vertex. It should be noted that this measurement made in each of the three regions separately and is then combined with each region weighted by its luminosity.

The value of  $\varepsilon_{bPerf}$  is extremely close to 1 in simulation, in this case the efficiency in data and the scale factor are the same. To assign a systematic for this correction the statistical error in data and simulation in addition to a shape systematic are used. The shape systematic, to account for possible variations of the shape with respect to jet- $\eta$ , is defined as half of the difference between the maximum efficiency and the minimum efficiency in any jet- $\eta$  bin, which effectively covers a flat distribution with respect to jet- $\eta$  to one where the shape is twice as extreme as observed.

Table 5.5 and Figure 5.19 summarises the event-level efficiency correction and the associated systematics.

Leading Jet $\eta$	SF	Total Error (%)	Data Stat. (%)	MC Stat. (%)	Shape Syst. (%)
-2.5–1.5	97.3	1.9	0.3	0.1	1.9
-1.5–1.0	97.4	1.9	0.1	0.0	1.9
-1.0–0.5	95.5	1.9	0.1	0.0	1.9
-0.5–0.0	93.8	1.9	0.2	0.0	1.9
0.0–0.5	93.9	1.9	0.2	0.0	1.9
0.5–1.0	95.5	1.9	0.2	0.0	1.9
1.0–1.5	97.3	1.9	0.1	0.0	1.9
1.5–2.5	96.4	1.9	0.3	0.1	1.9

**Table 5.5:** A table showing the event-level Data/MC scale factor (SF) as a function of leading jet- $\eta$  with total error and the contributions of the different systematics considered.

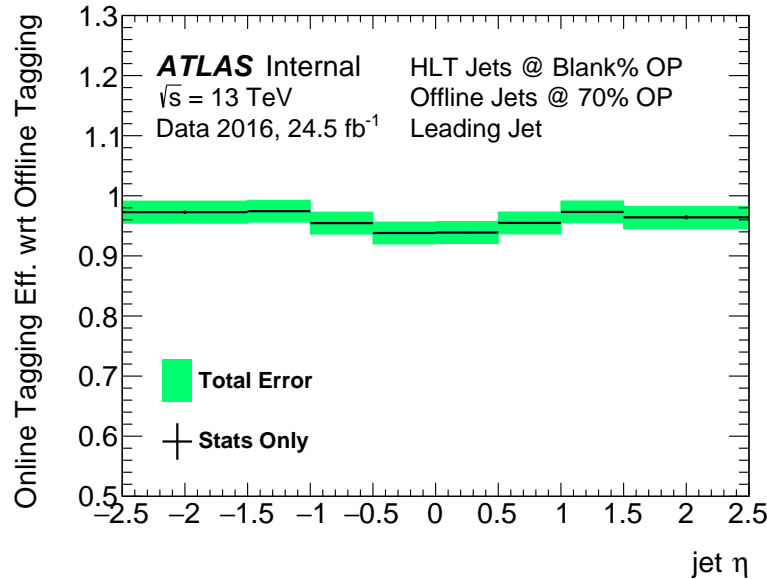


**Figure 5.19:** The measured  $\varepsilon_{bPerf}$  as measured in data as a function of offline leading jet- $\eta$ . The central values are shown in black with the statistical error and the green bands represent the total error including systematic errors.

### 5.3.8 Cross-checks

#### 5.3.8.1 Simulation checks

- Ttbar alone vs ttbar+tW
- Try powheg

#### 5.3.8.2 Electron/Muon overlap checks

#### 5.3.8.3 Event Level Eff: Showing correlation with $z_{bs}^{online}$

- Show that it comes from high beamspot z-position only.
- i.e.  $\varepsilon_{bPerf}$  vs eta for different bs regions.

#### 5.3.8.4 Event Level Eff: Re-weighting of sub-leading jet

- We did a test where we applied correction to leading and showes the subleading was flat within systematics (2%)

Any others that are good?

Cross-checks can be moved to appendix

## 5.4 To Do

These can be considered on my list. - Cite in plot caption

- Uncertainty instead of error
- Update plots to most current version (and label those that are not)
- In caption I want (a) before plot i.e. (a) jet-pT, (b) jet-eta. - Always use data/simulation instead of data/MC
- use Epoch instead of epoch

## Chapter 6

# Di-*b*-jet Search: Outline and Event Selection

In Chapter 2 it was shown that many Beyond Standard Model theories predict new particles decaying to one or two *b*-quarks that could be produced by the LHC. Chapters 3, 4 and 5 described the detectors and reconstruction techniques used to observe such events in the ATLAS detector. Hence, I have now outlined in the motivation and the tools required to perform a search for resonances decaying to one or two *b*-jets, an analysis known as a di-*b*-jet search.

In Chapters 6, 7 and 8 I will describe the di-*b*-jet search analysis using the ATLAS detector. Each chapter will describe a separate part of the analysis: specifically event selection, search phase and limit setting. The different parts are outlined Section 6.1. In this thesis, the di-*b*-jet analysis is performed using three different data-sets which are described in Section 6.2.

### 6.1 Analysis Outline

The strategy used for the di-*b*-jet analysis can be split up into three parts, which form the three di-*b*-jet analysis chapters. A brief outline of the parts is given here, and full detail can be found in the relevant chapter.

- **Di-*b*-jet Event Selection:** (*Chapter 6*)

The first step is to select events that are consistent with a resonance decaying to one or two *b*-quarks in a way such that the number of background events is minimised. Briefly, two high-momentum jets are required and two *b*-tag categories are considered; a category in which both jets have been *b*-tagged (2 *b*-tag) and a category where at least one jet has been *b*-tagged ( $\geq 1$  *b*-tag). This chapter will focus on event selection; Section 6.2 will describe the data-sets used, Section 6.3 will describe the signal and backgrounds considered when defining the selections and Section 6.4 will set out the details of the event selection used

for each of the data-sets.

- **Search Phase:** (*Chapter 7*)

Once events have been selected the next part of the analysis aims to determine if there is evidence of a new particle in the selected events; this step is known as the ‘search phase’. This step uses the dijet mass ( $m_{jj}$ ) spectrum, where dijet mass is the invariant mass of the two highest  $p_T$  jets<sup>1</sup>. A new particle will appear as a resonance (or ‘bump’) on the smoothly falling background dijet mass distribution from QCD dijet production, as illustrated in Figure 6.1. The background is modelled using a smoothly falling function and a model-independent search for resonances is performed using the BUMPHUNTER algorithm [93]. Chapter 7 contains a full description of the search phase strategy.

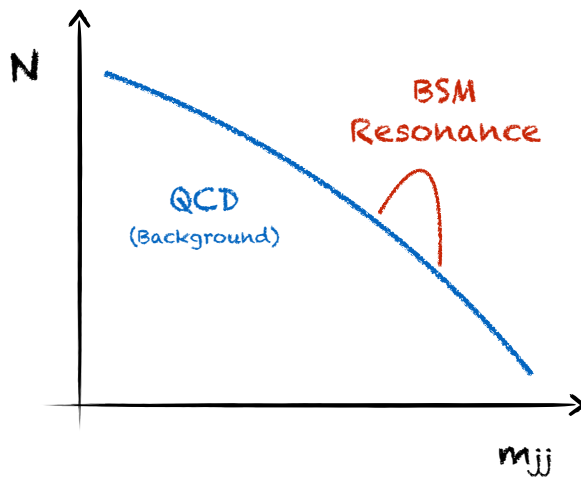


**Figure 6.1:** A cartoon illustrating the use of the dijet mass ( $m_{jj}$ ) distribution in the search phase of the di- $b$ -jet analysis. Shown is the smoothly falling distribution from QCD dijet production (SM) and a resonance shape caused by a Beyond Standard Model particle (BSM)

- **Limit Setting:** (*Chapter 8*)

If, in the search phase stage of the analysis, no significant evidence of a resonance is found then 95% confidence level limits are set on the mass and cross-section of the benchmark signal models. Chapter 8 presents the limit-setting methodology, a description of the systematic uncertainties and the limit setting results for each of the data-sets.

## 6.2 List of Data Sets Used

The di- $b$ -jet analysis is performed in several iterations as data is being collected, where each iteration uses a different data-set. This is done for two reasons; firstly it is important to know as soon as possible if there is evidence of a new resonance as this would affect the strategy

---

<sup>1</sup>The two highest  $p_T$  jets are selected before  $b$ -tagging is applied

of future di- $b$ -jet analyses and that of other analyses at ATLAS. Secondly, this allows us to incrementally expand, adapt and improve the analysis in each iteration.

In this thesis three different data-sets are considered by the di- $b$ -jet analysis. The overall analysis strategy is the same for each data-set, so the iterations are described together. However, there are some significant differences in the details; as such during the analysis description it will be clearly labelled which data-set is being referred to.

For any data-set a Good Run List (GRL) is applied to remove events of low data-quality, which is typically caused by an element of the detector not operating optimally. For example, data-taking periods where the inner-most layer of the inner detector, the IBL, was not operating are removed as this data-taking period has a lower  $b$ -tagging performance. A GRL is applied to all data-sets considered in this analysis.

The data-sets are listed below, the trigger used in each data-set is described. All quoted luminosities are given after the GRL has been applied.

- ***Summer16\_HighMass*:**

The *Summer16\_HighMass* data-set contains 13 TeV  $pp$  collision data collected between January 2015 to July 2016 which has an integrated luminosity  $13.3 \text{ fb}^{-1}$ . The trigger used in this data-set is `HLT_j380`, which requires an online <sup>2</sup> jet with  $p_T > 380 \text{ GeV}$ , and is chosen as it is the lowest unprescaled single jet trigger <sup>3</sup>. Section 5.1 contains a further details on single jet triggers. The analysis on this data-set has been published as a conference note in [10].

- ***Full16\_HighMass*:**

The *Full16\_HighMass* data-set contains 13 TeV  $pp$  collision data collected between January 2015 to December 2016, which has an integrated luminosity of  $36.1 \text{ fb}^{-1}$ . The trigger used in this data-set is `HLT_j380`, as used in the *Summer16\_HighMass* data-set. The analysis on this data-set is to be published soon.

- ***Full16\_LowMass*:**

The *Full16\_LowMass* data-set contains 13 TeV  $pp$  collision data collected between January 2016 to December 2016, which has an integrated luminosity of  $24.3 \text{ fb}^{-1}$ . The trigger used in this data-set is a double  $b$ -jet trigger which requires two online jets with  $p_T > 150 \text{ GeV}$  and  $p_T > 50 \text{ GeV}$  where both online jets have been  $b$ -tagged at the trigger level.

---

<sup>2</sup>Online refers to reconstructed objects used in the trigger decision whilst offline refers to objects reconstructed after events have passed the trigger at the data-processing level, from the definition in Section 5.3.

<sup>3</sup>Unprescaled means that the trigger accepts every event passing the trigger selection criteria

Section 5.2 contains further details of  $b$ -jet triggers and the particular trigger used in this analysis. The *Full16\_LowMass* data-set uses a  $b$ -jet trigger as the lower  $p_{\mathrm{T}}$  thresholds allow the analysis to probe a lower range of dijet mass. This analysis does not include data from 2015 which was collected using a significantly different  $b$ -jet trigger configuration. The *Full16\_LowMass* data-set uses a  $b$ -jet trigger aware GRL which additionally removes periods of data where the  $b$ -jet trigger was performing in a sub-optimal way, the GRL is described in Section 5.3.6. As a double  $b$ -jet trigger is used only the 2  $b$ -tag category is considered. The analysis on this data-set is to be published together with the *Full16\_HighMass* data-set.

## 6.3 Backgrounds and Signal

In the di- $b$ -jet analysis selection two benchmark signal models and one dominant background are considered. The signal models and dominant background are used to optimise event selection.

For both the background and the signal models Monte-Carlo simulations of the processes are produced. Unless specified, all Monte-Carlo simulations are produced using the PYTHIA8 [94] program for event generation, the EVTGEN package [92] to model the decays of the  $B$  and  $C$  hadrons, and the A14 parameter set [95] to model the parton shower, hadronisation and underlying event. The NNPDF23LO PDF set [96] is used to describe the Parton Distribution Function (PDF) and the detector response is modelled using the ATLAS detector simulation package [97].

- **Background: QCD Di-jet:**

Section 2.2 discussed the details of QCD dijet production. In particular in Section 2.2.3.3 it was noted that the relative strength of the strong force compared to other forces of the Standard Model means that QCD dijet production dominates all other backgrounds in a di- $b$ -jet event selection. A description of how the QCD dijet background is modelled in this analysis is described in Chapter 7. A simulated QCD dijet sample is also used in this analysis for background studies and background modelling validation.

Before describing the signal models used it is useful to clearly differentiate between the two definitions of mass used in this analysis. The dijet mass or reconstructed mass is the invariant mass of the two leading jets, and is denoted by  $m_{jj}$ . The simulated mass is defined as the pole mass of the signal model used in the generator. The two differ due to uncertainties in jet energy measurements.

- **Signal:  $Z'$  Boson:**

The  $Z'$  boson is an additional gauge boson that can decay to two  $b$ -quarks. The  $Z'$  boson models considered are described in detail in Section 2.3.2.1. The  $Z'$  boson provides a benchmark model in the 2  $b$ -tag category.

In the *Summer16\_HighMass*, *Full16\_HighMass* and *Full16\_LowMass* data-set analyses the Sequential Standard Model (SSM)  $Z'$  and the leptophobic  $Z'$  models are considered. The intrinsic width of the  $Z'$  boson has been set to 3% of the simulated mass. Monte-Carlo simulation is used to produce dijet mass signal templates at leading order (LO). Only decays to  $b\bar{b}$  are simulated; other decays of the  $Z'$  boson are ignored such that the results are easier to interpret for other signal models decaying to pairs of  $b$ -quarks. It has been shown that for a  $Z'$  boson model the cross-sections can increase by up to 30% from the addition of next-to-leading order (NLO) diagrams [98]. Therefore the signal template normalisation is corrected to account for NLO effects, the correction factors have been derived by comparing the LO and NLO matrix calculations performed using the MADGRAPH generator [99] and are found to be between 1.2 and 1.3 depending on the simulated mass. Simulated SSM and leptophobic  $Z'$  boson templates are produced at simulated mass points of 600, 800, 1000, 1250, 1500, 1750, 2000, 2500, 3000, 4000 and 5000 GeV.

Further to this, for the *Full16\_HighMass* and *Full16\_LowMass* data-sets the Dark Matter mediator (DM)  $Z'$  boson is also considered. For this model the DM  $Z'$  boson signal generation is performed at next-to-leading order using the MADGRAPH5\_AMC@NLO generator [100], whilst all other aspects of event modelling, including parton shower and hadronisation, are performed using the configuration with PYTHIA8 as described above. The coupling of the DM  $Z'$  boson to the Dark Matter fermion ( $g_\chi$ ) is set to 1 and the mass of the Dark Matter fermion ( $m_\chi$ ) is 10 TeV, the large value of  $m_\chi$  means that decays of the  $Z'$  boson to the Dark Matter fermion are suppressed. For the *Full16\_LowMass* data-set the coupling to quarks ( $g_{SM}$ ) is set to 0.1, decays to  $b$ ,  $c$  and light flavour quarks are considered, and the simulated mass points are 600, 800 and 1000 GeV. This configuration is chosen to be consistent with recommendations in [40] and to be consistent with other dijet searches at ATLAS [2]. In the *Full16\_HighMass* data-set the simulated mass points are 1250, 1500, 1750, 2000, 2500, 3000, 4000 and 5000 GeV and the coupling to quarks ( $g_{SM}$ ) is set to 0.25, as at high simulated mass the  $Z'$  boson has a significantly lower cross-section. In addition, for the *Full16\_HighMass* data-set only decays of the DM  $Z'$  boson to  $b$ -quarks is considered, which is required to create dijet mass signal template

with sufficient statistics<sup>4</sup>.

- **Signal:  $b^*$  Quark:**

The  $b^*$  quark is a third generation excited quark which results from quark compositeness models. The dominant decay mode of the  $b^*$  quark is to  $bg$ . The model considered is described in detail in Section 2.3.2.2. The  $b^*$  quark provides a benchmark model in the  $\geq 1$   $b$ -tag category.

For the *Summer16\_HighMass* and *Full16\_HighMass* data-sets the same  $b^*$  quark model is considered. Monte-Carlo simulation is used to produce a  $b^*$  quark dijet mass signal template. Only leading order calculations are considered. Decays to  $bg$ ,  $b\gamma$ ,  $bZ_0$  and  $tW^-$  are considered<sup>5</sup>. Simulated  $b^*$  quark signal templates are produced at simulated mass points of 1250, 1500, 1750, 2000, 2500, 3000, 4000 and 5000 GeV. In the *Full16\_LowMass* data-set the  $b^*$  quark model is not considered as only the 2  $b$ -tag category is used.

## 6.4 Event Selection

The overall aim when designing the di- $b$ -jet analysis event selection is two-fold. Firstly, events are selected to maximise sensitivity to signal; which is approximated in terms of  $S/\sqrt{B}$ , where  $S$  is the number of benchmark signal events and  $B$  is the number of background events. Secondly, the smoothly falling nature of the background needs to be maintained as this is the underlying assumption of the background estimation strategy, which will be described in Chapter 7. Here, smooth means that the spectrum is monotonically decreasing with no discontinuities. In addition, it is desirable that the event selection for the *Full16\_HighMass* and *Full16\_LowMass* data-set are harmonised where possible as the two analyses are to be published together. Any differences in event selection between the two must be well motivated.

The di- $b$ -jet event selection is split up into three sections each described separately. Firstly, a pair of jets are selected (Section 6.4.1), then a set of event-level kinematic cuts are applied using the selected jets (Section 6.4.2) and finally  $b$ -tagging is applied to the jets (Section 6.4.3). In Section 6.4.5 the full event selection is summarised and the signal acceptance is evaluated.

The event selection is slightly different for each of the data-sets considered, these dif-

---

<sup>4</sup>This is required as the signal acceptance of the di- $b$ -jet event selection is reduced at high mass. This will be shown in Section 6.4.5.

<sup>5</sup>Using the branching ratios described in Section 2.3.2.2.

ferences will be noted and discussed in the text.

### 6.4.1 Jet Selection

Jets are reconstructed using the anti- $k_T$  algorithm [67] with  $R = 0.4$  and calibrated using the EM+JES scheme; a full description of jets used in this analysis is in Section 4.2.

At least two jets are required in an event. The two highest  $p_T$  jets, referred to as the leading and subleading jet, are the jets used throughout this analysis. To reduce the number of fake jets from sources such as calorimeter noise both jets are required to pass *loose* jet cleaning cuts based on the properties and distributions of the energy deposits in the calorimeter associated to the jet; details can be found in [101].

Requirements are placed on the leading and subleading jet- $p_T$  such that events are on the trigger plateau; the kinematic region where all events that pass the offline jet- $p_T$  requirements also pass the online jet- $p_T$  requirements of the trigger. To be on the trigger plateau of a single jet trigger the offline jet- $p_T$  must be above some threshold value, which is referred to as the threshold jet- $p_T$ .

For the *Summer16\_HighMass* data-set; it is required that the leading jet has  $p_T > 430$  GeV to be on the trigger plateau of `HLT_j380`. This cut is derived by comparing the leading jet- $p_T$  distributions of jets that pass the trigger, `HLT_j380`, relative to a reference trigger with a lower jet- $p_T$  threshold, `L1_J75`. Figure 6.2(a) shows the leading jet- $p_T$  of events that pass the single jet triggers `HLT_j360` (red), `HLT_j380` (green) and `HLT_j400` and (blue) compared to events that pass the reference trigger `L1_J75` (black), in one run of data where `L1_J75` was unprescaled. In the ratio it is shown that for leading jet- $p_T > 430$  GeV events are on the trigger plateau of `HLT_j380`. The subleading jet is required to have jet- $p_T > 60$  GeV to reduce contamination from pile-up jets<sup>6</sup>. Both jets are required to have  $|\eta| < 2.4$  such that the jets lie within the volume of the ATLAS pixel detector, which is essential for optimal  $b$ -tagging performance.

For the *Full16\_HighMass* data-set the trigger `HLT_j380` is also used, and as such the leading jet is again required to have  $p_T > 430$  GeV. The subleading jet is required to have  $p_T > 80$  GeV to be consistent with the subleading jet- $p_T$  requirement of the *Full16\_LowMass* event selection, which will be described in the following paragraph. Both jets are required to have  $|\eta| < 2.0$ ; the tighter cut on  $|\eta|$  (relative to the *Summer16\_HighMass* data-set) is selected as the  $b$ -jet energy scale uncertainty is significantly

---

<sup>6</sup>Specifically, if jets have  $p_T < 60$  GeV then it is recommended that a pile-up suppression algorithm known as Jet Vertex Tagger (JVT) is used [102]. There is little gain in acceptance from the addition of low  $p_T$  subleading jets and complications from implementing the recommendations so the jets are removed.

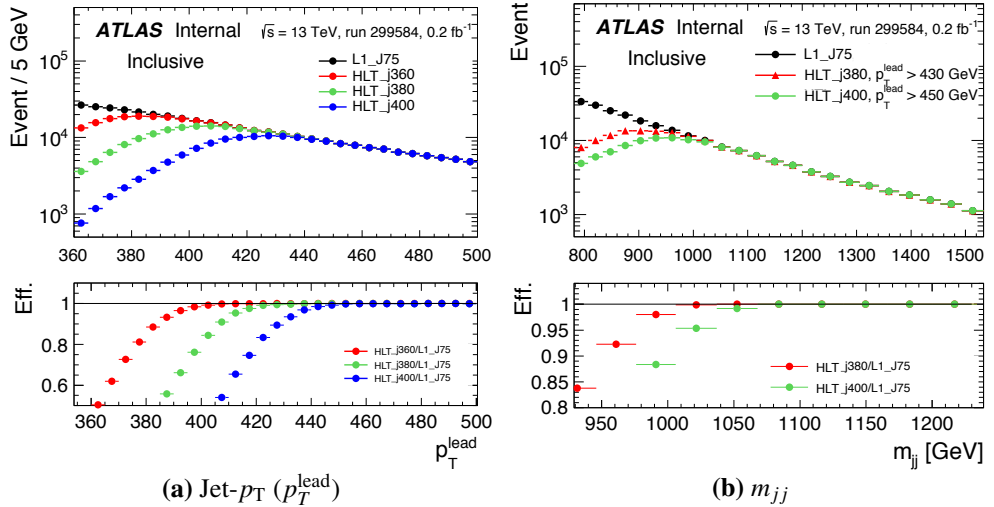


**Figure 6.2:** The comparisons of the (a) leading jet- $p_T$  ( $p_T^{\text{lead}}$ ) and (b) dijet mass ( $m_{jj}$ ) using events that passed an unprescaled L1\_J75 trigger (black) compared to events that pass a range of single-jet triggers (coloured) in one run of 2016 data. As shown in the legend, the single-jet triggers considered are HLT\_j380, HLT\_j400 and, in plot (a), HLT\_j360. In plot (b) the *Summer16+15* event selection (excluding  $b$ -tagging) is applied with a leading jet- $p_T$  cut as described in the legend. The ratio with respect to L1\_J75 is shown in the lower panel [10].

increased at large values of jet- $|\eta|$ .

For the *Full16\_LowMass* data-set a double  $b$ -jet trigger is used; which requires that there is one online jet with  $p_T > 150$  GeV and another online jet with  $p_T > 50$  GeV. As before, to be on the trigger plateau, it is required that the leading and subleading offline jets have a large enough jet- $p_T$  such that the corresponding online jets will pass the trigger-level  $p_T$  requirements. To derive the  $p_T$  requirements one can consider the threshold jet- $p_T$  of the equivalent single jet triggers, one that requires that there is an online jets with  $p_T > 150$  GeV and the other  $p_T > 50$  GeV. To find the threshold jet- $p_T$  of the two single-jet triggers, a linear fit to the threshold jet- $p_T$  of a range of single jet triggers is used, details are in Appendix B. Using the results of the linear fit the leading jet is required to have  $p_T > 200$  GeV and the subleading jet is required to have  $p_T > 80$  GeV. Both jets are required to have  $|\eta| < 2.0$  to be consistent with the *Full16\_HighMass* event selection.

### 6.4.2 Event-Level Cuts

The next part of the event selection is a set of event-level requirements using the two selected jets. Firstly, the primary vertex must have at least two tracks associated with it to ensure good primary vertex reconstruction,

Secondly, there is a cut applied to the variable  $y^*$ , defined as

$$y^* = \frac{(y_1 - y_2)}{2} \quad (6.1)$$

where  $y_1$  and  $y_2$  are the rapidities of the leading and subleading jet respectively. As discussed in Section 2.2.3.3, QCD dijet production can occur through  $t$ -channel processes leading to more background events at large values of  $|y^*|$ , whilst signal production occurs only through  $s$ -channel processes so will have no dependence on  $y^*$ . Therefore, by requiring that  $|y^*|$  is below some threshold value will lead to increased sensitivity.

In the *Summer16\_HighMass* data-set it is required that  $|y^*| < 0.6$ . This value has been shown to maximise  $S/\sqrt{B}$  when no  $b$ -tagging is applied at previous inclusive dijet searches at ATLAS [2]<sup>7</sup>. The effect of  $b$ -tagging on the optimal value of this cut is assumed to be small, as  $t$ -channel processes still dominate the background.

In the *Full16\_HighMass* data-set it is required that  $|y^*| < 0.8$ . This value is found by maximising  $S/\sqrt{B}$  in the 2  $b$ -tag category for a range of simulated mass points using the SSM  $Z'$  boson model as signal and the QCD background from simulation as background.

In the *Full16\_LowMass* data-set it is required that  $|y^*| < 0.6$ . The  $|y^*|$  cut was not harmonised with the *Full16\_HighMass* data-set as it was shown that the looser cut introduced a kinematic bias at low values of dijet mass. This will be demonstrated below.

Finally, the dijet mass,  $m_{jj}$ , is required to be above a threshold value to ensure that two conditions are met. Firstly it is required that there is no kinematic bias on the dijet mass distribution caused by the trigger or jet- $p_T$  requirements described in Section 6.4.1. Secondly, it is also required that the background is smooth in the dijet mass region chosen such that it can be described using our background modelling strategy.

In the *Summer16\_HighMass* data-set it is required that  $m_{jj} > 1378$  GeV; which ensures the two conditions listed above are met. Firstly, Figure 6.2(b) shows the dijet mass spectra for events that pass the trigger `HLT_j380` and the *Summer16\_HighMass* jet- $p_T$  requirements compared to events that pass a reference trigger, `L1_J75`, in one run of data where `L1_J75` was unprescaled. For both spectra events are required to pass the  $\eta$  and  $y^*$  requirements of the *Summer16\_HighMass* event selection. The ratio plot demonstrates that for  $m_{jj} > 1100$  GeV there is no kinematic bias from the trigger or event selection. Secondly, it has been shown using simulated events that  $m_{jj} > 1378$  GeV is required such that the dijet mass distribution from QCD dijet production can be described by our background model-

---

<sup>7</sup>Inclusive dijet analysis means a dijet analysis where no  $b$ -tagging is applied

ling strategy; this study is presented in Section 7.4.3. Hence,  $m_{jj} > 1378$  GeV is the loosest cut that meets both of the conditions.

In the *Full16\_HighMass* data-set it is required that  $m_{jj} > 1200$  GeV in the 2  $b$ -tag category and  $m_{jj} > 1341$  GeV in the  $\geq 1$   $b$ -tag category; which again ensures the two conditions discussed above are met. Firstly, Figure 6.3 compares the dijet mass spectrum for events that pass the trigger `HLT_j380` and the *Full16\_HighMass* jet- $p_T$  requirements to events that pass a reference trigger, `L1_J75`. The comparison is done in one run of data where `L1_J75` was unprescaled. For both spectra it is required that events pass the  $y^*$  and jet- $\eta$  requirements of the *Full16\_HighMass* event selection. The ratio plot demonstrates that for  $m_{jj} > 1200$  GeV there is no kinematic bias from the trigger or event selection. Secondly, it will be shown in Section ??LM Fix: Not written yet... that in the  $\geq 1$   $b$ -tag category a cut of  $m_{jj} > 1341$  GeV is required such that the dijet mass distribution from the background can be described by our background modelling strategy. No such effect was observed in the 2  $b$ -tag category. Hence,  $m_{jj} > 1200$  GeV is required in the 2  $b$ -tag category and  $m_{jj} > 1341$  GeV is required in the 1  $b$ -tag category.

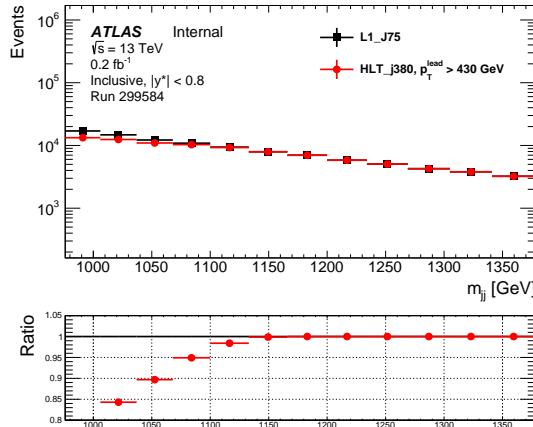


**Figure 6.3:** The comparisons of the dijet mass ( $m_{jj}$ ) spectrum of events that pass an unprescaled `L1_J75` trigger (black squares) and events that pass the `HLT_j380` trigger and the *Full16\_HighMass* event selection jet- $p_T$  requirements (red dots) in one run of 2016 data where `L1_J75` is unprescaled. The *Full16\_HighMass* event selection requires that leading jet  $p_T$  ( $p_T^{\text{lead}}$ )  $> 430$  GeV and subleading jet- $p_T > 80$  GeV. The jet- $|\eta|$  and  $|y^*|$  of the *Full16\_HighMass* event selection have been applied. The ratio with respect to `L1_J75` is shown in the lower panel.

For the *Full16\_LowMass* data-set it is found that for  $m_{jj} > 500$  GeV there is no kinematic bias from the jet- $p_T$  cuts used in the *Full16\_LowMass* data-set event selection. Figure 6.4(a) compares the dijet mass distribution of events that pass the event selection requirements that the leading (subleading) jet- $p_T > 200$  (80) GeV, labelled as ‘ana-

lysis cuts’, compared to events that pass lower requirements that the leading (subleading) jet- $p_T > 150$  (50) GeV, labelled as ‘low cuts’. Events are required to pass the L1\_J75 trigger and are taken from a run of 2016 data where L1\_J75 was unprescaled. The events are additionally required to pass the jet- $\eta$  and  $|y^*|$  requirements of the *Full16\_LowMass* data-set event selection. For  $m_{jj} > 500$  GeV there is no kinematic bias from the *Full16\_LowMass* event selection, this includes a one  $m_{jj}$  bin buffer that is used as a safety measure. Figure 6.4(b) shows an identical comparison of dijet mass distribution when it is required that  $|y^*| < 0.8$ . For  $|y^*| < 0.8$  there is a kinematic bias in the dijet mass range 500–544 GeV, and as such the  $|y^*| < 0.8$  is not used in the event selection.

For the *Full16\_LowMass* data-set the upper bound of the dijet mass range considered by the search phase is 1533 GeV. This value is chosen such that there is no gap in the mass range searched by the three data-sets. There is no need for the *Full16\_LowMass* analysis to consider higher masses as in this mass range the *Summer16\_HighMass* and *Full16\_HighMass* analyses are more sensitive to signal due to the looser  $b$ -tagging requirements.

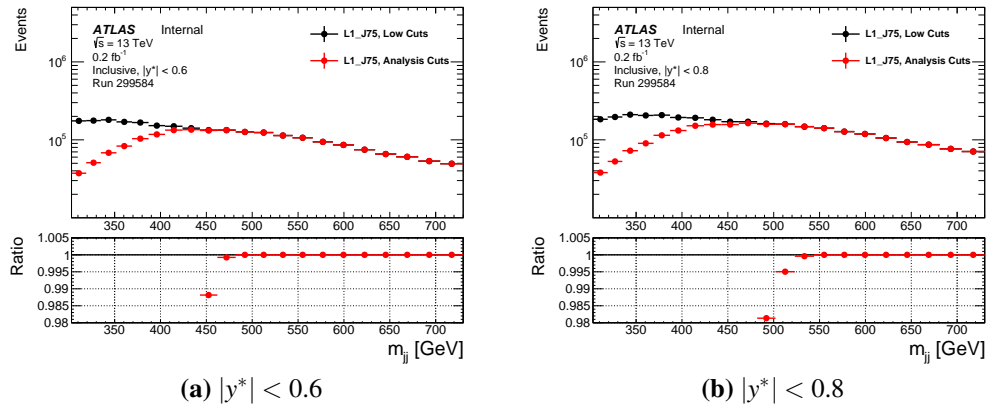


**Figure 6.4:** Comparisons of the dijet mass ( $m_{jj}$ ) of events that pass the analysis jet- $p_T$  cuts of leading (subleading) jet- $p_T > 200$  (80) GeV (black) compared to events that pass a set of low jet- $p_T$  cuts of leading (subleading) jet- $p_T > 200$  (80) GeV (red). The events are required to pass the L1\_J75 trigger and are taken from one run of 2016 data where the trigger L1\_J75 is unprescaled. In addition the events are required to have (a)  $|y^*| < 0.6$  and (b)  $|y^*| < 0.8$ . No  $b$ -tagging cuts have been applied.

However, for the *Full16\_LowMass* data-set there is an additional kinematic bias on dijet mass due to the effect of jets other than the leading or subleading jet that was discovered as the analysis progressed. To account for this effect it is required that  $m_{jj} > 566$  GeV. To the studies showing this effect are described below in Section 6.4.4 as the  $b$ -tagging selections used in the *Full16\_LowMass* event selection must be introduced first

### 6.4.3 *b*-Tagging

The selection of *b*-jets, known as *b*-tagging, forms an essential technique in the di-*b*-jet event selection. A detailed description of *b*-tagging is found in Section 4.3. *b*-Tagging is performed using a multi-variate algorithm known as MV2c10 which has been described in 4.3.3.

Two *b*-tagging categories are used for the two different types of signal model considered. The 2 *b*-tag category requires that both jets are *b*-tagged, and is used to search for resonances decaying to 2 *b*-quarks such as the  $Z'$  boson. The  $\geq 1$  *b*-tag category requires that at least one jet is tagged, and is used to search for resonances decaying to 1 *b*-quark and a quark/gluon such as the  $b^*$  quark. The exclusive 1 *b*-tag category was also considered but was found to be less sensitive to the  $b^*$  quark model.

In the *Summer16\_HighMass* and *Full16\_HighMass* data-sets *b*-tagging is performed using the 85% operating point of the MV2c10 algorithm, details on the operating points of MV2c10 are found in Section 4.3.3. This operating point was chosen to maximise  $S/\sqrt{B}$  for a range of simulated mass points in the 2 *b*-tag category.

In the *Full16\_LowMass* data-set *b*-tagging is performed using the 70% operating point of the MV2c10 algorithm. This operating point was chosen to maximise  $S/\sqrt{B}$  for a range of simulated mass points. A tighter operating point than the high-mass analyses is optimal as *b*-tagging has already been applied at the online level. As the double *b*-jet trigger used applies *b*-tagging to the leading and subleading jet at the online level only the 2 *b*-tag category is considered.

To select the *b*-tagging operating point for the *Full16\_HighMass* data-set the number of background events,  $B$ , is estimated in a narrow dijet mass window around each simulated mass point considered using a  $18.9 \text{ fb}^{-1}$  subset of data for the 2 *b*-tag category. The number of signal events,  $S$ , is estimated in the same narrow dijet mass windows using the simulated SSM  $Z'$  boson signal template described in Section 6.3 scaled to  $18.9 \text{ fb}^{-1}$ <sup>8</sup>. The full *Full16\_HighMass* event selection has been applied. Table 6.1 summarises  $S/\sqrt{B}$  for each operating point; the 85% operating point is selected as it performs well across the full range of mass points considered. The conclusions of this study are luminosity independent as  $S/\sqrt{B} \propto \sqrt{L}$  such that the relative sensitivity between operating points will be the same for all luminosities. Therefore the results also validate the choice of *b*-tagging operating point in the *Summer16\_HighMass* data-set.

Similarly, the *b*-tagging operating point is chosen for the *Full16\_LowMass* data-set by

---

<sup>8</sup>This is the amount of data collected when the studies were performed

Simulated Mass [GeV]	1500	2000	2500
Mass window [GeV]	1378-1573	1785-2114	2267-2659
$S/\sqrt{B}$ for 85% OP	2.02	0.72	0.21
$S/\sqrt{B}$ for 77% OP	2.12	0.64	0.17
$S/\sqrt{B}$ for 70% OP	1.73	0.47	0.12
$S/\sqrt{B}$ for 60% OP	0.96	0.21	0.07

**Table 6.1:** The estimated  $S/\sqrt{B}$  at  $18.9 \text{ fb}^{-1}$  for 4 different MV2c10 operating points (OP).  $S$  is estimated using a simulated SSM  $Z'$  boson sample and  $B$  is estimated using a  $18.9 \text{ fb}^{-1}$  subset of 2  $b$ -tag category data. The *Full16\_HighMass* data-set event selection has been applied. Three different simulated mass points are considered and the mass windows used to estimate  $S$  and  $B$  for each mass point are shown in the table [13].

estimating  $B$  and  $S$  in narrow dijet mass windows around a range of simulated mass points. The number of background events,  $B$ , is estimated using a  $3 \text{ fb}^{-1}$  subset of *Full16\_LowMass* data and the number of signal events,  $S$ , is estimated using the simulated SSM  $Z'$  boson signal template described in Section 6.3 scaled to  $3 \text{ fb}^{-1}$ <sup>9</sup>. The full *Full16\_LowMass* event selection has been applied. The 85% operating point is not considered, because the associated  $b$ -jet trigger systematic uncertainties are significantly larger as shown in Table 5.4<sup>10</sup>. Table 6.2 summarises  $S/\sqrt{B}$  for each operating point; the 70% operating point is selected as it performs well across the full range of mass points considered and, as shown in Table 5.4, has a smaller  $b$ -jet trigger uncertainty associated than the 77% operating point. Again the conclusions of this study are luminosity independent.

Simulated Mass [GeV]	800	1000	1250
Mass window [GeV]	657-861	861-1068	1068-1269
$S/\sqrt{B}$ for 77% OP	4.30	2.09	0.86
$S/\sqrt{B}$ for 70% OP	4.57	1.97	0.77
$S/\sqrt{B}$ for 60% OP	4.50	1.57	0.52

**Table 6.2:** The estimated  $S/\sqrt{B}$  at  $3 \text{ fb}^{-1}$  for 3 different MV2c10 operating points (OP).  $S$  is estimated using a simulated SSM  $Z'$  boson sample and  $B$  is estimated using a  $3 \text{ fb}^{-1}$  subset of data. The *Full16\_LowMass* data-set event selection has been applied. Three different simulated mass points are considered and the mass windows used to estimate  $S$  and  $B$  for each mass point are shown in the table [13].

To further understand the effect of  $b$ -tagging in this analysis the flavour composition of the background is studied. The dijet flavour composition is defined as the truth flavour of the jets used in the di- $b$ -jet analysis, using the definition of truth flavour from Section 4.3.1, and is estimated using the Monte Carlo simulated QCD dijet sample described in Section 6.3. Figure 6.5 shows the dijet flavour composition of the QCD background in the case where no  $b$ -tagging has been applied (inclusive) and in the  $\geq 1$  and 2  $b$ -tag categories. For this figure the *Summer16\_HighMass* data-set event selection has been applied, although the distribu-

<sup>9</sup>A subset of data was used such that the studies were not biased if signal is present in the final data-set.

<sup>10</sup>Section 5.3 contains a full description of the  $b$ -jet trigger systematic uncertainties.

tions are very similar for the *Full16\_HighMass* data-set as the same *b*-tagging operating point has been chosen.

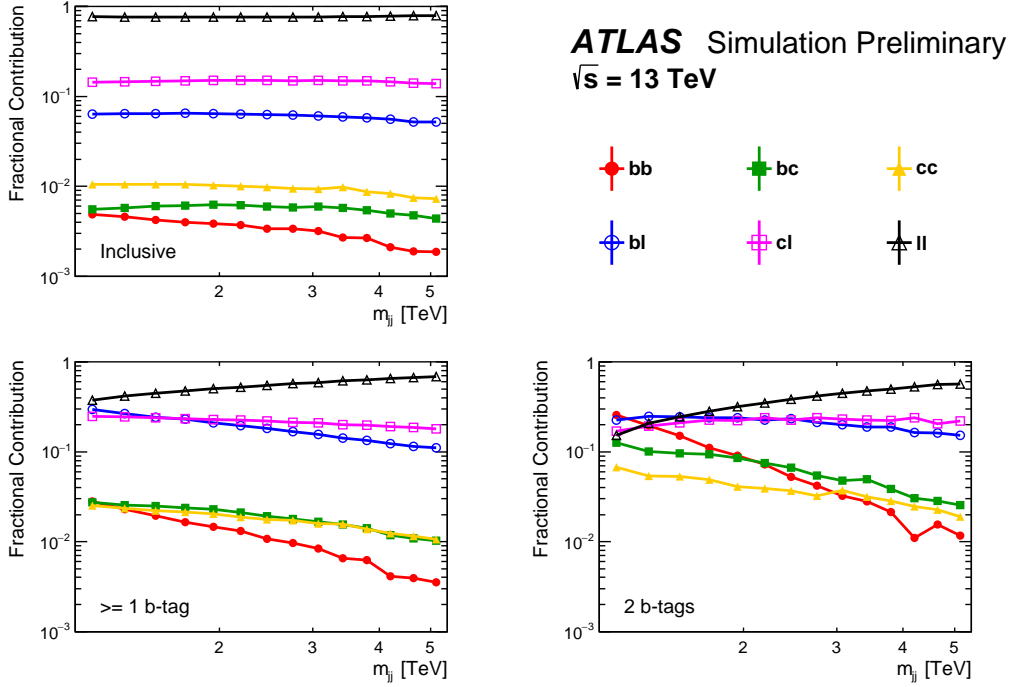


**Figure 6.5:** The dijet flavour composition of the simulated dijet background as a function of dijet mass ( $m_{jj}$ ) for the *Summer16+15* data-set shown without applying *b*-tagging (inclusive) and for  $\geq 1$  *b*-tag and 2 *b*-tag categories. In the legend *b*, *c* and *l* refer to a truth matched *b*-jet, *c*-jet and light jet respectively. The *Summer16+15* data-set event selection has been applied.

There are a few features that should be noted in this figure. Firstly, the background before *b*-tagging is dominated by light-jets for the reasons outlined in Section 2.2.3.3. As the background is dominated by light-jets the application of *b*-tagging can increase background rejection and thus increase sensitivity to signal models that decay to *b*-quarks. This motivates the use of *b*-tagging in the analysis.

Secondly, even after the application of *b*-tagging the largest contribution to the background is from light jets, except for a small region at low mass in the 2 *b*-tag category. This shows that the sensitivity of the analysis is limited by the light-jet rejection of *b*-tagging at high jet- $p_T$ .

Finally, in all three cases the dijet flavour fractions are smoothly changing, where smooth means monotonically changing with no discontinuities. This is evidence that the effect of *b*-tagging on the background does not produce a non-smooth feature in the background

dijet mass spectra.

Figure 6.6 shows the dijet flavour composition of the QCD dijet background when the *Full16\_LowMass* data-set event selection has been applied. In the *Full16\_LowMass* data-set the background is dominated by  $b$ -jets due to the tighter  $b$ -tagging operating point used and improved  $b$ -tagging performance at low jet- $p_T$ .

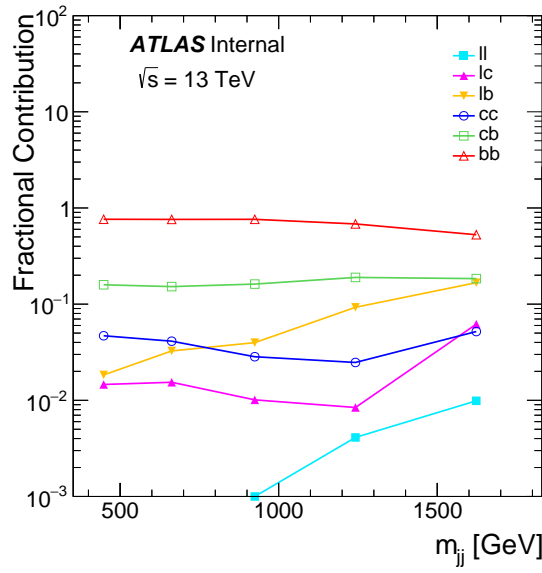


**Figure 6.6:** The dijet flavour composition of the simulated dijet background as a function of dijet mass for the *Full16\_LowMass* data-set shown after the application of online and off-line  $b$ -tagging requirements. In the legend b, c and l refer to a truth matched  $b$ -jet,  $c$ -jet and light jet respectively. The *Full16\_LowMass* data-set event selection has been applied [13].

#### 6.4.4 Effect of $b$ -Jet Trigger Matching in the *Full16\_LowMass* Data-set

As discussed in Section 5.2, the double  $b$ -jet trigger used in the *Full16\_LowMass* data-set requires that there is one online jet with  $p_T > 150 \text{ GeV}$ , another online jet with  $p_T > 50 \text{ GeV}$  and that both jets are  $b$ -tagged at the 60% online operating point.

As described in Section 6.4.1, it is required that the leading and subleading offline jet have a jet  $p_T$  above the threshold jet- $p_T$  of the two trigger level jet requirements <sup>11</sup>. Then, in Section 6.4.2 it was shown that in the *Full16\_LowMass* data-set there is no kinematic bias in the dijet mass distribution due to the leading and subleading offline jet  $p_T$  cuts for  $m_{jj} > 500 \text{ GeV}$ .

However, it has been discovered that one must also consider the effect of offline jets other than the leading and subleading jet, these jets I will refer to as ‘non-leading jets’. It is possible that, due to the application of online  $b$ -tagging, in an event that has passed the double  $b$ -jet trigger the leading and subleading offline jet do not correspond to the online jets that have been used by the double  $b$ -jet trigger. Instead a non-leading offline jet can be used by the double  $b$ -jet trigger. Therefore, it must be additionally shown that in the dijet mass range considered there is not a kinematic bias due to events where a non-leading jet is used by the trigger.

A study is performed to determine the effect of the  $b$ -jet trigger using non-leading jets on the dijet mass spectrum. For this study offline jets are matched to online jets in a process known as trigger matching. An offline jet is matched to an online jet if  $\Delta R$ <sup>12</sup> between the jets  $< 0.4$ . The matching is exclusive, which means that no online or offline jet can be involved in two matchings. In the case that an offline jet can be matched to two online jets, then the pair of jets with the smallest  $\Delta R$  is chosen. In the case where two offline jets can be matched to an online jet, the offline jet with the highest- $p_T$  is chosen; this is done as there is a prior reason to believe that the leading and subleading offline jets are responsible for passing the  $b$ -jet trigger requirements as they are known to pass offline  $b$ -tagging.

Then one can define ‘ $b$ -jet trigger matched events’ as events where the leading and subleading offline jets have successfully been matched to online jets and that these online jets pass the double  $b$ -jet trigger requirements described above. In  $b$ -jet trigger matched events it is known that there is no effect from the non-leading jets.

To study  $b$ -jet trigger matched events an additional complication has to be overcome.

<sup>11</sup>The offline jet- $p_T$  above which a single jet-trigger is on the trigger plateau is referred to as the threshold jet- $p_T$ .

<sup>12</sup>Defined as  $\Delta R = \sqrt{\Delta\eta^2 + \Delta\phi^2}$ . See Equation 3.3 for more details.

To perform trigger matching the  $p_T$ ,  $\eta$ ,  $\phi$  and MV2c20 output of the online jets is required. Data from the ATLAS collaboration is processed and stored in containers known as ‘derivation containers’<sup>13</sup>. To reduce the computer resources required to analyse a derivation container there are many types of derivation containers, where each contains only the events and the reconstructed object information required to perform an analysis. For the di- $b$ -jet analysis a derivation called *EXOT2* is used, however the online jet information required for trigger matching is not present in the *EXOT2* derivation containers. Instead, a derivation container called *FTAG1* is used, in which the online jet information is present. However, in the *FTAG1* derivation not all events that pass the double  $b$ -jet trigger are included. Therefore, neither derivation container contains the full information required to do  $b$ -jet trigger matching on the full *Full16\_LowMass* data-set.

To overcome this problem the effect of  $b$ -jet trigger matching can be studied using the *FTAG1* derivation to test if there is a kinematic bias. Firstly, one can consider the dijet mass spectrum of all events in the *FTAG1* derivation that pass the *Full16\_LowMass* data-set event selection before  $b$ -jet trigger matching is applied. I will refer to this as the dijet mass spectrum from *FTAG1*. Figure 6.7(a) shows the dijet mass spectrum from *FTAG1* compared to the full dijet mass spectrum from the *EXOT2* derivation, where all events are present. The full *Full16\_LowMass* data-set event selection has been applied to both. The ratio shows that there is a deficit of events in the dijet mass spectrum from *FTAG1* at low mass.

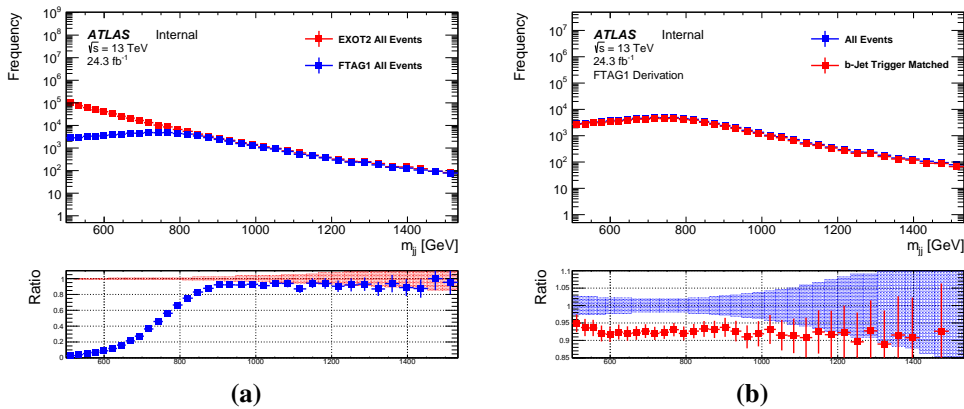


**Figure 6.7:** (a) A comparison of the dijet mass ( $m_{jj}$ ) spectra created using the *EXOT2* derivation and the *FTAG1* derivation. (b) A comparison of the dijet mass spectra of all events and  $b$ -jet trigger matched events using the *FTAG1* derivation. For both plots the full *Full16\_LowMass* event selection is applied. Details of the derivation containers is given in the text.

Figure 6.7(b) shows the comparison of the dijet mass spectrum from *FTAG1* before

<sup>13</sup>Formally the ‘derivation containers’ are known as Derived Analysis Object Data (DAODs)

and after the application of  $b$ -jet trigger matching. The full *Full16\_LowMass* data-set event selection has been applied in both cases. A ratio of the two spectra is in the lower panel. The ratio shows that  $\sim 8\%$  of events that pass the *Full16\_LowMass* event selection do not pass  $b$ -jet trigger matching requirement. In these events it can be concluded that a non-leading jet is used by the double  $b$ -jet trigger. For  $m_{jj} > 566$  GeV the ratio is smooth with respect to dijet mass. However in the region  $500 < m_{jj} < 566$  GeV, which is shown by the first three  $m_{jj}$  bins, there is a clear discontinuity in the ratio plot which indicates that a kinematic bias could be present in the final data-set.

The background estimation strategy (described in Section 7) requires that the dijet mass spectrum must be smooth, therefore it is required that there is no effect that can cause a non-smooth feature in the dijet mass spectrum. It has been shown that for  $m_{jj} > 566$  GeV there is no effect of non-leading jets in the double  $b$ -jet trigger that can cause an un-smooth feature in the final data-set. Therefore, for the *Full16\_LowMass* data-set it is required that  $m_{jj} > 566$  GeV.

Finally it should be noted that for future iterations of the di- $b$ -jet analysis the full information required for  $b$ -jet trigger matching will be included in the *EXOT2* derivation, and as such trigger matching can be applied such that analyses can search a dijet mass range beginning at 500 GeV.

### 6.4.5 Event Selection Summary

A summary of the key components of the di- $b$ -jet event selection for each of the data-sets considered is listed in Table 6.3.

Detail	<b>Summer16+15</b>	<b>Full16+15_HighMass</b>	<b>Full16+15_LowMass</b>
Luminosity	$13.3 \text{ fb}^{-1}$	$36.1 \text{ fb}^{-1}$	$24.3 \text{ fb}^{-1}$
Trigger	Single-jet	Single-jet	Double $b$ -jet (60% OP)
Online LJ $p_T$	$> 380 \text{ GeV}$	$> 380 \text{ GeV}$	$> 150 \text{ GeV}$
Online SLJ $p_T$	-	-	$> 50 \text{ GeV}$
Leading Jet- $p_T$	$> 430 \text{ GeV}$	$> 430 \text{ GeV}$	$> 200 \text{ GeV}$
Subleading Jet- $p_T$	$> 60 \text{ GeV}$	$> 80 \text{ GeV}$	$> 80 \text{ GeV}$
Jet- $ \eta $	$< 2.4$	$< 2.0$	$< 2.0$
$m_{jj}$	$> 1378 \text{ GeV}$	$> 1200 \text{ GeV} (2 \text{ } b\text{-tag})$ $> 1341 \text{ GeV} (\geq 1 \text{ } b\text{-tag})$	566 - 1533 GeV
$ y^* $	$< 0.6$	$< 0.8$	$< 0.6$
$b$ -Tagging OP	85%	85%	70%
$b$ -Tag Categories	2 and $\geq 1$	2 and $\geq 1$	2

**Table 6.3:** A summary of the key details of the di- $b$ -jet event selections applied for each of the data-sets considered. For full details refer to the text.

To visualise events that pass the event selection, Figure 6.8 show events displays for high dijet mass events that pass the  $\geq 1$  and 2  $b$ -tag event selection respectively. The figure was made using the VP1 event display package [103]. These events pass both the *Summer16\_HighMass* and *Full16\_HighMass* data-set event selection.

With the event selection now defined, the signal acceptance of the di- $b$ -jet analysis is studied to understand the performance of the analysis selection and as an input to the limit-setting phase of the analysis. The signal acceptance multiplied by trigger efficiency is defined as the fraction of signal events that pass the analysis' trigger and event selection. In addition, as  $b$ -tagging is a unique selection in our analysis relative to other dijet searches, the event-tagging efficiency is also considered, which is defined as the fraction of signal events that pass the  $b$ -tagging requirements given that the event has passed all other aspects of the event selection. Signal acceptance and event tagging efficiency are estimated using the Monte-Carlo signal templates discussed in Section 6.3.

For the *Summer16\_HighMass* data-set event selection; Figure 6.9(a) shows the signal acceptance multiplied by trigger efficiency for the  $b^*$  quark and SSM  $Z'$  boson signal models

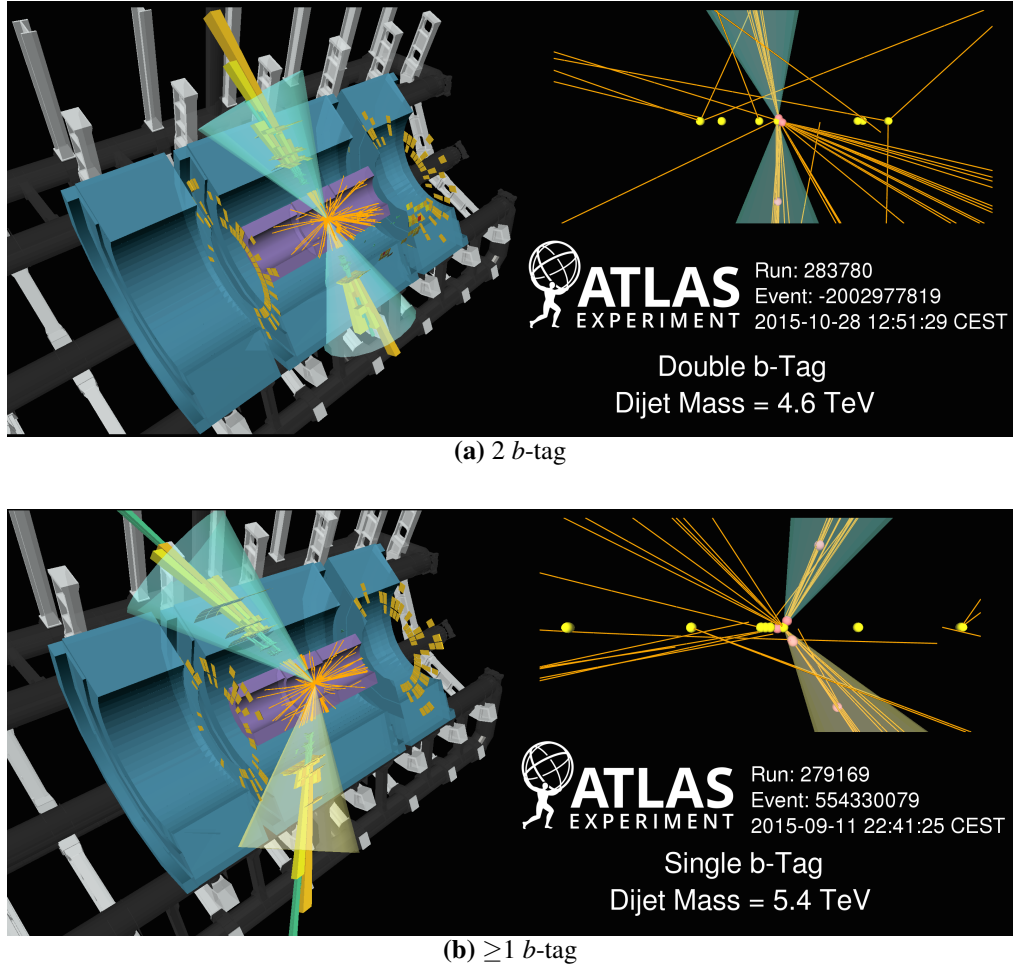


**Figure 6.8:** Event displays showing high dijet mass ( $m_{jj}$ ) events that pass the (a) 2 and (b)  $\geq 1$   $b$ -tag di- $b$ -jet event selection. The left section of the figures show a cut-away of the ATLAS detector; the inner detector is shown in purple, the hadronic calorimeter is shown in blue and the toroid magnet and supporting structure is shown in black and grey. The upper right section of the figures show a close-up view of the inner tracker in the  $r - z$  plane. In both sections tracks inside the inner detector are shown in orange and energy deposits in the EM and hadronic calorimeter are shown in green and yellow respectively. The two leading jets formed are indicated by the cones, a blue cone indicates that the jet has been  $b$ -tagged and a yellow cone indicates that it has not. In the upper right panel the yellow spheres show the primary vertex candidates and the red spheres show the secondary vertex candidates.

as a function of the simulated mass in the case that  $b$ -tagging is applied and when it is not applied. Figure 6.9(b) shows the event tagging efficiency for the  $b^*$  quark and SSM  $Z'$  boson for a range of simulated mass points as a function of the dijet mass. For the SSM  $Z'$  boson only decays to  $b$ -quarks are considered. In both plots the  $b$ -tagging category used is labelled in the legend.

For the *Full16\_HighMass* data-set event selection; Figure 6.10(a) shows the signal

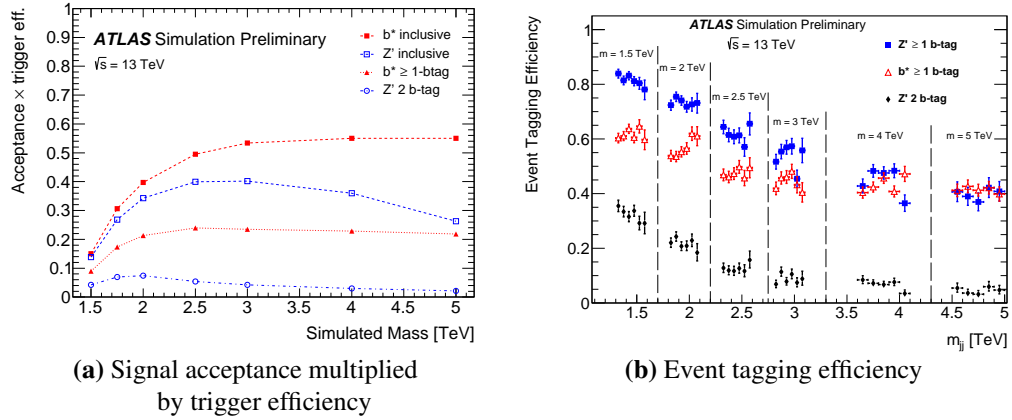


**Figure 6.9:** Plots to show the acceptance of the *Summer16+15* data-set event selection for the  $b^*$  quark and SSM  $Z'$  boson signal models. Panel (a) shows the signal acceptance multiplied by trigger efficiency as a function of the simulated mass of the signal model, in the case where  $b$ -tagging has been applied and not. Panel (b) shows the event tagging efficiency as a function of the dijet mass ( $m_{jj}$ ) for a range of simulated masses,  $m$ , as indicated on the plot. In both figures the  $b$ -tagging categories used are indicated in the legend. Details of the *Summer16+15* data-set event selection are described in the text. Figures taken from [10].

acceptance multiplied by trigger efficiency for the  $b^*$  quark, SSM  $Z'$  boson and Dark Matter mediator (DM)  $Z'$  boson signal models as a function of the simulated mass. For both models the signal acceptance is shown before and after the dijet mass and  $b$ -tagging requirements are applied. Figure 6.10(b) shows the event tagging efficiency for the  $b^*$  quark and SSM  $Z'$  boson for a range of simulated mass points as a function of the dijet mass ( $m_{jj}$ ). The SSM  $Z'$  boson is used to show the event tagging efficiency such that the comparisons can be made between the different data-sets. In both plots the  $b$ -tagging category used is labelled in the legend.

For the *Full16\_LowMass* data-set event selection; Figure 6.11(a) shows the signal acceptance multiplied by trigger efficiency for the SSM  $Z'$  boson and Dark Matter mediator (DM)  $Z'$  boson signal models as a function of the simulated mass. For both models the signal acceptance is shown before and after the dijet mass and offline  $b$ -tagging requirements are applied. The signal acceptance is considerably lower for the DM  $Z'$  boson model in the *Full16\_LowMass* data-set as decays to light,  $c$  and  $b$  quarks are considered whilst for the SSM model only decays to  $b$ -quarks are considered. Figure 6.11(b) shows the event tagging efficiency of just online  $b$ -tagging and the combination of online and offline  $b$ -tagging for the SSM  $Z'$  boson for a range of simulated mass points as a function of the dijet mass,  $m_{jj}$ .

There are a few features of the signal acceptance and tagging efficiency that should be commented on. There is a reduced signal acceptance at lower values of simulated mass

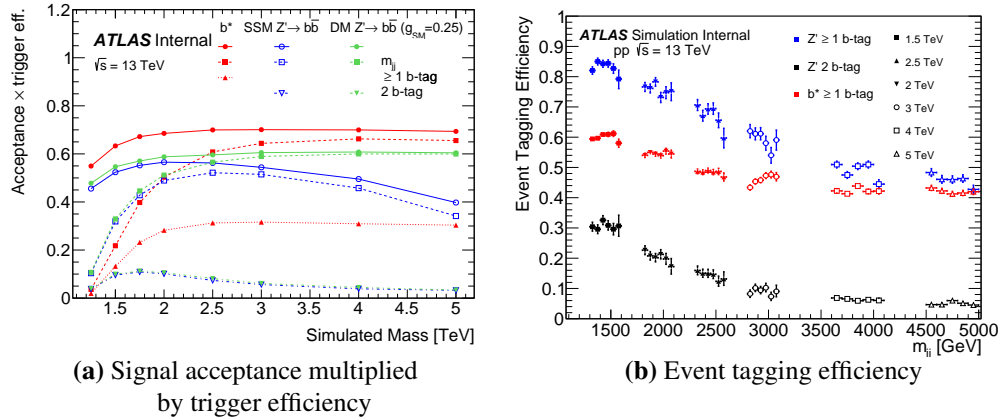


**Figure 6.10:** Plots to show the acceptance of the *Full16\_HighMass* data-set event selection for the  $b^*$  quark, Sequential Standard Model (SSM)  $Z'$  boson and Dark Matter mediator (DM)  $Z'$  boson signal models. Panel (a) shows the signal acceptance multiplied by trigger efficiency as a function of the simulated mass of the signal model, before and after the dijet mass and  $b$ -tagging requirements are applied. Panel (b) shows the event tagging efficiency as a function of the dijet mass ( $m_{jj}$ ), for the  $b^*$  quark and SSM  $Z'$  boson models for a range of simulated masses,  $m$ , as indicated in the legend. In both figures the  $b$ -tagging categories used are indicated in the legend. Details of the *Full16\_HighMass* data-set event selection are described in the text. Figures taken from [13].

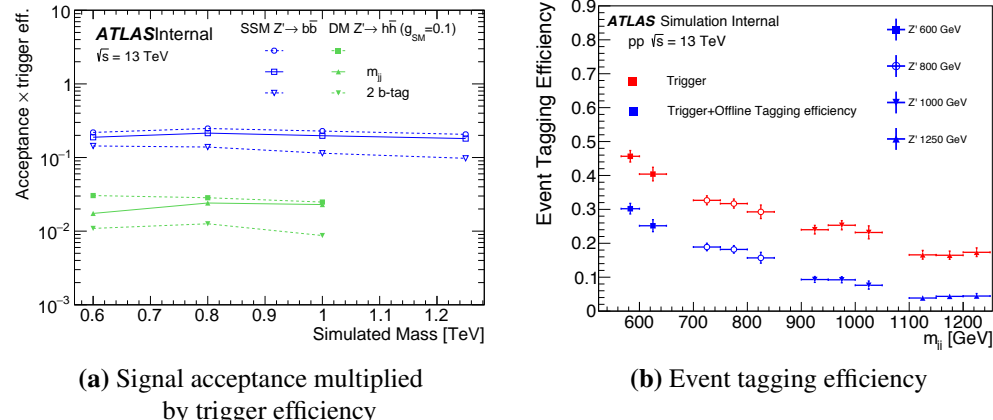


**Figure 6.11:** Plots to show the acceptance of the *Full16\_LowMass* data-set event selection for the Sequential Standard Model (SSM)  $Z'$  boson and Dark Matter mediator (DM)  $Z'$  boson signal models. Panel (a) shows the signal acceptance multiplied by trigger efficiency as a function of the simulated mass of the signal model, before and after the dijet mass and offline  $b$ -tagging requirements are applied. Panel (b) shows the event tagging efficiency of just online  $b$ -tagging and the combination of online and offline  $b$ -tagging as a function of the dijet mass,  $m_{jj}$ , for the SSM  $Z'$  boson at a range of simulated masses,  $m$ , as indicated in the legend. Details of the *Full16\_LowMass* data-set event selection are described in the text. Figures taken from [13].

because the dijet mass template has a bias towards low mass events which can be rejected by the dijet mass requirements of the event selection. The low mass bias is caused by a

preference for low values of dijet mass by the PDFs. In addition, the event tagging efficiency decreases at high values of dijet mass due to a lower performance of  $b$ -tagging at high jet- $p_T$ , which has been discussed in Section ?? **LM Fix: add high-pT  $b$ -tagging is b-tag chapter.** Finally, the  $b^*$  quark has a similar tagging efficiency as the  $Z'$  boson in the  $\geq 1$   $b$ -tag category when  $m_{jj} > 3$  TeV; whilst naively one would expect that the SSM  $Z'$  boson should have a higher event tagging efficiency as it decays to two  $b$ -quarks, the gluon from the  $b^*$  quark decay can split into a pair of lower  $p_T$   $b$ -quarks which can often be tagged leading to a similar tagging efficiency.

## Chapter 7

# Di-*b*-jet Search: Search Phase

The role of the search phase is to determine if there is any evidence of Beyond Standard Model (BSM) physics in the form of a resonance (or a bump) in the dijet mass spectra of the di-*b*-jet events selected. This is performed in two parts; firstly a background fit is used to estimate the dijet mass spectrum of the QCD dijet background. Then, the difference between the data and the background estimation is used to search for a significant excess that would be evidence of BSM physics.

This chapter presents the details of the dijet mass spectra used in the analysis (Section 7.1), the background estimation strategy (Section 7.2) and the technique used to search for excesses (Section 7.3). Then the specific details, validation and results of the search phase for each of the data-sets are then shown in Section 7.4 and 7.5.

## 7.1 Dijet Mass Spectrum

The dijet mass ( $m_{jj}$ ) spectrum is the distribution of the invariant mass of the leading and subleading jet of events that have passed the di-*b*-jet event selection. The dijet mass spectrum is analysed in a binned histogram, the bin width is chosen to be approximately the same size as the dijet mass resolution whilst still giving a smooth dijet mass spectrum [2]. The exact bins chosen are shown in Appendix A.

Searching for resonances using the dijet mass spectrum is effective for narrow resonances where the majority of signal events are localised in dijet mass, such that a significant excess will be created. The benchmark models considered for this analysis are examples of narrow resonances. For signals that are much wider than the dijet mass resolution, signal is hard to distinguish from the background using a dijet mass spectrum. Inclusive dijet

searches for wide signals have been performed using angular distributions [2]<sup>1</sup>.

## 7.2 Background Estimation

Many analyses at ATLAS use Monte-Carlo simulation to model backgrounds [63]. However, simulation is not used to model the background in the di-*b*-jet search due to three problems [1]. Firstly, due to the large cross-section of QCD dijet production it is difficult to produce Monte-Carlo simulation with the required statistical precision. Secondly, there are large theoretical uncertainties associated with simulations of QCD dijet production, such as hadronisation modelling and PDF uncertainties. Finally, there are experimental uncertainties affecting data-simulation comparisons, such as jet energy scale and *b*-tagging uncertainties.

Instead, the background is described using a smooth fit function. This approach utilises the fact that the dijet mass spectrum from QCD dijet production is smoothly falling, as discussed in Section 2.2.3.3. Smoothly falling functions have been widely used to model smoothly falling backgrounds in a wide range of searches for resonances including inclusive dijet, di-*b*-jet and di-photon searches [2, 11, 104].

This approach sets two requirements on a fit function; firstly the fit function must be able to describe the dijet mass spectrum from QCD dijet production including the impact of any detector or reconstruction effects that could change the dijet mass spectrum, such as *b*-tagging. Secondly, the fit function used must be constrained enough such that there is not a significant change in the background estimate if a resonance is present in the dijet mass spectrum, such a change is referred to as a signal induced fit bias. As evidence of such a resonance is found when the data diverges from the background estimate, a signal induced fit bias would reduce the sensitivity to signal. The fit functions considered in this analysis will be described in the following section.

For any given fit function, the parameters of the function are chosen to maximise the likelihood, which is defined as

$$\mathcal{L} = \prod_i \left( \frac{b_i^{n_i} e^{-b_i}}{n_i!} \right) \quad (7.1)$$

where  $n_i$  is the number of data events observed in bin  $i$ ,  $b_i$  is the number events predicted by the background estimation in bin  $i$  and the product is over all bins in the dijet mass spectrum.

---

<sup>1</sup>Inclusive dijet analysis means a dijet analysis where no *b*-tagging is applied

### 7.2.1 Functional Form

The dijet mass spectrum of the di-*b*-jet events will be described by dijet fit functions, a family of functions with a varying number of parameters. The dijet fit functions used in this analysis are listed in Table 7.1.

Function Name	Equation	$x$
3 parameter	$f(x) = p_1(1-x)^{p_2}x^{p_3}$	$m_{jj}/\sqrt{s}$
4 parameter	$f(x) = p_1(1-x)^{p_2}x^{p_3+p_4 \ln x}$	$m_{jj}/\sqrt{s}$
5 parameter	$f(x) = p_1(1-x)^{p_2}x^{p_3+p_4 \ln x+p_5 (\ln x)^2}$	$m_{jj}/\sqrt{s}$
6 parameter	$f(x) = p_1(1-x)^{p_2}x^{p_3+p_4 \ln x+p_5 (\ln x)^2}$	$m_{jj}/p_6$

**Table 7.1:** The functional form of the dijet fit functions. The fit functions are named by the number of free parameters used.  $p_i$  are the free parameters of the fit function.  $\sqrt{s}$  is the centre-of-mass energy of the collisions.

The dijet fit functions are motivated using a theoretical understanding of the QCD dijet production and experience from previous dijet searches [1]. The 3 parameter dijet fit function has been used in dijet searches beginning with CDF [105] and the three components are motivated as follows: the  $p_1$  term gives the normalisation, the  $(1-x)^{p_2}$  term is a common parameterisation for the behaviour of the PDFs with the property of vanishing as  $x$  approaches unity, and the  $x^{p_3}$  term is motivated by the  $1/m_{kl}^2$  term in the matrix element (shown in Equation 2.6). The  $\sqrt{s}$  term is the centre-of-mass energy of the  $pp$  collisions, which is 13 TeV for analyses in this thesis. Additional parameters of  $x^{p_4 \ln x}$  and  $x^{p_5 \ln x^2}$  have been considered in dijet searches to give an adequate description of high dijet mass region when large mass ranges are considered [2, 106]. Finally, the  $x = m_{jj}/p_6$  term is added as an additional degree of freedom [22].

The dijet fit functions are ‘nested functions’, which are defined as a sequence of functions where each function can be formed from the next function in the sequence by fixing the value of one parameter. For example the 3 parameter dijet fit function can be formed from the 4 parameter dijet fit function by setting  $p_4 = 0$  and so on.

The dijet fit functions have been developed for and used in inclusive dijet analyses [1], using the dijet mass spectrum of events with no requirements on *b*-tagging. The effect of *b*-tagging on the dijet mass spectrum has been found to be smooth such that the dijet mass spectrum of di-*b*-jet events can still be described by the dijet fit functions [11]. Validation studies are performed to show that dijet fit functions are able to adequately describe the dijet mass spectrum of the data-sets considered in this thesis; the search phase validation studies are presented in Sections 7.4 and 7.5.

Functions with higher number of parameters may be required to describe the dijet mass spectrum from QCD dijet production; especially in large data-sets where small statistical uncertainties reveal finer details of the dijet mass shape and large mass ranges where stronger constraints are applied to the fit in each mass range. However, additional parameters also allow for more flexibility in the background shape which may allow a signal induced fit bias to occur. Hence, the dijet fit function with fewest number of parameters that can adequately describe the background is used, such that sensitivity to signal is maximised.

## 7.2.2 Wilks' Test Statistic

To determine if a dijet fit function has sufficient number of parameters to adequately describe the dijet mass spectrum an approach using the Wilks' test statistic is used, as employed in previous iterations of both inclusive and di-*b*-jet searches at ATLAS [2, 11]. For this test one considers the null hypothesis that a nominal dijet fit function is the true parameterisation of the dijet mass spectrum and the alternative hypothesis that a dijet fit function with an additional parameter is required.

The Wilks' test statistic,  $t_W$ , is defined as

$$t_W = -\log \left( \frac{\mathcal{L}_{\text{Nom}}}{\mathcal{L}_{\text{Alt}}} \right) \quad (7.2)$$

where  $\mathcal{L}_{\text{Nom}}$  and  $\mathcal{L}_{\text{Alt}}$  are the maximised likelihoods of the nominal and alternative function respectively, using the definition of likelihood given in Equation 7.1. A Wilks' test statistic close to zero indicates that the observed data is compatible with the null hypothesis.

Wilks' theorem states that for nested functions, such as the dijet fit functions, in the null hypothesis the Wilks' test statistic will follow a  $\chi^2$  distribution with 1 degree of freedom [107]. As a result the Wilks' *p*-value can be calculated, which is defined as the probability of obtaining a Wilks' test statistic of the same value or larger than the one observed in data under the assumption of the null hypothesis. If the *p*-value  $< 0.05$  it is concluded that the nominal dijet fit function does not have sufficient parameters to provide an adequate description of the data.

The Wilks' *p*-value is employed to determine the background estimation strategy in both the *Summer16\_HighMass* and *Full16\_LowMass* data-set analyses in different ways, which will be described below in Sections 7.4.1 and 7.5.4 respectively.

### 7.3 Resonance Search Strategy

After a background estimation is created, the next step is to determine if there is evidence of a resonance in the dijet mass spectra of the selected di-*b*-jet events. A resonance can be observed if there is a discrepant excess in the dijet mass spectrum, as illustrated in Figure 6.1; an excess is defined as any set of consecutive bins that contains more events in data than the background estimation, and discrepant describes how inconsistent an excess is with the background estimation. In terms of hypothesis testing, the null hypothesis states that the dijet mass spectrum contains only events created by QCD dijet production which are modelled by the background estimation, this is referred to as the background-only hypothesis. The alternate hypothesis states that there is also a resonance at some unknown mass point causing an excess in the dijet mass spectrum.

Due to statistical fluctuations in the number of background events, excesses in the dijet mass spectrum are expected in the background-only hypothesis. Therefore, to discover a new resonance a significant excess is required, which is an excess that is highly unlikely to have occurred from such a fluctuation. A *p*-value is used to quantify the significance of an excess, where a *p*-value is defined as the probability of an excess which is at least as discrepant as the excess found in data occurring in the background-only hypothesis. Hence, a small *p*-value indicates the excess is inconsistent with the background hypothesis and that new physics might be present; in particle physics it is conventional to consider a *p*-value below  $\sim 0.001$  ( $3\sigma$ ) as evidence of new physics whilst a *p*-value below 1 in  $\sim 3.5$  million ( $5\sigma$ ) is considered as the discovery of new physics.

In this analysis the BumpHunter algorithm [93] is employed; this algorithm uses the BumpHunter test statistic to search for the most discrepant excess in the data and calculate the *p*-value of such an excess. The BumpHunter test statistic gives a quantitative measure of how discrepant any given excess is. To derive the test statistic let's consider  $N$  consecutive bins for which a total of  $d$  data events are found and a total of  $b$  background events are expected. As this is a search for excesses we will consider the case where  $d > b$ . Using Poisson statistics one can calculate the probability that an excess which is at least as discrepant would occur in the background-only hypothesis in this set of bins:

$$P(d, b) = \sum_{n=d}^{\infty} \left( \frac{b^n e^{-b}}{n!} \right) \quad (7.3)$$

From this probability, the BumpHunter test statistic,  $t$ , is defined as

$$t = -\log(P(b, d)) \quad (7.4)$$

The size of the test statistic represents how discrepant an excess is. Using the same logic and requiring that  $d < b$  it is possible to also search for deficits, this is referred to as the DeficitHunter  $p$ -value.

The BumpHunter algorithm calculates the value of  $t$  for all excesses in the dijet mass spectrum by scanning over all possible combinations of consecutive bins. The narrowest excess allowed is two bins and the widest excess allowed contains half the number of bins in the spectrum. The excess with the largest BumpHunter test-statistic is the most discrepant excess and the value of  $t$  observed is labelled  $t_{obs}$ .

To calculate the  $p$ -value of the most discrepant excess, Poisson fluctuations are applied to the background estimation to create pseudo-experiments which represent the range of dijet mass spectra possible under the background-only hypothesis. In each pseudo-experiment the BumpHunter scan is performed to find the most discrepant excess and corresponding value of  $t$ . This is done for many pseudo-experiments to estimate the probability density function of  $t$  under the assumption of the null hypothesis,  $f_{PE}(t|H_{Bkg})$ . The BumpHunter  $p$ -value of the most discrepant excess in data is then calculated using

$$\text{BumpHunter } p\text{-value} = \int_{t_{obs}}^{\infty} f_{PE}(t|H_{Bkg}) \quad (7.5)$$

An example of this calculation is shown in Figure 7.8, the details of this example will be described in Section 7.4.4.

The BumpHunter algorithm is chosen to search for excesses due to two important features. Firstly, the BumpHunter  $p$ -value is model independent; the algorithm makes no prior assumptions about the nature of the new physics model that could be present other than it would produce extra events and that the extra events would occur in consecutive  $m_{jj}$  bins. Secondly, the BumpHunter  $p$ -value is naturally global; this means that the  $p$ -value accounts for the fact that under the null hypothesis an excess such as the one observed could have occurred at any mass point in the dijet mass spectrum. This is due to the fact that in the pseudo-experiments there is no prior assumption on the location of the most discrepant excess.

The combined process of creating an estimation of the background and then finding the most discrepant excess and associated  $p$ -value using the BumpHunter algorithm is referred to as the search phase throughout this Chapter.

## 7.4 Summer16\_HighMass Search Phase

This section presents the search phase for the *Summer16\_HighMass* data-set: Section 7.4.1 describes the background modelling strategy used, Section 7.4.2-7.4.4 present validation studies of the search phase and Section 7.4.6 presents the results of the search phase.

As described in Chapter 6 there are two  $b$ -tag categories considered for the *Summer16\_HighMass* data-set (2  $b$ -tag and  $\geq 1$   $b$ -tag) giving two dijet mass spectra. An independent search phase is performed for both categories.

### 7.4.1 Background Modelling Strategy

For the *Summer16\_HighMass* data-set the background is estimated using a global fit strategy that uses a single fit function for the full range of the dijet mass spectra. A global fit strategy has been used in previous inclusive dijet and di- $b$ -jet searches at ATLAS [2, 11].

A dijet fit function (described in 7.1) is selected using the following strategy. The 3 parameter dijet function is used as the initial nominal function and hence the 4 parameter dijet fit function function is the initial alternate function. If the Wilks'  $p$ -value (described in Section 7.2.2) is less than 0.05, the nominal fit function is rejected and the alternative function becomes the nominal. The process is iteratively run until a dijet fit function with a Wilks'  $p$ -value  $> 0.05$  is selected.

For the *Summer16\_HighMass* data-set the choice of the dijet fit function choice was fixed using a  $8.8\text{ fb}^{-1}$  subset of data. A subset was used such that the function choice could be finalised before the full data-set was collected. This meant that the analysis strategy and search phase validation studies could be scrutinised by the other members of the ATLAS collaboration before the conference note publication. Figure 7.1 shows the Wilks'  $p$ -value as a function of luminosity for the  $\geq 1$   $b$ -tag and 2  $b$ -tag categories for a  $8.8\text{ fb}^{-1}$  subset of data. For both categories the 3 parameter dijet fit function when compared to the 4 parameter dijet fit function has a Wilks'  $p$ -value  $> 0.05$ , therefore the 3 parameter dijet fit function is selected in both categories. Given that the 3 parameter dijet fit function adequately describes the dijet mass spectra of the majority of the data-set it is concluded that it has sufficient parameters to describe the dijet mass spectrum of the full data-set. With hindsight, I think it would have been more rigorous to calculate Wilks'  $p$ -value on the full data-set.

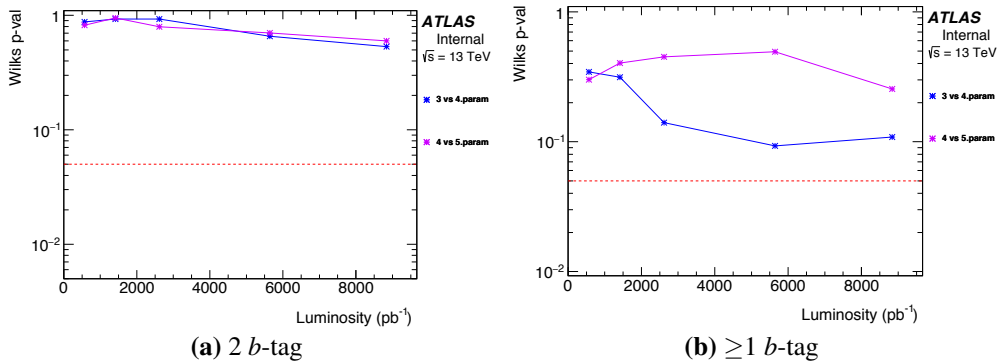


**Figure 7.1:** The Wilks'  $p$ -value as a function of luminosity in the case that the 3 parameter function is the nominal and the 4 parameter is the alternate (blue) and the case where the 4 parameter is the nominal function and the 5 parameter is the alternate (purple) for a  $8.8 \text{ fb}^{-1}$  subset of data in the (a) 2  $b$ -tag and (b)  $\geq 1$   $b$ -tag category. The *Summer16\_HighMass* data-set event selection has been applied [10].

#### 7.4.2 Validation Studies: Background-Only Data-set

It is important to perform search phase validation studies to demonstrate that the dijet fit functions are a valid description of the background dijet mass spectrum caused by QCD dijet production. In this and the following sections the validation studies for the *Summer16\_HighMass* data-set are presented.

To perform the validation studies a dijet mass spectrum that represents the shape of the background with no signal contamination is required. The simulated QCD dijet sample described in Section 6.3 is used as the representative background-only data-set. The simulation sample is produced in several slices of leading jet  $p_T$ , where each slice contains the same number of events. A weight is applied to each event such that the dijet mass spectrum of the merged samples is representative of the smoothly falling dijet mass spectrum that is expected, whilst still maintaining the same statistical precision across the full mass range. The weighted dijet mass distribution is then scaled to  $10 \text{ fb}^{-1}$ <sup>2</sup>, this is referred to as the ‘scaled distribution’, and is the expected number of data events in a specific mass bin. The statistical precision of the scaled distribution in each  $m_{jj}$  bin is represented by the number of ‘effective entries’; defined as the number of data events that would be required to give the same statistical precision. The number of effective entries can be calculated from the event weights as shown in Equation 7.6.

$$N_{eff} = (\sum w_i)^2 / \sum w_i^2 \quad (7.6)$$

<sup>2</sup>The search phase validation studies were performed during data-taking and as such the final integrated luminosity of the data-set had to be estimated,  $10 \text{ fb}^{-1}$  was used in the validation studies where the final data-set is  $13.3 \text{ fb}^{-1}$ .

Figure 7.2 shows the scaled and effective entries distributions as a function of dijet mass for the 2  $b$ -tag and  $\geq 1$   $b$ -tag categories. The number of effective entries is larger than the number of scaled entries, meaning that the scaled distribution contains smaller statistical fluctuations than are present in the final data-set. The oscillating pattern in the effective entry distribution is caused by the merging of the different jet- $p_T$  slices of the simulated sample.

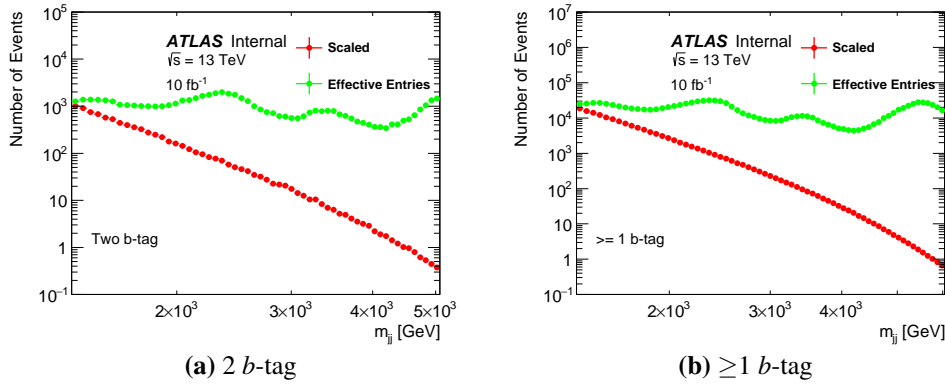


**Figure 7.2:** The scaled dijet mass distribution (red) compared to the effective entries dijet mass distribution (green) of Monte-Carlo simulation of QCD dijet production for the (a) 2  $b$ -tag and (b)  $\geq 1$   $b$ -tag category. The *Summer16\_HighMass* data-set event selection has been applied.

### 7.4.3 Validation Studies: Dijet Mass Range Studies

To demonstrate that the dijet fit functions are able to describe the dijet mass spectra in the mass range considered, the search phase is applied to the scaled dijet mass spectra from simulation. The statistical uncertainties of the simulated sample are used, which are given by the square root of the number of effective entries. 10,000 pseudo-experiments are used to calculate BumpHunter and DeficitHunter  $p$ -values in all *Summer16\_HighMass* search phase validation studies.

The initial dijet mass spectra are considered with the lower edge of the dijet mass spectrum at  $m_{jj} = 1100$  GeV, selected such that there is no kinematic bias from the single jet trigger, and an upper mass edge at the lowest  $m_{jj}$  bin which contains less than one entry. Figure 7.3 shows the search phase for both  $b$ -tag categories, using the 4 parameter dijet fit function. The most discrepant excess is indicated by the blue lines and the BumpHunter  $p$ -value of the excess is shown on the plot. The lower panel shows the significance in each  $m_{jj}$  bin, defined as the difference between the data and the background estimate divided by the uncertainty on the data point.

In the  $\geq 1$   $b$ -tag category, a discrepant excess is observed which has been assigned a BumpHunter  $p$ -value of  $<0.0001$ <sup>3</sup>. A BumpHunter  $p$ -value of  $<0.0001$  is also found when the search phase is performed using the 5 parameter dijet fit function. This shows that the 4 and 5 parameter dijet fit functions provide a poor description of the background dijet mass spectrum in the  $\geq 1$   $b$ -tag category. It can also be concluded that the 3 parameter dijet fit function will also be inadequate, as it is a subset of the 4 parameter dijet fit function.

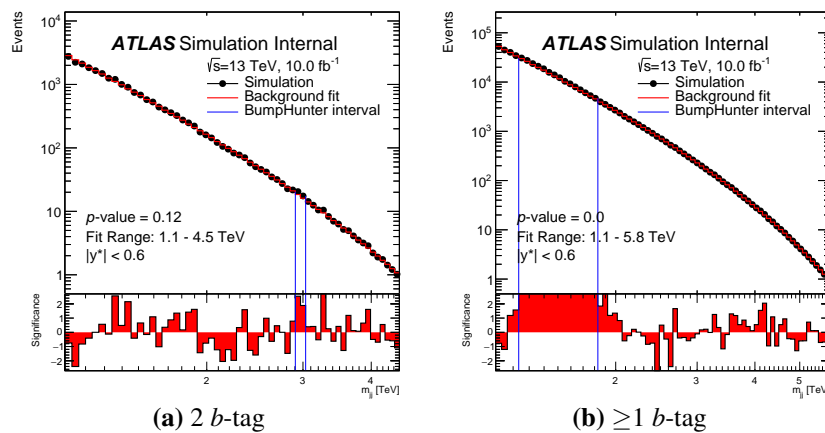


**Figure 7.3:** The dijet mass distribution taken from multi-jet simulation for the (a) 2  $b$ -tag and (b)  $\geq 1$   $b$ -tag, category, fitted to using the 4 parameter dijet fit function, with the lower edge of the dijet mass spectrum at  $m_{jj} = 1100$  GeV. The BumpHunter algorithm is run to identify the most discrepant excess, as indicated by the blue lines. Pseudo-experiments are used to assign the excess a  $p$ -value, which is shown on the plot. The *Summer16\_HighMass* data-set event selection has been applied.

However, by changing the lower edge of the dijet mass spectrum, a region can be found where the dijet fit functions are able to describe the background accurately. To find the largest region with a stable fit quality, the simulated dijet mass spectrum is fitted to using the 4 parameter dijet fit function with the lower edge of the dijet mass spectrum increased one bin at a time from 1100 to 1500 GeV. For each lower edge considered the  $p$ -value of the most discrepant excess is calculated using the BumpHunter algorithm as before, the  $p$ -value of the most discrepant deficit is calculated using the DeficitHunter algorithm, and an overall quality of fit is represented using a  $\chi^2$   $p$ -value. Figure 7.4 shows the distributions of the BumpHunter, DeficitHunter and  $\chi^2$   $p$ -values as the lower edge of the dijet mass spectra is increased for both  $b$ -tagging categories. In both categories the background estimations are stable if the lower mass edge of the dijet mass spectrum is  $m_{jj} = 1378$  GeV or above. This demonstrates that at low mass there are features in the background dijet mass spectrum that are causing a poor fit quality, which can be removed by requiring that  $m_{jj} > 1378$  GeV.

<sup>3</sup>This means that the observed BumpHunter test-statistic was greater than in all 10,000 pseudo-experiments.

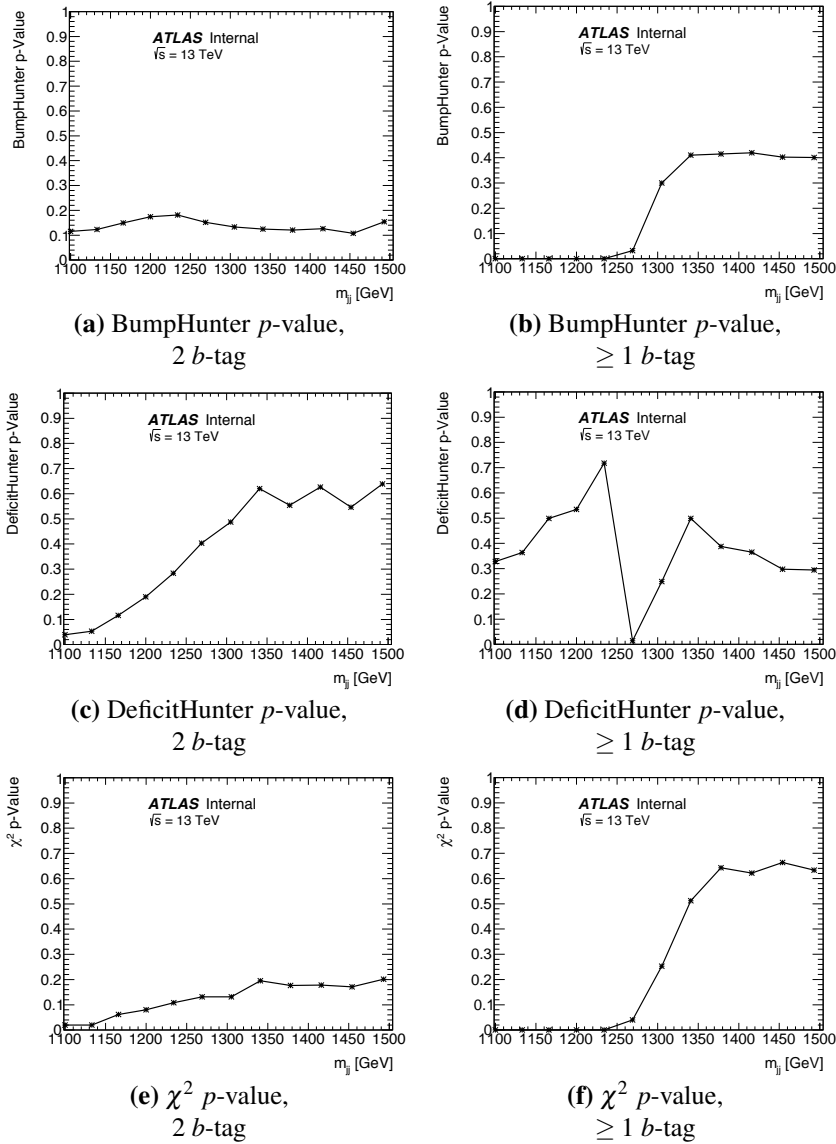


**Figure 7.4:** The BumpHunter (top row), DeficitHunter (middle row) and  $\chi^2$  (bottom row)  $p$ -values for the search phases using the 4 parameter dijet fit function performed to the dijet mass spectrum taken from the simulation of QCD dijet production for the 2  $b$ -tag category (left column) and  $\geq 1 b$ -tag category (right column) as a function lower edge of the dijet mass ( $m_{jj}$ ) spectrum used in search phase. The *Summer16\_HighMass* data-set event selection has been applied to the simulation.

Figure 7.5 shows the search phase applied to the dijet mass spectra of the simulated QCD dijet sample with a lower edge at  $m_{jj} = 1378$  GeV for both  $b$ -tagging categories using the 4 parameter dijet fit function. The most discrepant excess, as found by the BumpHunter algorithm, is indicated by the blue lines and the  $p$ -value of the excess is shown on the plot. The study presented in this section motivates the requirement that  $m_{jj} > 1378$  GeV in the *Summer16\_HighMass* data-set event selection.

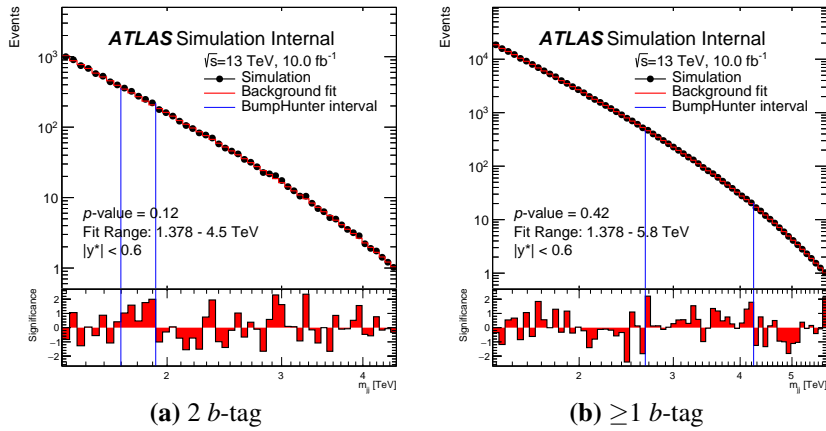


**Figure 7.5:** The dijet mass spectrum taken from multi-jet simulation for the (a) 2  $b$ -tag and (b)  $\geq 1$   $b$ -tag, category, fitted to using the 4 parameter dijet fit function, with lower mass bound of the fit range  $m_{jj} = 1378$  GeV. The BumpHunter algorithm is run to identify the most discrepant excess, as indicated by the blue lines. Pseudo-experiments are used to assign the excess a  $p$ -value, which is shown on the plot. The *Summer16\_HighMass* data-set event selection has been applied.

#### 7.4.4 Validation Studies: Spurious Signal

If an inadequate background estimation is used fit biases can occur, where a fit bias is defined a difference between the true background dijet mass distribution and the background estimation. Fit biases that are large compared to the statistical fluctuations of the background can appear as false signal or could hide a true signal, the former is referred to as spurious signal. For the di- $b$ -jet search to be able to observe a new particle with confidence it is important to demonstrate that spurious signal cannot occur.

To demonstrate that fit biases are not occurring, the search phase is performed to the simulated QCD dijet sample, which is a background-only representative data-set. As described in Section 7.4.2, the simulated dijet mass spectrum contains smaller statistical fluctuations than are present in the final data-set. Therefore to create a dijet mass spectrum representative of the one that is expected in data Poisson fluctuations are applied to the scaled distribution to create ‘data-like’ distributions. Figure 7.6 shows the scaled and effective entries distributions for both  $b$ -tag categories overlaid with a data-like distribution in blue.

The search phase is then applied to the data-like distributions in both  $b$ -tag categories. Figure 7.7 shows the search phase using the 3 parameter dijet fit function applied to a data-like distribution in both  $b$ -tag categories. The most discrepant excess is indicated by the blue lines and the BumpHunter  $p$ -value of the excess is shown on the plot. Figure 7.8 illustrates the calculation of the BumpHunter  $p$ -value in the search phase. For this data-

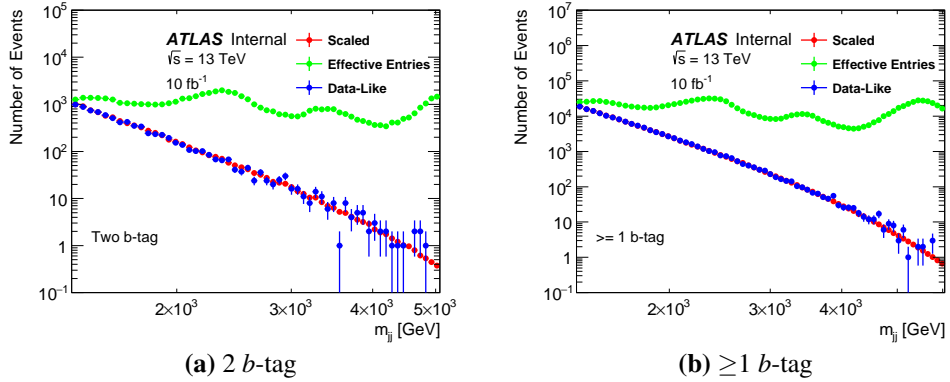


**Figure 7.6:** The scaled dijet mass distribution (red) compared to the effective entries of the dijet mass distribution (green) for the 2  $b$ -tag category, for the (a) 2  $b$ -tag and (b)  $\geq 1$   $b$ -tag case. Overlaid is a data-like distribution (blue) created by applying Poisson fluctuations to the scaled distribution. The *Summer16\_HighMass* data-set event selection has been applied.

like distribution, in the 2  $b$ -tag category the BumpHunter, DeficitHunter and  $\chi^2$   $p$ -value are found to be 0.57, 0.80 and 0.39 respectively. Similarly, in the  $\geq 1$   $b$ -tag category the BumpHunter, DeficitHunter and  $\chi^2$   $p$ -values are 0.93, 0.77 and 0.86 respectively. Therefore, a valid background estimation has been found in both  $b$ -tagging categories for this data-like distribution.

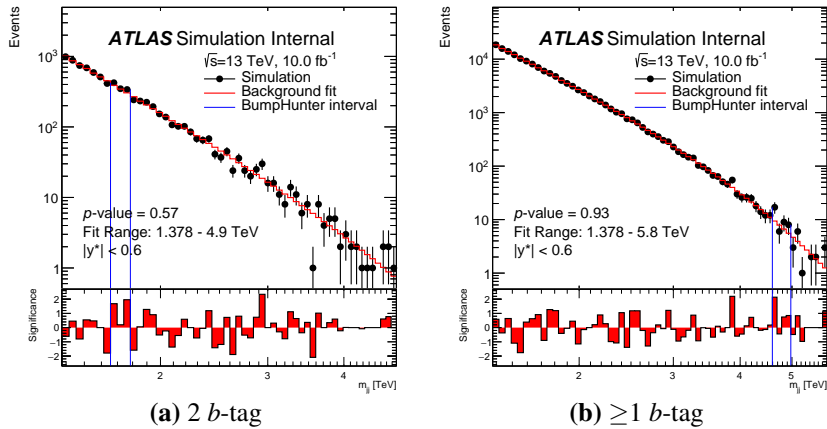


**Figure 7.7:** A data-like distribution taken from multi-jet simulation for the (a) 2  $b$ -tag and (b)  $\geq 1$   $b$ -tag, category, fitted to using the 3 parameter dijet fit function. The BumpHunter algorithm is run to identify the most discrepant excess, as indicated by the blue lines. Pseudo-experiments are used to assign the excess a  $p$ -value, which is shown on the plot. The *Summer16\_HighMass* data-set event selection has been applied.

However, one data-like distribution does not represent the full range of possible fluctuations that are possible. Therefore, the search phase is applied to an ensemble of data-like distributions, each created using a different set of Poisson fluctuations. Figure 7.9 shows the

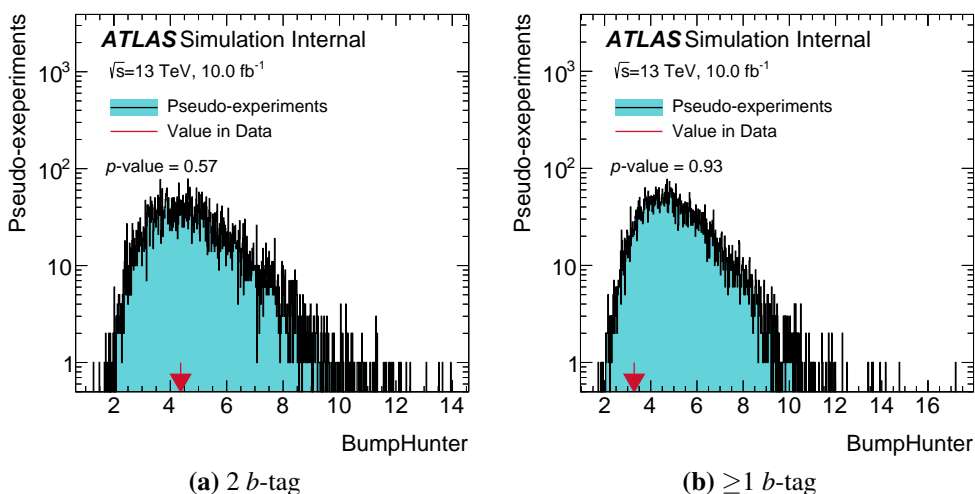


**Figure 7.8:** The BumpHunter test statistic observed when the search phase is applied to a data-like distribution from a simulated QCD dijet sample compared to the distributions of the BumpHunter test statistic for 10,000 pseudo-experiments applied to the background estimation for the (a) 2  $b$ -tag and (b)  $\geq 1$   $b$ -tag categories. The fraction of pseudo-experiments with a BumpHunter test statistic greater than the observed value is the BumpHunter  $p$ -value.

distribution of the BumpHunter, DeficitHunter and  $\chi^2$   $p$ -values for 200 different data-like distributions, for the 2  $b$ -tag and  $\geq 1$   $b$ -tag category respectively. There is no evidence of a fit bias in either category, which would be observed as a bias towards low BumpHunter  $p$ -values causing spurious signal or a bias toward low DeficitHunter  $p$ -values causing fake deficits. The distribution of the  $\chi^2$   $p$ -values also indicates that there is good fit quality in both tagging categories.

### 7.4.5 Validation Studies: Signal Injection

If an excess with a BumpHunter  $p$ -value  $< 0.01$  is observed then the background estimation is performed again with an exclusion region applied. The exclusion region is defined as the mass range of the excess with one additional bin on the low mass side. The fit ignores all bins in the exclusion region, meaning that signal induced fit biases are removed.

It has been shown in previous iterations of the inclusive dijet and di- $b$ -jet searches at ATLAS [2, 11] that, using the region exclusion procedure, the 3 parameter dijet fit function is able to describe a simulated QCD background when a signal has been injected. This is because the parameters of the 3 parameter dijet fit function are highly constrained by the QCD background and the region exclusion procedure will remove any signal induced fit bias caused by a large signal. Hence, it is concluded the search phase using the 3 parameter dijet fit function is robust against the presence of signal.

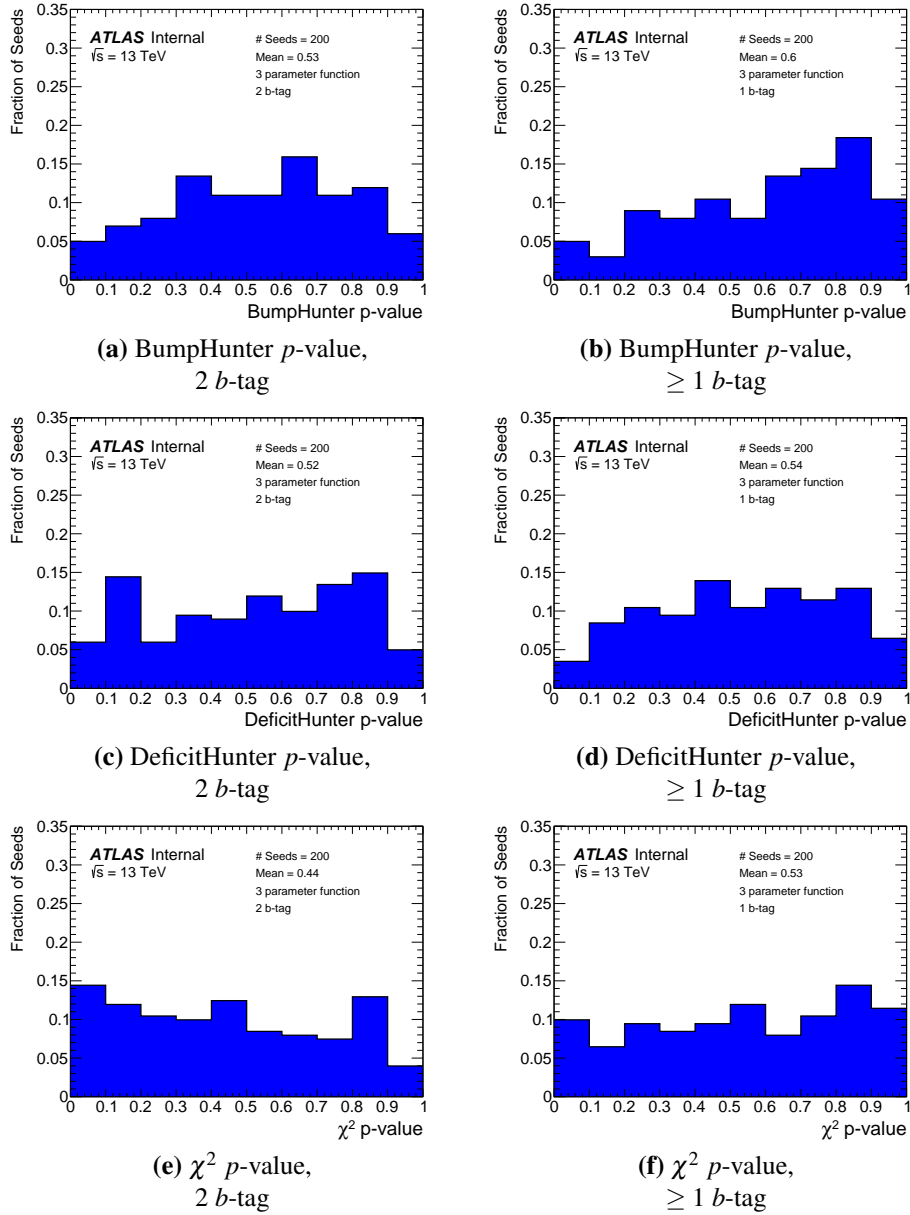


**Figure 7.9:** The distribution of BumpHunter (top row), DeficitHunter (middle row) and  $\chi^2$  (bottom row)  $p$ -values for the search phase using the 3 parameter dijet fit function performed on 200 data-like dijet mass spectra taken from the simulation of QCD dijet production for the 2  $b$ -tag category (left column) and  $\geq 1$   $b$ -tag category (right column). The *Summer16\_HighMass* data-set event selection has been applied to the simulated sample.

To conclude the search phase validation studies for the *Summer16\_HighMass* data-set analysis, it has been shown that the 3 parameter dijet fit function has a sufficient number of parameters to provide an adequate background and that there is no evidence that spurious signal can occur. It is also known that the search phase using the 3 parameter dijet fit function will not produce large signal induced fit biases. Hence, for the *Summer16\_HighMass* data-set the 3 parameter dijet fit function provides a valid background estimation in both

categories.

### 7.4.6 Search Phase Results

Figure 7.10 shows the dijet mass spectrum of the *Summer16\_HighMass* data-set and the background estimate created using the 3 parameter dijet fit function in the 2 and  $\geq 1$   $b$ -tag categories. The upper panel shows the data compared to the background estimation, in addition the benchmark signal models with enhanced cross sections have been overlaid. The lower panel shows the significance of the difference between the data and background estimate.

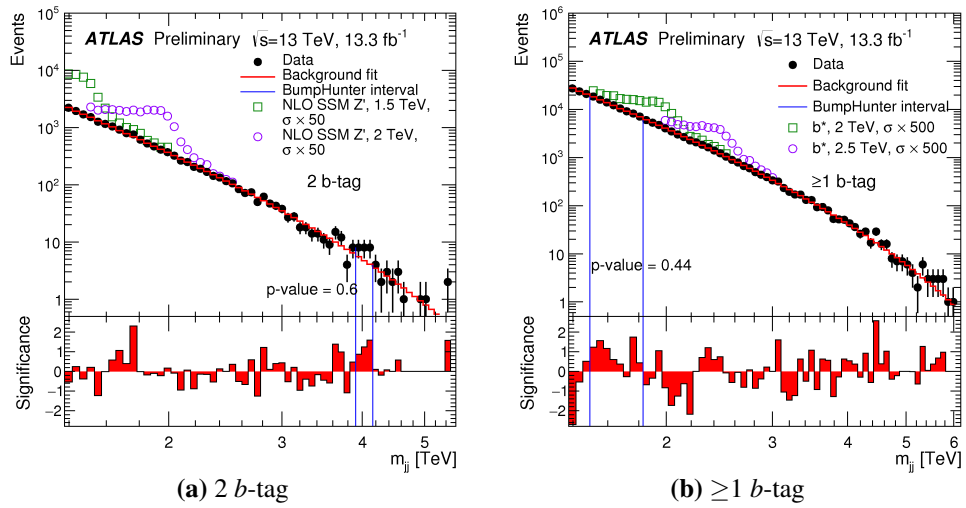


**Figure 7.10:** The dijet mass spectrum of the *Summer16\_HighMass* data-set in the (a) 2  $b$ -tag and the (b)  $\geq 1$   $b$ -tag category compared to the background estimation created using the 3 parameter dijet fit function. The upper panel shows the data compared to the background estimate, benchmark signal models with enhanced cross sections are overlaid. The lower panel shows the significance of the difference between the data and the background estimate. The most discrepant excess as found by the BumpHunter algorithm is indicated by the vertical blue lines and the  $p$ -value of this excess is printed on the plot [10].

In both cases the BumpHunter algorithm has identified the most discrepant excess indicated in the figure using vertical blue lines. The BumpHunter  $p$ -value has been calculated using 10,000 pseudo-experiments. The BumpHunter  $p$ -value is 0.60 in the 2  $b$ -tag category and 0.44 in the  $\geq 1$   $b$ -tag category. No significant excess is found in either  $b$ -tag category and it is therefore concluded that there is no evidence of a BSM resonance in the *Summer16\_HighMass* data-set. As no significant excess is found, limits on the benchmark signal models are set using the *Summer16\_HighMass* data-set, which will be shown in Chapter 8.

## 7.5 Full16\_LowMass Search Phase

This section presents the search phase for the *Full16\_LowMass* data-set: Section 7.5.1 describes the background-only samples used for the search phase validation studies. Section 7.5.2 demonstrates that the global fit strategy is not a valid strategy for the *Full16\_LowMass* data-set. Section 7.5.3 introduces an alternative background estimation strategy called the Sliding Window Fit (SWiFt) and Section 7.5.4 describes the strategy used for selecting the parameters of the SWiFt background estimation. Sections 7.5.5, 7.5.6 and 7.5.7 show validation studies of the search phase performed using the SWiFt background estimation. Section 7.5.8 and Section 7.5.9 presents the results of the search phase using the *Full16\_LowMass* data-set.

### 7.5.1 Background-Only Samples

To perform the validation studies of the *Full16\_LowMass* search phase a dijet mass spectrum that represents the shape of the background with no signal contamination is required. In the *Summer16\_HighMass* data-set analysis Monte-Carlo simulation was used, as described in Section 7.4.2. However, for the *Full16\_LowMass* data-set Monte-Carlo simulation cannot be produced with a large enough statistical precision to perform an adequate test of the background estimation strategy.

Instead two fitting test data-sets are used: a  $3 \text{ fb}^{-1}$  subset of data and a high statistical precision fitting control region. The  $3 \text{ fb}^{-1}$  subset of data is created from events drawn at random from the final data spectrum. Figure 7.11 shows the dijet mass spectrum of the  $3 \text{ fb}^{-1}$  subset and the full *Full16\_LowMass* data-set. The dijet mass spectrum of the subset represents the shape of the dijet mass spectrum in full data-set, except with a lower statistical precision. The luminosity of the subset of data was chosen to be similar to that of a previous low mass di- $b$ -jet search in an equivalent mass range [12], such that this subset of data is known not to be sensitive to signal.

To create the *Full16\_LowMass* fitting control region, the dijet mass spectrum of events that have passed the *Full16\_LowMass* event-selection except offline  $b$ -tagging selection is used, this is referred to as the 0-tag dijet mass spectrum. This dijet mass spectrum contains more events than the final dijet mass spectrum and will have a similar shape as most of the event selection, including online  $b$ -tagging, has been applied.

To account for the effect of offline  $b$ -tagging in the fitting control region, the 0-tag data must be multiplied by the event-level offline  $b$ -tagging efficiency with respect to online  $b$ -tagging,  $\varepsilon_b^{\text{offline}}$ , which is defined as the fraction of events that pass offline  $b$ -tagging re-

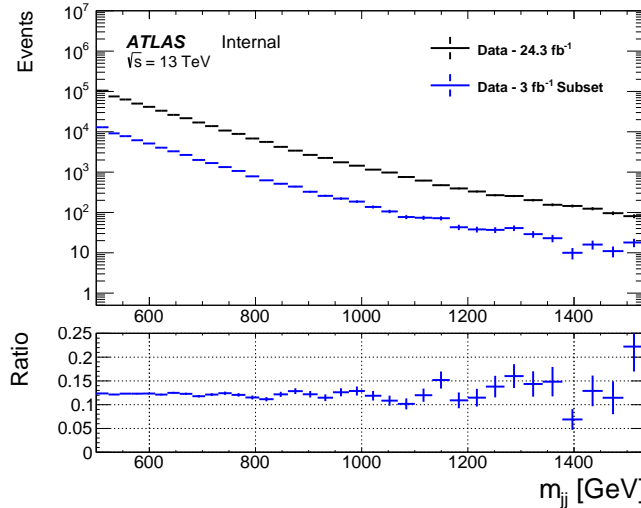


**Figure 7.11:** The dijet mass ( $m_{jj}$ ) spectra of the full *Full16\_LowMass* data-set and a  $3\text{ fb}^{-1}$  subset of *Full16\_LowMass* data. The lower panel shows a ratio.

quirements given that the events have passed all other requirements of the *Full16\_LowMass* event selection, including online  $b$ -tagging.  $\varepsilon_b^{\text{offline}}$  is estimated using the ratio of the dijet mass spectrum from the 0-tag data to the  $3\text{ fb}^{-1}$  subset of data; Figure 7.12(a) shows the two dijet mass spectra and the ratio. The ratio is scaled by  $24.3/3$  to account for the lower luminosity of the subset of data, and is smoothed using the five parameter dijet fit function. Figure 7.12(b) shows the luminosity adjusted ratio (black points) and the fit (red line). The goodness of fit is estimated by comparing the  $\chi^2$  test statistic to a  $\chi^2$  distribution with the same number of degrees of freedom; a  $\chi^2$   $p$ -value of 0.053 is observed indicating a reasonable fit quality.

The 0-tag spectrum is then scaled by the smoothed estimation of  $\varepsilon_b^{\text{offline}}$  to create the dijet mass spectrum of the fitting control region. Figure 7.12(c) shows the dijet mass spectrum from the full *Full16\_LowMass* data-set and the fitting control region, showing that the fitting control region gives a reasonable background-only sample for search phase validation studies.

Two types of dijet mass spectra are created using the fitting control region for the search phase validation studies. The first is a ‘smooth’ dijet mass spectrum, where the uncertainties on the fitting control region are set to be Poisson like, which means that the uncertainty is the square root of the number of events. This is done such that the uncertainties represent the size of statistical fluctuations expected in the full *Full16\_LowMass* data-set. The second type of dijet mass spectrum is a ‘data-like’ spectrum, where a random set of Poisson fluctuations are applied to the fitting control region, to represent the statistical fluctuations that are observed in data. Many data-like spectra can be made, each representing a different set

of random fluctuations. Figure 7.12(d) shows the comparison of the smooth spectrum and a data-like spectrum.

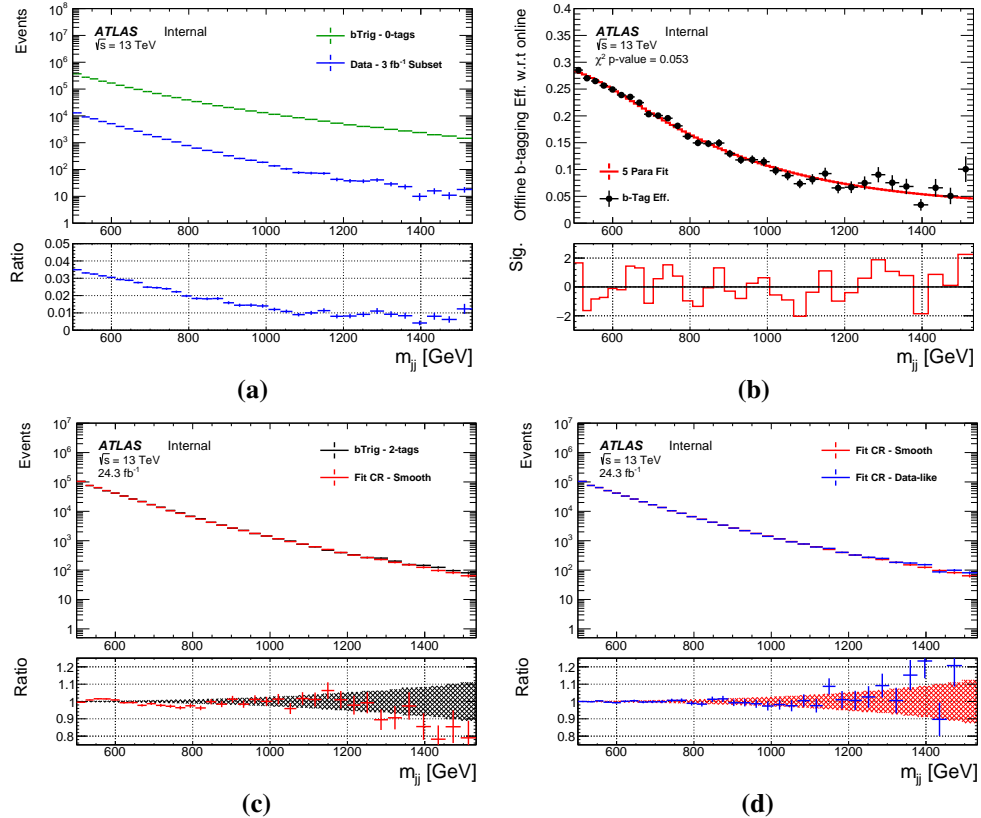


**Figure 7.12:** A figure showing the process of obtaining the *Full16\_LowMass* fitting control region dijet mass ( $m_{jj}$ ) spectrum used for the *Full16\_LowMass* data-set fit studies. Panel (a) shows the dijet mass spectrum of events before  $b$ -tagging is applied (0-tag) and of a  $3 \text{ fb}^{-1}$  subset of *Full16\_LowMass* data. Panel (b) shows the offline  $b$ -tagging efficiency with respect to online tagging estimated using the luminosity adjusted ratio of the two spectra in plot (a), the lower panel shows the significance of difference between the luminosity adjusted ratio and the fit. Panel (c) shows the dijet mass spectrum of the fitting control region and the full *Full16\_LowMass* data-set. Panel (d) shows the smooth and data-like dijet mass spectra from the fitting control region.

As no offline  $b$ -tagging is applied, the 0-tag data contains larger light jet and  $c$ -jet impurities than the full *Full16\_LowMass* data-set and hence is considered insensitive to signal. As has been discussed above, the  $3 \text{ fb}^{-1}$  subset of data will not be sensitive to signal. Therefore the fitting control region is insensitive to signal and can be considered a background-only spectrum.

All search phase validation studies for the *Full16\_LowMass* data-set are performed in the mass region outlined by the *Full16\_LowMass* event selection, 566–1533 GeV. However,

the fitting control region is created in the dijet mass region 500-1533 GeV because the fitting control region was created before the bias due to non-leading jets, described in Section 6.4.4, was observed. As the fitting control region is created by applying a smoothed efficiency to each independent dijet mass bin, the bias will not effect events with the  $m_{jj} > 566$  GeV.

The use of the subset of data and the fitting control region gives two complementary dijet mass spectra to perform search phase validation studies. The subset is representative of the same underlying dijet mass spectrum as the full *Full16\_LowMass* data-set but has lower precision. The fitting control region, provides a high-statistic background-only spectra with a similar shape to the dijet mass spectrum of the full *Full16\_LowMass* data-set.

### 7.5.2 Global Fit Strategy

Using a single dijet fit function to model the full mass range considered is known as the global fit strategy. Previous di-*b*-jet searches have used a global fit strategy [11], including the *Summer16\_HighMass* analysis described above.

Figure 7.13 shows the smooth dijet mass spectrum from the fitting control region fitted to using the global fit strategy with the 3, 4 and 5 parameter dijet fit functions. The lower panel shows the significance of the difference between the data and the various fits. One would expect an excellent fit quality when an appropriate background estimation is used to model the smooth spectrum as the uncertainties are larger than the true statistical fluctuations present. The 3 parameter dijet fit function has a  $\chi^2/n.d.f. \gg 1$ , where *n.d.f* represents the number of degrees of freedom, demonstrating an extremely poor fit quality. Hence, the 3 parameter fit is rejected as a fit function option. Further to this, there is a fit bias present for all dijet fit functions, where a fit bias is defined as a difference between the background estimation and the true underlying dijet mass distribution of the background. The bias is observed as a set of peaks and troughs in the significance plot. A fit bias that is similar in size to the statistical fluctuations may cause a peak to be falsely interpreted as signal or for a trough to mask true signal.

To further quantify the effect of the fit biases in the 4 and 5 parameter case, Figure 7.14 shows the two global fits after the BumpHunter algorithm has been performed. The BumpHunter algorithm assigns *p*-values of 0.096 and 0.247 to the largest excess in the 4 parameter and 5 parameter case respectively. In the case of the smooth spectrum, the BumpHunter *p*-value cannot be interpreted in the conventional way, as the smooth distribution does not contain the Poisson fluctuations that are present in the pseudo-experiments it is being compared to. Instead, it provides an approximate estimation of the size of the largest fit bias to the size of the largest excesses expected in data due to statistical fluctuations. The

fit biases in the global fit for the 4 and 5 parameter dijet fit functions are large relative to the size of statistical fluctuations expected,

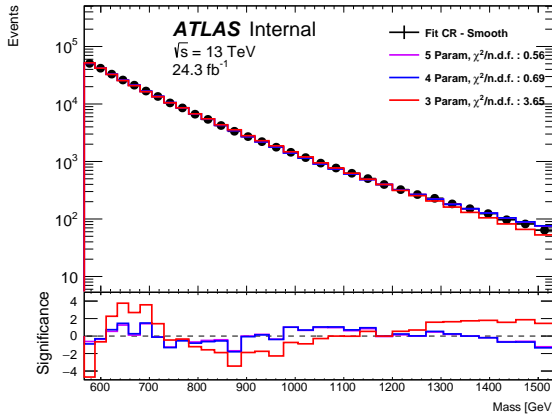


**Figure 7.13:** The smooth dijet mass spectrum from the *Full16\_LowMass* fitting control region fitted to using the 3, 4 and 5 parameter global fits. The lower panel shows the significance of the difference between the data and the background fits.

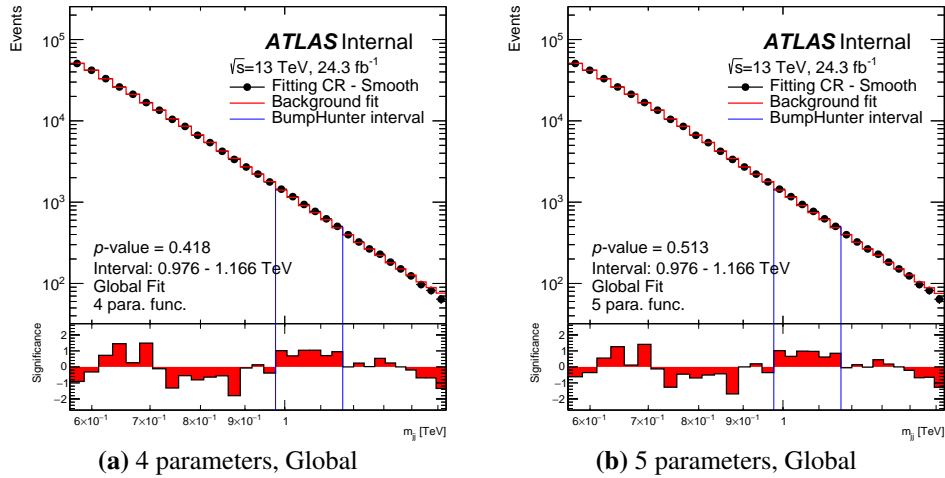


**Figure 7.14:** The global fit and BumpHunter algorithm procedure run on the smooth dijet mass spectrum from the *Full16\_LowMass* fitting control region using the global 4 and 5 parameter dijet fit functions. The upper panel shows the data compared to the background estimate and the lower panel shows the significance of the difference between the two. The most discrepant excess as found by the BumpHunter algorithm is indicated by the vertical blue lines and the  $p$ -value of this excess is printed on the plot.

It is therefore concluded that neither fit function provides an adequate description of the background. This is not unexpected for large luminosities and wide mass ranges, as the resulting small statistical uncertainties and large fit ranges mean that any difference between the underlying shape of the QCD dijet mass spectrum and the dijet fit functions is magnified. Hence, the global fit strategy is rejected and an alternative background modelling strategy is used.

### 7.5.3 Sliding window background estimation (SWiFT)

As the global fit strategy cannot provide a valid background estimation in the *Full16\_LowMass* fitting control region, an alternate background modelling strategy must be used.

The Sliding Window Fit (SWiFt) background estimation divides the dijet mass spectrum into smaller overlapping windows, and performs a local fit in each window to provide one point in the dijet mass background estimate. This makes the SWiFt method more stable than the global fit at higher luminosities as the mass range of each fit is reduced. The SWiFt background estimation has been used in the inclusive dijet analysis on the full 2015+2016 ATLAS data-set [3].

The windows used by the SWiFT background estimate are centred at each of the bin boundaries defined by the dijet mass bins, which are shown in Appendix A. The window width is defined by fixing the number of bins below the window centre ( $n_{\text{Low}}$ ) and fixing the number of bins above the window centre ( $n_{\text{High}}$ ). For this analysis symmetric windows are used, defined by their window half-width ( $wHW$ ); i.e.  $n_{\text{Low}} = n_{\text{High}} = wHW$ . Symmetric windows are chosen as this ensures that there will be an adequate side band on either side of the window centre where possible, and reduces the number of parameters that have to be tested. Windows are required to have a lower mass bound that is  $\geq 566$  GeV, which is the  $m_{jj}$  requirement of the event-selection. Figure 7.15 shows the SWiFt windows used in the *Full16\_LowMass* data-set analysis for the window half-widths of 10, 12, 14 and 16. The procedure for choosing the window half-width is described in Section 7.5.4

In each window a fit to the data is performed using one of the dijet fit functions listed in Table 7.1. The same function is used in all windows, with initial parameters seeded initially from a configuration file and then from the previous fit. Each of the fits are evaluated at the dijet mass bin which is at the centre of the window, this value forms the background estimation for that bin. The SWiFt background estimation for the full dijet mass spectrum is constructed by combining the single bin background estimations from each of the window fits.

Once, a SWiFt background estimation is constructed, it is then compared to data using the BumpHunter algorithm which finds the most discrepant excess region and assigns a  $p$ -value to it. The combination of the SWiFt background estimation and BumpHunter algorithm is referred to as the SWiFt search phase. In the following SWiFt validation studies 1,000 pseudo-experiments are used to calculate the BumpHunter  $p$ -value.

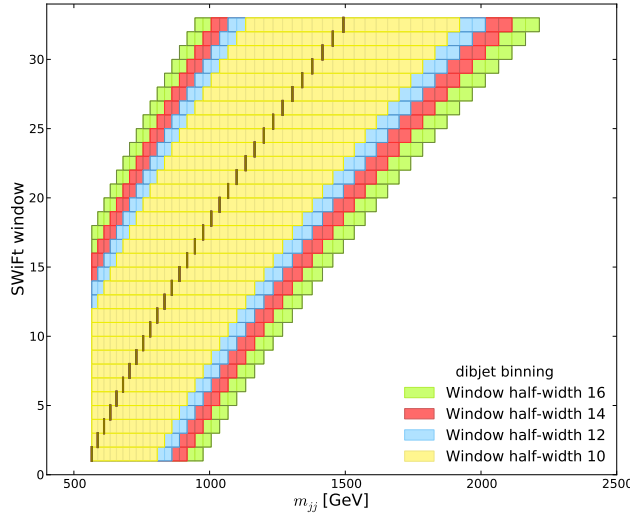


**Figure 7.15:** The windows used by the SWiFt background estimate in the *Full16\_LowMass* data-set analysis for a range of window half-widths. The bin centre is indicated by the black mark and the corresponding window is indicated by the coloured squares.

#### 7.5.4 Window Selection Strategy

There are two key input parameters of the SWiFt background estimation:

**1. The window width:**

In this analysis symmetric windows are used, therefore the width of the windows is defined by the window half-width ( $wHW$ ) parameter.

**2. Fit function:**

The dijet fit functions are used, as used in the global fit strategy.

The functions are listed in Table 7.1.

The choice window half-width and fit function is referred to as the SWiFt configuration. The largest sensitivity is found by using the largest window width and the dijet fit function with the fewest number of parameters, whilst still obtaining sufficient fit quality. Sensitivity studies that demonstrate this statement are shown below in Section 7.5.7.

To define ‘sufficient fit quality’ the following fit quality criteria is used:

- **Global  $\chi^2$  p-value > 0.05:**

The  $\chi^2$  test statistic is calculated by comparing the data to the SWiFt background estimate. The global  $\chi^2$  p-value is then calculated by comparing the test statistic to a  $\chi^2$  distribution with the number of degrees of freedom equal to the number of bins minus the number of parameters of the fit function.

- **Number of windows with Wilks'  $p$ -value  $< 0.1$  must be  $\leq 10$ :**

The Wilks'  $p$ -value is used to test if an additional parameter is required in the fit function to provide an adequate description of the data, as described in 7.2.2. However, it is not appropriate to require that every window fit passes the Wilks'  $p$ -value  $> 0.05$  criteria used in the global fit strategy, as this does not account for the fact that many fits are performed and it is expected that by chance some fits would fail this requirement. Instead, a requirement is placed that in the large majority of windows pass a tighter requirement the Wilks'  $p$ -value ( $> 0.1$ ), as this indicates that the correct functional form is being used.

To select the optimal SWiFt configuration, a predefined iterative window selection procedure is performed on the full *Full16\_LowMass* data-set. A predefined procedure is used as this means that the most sensitive SWiFt configuration that provides an adequate fit to the final data-set can be selected in a manner in which no personal bias can be introduced.

In the *Full16\_LowMass* data-set, the mass range is 566 - 1533 GeV. This contains 32 bins, which in turn requires 32 windows and 32 fits. A window half-width of 16 is the widest window that is considered, as this configuration is similar to the size of the dijet mass spectrum. A window half-width of 10 is the narrowest window considered for the purposes of the SWiFt search phase validation studies, as at this point the windows are becoming excessively narrow. Figure 7.15 shows the SWiFt windows used in the for the window half-widths of 16, 14, 12 and 10

The 5 parameter dijet fit function is used for the SWiFt background estimation. The 3 parameter dijet fit function was not considered due to its exceptionally poor performance in the global fit, as noted in Section 7.5.2. The 4 parameter dijet fit function was rejected for two reasons. Firstly the SWiFt background estimation using the 4 parameter dijet fit function shows evidence of spurious signal for most window widths, as will be demonstrated below in Section 7.5.6. Secondly, the SWiFt background estimates for the 4 parameter dijet fit function is less sensitive to signal than using the SWiFt background procedure with the 5 parameter dijet fit function and wider windows, as is demonstrated in Section 7.5.7.

Given the quality requirements outlined above, the strategy for selecting a window width is:

1. Perform the SWiFt background estimate using a window half-width of 16.
2. Use the BumpHunter algorithm to search for any significant discrepant excesses ( $p$ -value  $< 0.01$ ), if one is then a region exclusion procedure is applied.
3. If the fit quality criteria outlined above is passed, select this window width.
4. If not then drop the window half-width by 2, and repeat step (2).

This procedure is repeated until a window half-width is found where the fit quality criteria have been passed.

The region exclusion procedure if BumpHunter  $p$ -value  $< 0.01$  is introduced as a large signal can cause a signal induced fit bias. To remove this bias the region containing the excess is excluded when creating the SWiFt background estimation. The exact region exclusion procedure is outlined in Section 7.5.7. A threshold of 0.01 is used as this signifies an excess that is greater than  $2\sigma$  in significance, and is consistent with the threshold used in previous dijet searches [22]. Therefore, the observation of a BumpHunter  $p$ -value of 0.01 becomes a critical point in this analysis, and as such will be considered as the point at which signal becomes significant for the purposes of the following SWiFt search phase validation studies.

The results of the window selection procedure applied to the full data-set are shown in Section 7.5.8. after the SWiFt search phase validation studies are presented.

### 7.5.5 SWiFt Validation Studies: Window Width Selection Procedure

The SWiFt window selection strategy, described in Section 7.5.4, has been tested in the fitting test data-sets, described in Section 7.5.1.

Firstly, let's examine the results from the SWiFt background procedure applied to 100 different seeds of data-like spectra from the fitting control region. Figure 7.16 shows the cumulative probability of the two fit quality variables used in the window selection procedure, the fraction of seeds that pass the fit quality requirements for each window half-width is printed on the bottom right of the plot. It is shown that in  $> 99\%$  of cases a window half-width in the range considered would pass the Wilks'  $p$ -value requirement and that in  $> 80\%$  of cases a window half-width in the range considered would pass the global  $\chi^2$   $p$ -value requirement.

The window selection procedure is also tested using the  $3 \text{ fb}^{-1}$  subset of data. Figure 7.17 shows the fit quality measures used in the window width selection procedure, using a range of window half-widths of 16 to 10, for both the 4 and 5 parameter dijet fit function. The requirements placed on each fit quality measure by the window selection procedure are indicated by dotted lines on the figure. According to the window selection procedure the 5 parameter dijet fit function with a window half-width of 16 would have been selected, although the 4 parameter dijet fit function with window half-width of 16 has also passed the fit quality criteria.

It is notable that the window selection procedure for the subset of data has chosen

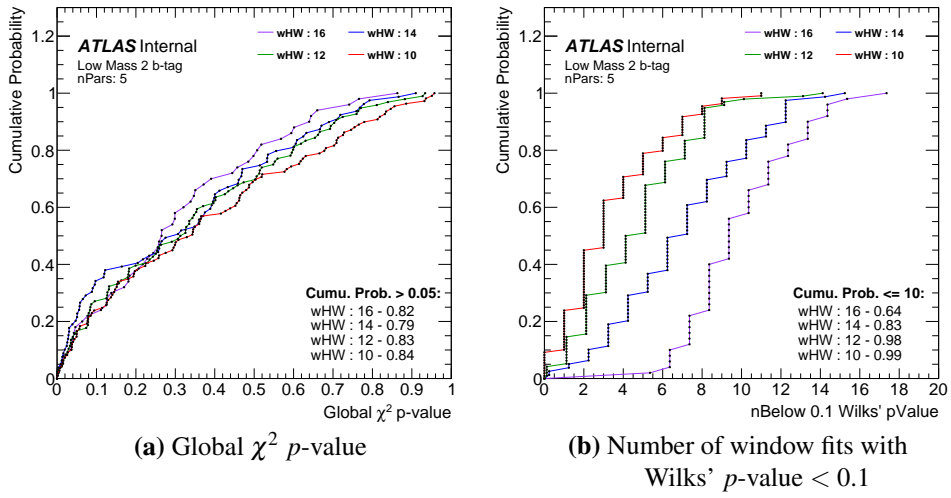


**Figure 7.16:** The cumulative probability of the global  $\chi^2$  *p*-value, and number of window fits with Wilks' *p*-value  $< 0.1$  of the SWiFt background estimation for 100 data-like distributions taken from the *Full16\_LowMass* fitting control region. The SWiFt procedure has been performed using the 5 parameter dijet fit function for the range of window half-widths (*wHW*) of 10 to 16. The fraction of seeds that pass the fit quality requirements for each swift configuration is shown in the bottom right of the plot.

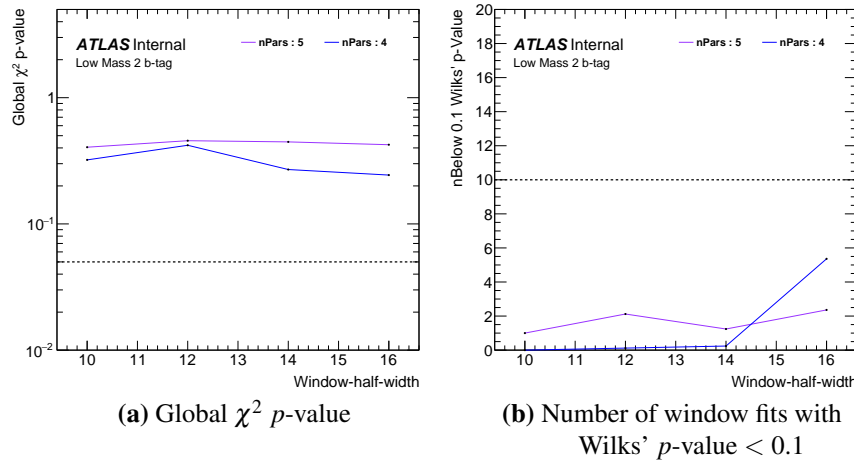


**Figure 7.17:** An illustration of the window selection procedure for a  $3 \text{ fb}^{-1}$  subset of *Full16\_LowMass* data. It shows the global  $\chi^2$  *p*-value, and number of window fits with Wilks' *p*-value  $< 0.1$  for the SWiFt background estimate using a range of window half-widths (*wHW*) and number of parameters (*nPars*) of the dijet fit function. The dotted lines indicate thresholds that are used in the window selection procedure.

a wide window and could have chosen the lower order function, in contrast to the fitting control region case. This shows that either the fitting control region often selects narrower windows because it is not a perfect representation of the true dijet mass spectra or because at the higher precision of the  $24.3 \text{ fb}^{-1}$  narrower windows are required than at  $3 \text{ fb}^{-1}$ . Either way, this shows the utility of choosing the window width on the final data-set using a pre-defined procedure.

### 7.5.6 SWiFt Validation Studies: Spurious Signal

As described in Section 7.4.4, it is important to demonstrate that the fit biases and spurious signal will not occur for the SWiFt background estimation strategy, where a fit bias is a difference between the true background dijet mass distribution and the background estimation and spurious signal is a false positive caused by a fit bias.

To demonstrate that fit biases are not occurring the SWiFt search phase is performed to background-only representative data-sets and the BumpHunter  $p$ -values are studied for evidence of spurious signal. The SWiFt configurations considered use the 4 and 5 parameter dijet fit function and window half-widths range of 10, 12, 14 and 16; giving 8 different configurations. Only SWiFt configurations that show no evidence of spurious signal are considered by window selection procedure.

Firstly, we consider the results from the subset of data. Figure 7.18 shows the SWiFt search phase performed on the dijet mass spectrum of the  $3 \text{ fb}^{-1}$  data subset, for the 4 and 5 parameter dijet fit function for a window half-width of 16. The blue-lines indicate the largest excess found by the BumpHunter algorithm and the  $p$ -value assigned is printed on the plot. In both cases the background is well modelled and there is no evidence of spurious signal, similar results are found for all window half-widths considered. However, searches for spurious signal using the subset of data are limited by the small statistical precision of the subset relative to the final data-set.

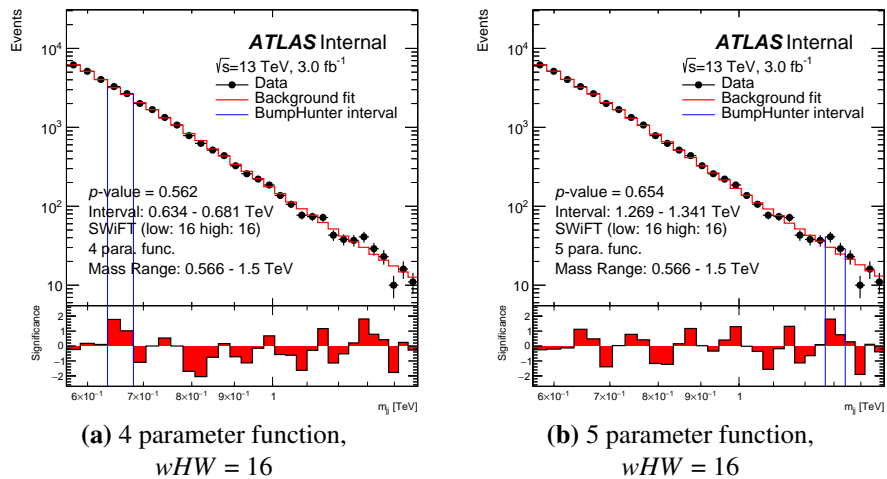


**Figure 7.18:** The SWiFt search phase run on a  $3 \text{ fb}^{-1}$  subset of the *Full16\_LowMass* data-set. The SWiFt procedure has been run for the 4 and 5 parameter dijet fit function for a window half-width ( $wHW$ ) of 16. The upper panel shows the data compared to the background estimate and the lower panel shows the significance of the difference between the two. The most discrepant excess as found by the BumpHunter algorithm is indicated by the vertical blue lines and the  $p$ -value of this excess is printed on the plot.

Next, the SWiFt search phase is applied to the smooth dijet mass spectrum from the fitting control region where the uncertainties are set to be Poisson like, as described in Section 7.5.1. Performing the SWiFt search phase to the smooth dijet mass spectra gives a direct comparison of any fit biases relative to the background fluctuations expected in data. Figure 7.19 shows the SWiFt search phase performed on the smooth dijet mass spectrum taken from the fitting control region, for a SWiFt configuration using the 4 and 5 parameter dijet fit functions and a  $wHW$  of 16 and 10, the full set of plots for all SWiFt configurations considered are in Appendix C. The blue-lines indicate the largest excess found by the BumpHunter algorithm and the  $p$ -value assigned is printed on the plot.

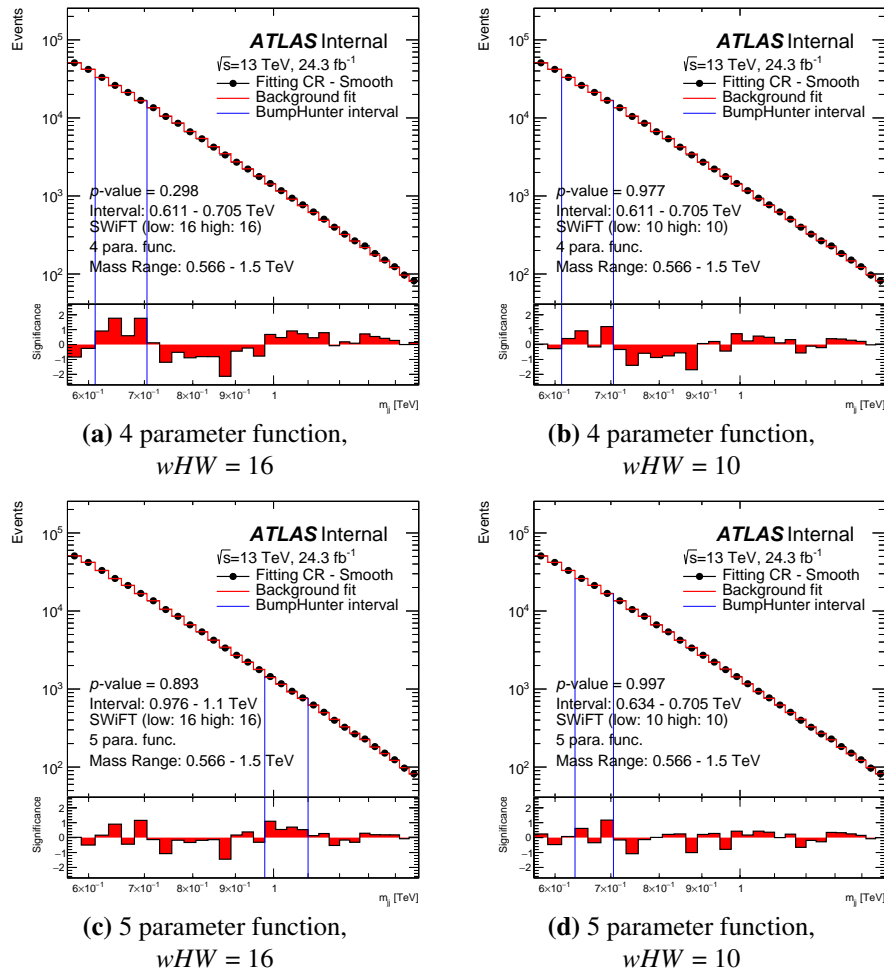


**Figure 7.19:** The SWiFt search phase run on the smooth distribution from the *Full16\_LowMass* fitting control region. The SWiFt procedure has been run for the 4 and 5 parameter dijet fit function for a window half-width ( $wHW$ ) 10 and 16. The upper panel shows the data compared to the background estimate and the lower panel shows the significance of the difference between the two. The most discrepant excess as found by the BumpHunter algorithm is indicated by the vertical blue lines and the  $p$ -value of this excess is printed on the plot.

As was discussed in Section 7.5.2, in the case of the smooth spectrum the BumpHunter  $p$ -value provides an approximate estimation of the size of the largest fit bias relative to the size of the largest excesses expected in data due to statistical fluctuations, therefore a low  $p$ -value is an indication that spurious signal can occur. For the 4 parameter dijet fit function with a window half-width of 16 a BumpHunter  $p$ -value of 0.298 is observed indicating that there is a fit bias which is large relative to the expected statistical fluctuations. It is also notable that for the 4 parameter dijet fit function there is a large deficit observed in the middle of the mass range for both window half-widths shown. In the 5 parameter dijet fit function BumpHunter  $p$ -values of 0.826 and 0.987 are observed in the window half-width of 16 and 10 respectively, which indicates that the largest fit bias is not larger than the size of the excesses expected from statistical fluctuations.

The SWiFt search phase performed on the smooth distribution provides a good visual representation and approximate size of possible fit biases. However, it is possible that fit biases could enhance statistical fluctuations to create spurious signal in data-sets containing Poisson fluctuations. To demonstrate that this is not occurring, the SWiFt search phase is applied to many data-like dijet mass spectra, where Poisson fluctuations are applied to the fitting control region as described in Section 7.5.1. Figure 7.20 shows an example of the SWiFt search phase performed on a data-like dijet mass spectrum taken from the fitting control region. The SWiFt configurations with a window half-width of 16 for the 4 and 5

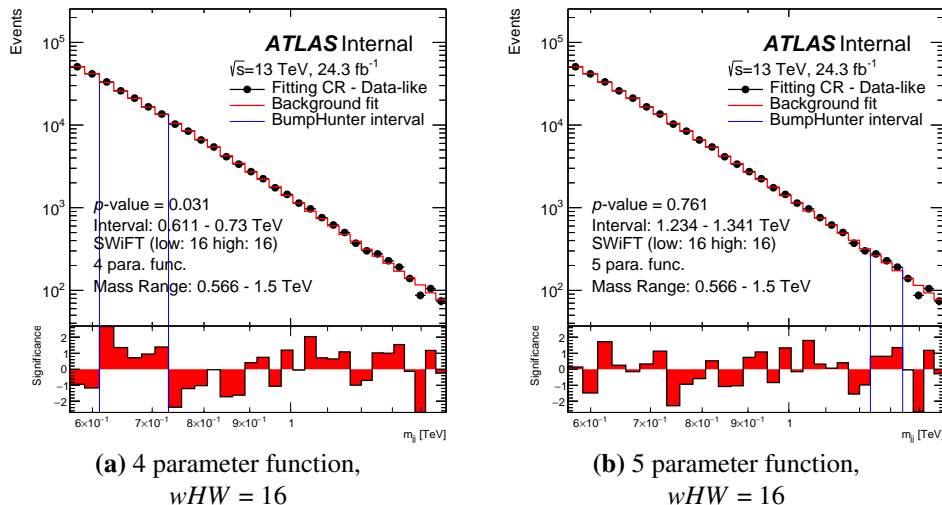


**Figure 7.20:** The SWiFt search phase run on a data-like dijet mass spectrum of the *Full16\_LowMass* fitting control region. The SWiFt procedure has been run for the 4 and 5 parameter dijet fit function for a window half-width ( $wHW$ ) of 16. The upper panel shows the data compared to the background estimate and the lower panel shows the significance of the difference between the two. The most discrepant excess as found by the BumpHunter algorithm is indicated by the vertical blue lines and the  $p$ -value of this excess is printed on the plot.

parameter dijet fit function are shown, the full set can be found in Appendix C. The fit biases noted in Figure 7.19 are still visible in the 4 parameter case. In the 5 parameter case the BumpHunter algorithm has not identified a discrepant excess indicating there is no spurious signal for this particular data-like spectrum.

This process is repeated for 100 data-like dijet mass spectra and the distribution of BumpHunter  $p$ -values is studied to search for evidence of spurious signal. 500 data-like distributions are used in the case of the 5 parameter fit for window half-widths of 14 and 16 as increased statistical precision is required to make the necessary conclusion for these configurations. Each data-like distribution is referred to as a ‘seed’.

Figure 7.21 shows the normalised distribution of  $p$ -values for the ensemble of data-like distributions for a subset of the SWiFt configurations considered, the full range of plots can be found in Appendix C. Table 7.2 shows the percentage of data-like distributions (or seeds) that have a BumpHunter  $p$ -value less than 0.05 and 0.01 for the full range of SWiFt configurations considered; in particular 0.01 is important as it is the threshold for an excess region to be considered significant enough to exclude from the background estimate procedure.

For the 4 parameter dijet fit function and a window half-width of 10, 12 and 14 there is a clear bias towards low BumpHunter  $p$ -values; in particular significantly more than 1% of seeds have a BumpHunter  $p$ -value of less than 0.01. Hence, it is concluded that all SWiFt configurations with the 4 parameter dijet fit function with window half-width greater than 10 show evidence of spurious signal. For the 4 parameter dijet fit function with a window half-width of 10, there is no evidence of spurious signal. However this SWiFt configuration is not used as it is less sensitive to signal than SWiFt configurations using the 5 parameter dijet function with wider windows, as will be shown in Section 7.5.7. In the case of all SWiFt configurations using the 5 parameter dijet fit function there is no significant bias towards low BumpHunter  $p$ -values, specifically the number of seeds with a BumpHunter  $p$ -value of less than 0.01 is consistent with expectations. There is a deficit of seeds with a BumpHunter  $p$ -value  $> 0.9$  for all SWiFt configurations. This is because the dijet mass spectrum of the fitting control region is not perfectly smooth, as there are small statistical fluctuations present in the 0-tag dijet mass spectrum.

Therefore, it is concluded that for SWiFt configurations using the 5 parameter dijet fit function there is no evidence that spurious signal can occur in the window half-widths considered.

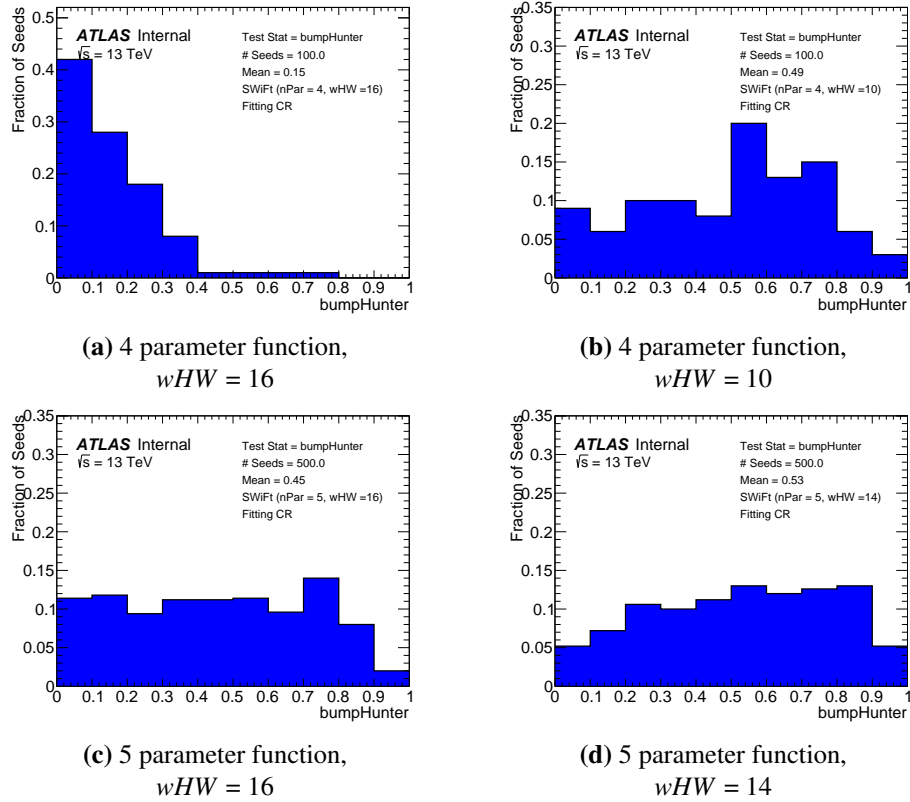


**Figure 7.21:** This figure shows the normalised distribution of BumpHunter  $p$ -values from performing the SWiFt background estimate to an ensemble of data-like distributions taken from the *Full16\_LowMass* fitting control region. This is repeated for the 4 and 5 parameter dijet fit function for a symmetric window with window half-width ( $wHW$ ) range of 10 to 16, giving the 8 different window width and fit function combinations. The number of data-like distributions or seeds is given on the plot.

Dijet Fit Function	$wHW$	Fraction of Seeds with BH $p$ -value <		Number of Seeds
		0.05	0.01	
4 parameter	16	31% (26-35%)	7.0% (4-10%)	100
	14	13% (9-16%)	4.0% (2-6%)	100
	12	10% (7-13%)	4.0% (2-6%)	100
	10	2% (1-4%)	1.0% (0-3%)	100
5 parameter	16	4.0% (3.2-4.9%)	1.2% (0.8-1.8%)	500
	14	2.4% (1.8-3.1%)	0.8% (0.5-1.3%)	500
	12	1% (0-3%)	0.0% (0-1%)	100
	10	2% (1-4%)	1.0% (0-3%)	100

**Table 7.2:** The fraction of data-like distributions (seeds) with a BumpHunter  $p$ -value less 0.1 and 0.05, when the SWiFt search phase with the 4 and 5 parameter dijet fit function and various window half-widths ( $wHW$ ) is performed to an ensemble of data-like distributions taken from the *Full16\_LowMass* fitting control region.  $1\sigma$  confidence interval on the fractions are shown in brackets. The number of seeds used for each SWiFt configuration is shown on the table.

### 7.5.7 SWiFt Validation Studies: Signal Injection

In the previous two subsections it is shown that the SWiFt background estimate procedure is effective in the case that there is no signal. However, it is also required to test the SWiFt search phase in the case that signal is present, to show that signal can be identified and the remaining background estimate is valid.

To identify signal, the SWiFt search phase uses the BumpHunter algorithm to identify the most discrepant excess region and assigns that region a  $p$ -value. If the  $p$ -value is  $< 0.01$  then a exclusion region procedure is used to remove any signal induced fit bias in the background estimation. The exclusion region procedure is as follows.

1. If a discrepant excess is found, define an exclusion region as the excess region identified by the BumpHunter algorithm with an additional  $m_{jj}$  bin added to the low mass side. It has been shown that the additional bin is required to remove signal induced fit bias [2].
2. Re-run SWiFt, ignoring the exclusion region in all fits and fit quality measures.
3. A new excess is found using the new background and the BumpHunter algorithm, the excess can include bins in the exclusion region.
4. If the new excess is not covered by the exclusion region the excess region is then widened and the procedure returns to Step 2. This step ensures that the full effect of the signal induced fit bias is removed.
5. Otherwise, the new background is tested using the fit quality criteria outlined in Section 7.5.4. If the fit quality criteria is passed, the background estimation is used. If the fit quality criteria is failed, then a narrower window is tested.

This process will be illustrated with an example below for clarity.

Signal injected dijet mass spectra are used to validate the SWiFt search phase if signal is present. To create the signal injected spectra, the dijet mass signal templates, described in Section 6.3, are added to the data-like dijet mass spectrum taken from the background-only fitting control region. The dijet mass signal templates of a sequential standard model (SSM)  $Z'$  boson with a simulated mass of 600, 800 and 1000 GeV are used in the following studies. The size of the signal is varied by applying a normalisation factor of 1, 2 or 3 to the simulated signal templates. Therefore the size of signal in these studies is given relative to the nominal simulated cross-section from PYTHIA8; for example ‘xs\*2’ means that a normalisation factor of 2 is used.

In the following section two studies with the signal injected spectra are shown:

### 1. Sensitivity Studies

Studies are performed to show that the SWiFt search phase is sensitive to signal, and to determine which choices of window half-width and fit function are most sensitive. In these studies the SWiFt search phase is applied to the signal injected spectra described above and the BumpHunter  $p$ -values for various SWiFt configurations are studied. A  $p$ -value  $< 0.01$  is considered significant in this study, as in these cases the region exclusion procedure would be applied. For comparing the sensitivity of two SWiFt configurations a comparison of observed BumpHunter  $p$ -values is used, where a lower  $p$ -value indicates a higher sensitivity.

### 2. Robustness of Window Selection Procedure

Studies are performed to show that, if signal is present, the window selection procedure is able to select a window and the SWiFt search phase can create an adequate description of the background. In these studies, the region exclusion and window selection procedure described in the previous paragraph is applied to SWiFt search phases that find a BumpHunter  $p$ -value  $< 0.01$  in the sensitivity study.

As an example let's first consider the  $Z'$  boson with mass of 800 GeV. The SWiFt search phase is performed on a data-like mass spectrum with an injected  $Z'$  boson with mass of 800 GeV and the nominal cross section. Figure 7.22 shows the results of the SWiFt search phase using the 5 parameter dijet fit function and a range of window half-widths of 16 to 10. For all window widths, the BumpHunter algorithm has correctly identified the signal region location and in the case of the window half-width of 14 and 16, has assigned a significant  $p$ -value ( $< 0.01$ ).

Therefore, in the case of the window half-width of 14 and 16 the region exclusion procedure is applied. The region excluded is 705-834 GeV, derived by adding one bin on the low mass side of the excess region identified by the BumpHunter algorithm (730-834 GeV). Figure 7.23 shows the SWiFt search phase performed on the same spectrum when a region exclusion of 705-834 GeV is applied. The new excess found lies within the exclusion region which indicates that any signal induced fit bias has been removed and therefore the exclusion region does not need to be widened.

Figure 7.24 shows the fit quality measures used in the window selection procedure after the region exclusion of 705-834 GeV is applied, for a window half-width of 14 and 16 for the 5 parameter dijet fit function. Only two window half-widths are considered as these are the only windows that had a significant enough  $p$ -value to trigger the region

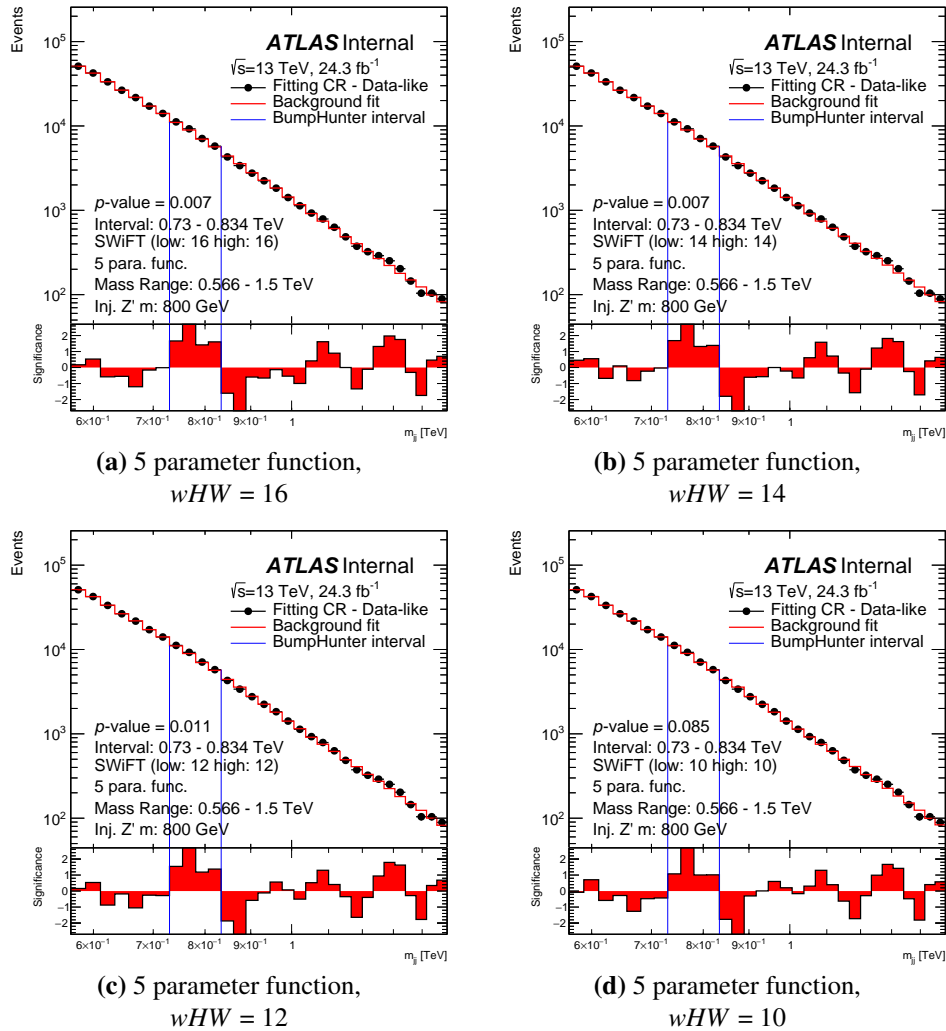


**Figure 7.22:** The SWiFT search phase run on a data-like distribution from the fitting control region with a simulated SSM  $Z'$  boson of mass 800 GeV injected. The SWiFT procedure has been run for the 5 parameter dijet fit function for a window half-width ( $wHW$ ) range of 10 to 16.

exclusion procedure in Figure 7.22. The window selection procedure has chosen the SWiFT background estimate with the 5 parameter dijet fit function and a window half-width of 14.

Hence, it can be concluded that the SWiFT search phase and region exclusion procedure can identify a  $Z'$  boson with a mass of 800 GeV at the nominal cross-section. The BumpHunter  $p$ -value assigned after region exclusion is applied is  $< 0.001$  using 10,000 pseudo-experiments, which shows that the excess has a significance greater than  $3\sigma$ .

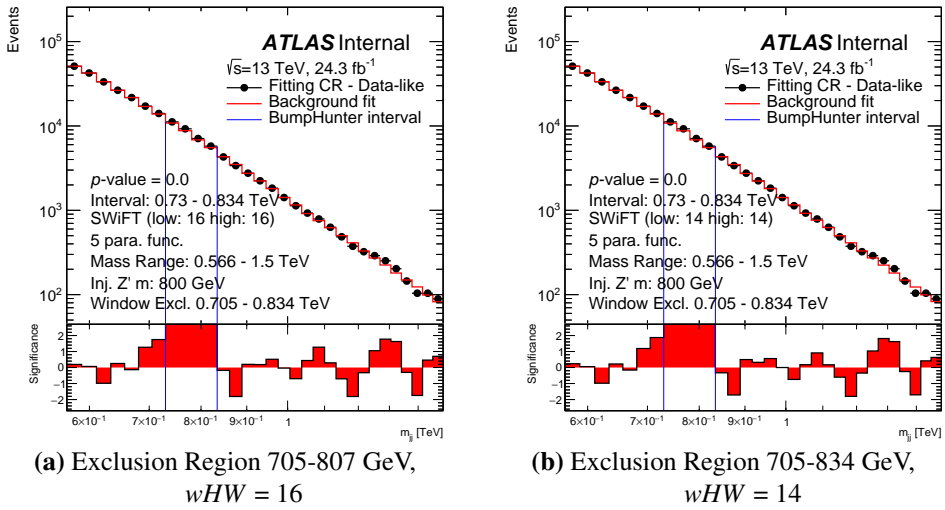


**Figure 7.23:** The SWiFt search phase run on a data-like distribution from the fitting control region with a simulated SSM  $Z'$  boson of mass 800 GeV and the nominal cross-section injected. The SWiFt search phase is run for the 5 parameter dijet fit function for a window half-width ( $wHW$ ) of (a) 16 and (b) 14 with an exclusion region of 705-834 GeV.

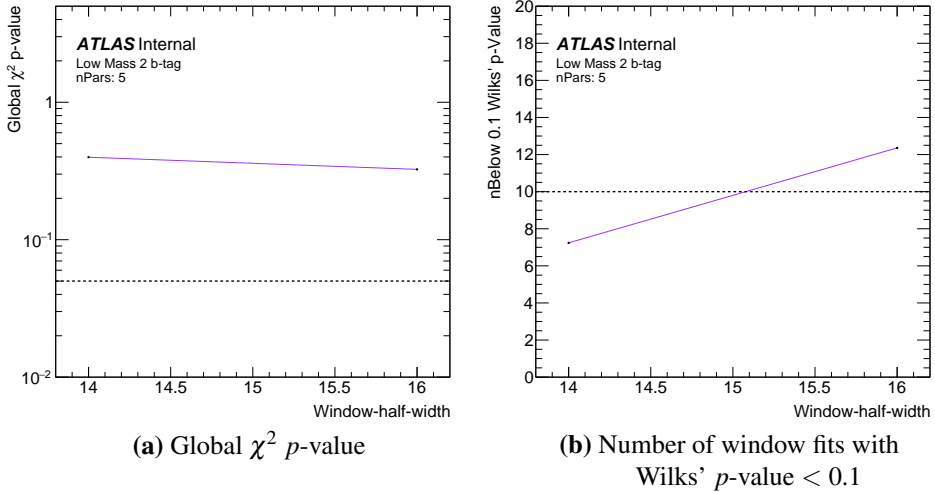


**Figure 7.24:** An illustration of the window selection procedure a data-like distribution when a simulated SSM  $Z'$  boson has been injected of mass 800 GeV with the nominal cross-section, and a region 705-834 GeV of has been excluded from the SWiFt background estimation. It shows the global  $\chi^2$  p-value and number of window fits with Wilks' p-value  $< 0.1$  for SWiFt background estimate, for a range of window half-widths ( $wHW$ ) and the 5 parameter dijet fit function. The procedure would have selected the 5 parameter dijet fit function with a window half-width of 14.

Similar tests are performed for data-like mass spectrum with an injected  $Z'$  bosons with mass of 600, 800 and 1000 GeV. The SWiFt configurations considered use the 4 and 5 parameter dijet fit function and window half-widths ranging from 10 to 16. The 4 parameter dijet fit function is also considered to compare of sensitivity of the two fit functions. Table 7.3 shows the BumpHunter  $p$ -value when performing the SWiFt search phase on each

of the injected spectra for all SWiFt configurations considered, with no region exclusion applied. A dash indicates that the largest excess found by the BumpHunter algorithm is not consistent with the mass of the injected signal. Bold text indicates that the SWiFt configuration has a BumpHunter  $p$ -value  $< 0.01$  and is selected by the window selection procedure after the region exclusion procedure has been applied.

Simulated Mass [GeV]	Signal Norm.	nPars	Window Half-Width			
			10	12	14	16
600	2	4	0.061	0.071	-	-
		5	0.110	0.093	0.104	0.045
	3	4	<0.001	0.001	0.001	0.005
		5	0.003	0.001	0.001	< <b>0.001</b>
800	1	4	0.100	0.069	-	-
		5	0.085	0.011	<b>0.007</b>	0.007
	2	4	<0.001	<0.001	<0.001	<0.001
		5	< <b>0.001</b>	<0.001	<0.001	<0.001
1000	1	4	0.120	0.112	0.098	0.074
		5	-	-	0.107	0.093
	2	4	<0.001	<0.001	<0.001	<0.001
		5	<0.001	<0.001	<0.001	<b>0.001</b>

**Table 7.3:** The BumpHunter  $p$ -value when performing the SWiFt search phase with no region exclusion applied on a data-like spectrum that has been injected with a sequential standard model  $Z'$  with a variety of simulated masses when the cross-section has been multiplied by a normalisation factor 1, 2 or 3 (Signal Norm.). The SWiFt search phase has been performed using a window half-width range of 10 to 16 and the number of parameters used in the dijet fit function (nPars) are 4 or 5. A dash indicates that the largest excess found by BumpHunter algorithm is not consistent with the simulated mass of the injected signal. Bold text indicates that the SWiFt configuration has a BumpHunter  $p$ -value  $< 0.01$  and is selected by the window selection procedure after the region exclusion procedure has been applied.

There are a few conclusions that are taken from Table 7.3. Firstly, all SWiFt configurations are able to obtain a BumpHunter  $p$ -value  $< 0.01$  if the cross-section is high enough. At 800 GeV the cross-section required is that of the nominal Monte-Carlo, whilst for the 600 and 1000 GeV points the cross-section needs to be increased to 3 and 2 times respectively. For the  $Z'$  boson at 600 GeV, a large cross-section is required indicating that there is a signal induced fit bias in this case; this is due to the fact that it is at the low mass edge of the dijet mass spectrum meaning there is no side-band to constrain the background estimate at a dijet mass of 600 GeV. Secondly, for all signals considered that trigger the region exclusion procedure a window width can be selected. This shows that region exclusion and window selection procedure is robust in the case that signal is present. Thirdly, by comparing BumpHunter  $p$ -values for identical injected signals across SWiFt configurations, it can be seen that SWiFt configurations that use large window-half-widths are more sensitive.

Finally, for both the 800 and 1000 GeV SSM  $Z'$  boson, the SWiFt search phase with a 4 parameter dijet function and window half-width of 10 is less sensitive than the SWiFt search phase with a 5 parameter dijet fit function and a window half-width of 16. The final two conclusions are important factors in the development of the window selection procedure, described in Section 7.5.4.

It should also be noted that all BumpHunter  $p$ -values shown in Table 7.3 are before region exclusion is applied. The BumpHunter  $p$ -values are always smaller after region exclusion is applied as the effect of any signal induced fit bias in the background estimation has been removed; this has been shown in the case of the  $Z'$  boson of mass of 800 GeV.

To conclude the search phase validation studies for the *Full16\_LowMass* data-set analysis, it has been shown the SWiFt search phase is able to provide an adequate background estimation and that there is no evidence that spurious signal can occur. It is has also been shown that the SWiFt search phase is able to identify  $Z'$  boson with a mass of 600, 800 and 1000 GeV if the cross-section is large enough and still provide an adequate description of the background.

### 7.5.8 Results of Window Width Selection Procedure

For the full *Full16\_LowMass* data-set a window half-width is chosen using the window selection procedure outlined in Section 7.5.4. The SWiFt background estimation is performed using the 5 parameter dijet fit function and a window half-width range of 16 to 10.

For each SWiFt configuration, Figure 7.25 shows the two fit quality measures used in the window selection procedure, the global  $\chi^2$   $p$ -value and the number of windows with a Wilks'  $p$ -value  $< 0.1$ . The requirements placed on each fit quality measure by the window selection procedure are indicated by dotted lines on the figure. A window half-width of 16 is selected as it is the widest window that passes the fit quality criteria.

Figure 7.26 shows the Wilks'  $p$ -value and  $\chi^2$   $p$ -value for fits in each of the windows as a function of the window centre for the SWiFt background estimation using the 5 parameter dijet fit function and a window half-width of 16, further showing that all fits used in the SWiFt background estimation are of good quality.

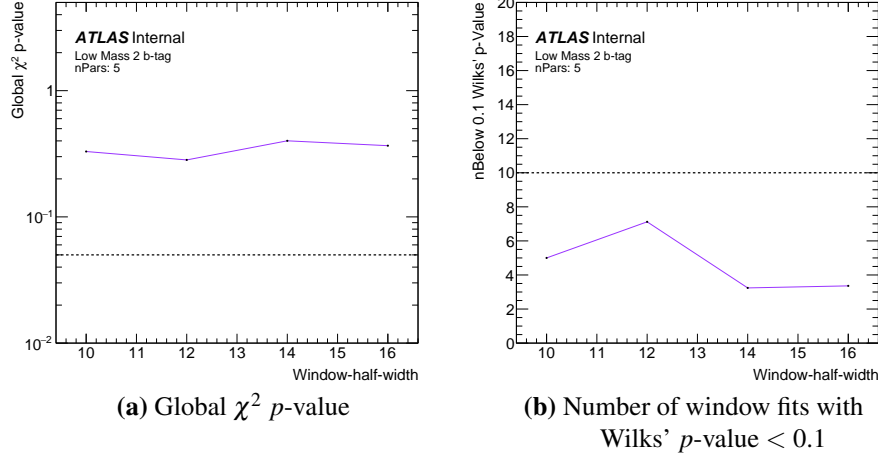


**Figure 7.25:** An illustration of the window selection procedure for the full *Full16\_LowMass* data-set. It shows the global  $\chi^2$  p-value and number of window fits with Wilks' p-value  $< 0.1$  for the SWiFt background estimate using a range of window half-widths ( $wHW$ ) and the 5 parameter dijet fit function. The dotted lines indicate the requirements used in the window selection procedure. A window half-width of 16 is selected.

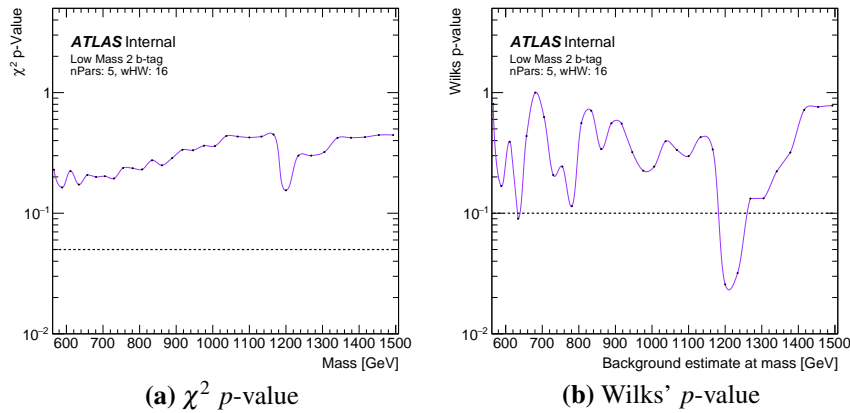


**Figure 7.26:** The  $\chi^2$  p-value and Wilks' p-value for each window fit in the SWiFt background estimate performed on the full *Full16\_LowMass* data-set, shown as a function of the window centre. The 5 parameter dijet fit function with a window half-width of 16 is used as the SWiFt configuration. The dotted lines indicate thresholds that are used in the window selection procedure.

### 7.5.9 Search Phase Results

Figure 7.27 shows the dijet mass spectrum of the full *Full16\_LowMass* data-set and the SWiFt background estimation created using the 5 parameter dijet fit function and a window half-width of 16. The BumpHunter algorithm has identified the most discrepant excess, indicated in the figure using vertical blue lines, and assigned the excess a  $p$ -value of 0.603, which has been calculated using 10,000 pseudo-experiments.

The observed BumpHunter  $p$ -value shows that no significant excess is observed. Therefore it is concluded that there is no evidence of a BSM resonance in the *Full16\_LowMass* data-set. As no significant excess is found, the *Full16\_LowMass* data-set is used to set limits on the benchmark signal models, which will be described in the proceeding Chapter.

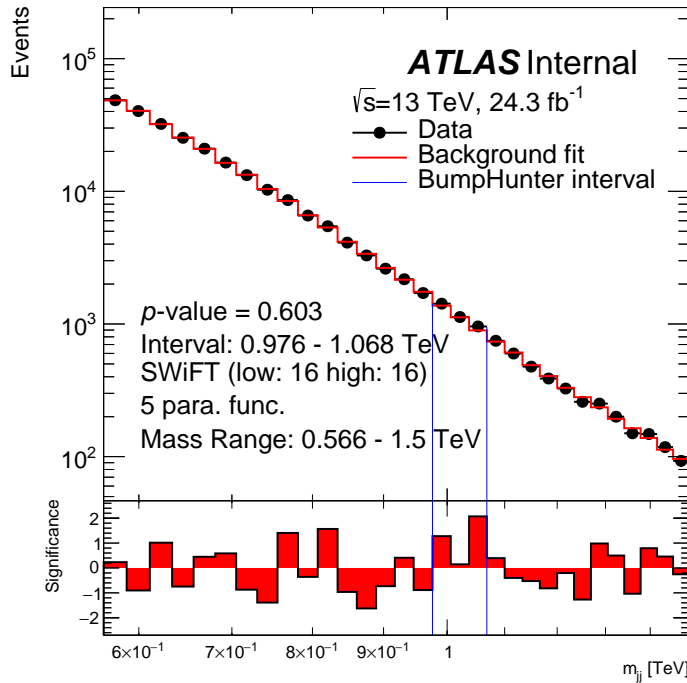


**Figure 7.27:** The dijet mass spectrum ( $m_{jj}$ ) of the *Full16\_LowMass* data-set and the SWiFt background estimation created using the 5 parameter dijet fit function and a window half-width ( $wHW$ ) of 16. The upper panel shows the data compared to the background estimate and the lower panel shows the significance of the difference between the two. The most discrepant excess found by the BumpHunter algorithm is indicated by the vertical blue lines and the  $p$ -value of this excess is printed on the plot.

## Chapter 8

# Di-*b*-jet Search: Limit Setting Phase

In Chapter 7 it was shown that there is no evidence of new physics in the dijet mass spectra of the observed di-*b*-jet events <sup>1</sup>. However, it is also useful to quantify what this result means in the context of the signal models that are being searched for. Specifically, one can estimate the degree of belief that a signal model is true given the di-*b*-jet events that have been observed. If the degree of belief of a specific model is less than a certain threshold it is concluded that this model is excluded. This process is known as the limit setting phase.

In this Chapter, Section 8.1 will describe the limit setting methodology and Section 8.2 will discuss the systematic uncertainties considered. Then Sections 8.3 and 8.4 present the details and the results of the limit setting phase for the *Summer16\_HighMass* and *Full16\_LowMass* data-sets respectively.

### 8.1 Limit Setting Methodology

In this analysis a Bayesian limit setting approach is used [108]. To set a limit on a particular model, one considers the hypothesis that the di-*b*-jet events are produced by a combination of the QCD background and the new physics process. A background template is produced using the estimation procedures described in the previous chapter and the BSM physics model is described by a dijet mass signal template, normalised such that  $\mu$  di-*b*-jet events <sup>1</sup> are produced. This signal plus background hypothesis is denoted by the symbol  $H_\mu$ .

Now let us consider this hypothesis in the context of the data, denoted by  $D$ , which in this case is one of the observed dijet mass spectra. For the hypothesis,  $H_\mu$ , the probability of producing the data is known as the likelihood. In each dijet mass bin, labelled by the index  $i$ , the hypothesis  $H_\mu$  predicts  $s_i(\mu)$  signal events,  $b_i$  background events and  $n_i$  events were

---

<sup>1</sup>Defined as events that pass the di-*b*-jet event selection

observed in data. Therefore, by only considering statistical uncertainties, the likelihood for a given value of  $\mu$  can be calculated using Poisson probabilities:

$$\mathcal{L}(\mu, D) = P(D | \mu) = \prod_i \left( \frac{(s_i(\mu) + b_i)^{n_i} e^{-(s_i(\mu) + b_i)}}{n_i!} \right) \quad (8.1)$$

where the product is over all dijet mass bins and the notation  $P(A | B)$  represents the probability of event  $A$  occurring under the assumption of  $B$ .

Then, one can employ Bayes' theorem which states that

$$P(A | B) = \frac{P(B | A) P(A)}{P(B)} \quad (8.2)$$

to obtain the probability density function of  $\mu$  given the observed dijet mass spectrum,

$$P(\mu | D) = \frac{P(D | \mu) \Pi(\mu)}{\Pi(D)} \quad (8.3)$$

This quantity, known as the posterior, is an expression of the degree of belief in the hypothesis  $H_\mu$  for any particular value of  $\mu$ . The  $\Pi(\mu)$  term in the posterior is called the signal prior and gives the probability density of  $\mu$  before the experiment took place. A prior flat with respect to  $\mu$  is chosen<sup>2</sup> which represents ignorance to the size of the signal. The  $\Pi(D)$  term does not depend on  $\mu$  and as such can be considered as a normalisation term.

To accurately represent a true degree of belief in a model one must consider the systematic uncertainties in the values of  $b_i$  and  $s_i$  in Equation 8.1. The sources of systematic uncertainty considered in this analysis are listed in Section 8.2. The systematic uncertainties are incorporated by explicitly considering  $s_i$  and  $b_i$  as a function of the parameters which are considered as sources of systematic uncertainty, the parameters used are known as nuisance parameters. For example, the number of signal events in a dijet mass bin,  $s_i$ , is linearly dependant on luminosity ( $L$ ) such that  $s_i(L) \propto L$ . Luminosity is a source of systematic uncertainty, so is an example of a nuisance parameter.

Therefore the likelihood becomes a function of the nuisance parameters

$$\mathcal{L}(\mu, D, \vec{\theta}) = P(D | \mu, \vec{\theta}) = \prod_i \left( \frac{[s_i(\mu, \vec{\theta}) + b_i(\vec{\theta})]^{n_i} e^{-[s_i(\mu, \vec{\theta}) + b_i(\vec{\theta})]}]}{n_i!} \right) \quad (8.4)$$

where  $\vec{\theta}$  represents the set of nuisance parameters.

A prior probability is introduced for each of the nuisance parameters, given by  $\Pi(\vec{\theta})$ ,

---

<sup>2</sup>Flat from  $\mu = 0$  to the value of  $\mu$  where the likelihood has fallen to  $10^{-5}$  of the optimal likelihood value.

that describes systematic uncertainty on each of the nuisance parameters. Then, by integrating over the nuisance parameters, one obtains the posterior for  $\mu$  that accounts for systematic uncertainties

$$P(\mu | D) \propto \int d\vec{\theta} \mathcal{L}(\mu, D, \vec{\theta}) \Pi(\mu) \Pi(\vec{\theta}) \quad (8.5)$$

One can calculate the likelihoods for the data, perform the integral over nuisance parameters and then normalise to calculate the probability density of  $\mu$ <sup>3</sup>.

Using the posterior calculated from Equation 8.5, the 95% credibility level upper limit of  $\mu$ , denoted by  $\mu_{\text{up}}$ , is calculated using the expression

$$\int_0^{\mu_{\text{up}}} P(\mu | D) = 0.95 \quad (8.6)$$

There is a 95% probability that the parameter  $\mu$  lies within the credibility interval defined as  $0 \leq \mu < \mu_{\text{up}}$ . Therefore, any model under the hypothesis  $H_\mu$  that predicts a  $\mu$  value above the upper limit,  $\mu_{\text{up}}$ , is excluded at the 95% credibility level.

In the di- $b$ -jet analysis limits are set on the benchmark models for a range of simulated mass points, the dijet mass signal templates used are described in Section 6.3. Upper limits are set on the product of cross-section, detector acceptance and tagging efficiency,  $\sigma \times A \times \epsilon$ , which is related to the parameter  $\mu$  used in the limit setting description<sup>4</sup>.  $A$  and  $\epsilon$  have been measured in Section 6.4.5 for the benchmark signal models.

Further to this many BSM models predicting a narrow resonance not explicitly considered by this analysis can be approximated by a Gaussian distribution, if low-mass off-shell tails and non-perturbative effects are neglected. Therefore, limits are also set on a signal template with a Gaussian shape, which can be reinterpreted for a wider range of models.

The di- $b$ -jet analysis will present two limits. The first is the observed limit, which is set using the observed dijet mass spectra, as described above. The second is the expected limit, which is the upper limit that would be set if there is no signal present in the dijet mass spectrum; the expected limit represents the sensitivity of the limit setting phase. To calculate the expected limit, the limit setting phase is performed on pseudo-experiments created by varying the background estimate within the systematic uncertainties. This process is done for many pseudo-experiments; the median upper limit found gives the expected limit and

<sup>3</sup>This integral is performed using a Markov chain Monte-Carlo using the Bayesian Analysis Toolkit. Full details on the implementation can be found here [22].

<sup>4</sup>Specifically  $\mu = L \times \sigma \times A \times \epsilon$ , where  $L$  is the luminosity.

the 68% and 95% percentiles give the 1 and 2  $\sigma$  uncertainty bands on the expected limit.

In this analysis the Bayesian approach for limit setting is used, while there is a widely used alternative known as the frequentist approach [109]. The Bayesian approach defines a credibility interval using the probability (or degree of belief) in a hypothesis given the observed data ( $P(\mu | D)$ ). On the other hand, the frequentist approach calculates the probability (or fraction of trials) of obtaining the data assuming a given signal model is true ( $P(D | \mu)$ ) and rejects models that produce a low probability. Both approaches are valid and logically consistent, but it is important that one states clearly which approach is being taken<sup>5</sup>.

## 8.2 Description of Systematic Uncertainties

The sources of systematic uncertainty in the di- $b$ -jet analysis are grouped into two categories. The first group are uncertainties on the dijet mass signal templates used in the limit setting phase, which are produced using Monte-Carlo simulations.

The signal systematic uncertainties considered are:

- **Jet Energy Scale, Jet Energy Resolution and  $b$ -Jet Energy Scale (Signal):**

Jet energy scale (JES), jet energy resolution (JER) and  $b$ -jet energy scale ( $b$ JES) uncertainties represent uncertainties in the energy measurement of a  $b$ -jet. The JES and JER uncertainties used in this analysis were described in Section 4.2.4. The ( $b$ JES) uncertainty used in this analysis has been described in Section 4.3.5. The uncertainties on the jet energy measurement cause an uncertainty on the width of the dijet mass signal templates.

- **$b$ -Tagging (Signal):**

The modelling of  $b$ -tagging in Monte-Carlo simulation is calibrated to data using measured  $b$ -tagging scale factors, the scale factors and associated uncertainties are discussed in Section 4.3.4. The uncertainty on the  $b$ -tagging scale factors cause an uncertainty on the normalisation of each bin in the dijet mass signal template.

- **$b$ -Jet Trigger (Signal) - *Full16\_LowMass* data-set only:**

Similarly, when using the  $b$ -jet trigger, the modelling of the online  $b$ -tagging efficiency in simulation is corrected to data using  $b$ -jet trigger scale factors. The  $b$ -jet trigger scale factors and relevant uncertainties are derived in Section 5.3. The uncertainty on the  $b$ -jet trigger scale factors cause an uncertainty on the normalisation of each point in the dijet mass signal template. This systematic uncertainty is only used in the *Full16\_LowMass* data-set, as this is the only data-set using a  $b$ -jet trigger.

---

<sup>5</sup>As a side note the BumpHunter  $p$ -value uses the frequentist approach to calculate a  $p$ -value.

- **Luminosity (Signal):**

The luminosity uncertainty is determined using the methodology outlined in [110]. The luminosity uncertainties used are 2.9% in the *Summer16\_HighMass* data-set and 2.2% in the *Full16\_LowMass* data-set. The uncertainty on luminosity causes an uncertainty on the normalisation of the dijet mass signal template.

- **Parton Distribution Functions (PDFs) (Signal):**

The PDFs are important in calculating the cross-section of any process at the LHC. As shown in Section 2.2.3.2 there are uncertainties on the measurements of the PDFs which cause an uncertainty on the dijet mass signal template used. A flat 1% uncertainty on the normalisation of the dijet mass signal templates is applied, which has been found at previous dijet searches to conservatively cover the effect of the PDF uncertainties [2].

The second group are systematic uncertainties on the background estimation. As the background estimate is data-driven, the set of uncertainties related to modelling in simulation are not required.

The uncertainties on the background estimation model are:

- **Fit Function Parameters (Background):**

The choice of fit parameters is made by maximising the likelihood of the fit function with respect to our data-set. However, due to the statistical fluctuations in data the optimal parameters to describe the true background shape may not have been chosen. To estimate the uncertainty on the choice of parameters, the background estimation procedure is performed on pseudo-experiments created by applying Poisson fluctuations to the nominal background estimate. The root mean square (rms) of the difference between the nominal background estimate and those from the pseudo-experiments is taken as a symmetric uncertainty.

- **Fit Function Choice (Background):**

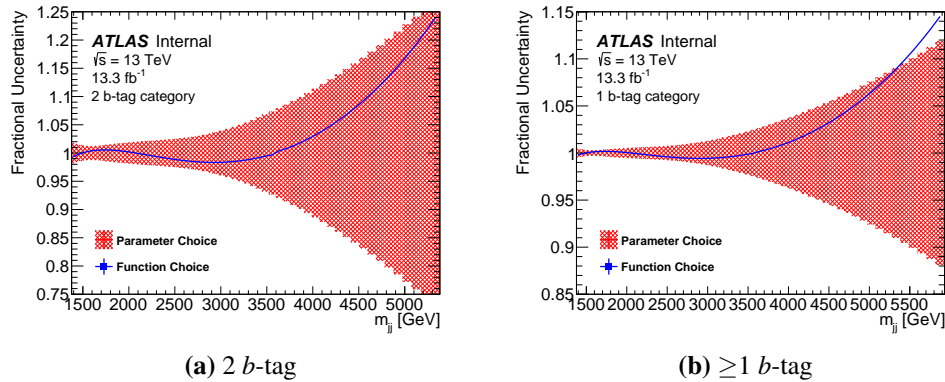
A different background estimation can be obtained if a different fit function is chosen. To obtain an uncertainty on the choice of fit function an alternate function is considered, which is the dijet fit function with one extra degree of freedom than the nominal function. The alternate function is then used to fit to the pseudo-experiments described in the previous bullet point. The mean of the difference between the nominal and alternate functions is taken as a one-sided uncertainty.

### 8.3 Summer16\_HighMass Data-set Limits

Table 8.1 summarises the systematic uncertainties on the signal templates used in the *Summer16\_HighMass* data-set at three different dijet masses. Figure 8.1 shows the systematic uncertainties on the background estimate for both  $b$ -tagging categories as a function of dijet mass.

Dijet Mass	Signal Systematic Uncertainties					
	JES	JER	$b$ JES	$b$ -Tagging ( $\geq 1 / 2$ )	PDF	Lumi
1.5 TeV	1.2%	1.0%	2.2%	20% / 10%	1%	2.9%
3 TeV	1.4%	0.7%	0.7%	50% / 60%	1%	2.9%
5 TeV	2.3%	0.3%	0.3%	50% / 70%	1%	2.9%

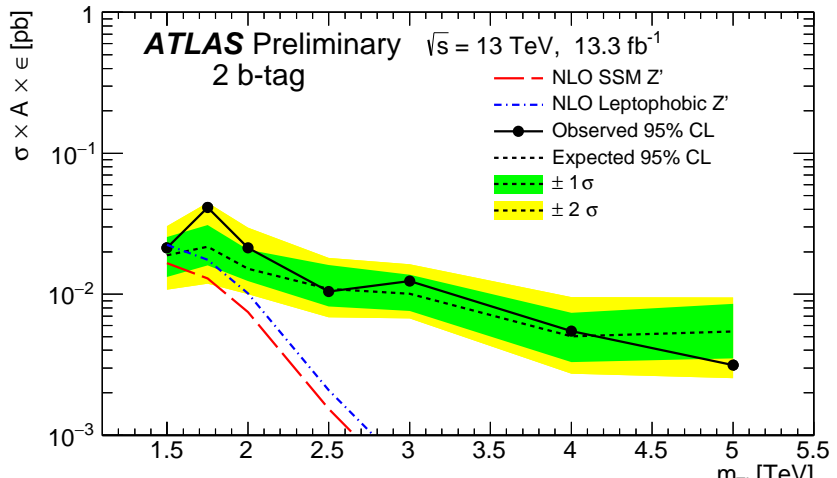
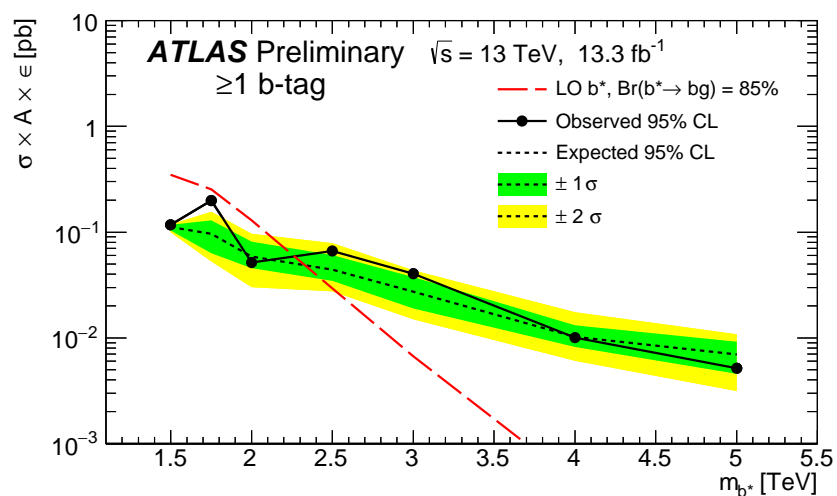
**Table 8.1:** A table summarising the signal systematic uncertainties used in the *Summer16+15* data-set. Jet Energy Scale (JES), Jet Energy Resolution (JER) and  $b$ -Jet Energy Scale ( $b$ JES) are uncertainties on the dijet mass of a simulated event, whilst  $b$ -tagging, PDF and luminosity are uncertainties on simulated event weight. Values taken from [10].



**Figure 8.1:** The fractional background systematic uncertainties for the (a) 2 and (b)  $\geq 1$   $b$ -tag categories as a function of dijet mass,  $m_{jj}$ , for the *Summer16+15* data-set analysis. The red shaded region shows the function parameter uncertainty and the blue line shows the function choice uncertainty.

Figure 8.2 shows the 95% credibility level upper limits set on  $\sigma \times A \times \epsilon$  as a function of simulated mass for the  $Z'$  boson and  $b^*$  quark. The observed limit, the expected limit and the 1 and 2  $\sigma$  uncertainty bands on the expected limit are shown. The  $\geq 1$   $b$ -tag category is used for the  $b^*$  quark model and the 2  $b$ -tag category is used for the  $Z'$  boson models. Overlaid are theoretical predictions of  $\sigma \times A \times \epsilon$  for the benchmark models described in Section 6.3.

The observed and expected limits decrease with increasing simulated mass due to reduced number of background events at higher mass. The theoretical  $\sigma \times A \times \epsilon$  predictions decrease rapidly as mass increases, due to a combination of lower signal acceptance times

(a)  $Z'$  boson, 2  $b$ -tag(b)  $b^*$  quark,  $\geq 1$   $b$ -tag

**Figure 8.2:** 95% credibility level upper limits on cross-section times acceptance times tagging efficiency for the (a)  $Z'$  boson and (b)  $b^*$  quark as a function of simulated mass using the *Summer16+15* data-set in the 2 and  $\geq 1$   $b$ -tag category respectively. The observed limit is shown by the solid black line, the expected limit is shown by the dotted black line and the 1 and 2  $\sigma$  uncertainty bands on the expected limit are shown by the green and yellow bands. The theoretical prediction of  $\sigma \times A \times \epsilon$  for the Sequential Standard Model (SSM) and leptophobic  $Z'$  boson and the  $b^*$  quark are overlaid [10].

efficiency at high mass, as shown in Figures 6.9, and a smaller signal cross-section at high mass. The signal cross-section is smaller at high mass because of PDF and matrix element effects, similar to those that caused a smaller QCD dijet production at high mass as described in Section 2.2.3.3. **Q for AK: Do I need this para?**

In the mass regions where the theoretical prediction of  $\sigma \times A \times \epsilon$  is larger than the upper limit, it can be concluded that the model is excluded at the 95% credibility level. Using the

*Summer16\_HighMass* data-set: the  $b^*$  quark is excluded in the mass range of 1.4 - 2.3 TeV, the SSM  $Z'$  boson cannot be excluded, and the leptophobic  $Z'$  boson is excluded at a mass of 1.5 TeV.

To produce generic Gaussian limits, a signal template with a Gaussian shape in dijet mass is used. The Gaussian shapes are centred on a range of masses and the width of the considered Gaussians are 15%, 10% and 7% of the simulated mass in addition to a Gaussian with the width of the detector mass resolution. The detector mass resolution has been estimated at previous dijet searches [2] and varies from 3% at 1.5 TeV to 2% at 5 TeV. The sources of the systematic uncertainty considered for the Gaussian limits are the luminosity uncertainty, the background modelling uncertainties, and a 10% flat uncertainty to account sources for experimental uncertainties related to signal modelling, such as jet-energy scale.

Figure 8.3 shows the observed 95% credibility upper limits on the product of cross-section, detector acceptance, tagging efficiency and branching ratio,  $\sigma \times A \times \epsilon \times BR$ , for the full range of Gaussian signals described above in both  $b$ -tagging categories. For the *Summer16\_HighMass* data-set analysis an upper limit is set on a generic Gaussian signal ranging from 0.2 to 0.001 pb in the mass range 1.4 to 6 TeV.

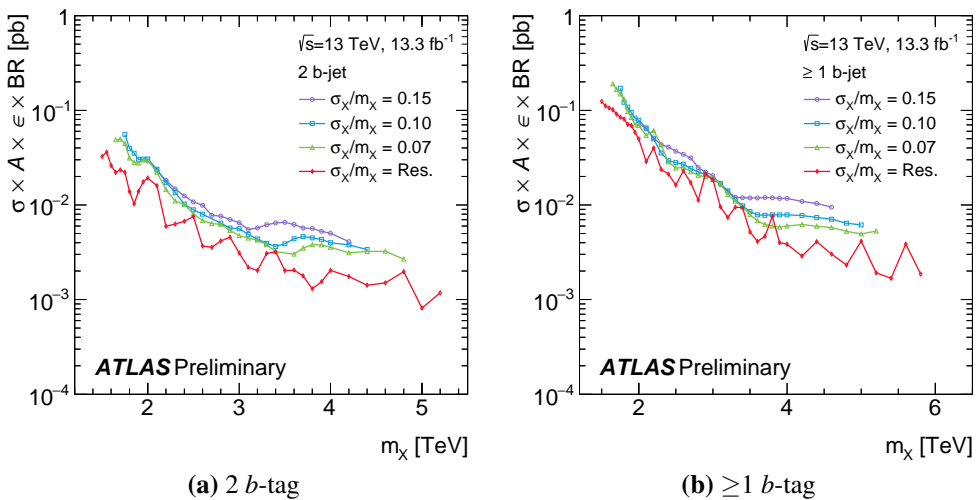


**Figure 8.3:** 95% credibility observed upper limits on the product of cross-section, detector acceptance, tagging efficiency and branching ratio,  $\sigma \times A \times \epsilon \times BR$ , for Gaussian signals for both  $b$ -tagging categories using the *Summer16+15* data-set. The signal templates are Gaussian in dijet mass with widths of 15%, 10% and 7% of the simulated mass in addition to a Gaussian with the width of the detector mass resolution [10].

## 8.4 Full16\_LowMass Data-set Limits

### 8.4.1 Signal Morphing

The limit setting phase requires dijet mass signal templates as an input. For the *Full16\_LowMass* data-set analysis, simulated dijet mass signal templates of the SSM  $Z'$  boson are created at simulated mass points of 600, 800, 1000 and 1250 GeV, as described in Section 6.3. To obtain dijet mass signal templates for intermediate points a signal morphing technique is used, first implemented in an inclusive dijet search at ATLAS [3].

A ‘Gaussian + reverse Landau’ fit is performed to the simulated dijet mass signal templates. The reverse Landau function is the transformation of the Landau function [111] under  $x \rightarrow -x$ . The Gaussian + reverse Landau fit function is therefore defined as:

$$f(x) = p_0 [p_3 \text{Gauss}(x, p_1, p_2) + (1 - p_3) \text{Landau}(-x, p_4, p_5)] \quad (8.7)$$

The Gaussian distribution models the convolution of a Breit-Wigner resonance distribution and mass resolution effects. The reverse Landau distribution provides a description of the off-shell contributions to the dijet mass signal templates which are enhanced at low mass by PDF effects.

The parameters of the Gaussian + reverse Landau fits are interpolated to produce dijet mass signal templates at intermediary simulated mass points in the range 600 to 1250 GeV with a separation of 50 GeV<sup>6</sup>. Figure 8.4 shows the simulated SSM  $Z'$  boson dijet mass sig-

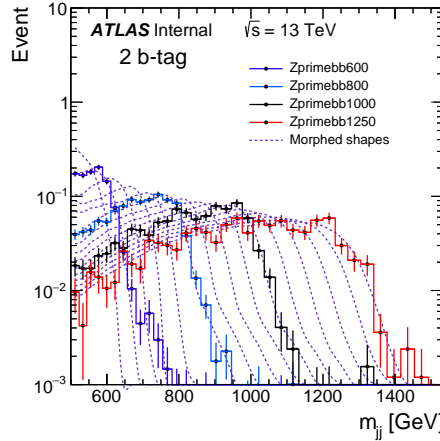


**Figure 8.4:** Simulated SSM  $Z'$  boson dijet mass ( $m_{jj}$ ) signal templates (solid points lines) at simulated mass points of 600, 800, 1000 and 1250 GeV and the dijet mass signal templates created using the signal morphing technique (dotted lines) used in the *Full16\_LowMass* data-set limit setting phase [13].

---

<sup>6</sup>Explicitly morphed signal templates are created at simulated mass points of 650, 700, 750, 850, 900, 950, 1050, 1100, 1150 and 1200 GeV.

nal templates and the intermediate dijet mass signal templates produced using the morphing procedure. The simulated and morphed signal dijet mass spectra are used as signal templates in the limit setting phase for the *Full16\_LowMass* data-set analysis.

### 8.4.2 Summary of Systematic Uncertainties

Table 8.2 summarises the systematic uncertainties considered for the signal templates used in the *Full16\_LowMass* data-set at three different dijet masses ( $m_{jj}$ ). Figure 8.5(a) shows the total  $b$ -jet trigger systematic uncertainty as a function of dijet mass; this includes both the jet-level and event-level uncertainties described in Section 5.3. Figure 8.5(b) shows the systematic uncertainties on the background estimate as a function of dijet mass.

$m_{jj}$	Signal Systematic Uncertainties						
	JES	JER	$b$ JES	$b$ -Tagging	$b$ -Jet Trigger	PDF	Lumi
0.5 TeV	0.9%	1.4%	5%	5%	5.4%	1%	2.2%
1.0 TeV	0.8%	1.2%	3%	7%	15%	1%	2.2%
1.5 TeV	1.1%	1.0%	1.8%	10%	29%	1%	2.2%

**Table 8.2:** A table summarising the signal systematic uncertainties used in the *Full16\_LowMass* data-set for three different dijet mass ( $m_{jj}$ ) points. Jet Energy Scale (JES), Jet Energy Resolution (JER) and  $b$ -jet Energy Scale ( $b$ JES) are uncertainties on the dijet mass of a simulated event, whilst  $b$ -tagging,  $b$ -jet trigger, PDF and luminosity uncertainties are uncertainties on simulated event weight. All values except  $b$ -jet the trigger uncertainty taken from [13]

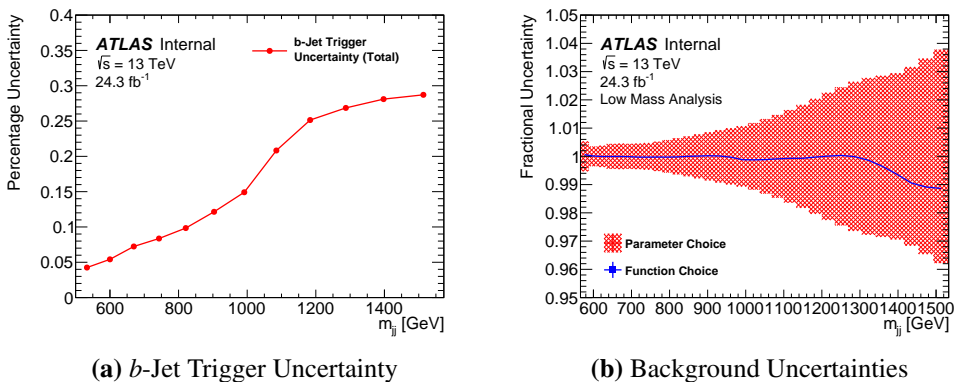


**Figure 8.5:** Panel (a) shows the total  $b$ -jet trigger systematic uncertainty as a fraction for the *Full16\_LowMass* data-set as a function of dijet mass ( $m_{jj}$ ). Panel (b) shows the background systematic uncertainties as a fraction for the *Full16\_LowMass* data-set as a function of dijet mass. The red shaded region shows the function parameter uncertainty and the blue line shows the function choice uncertainty.

### 8.4.3 Signal Subtracted Background Estimation

Section 7.5.3 described the SWiFt background estimation procedure used for the *Full16\_LowMass* data-set, for clarity this will be referred to as the nominal SWiFt background estimation in this section. The nominal SWiFt background estimation is model independent meaning that there is no assumption of any signal models in the procedure. In Section 7.5.7 it was found that there is a signal induced fit bias present when the nominal SWiFt background estimation is performed on a background-only test data-set with a SSM  $Z'$  boson injected. This was particularly notable for a SSM  $Z'$  boson with a simulated mass of 600 GeV, as this is near the edge of the dijet mass spectrum considered.

To remove any signal induced fit bias in the limit setting phase a Signal Subtracted Background (SSB) estimation is created for each simulated mass point considered, this technique has been used in a previous inclusive dijet search at ATLAS [3]. The signal subtracted background estimate is created by performing two fits; the first is a signal plus background fit, performed in the SWiFt window in which the simulated mass of the signal being considered is at the window centre. The signal is modelled using the dijet mass signal templates described in Section 8.4.1 and the background is modelled using the 5 parameter dijet fit function. The normalisation of the signal template and the parameters of the background function are chosen to maximise the likelihood (defined in Eqn. 8.1), the signal normalisation is required to be greater or equal to zero. The signal template, normalised by the signal plus background fit, is then subtracted from the data. Finally, the SWiFt background estimation procedure is performed to the signal subtracted data using the 5 parameter dijet fit function and a window half-width of 16, the same SWiFt configuration used in the search phase results shown in Section 7.5.9. This second background estimation is called the signal subtracted background estimation and is used as the background template in the limit setting phase. A signal subtracted background estimation is created for each simulated mass point.

To demonstrate that the signal subtracted background estimation will remove the signal induced fit bias, the procedure is performed to a data-like dijet mass spectrum from the fitting control region when SSM  $Z'$  boson dijet mass signal templates are injected. The same distributions were used in the signal injection studies presented in Section 7.5.7. The performance of the signal subtracted background estimation can be compared to that of the nominal SWiFt background estimation.

In Figure 8.6(a) the signal subtracted background (blue) and nominal SWiFt background (red) estimations for a data-like dijet mass spectrum from the fitting control region with a SSM  $Z'$  boson injected at 600 GeV are shown as a ratio to the nominal SWiFt back-

ground estimation for the same data-like dijet mass spectrum when no signal is injected (black). This ratio is used to clearly show any fit biases caused by the injected signal. The signal injected dijet mass spectrum is shown by the green points and the grey area represents the statistical uncertainty of the data. Figure 8.6(b) shows the same comparison using a SSM  $Z'$  boson injected at 1000 GeV. These two mass points are shown as the signal injection studies, presented in Section 7.5.7, found that the search phase would not produce a significant observation of a SSM  $Z'$  boson at these simulated mass points.

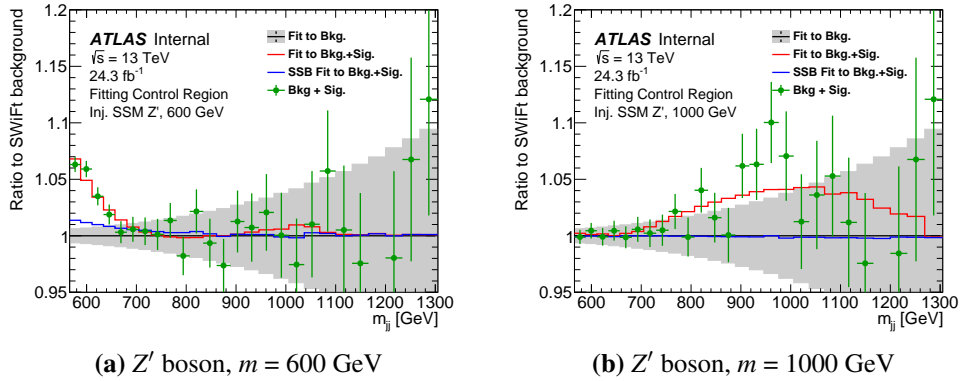


**Figure 8.6:** The nominal SWiFt background (red) and signal subtracted background (SSB) (blue) estimations for a data-like dijet mass ( $m_{jj}$ ) spectrum from the fitting control region with a SSM  $Z'$  boson injected (green points) as a ratio to the nominal SWiFt background estimation performed on the same data-like dijet mass spectrum when no signal is injected. The grey area represents the statistical uncertainties in the data-set. The simulated mass of the SSM  $Z'$  boson is (a) 600 GeV and (b) 1000 GeV.

The nominal SWiFt background estimation has a large signal induced fit bias when a SSM  $Z'$  boson is injected, shown by the fact that the red line is significantly drawn towards the injected signal in Figure 8.6. The signal induced fit bias is approximately the same size of the injected signal in the case of a SSM  $Z'$  boson at 600 GeV. The signal induced fit bias of the signal subtracted background is small relative to the size of the injected signal, shown by the fact that the blue line lies close to 1 for all dijet masses. Therefore, the signal subtracted background estimation is used in the limit setting phase, for both the  $Z'$  boson and generic Gaussian signals.

Figure 8.7 shows the ratio of the signal subtracted background (SSB) estimations to the nominal SWiFt background estimate (black) performed on the full *Full16\_LowMass* data-set<sup>7</sup>. The grey area represents the parameter choice uncertainty of the nominal SWiFt background estimation. Signal subtracted background estimations are created for all simulated mass points considered, but for clarity only those at mass points 600, 800, 1000

<sup>7</sup>The SWiFt background estimate for the full data-set is shown in comparison to the data in Figure 7.27.

and 1250 GeV are shown in the figure. For all simulated mass points, including those not shown in the figure, the signal subtracted background estimate is consistent with the nominal SWiFt background estimation within background uncertainties. Therefore the results of the limit setting phase would be consistent if either the signal subtracted or nominal SWiFt background estimation are used. Furthermore, it can be inferred that there is no signal induced fit bias due to a  $Z'$  boson in the nominal SWiFt background estimation performed to the *Full16\_LowMass* data-set.

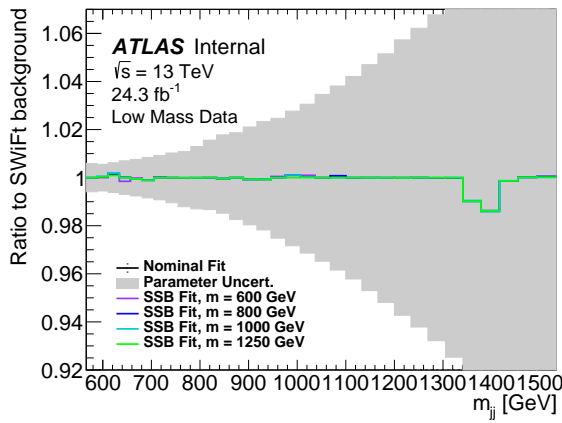


**Figure 8.7:** The ratio of signal subtracted background (SSB) estimations (coloured lines) and the nominal SWiFt background estimate (black) performed on the full *Full16\_LowMass* data-set. The parameter choice uncertainty on the background is shown by the grey area. The signal mass points used in the subtracted background estimations are indicated in the legend.

Finally, it is important to note that no signal plus background fit is considered in the search phase result, as this would mean that the search phase result is not model independent. However, it is clear that the nominal SWiFt background estimation can be affected by a signal induced fit bias, as shown in Figure 8.6. As a result the sensitivity of the search phase is reduced to specific signal models relative to the results of the limit-phase presented below; the reduced sensitivity is accepted to maintain model independence.

#### 8.4.4 Results

Figure 8.8 shows the 95% credibility level upper limits set on  $\sigma \times A \times \epsilon$  of a  $Z'$  boson as a function of simulated mass. The observed limit, expected limit and 1 and 2  $\sigma$  uncertainty bands on the expected limit are shown. Overlaid are theoretical predictions of  $\sigma \times A \times \epsilon$  for the Sequential Standard Model (SSM), leptophobic and DM  $Z'$  boson benchmark models, which have been described in Section 6.3. These limits have not yet been published so should be considered as preliminary.

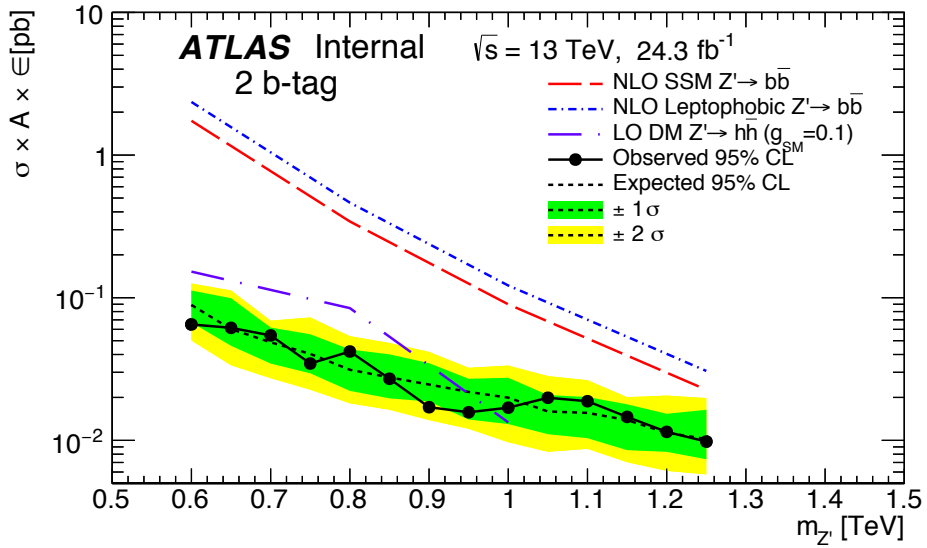


**Figure 8.8:** 95% credibility level upper limits on cross-section times acceptance times tagging efficiency ( $\sigma \times A \times \varepsilon$ ) for the  $Z'$  boson and as a function of simulated mass using the *Full16\_LowMass* data-set. The observed limit is shown by the solid black line, the expected limit is shown by the dotted black line and the 1 and 2  $\sigma$  uncertainty bands on the expected limit are shown by the green and yellow bands. The theoretical prediction of  $\sigma \times A \times \varepsilon$  for the Sequential Standard Model (SSM), leptophobic and DM  $Z'$  bosons are overlaid [13].

Using the *Full16\_LowMass* data-set it is anticipated that the SSM and leptophobic  $Z'$  boson will be excluded in the simulated mass range 0.6 - 1.25 TeV at the 95% credibility level. Additionally it is anticipated the DM  $Z'$  boson will be excluded in the simulated mass range 0.6 - 0.95 TeV at the 95% credibility level.

For the generic Gaussian limit setting phase there is a significant difference with respect to the *Summer16\_HighMass* data-set analysis. In the *Summer16\_HighMass* data-set analysis a signal template with a Gaussian distribution in dijet mass is used, whilst for the *Full16\_LowMass* data-set analysis a signal template with a Gaussian distribution in the truth mass distribution is used. The truth mass is defined as the invariant mass of the leading and subleading truth jets, using the definition of truth jet from Section 4.2.3. The Gaussian shapes are centred on a range of simulated masses and the width of the considered Gaussians are 15%, 10%, 7%, 5%, 3% and 0% of the simulated mass; a Gaussian with a 0% width is a Dirac delta peak. The transformation of the signal templates from truth mass to dijet mass is performed using transfer matrices calculated in a Monte-Carlo simulated QCD dijet sample following the procedure outlined in [3]. The Gaussian with a 0% width in truth mass will have a width of the mass resolution of the detector in dijet mass.

For the Gaussian limit setting the sources of systematic uncertainties are the luminosity uncertainty, the background modelling uncertainties and a flat 5% uncertainty to cover the JES, JER and  $b$ JES systematic uncertainties. Other systematic uncertainties are not included in the preliminary limits, as these are found to have a small effect on the upper limit relative to the jet energy uncertainties. This is because the jet energy uncertainties can significantly affect the width of the dijet mass signal template.

Figure 8.9 shows the observed 95% credibility upper limits set on the product of cross-section, detector acceptance, tagging efficiency and branching ratio,  $\sigma \times A \times \epsilon \times BR$ , for the full range of Gaussian signals described above. The expected limits for a Gaussian signal with a 0% width in simulated mass is shown by the dotted lines and associated 1 and 2  $\sigma$  uncertainty bands are shown in green and yellow. The results have not yet been published so should be considered as preliminary.

For the *Full16\_LowMass* data-set it is anticipated that an upper limit will be placed on a generic Gaussian signal ranging from 0.05 to 0.003 pb in the mass range 0.65 to 1.4 TeV.

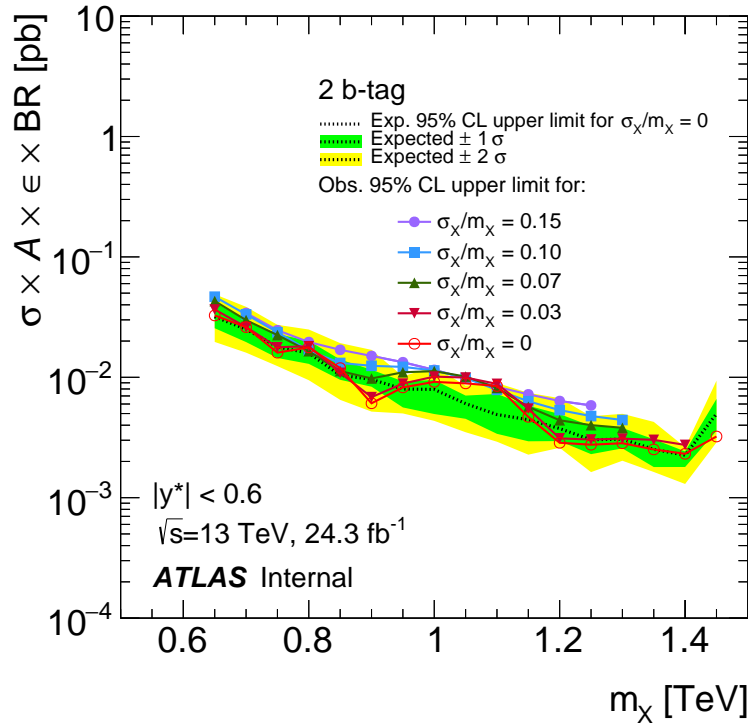


**Figure 8.9:** 95% credibility observed upper limits on the product of cross-section, detector acceptance, tagging efficiency and branching ratio,  $\sigma \times A \times \epsilon \times BR$ , for Gaussian signals using the *Full16\_LowMass* data-set as a function of simulated mass ( $m_X$ ) are shown by the solid lines. The signal templates are Gaussian in simulated mass with widths of 15%, 10%, 7%, 5%, 3% and 0% of the simulated mass. Also shown are the expected 95% credibility observed upper limit on the Gaussian signal shape with a 0% width (dotted line) and the associated 1 and 2  $\sigma$  uncertainty bands (green and yellow) [13].

## Chapter 9

# Future Prospects of Di-*b*-Jet Searches

This chapter will consider the future prospects of di-*b*-jet searches at ATLAS, including a discussion of possible improvements and developments of the analyses presented in this thesis.

## 9.1 Di-*b*-Jet Searches at Higher Luminosities

The LHC has been collecting 13 TeV  $pp$  collision data since May 2015 and is scheduled to continue until 2038 [112]. The di-*b*-jet searches presented in Chapters 6-8 used 13 TeV  $pp$  collision data collected in 2015 and 2016. It is expected that the integrated luminosity of  $pp$  collision data collected by the end of 2022 will be  $\sim 300 \text{ fb}^{-1}$  [112]. After 2022, significant upgrades to the LHC accelerator and ATLAS detector are planned such that data can be taken at a higher instantaneous luminosity, this is known as the High-Luminosity LHC. The High-Luminosity LHC is expected to collect 13 TeV  $pp$  collision data with an integrated luminosity of  $\sim 3000 \text{ fb}^{-1}$  by the end of 2038 [112].

Table 9.1 summarises the integrated luminosity of the data-sets used by di-*b*-jet searches at ATLAS and the expected integrated luminosities at the key points in the LHC schedule discussed above. All di-*b*-jet searches at ATLAS use 13 TeV  $pp$  collisions. The table includes the *Full16\_LowMass* and *Full16\_HighMass* data-set analyses that are soon to be published together.

The sensitivity to signal of the search phase in the di-*b*-jet analysis can be estimated as  $\sqrt{S/B}$ , where  $S$  and  $B$  are the number of signal and background events passing the di-*b*-jet event selection in the mass region of the signal. This approximation assumes that a perfect background estimation model is used, where no signal induced fit bias can occur. Therefore the estimated sensitivity of the di-*b*-jet analysis is proportional to the square root of the

End of Data Collection	Integrated Luminosity using a Single Jet Trigger	Integrated Luminosity using a Double $b$ -Jet Trigger
End of 2015	$3.2 \text{ fb}^{-1}$ [11]	$3.2 \text{ fb}^{-1}$ [12]
July 2016	$13.3 \text{ fb}^{-1}$ [10] ( <i>Summer16_HighMass</i> )	No analysis performed
End of 2016	$36.1 \text{ fb}^{-1}$ ( <i>Full16_HighMass</i> )	$24.3 \text{ fb}^{-1}$ ( <i>Full16_LowMass</i> )
End of 2022	$\sim 300 \text{ fb}^{-1}$ ( <i>Projection</i> )	$\sim 300 \text{ fb}^{-1}$ ( <i>Projection</i> )
End of 2038	$\sim 3000 \text{ fb}^{-1}$ ( <i>Projection</i> )	$\sim 3000 \text{ fb}^{-1}$ ( <i>Projection</i> )

**Table 9.1:** A summary of the integrated luminosity of data-sets used by the di- $b$ -jet analyses performed at ATLAS and the expected integrated luminosities at key points in the LHC schedule [112]. All data-sets contain 13 TeV  $pp$  collision data collected since May 2015, with the exception of the *Full16\_LowMass* data-set which is collected from April 2016.

integrated luminosity. Using this approximation and the values in Table 9.1, it can be seen that the addition of data collected in 2016 increased the sensitivity of di- $b$ -jet searches by a factor of  $\sim \sqrt{10}$ . The next analysis to obtain a similar gain in sensitivity must contain all  $pp$  collision data collected up to end of 2022, and then for the same increase again all data collected up to the end of 2038 must be included.

Therefore it can be seen that the increasing integrated luminosity of data collected by ATLAS will allow for di- $b$ -jet searches with increased sensitivity in the future, although the time intervals between similar improvements of sensitivity become large. Therefore, it is important to investigate other techniques to increase the sensitivity on a shorter time-scale.

## 9.2 Combination of $b$ -Tagging Categories

The *Summer16\_HighMass* data-set analysis presented in Chapters 6-8 uses two  $b$ -tag categories; the 2  $b$ -tag and  $\geq 1$   $b$ -tag category. The two categories are considered independently; the former is used to search for a  $Z'$  boson and the later is used to search for a  $b^*$  quark.

However, a  $Z'$  boson can sometimes have only one  $b$ -tag as a true  $b$ -jet may not be  $b$ -tagged. Similarly, a  $b^*$  quark can have two  $b$ -tags as a gluon can split into two  $b$ -quarks which can be tagged. The two features described above can be seen in Figure 6.9(b).

Hence, to increase the signal acceptance of the current analysis one could consider three exclusive  $b$ -tagging categories; where there are two jets that contain exactly 0, 1 or 2  $b$ -tags. Limits are then set on the benchmark models using a statistical combination of the three  $b$ -tagging categories. This would allow for limits to be set on each model using the information from all three categories.

A di- $b$ -jet search using a combination of the three  $b$ -tagging categories has been performed by the CMS collaboration [9]. The CMS analysis uses 8 TeV  $pp$  collision data with an integrated luminosity of  $19.6 \text{ fb}^{-1}$  in the mass region  $m_{jj} > 1.1 \text{ TeV}$ . Table 9.2 shows a comparison of the 95% credibility-level observed upper mass limits set on the benchmark models by the *Summer16\_HighMass* data-set analysis and the CMS di- $b$ -jet search, where the upper mass limit is the highest mass excluded. The *Summer16\_HighMass* data-set analysis sets a higher upper mass limit on the  $b^*$  quark than the CMS search; likely due to the larger centre-of-mass energy used. The improvement from combining categories is smaller for the  $b^*$  quark as the  $\geq 1$   $b$ -tag category is already used by the *Summer16\_HighMass* analysis. However, the CMS search is able to set a limit on the SSM  $Z'$  boson, where the *Summer16\_HighMass* data-set analysis cannot. Therefore, it is inferred that a combination of categories would lead to a significant improvement of the sensitivity to the  $Z'$  boson signal models in future ATLAS di- $b$ -jet analyses.

Analysis	$\sqrt{s}$	Integrated Luminosity	95% CL Observed Upper Mass Limit	
			SSM $Z'$ boson	$b^*$ quark
ATLAS [10]	13 TeV	$13.3 \text{ fb}^{-1}$	-	2.3 TeV
CMS [9]	8 TeV	$19.6 \text{ fb}^{-1}$	1.7 TeV	1.5 TeV

**Table 9.2:** A comparison of the observed 95% credibility level (CL) upper mass limits set on the SSM  $Z'$  boson and  $b^*$  quark by the *Summer16\_HighMass* data-set analysis and a di- $b$ -jet search performed by the CMS collaboration [9]. The upper mass limit represents the highest mass excluded by the analysis on the two benchmark models considered. A dash indicates that no limit was set.

### 9.3 Improvement of $b$ -Jet Trigger Efficiency Measurement

In Section 8.4 it was shown that in the *Full16\_LowMass* data-set analysis there is a large systematic uncertainty at high dijet mass due to the measurement of the  $b$ -jet trigger efficiency, the details of which are described in Chapter 5. Tables 5.3 and 5.5 show that the largest sources of uncertainty on the measurement of the  $b$ -jet trigger efficiency are non- $b$ -jet impurities and the high- $p_T$  extrapolation process required due to the low number of high- $p_T$  jets in di-lepton  $t\bar{t}$  events.

Techniques have been developed to reduce the same sources of systematic uncertainties in measurements of the offline <sup>1</sup>  $b$ -tagging efficiency [75, 76], described in Section 4.3.4. For example a Boosted Decision Tree (BDT) is used to increase the  $b$ -jet purity of the selected jets and di-lepton  $t\bar{t}$  events containing two electrons or two muons are included to

---

<sup>1</sup>Offline refers to objects reconstructed after events have passed the trigger at the data-processing level and online refers to reconstructed objects used in the trigger decision. From the definition in Section 5.3.

increase the number of di-lepton  $t\bar{t}$  events. Such techniques can be used to improve the  $b$ -jet trigger efficiency measurements.

A possible future development is to combine the frameworks used by the  $b$ -jet trigger and offline  $b$ -tagging efficiency measurements. This would allow for a combined offline plus online  $b$ -tagging efficiency measurement using the improved techniques from the offline  $b$ -tagging measurement described above.

## 9.4 Signal Plus Background Fit in the Search Phase

In Figure 8.6 it was shown that, for the *Full16\_LowMass* data-set analysis, there is a signal induced fit bias when the nominal background estimate is applied to a background-only dijet mass spectrum injected with a dijet mass signal template of a SSM  $Z'$  boson. This could be because higher order dijet fit functions and more complex fitting models, such as SWiFt, are required to estimate the background from QCD dijet production at high luminosity. The signal induced fit bias is removed when a technique employing a signal plus background fit is applied. The signal plus background fit is not used in the search phase of the *Full16\_LowMass* analysis such that model independence can be maintained.

Therefore, to improve the sensitivity of the search phase in future analyses a signal plus background fit should be considered, such that the signal induced fit biases are removed. To reduce the dependence of such a search phase on any signal model, a large range of signal widths should be considered. A similar approach has been used in a search for resonances decaying into a pair of photons at ATLAS [113].

## Chapter 10

# Conclusions

Two searches for Beyond Standard Model (BSM) resonances in the invariant mass of pairs of jets, where at least one or both jets contain a  $b$ -quark, have been performed using 13 TeV  $pp$  collision data collected by the ATLAS detector. Such searches are sensitive to BSM resonances that preferentially decay to one or two  $b$ -quarks, such as the excited  $b^*$  quark and the  $Z'$  boson.

A high-mass di- $b$ -jet search probes the mass region 1.4 – 6 TeV using data collected in 2015-16 with an integrated luminosity of  $13.3 \text{ fb}^{-1}$ . No evidence of a BSM resonance is found. The excited  $b^*$  quark with a mass in the interval 1.4 – 2.3 TeV and the leptophobic  $Z'$  boson with a mass of 1.5 TeV are excluded at the 95% credibility level. 95% credibility level upper limits on  $\sigma \times A \times \epsilon \times BR$  are set in the range 0.2 to 0.001 pb for generic Gaussian signals with widths from 15% to 3% and masses in the interval 1.4 – 6 TeV. This di- $b$ -jet search has been published as a conference note [10].

A low-mass di- $b$ -jet search probes the mass region 0.6 – 1.5 TeV using data collected using the ATLAS  $b$ -jet trigger in 2016 with an integrated luminosity of  $24.3 \text{ fb}^{-1}$ . No evidence of a BSM resonance is found. The sequential standard model and leptophobic  $Z'$  boson models with a mass in the interval 0.6 – 1.25 TeV and a Dark Matter inspired  $Z'$  boson model with a mass in the interval 0.6 – 0.95 TeV are excluded at the 95% credibility level. 95% credibility level upper limits on  $\sigma \times A \times \epsilon \times BR$  in the range 0.05 to 0.003 pb are set for generic Gaussian signals with widths from 15% to 0% and masses in the interval 0.65 – 1.4 TeV. This di- $b$ -jet search is soon to be published.

The low-mass di- $b$ -jet search uses the ATLAS  $b$ -jet trigger; therefore a detailed understanding of the  $b$ -jet trigger performance is required. It was identified that some regions of data collected by the ATLAS  $b$ -jet trigger in 2016 were defective and a strategy was developed to mitigate the observed issues. Then, a measurement of the  $b$ -jet trigger efficiency

in 2016 data was performed. The  $b$ -jet trigger studies and efficiency measurement presented in this thesis will be used by a number of other ATLAS analyses, such a proposed update to a search for resonances decaying to 4  $b$ -quarks via a pair of Higgs bosons [86] using 2016 data.

The outlook for future di- $b$ -jet searches at the ATLAS detector has been considered, including a summary of the prospects for di- $b$ -jet searches at high luminosities and a discussion of possible future developments to further develop the analyses presented in this thesis.

## **Appendix A**

# **Dijet Binning**

The binning used in the di-*b*-jet analysis is:

203, 216, 229, 243, 257, 272, 287, 303, 319, 335, 352, 369,  
387, 405, 424, 443, 462, 482, 500, 523, 544, 566, 588, 611,  
634, 657, 681, 705, 730, 755, 781, 807, 834, 861, 889, 917,  
946, 976, 1006, 1037, 1068, 1100, 1133, 1166, 1200, 1234,  
1269, 1305, 1341, 1378, 1416, 1454, 1493, 1533, 1573, 1614,  
1656, 1698, 1741, 1785, 1830, 1875, 1921, 1968, 2016, 2065,  
2114, 2164, 2215, 2267, 2320, 2374, 2429, 2485, 2542, 2600,  
2659, 2719, 2780, 2842, 2905, 2969, 3034, 3100, 3167, 3235,  
3305, 3376, 3448, 3521, 3596, 3672, 3749, 3827, 3907, 3988,  
4070, 4154, 4239, 4326, 4414, 4504, 4595, 4688, 4782, 4878,  
4975, 5074, 5175, 5277, 5381, 5487, 5595, 5705, 5817, 5931,  
6047, 6165, 6285, 6407, 6531, 6658, 6787, 6918, 7052, 7188,  
7326, 7467, 7610, 7756, 7904, 8055, 8208, 8364, 8523, 8685,  
8850, 9019, 9191, 9366, 9544, 9726, 9911, 10100, 10292,  
10488, 10688, 10892, 11100, 11312, 11528, 11748, 11972,  
12200, 12432, 12669, 12910, 13156

## Appendix B

# Single Jet Trigger Threshold $p_T$ Fit

The trigger plateau is defined as the kinematic region where all events that pass the offline jet- $p_T$  selection also pass the online jet- $p_T$  selection at the trigger level. To be on the trigger plateau of a single jet trigger the offline jet- $p_T$  must be above some threshold value, which is referred to as the threshold jet- $p_T$ .

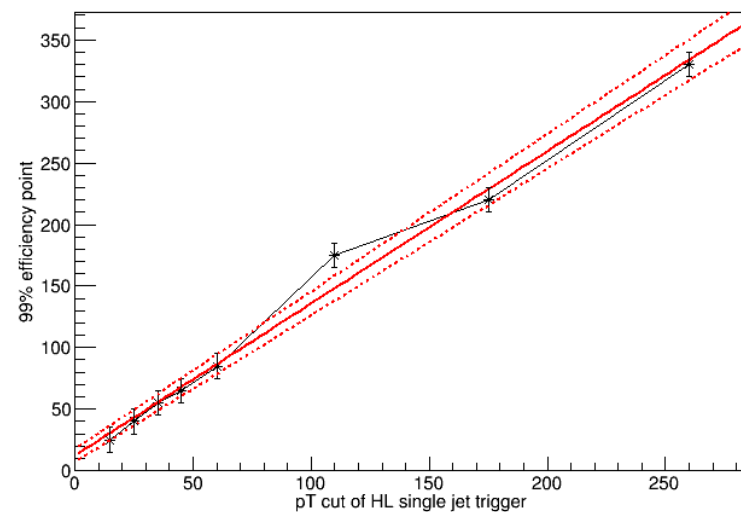
For single jet triggers it is found that the threshold jet- $p_T$  follows a linear behaviour with respect to the online jet- $p_T$  requirements at the trigger level. Therefore a linear fit can be used to predict the threshold jet- $p_T$  of any single jet trigger from considering a small number of single jet triggers. The single jet triggers considered require that there is an online jet with  $p_T$  above 15, 25, 35, 45, 60, 110, 175, 260 and 360 GeV respectively.

Figure B.1 shows the threshold jet- $p_T$  at which a trigger is 99% efficient with respect to a lower- $p_T$  benchmark trigger as a function of the jet- $p_T$  requirement of the single jet trigger. A linear fit is performed, as shown by the red line. The  $1\sigma$  error band on the fit slope is shown by the dotted lines [114].

The resulting linear fit has a normalisation of 12.3 and a slope of 1.24. Applying the fit to the trigger level jet requirements of the double  $b$ -jet trigger we obtain:

- Trigger Level Jet  $p_T > 150$  GeV, Threshold Jet  $p_T > 74.1$  GeV
- Trigger Level Jet  $p_T > 50$  GeV, Threshold Jet  $p_T > 198$  GeV

The values are rounded up in the analysis to give a safety margin.



**Figure B.1:** A plot showing the threshold jet- $p_T$  at which a trigger is 99% efficient with respect to a lower- $p_T$  benchmark trigger as a function of the trigger-level  $p_T$  requirements of the single jet trigger. A linear fit is performed, as shown by the red line. The  $1\sigma$  error band on the fit slope is shown by the dotted lines [114].

## Appendix C

# All Configurations for Low Mass Fit Studies

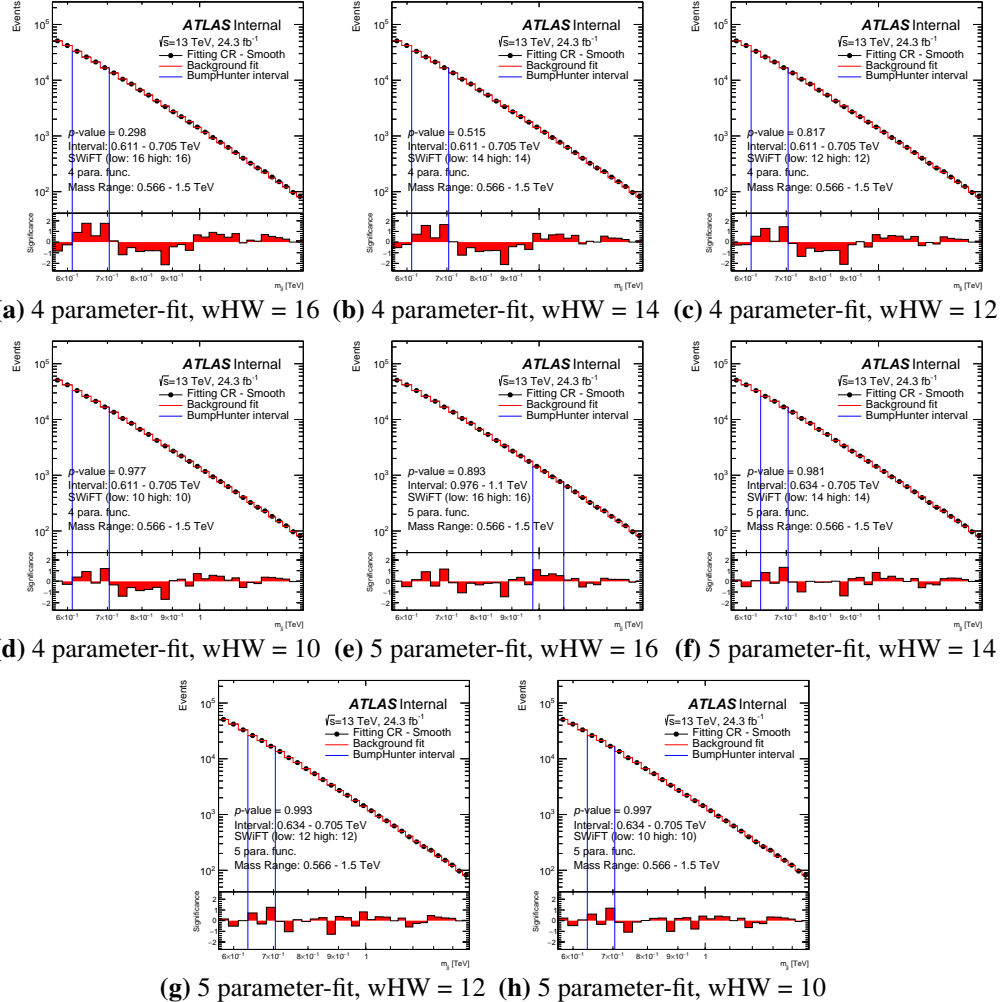


**Figure C.1:** The SWiFt search phase procedure run on the smooth distribution from the fitting control region in the low-mass category. The SWiFt configurations are 4 and 5 parameter fit function for a window-half-width (wHW) range of 10 to 16.

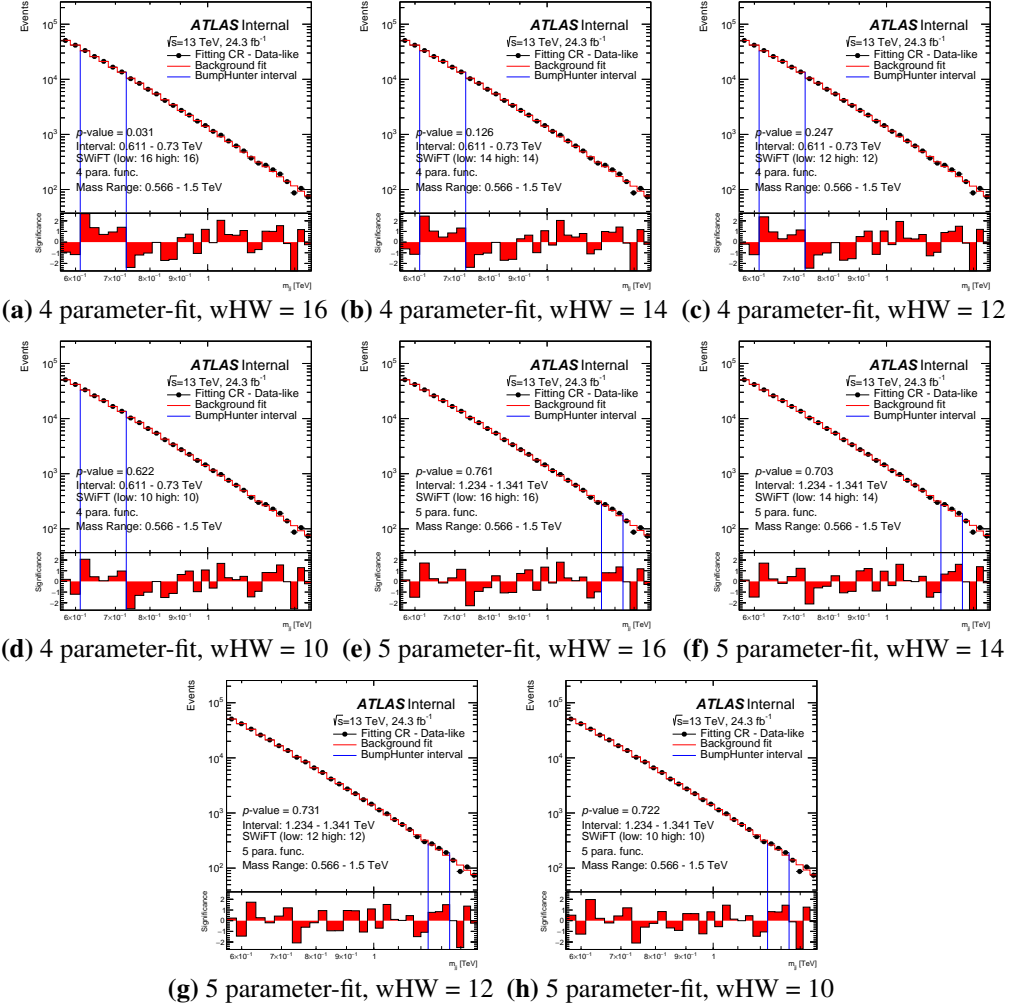


**Figure C.2:** The SWiFt search phase procedure run on a data-like distribution from the fitting control region in the low-mass category. The SWiFt configurations are 4 and 5 parameter fit function for a window-half-width (wHW) range of 10 to 16.

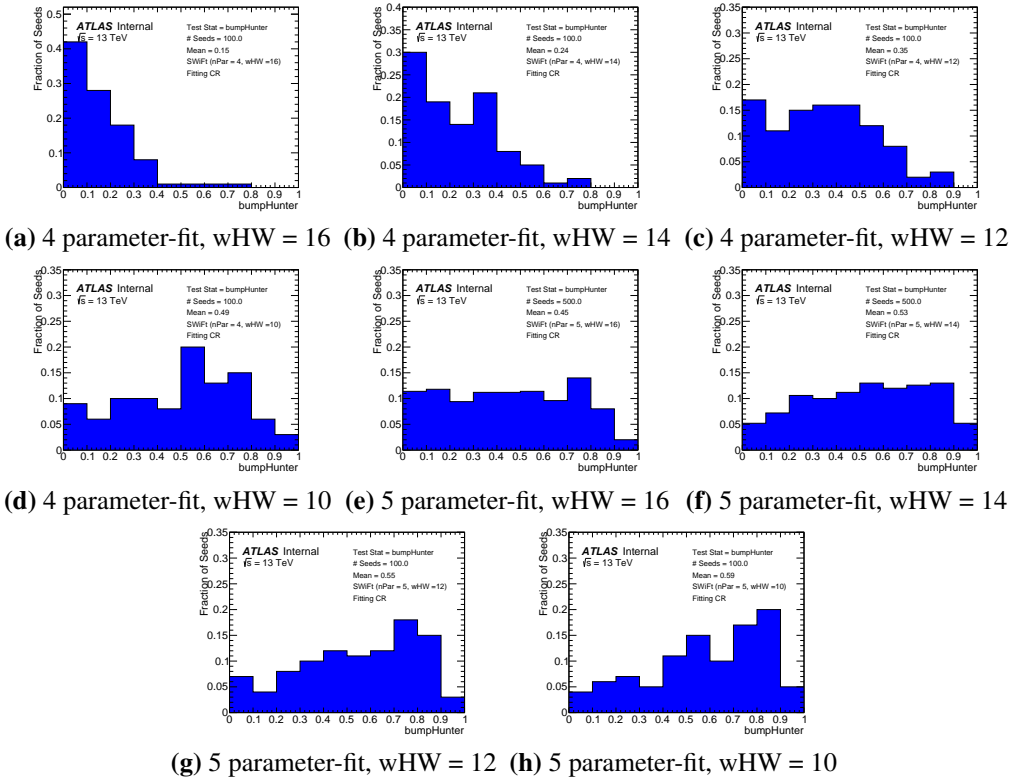


**Figure C.3:** This figure shows the normalised distribution of BUMPHUNTER  $p$ -values from performing the SWiFt background estimate to an ensemble of data-like distributions taken from the fitting control region in the low-mass category. The SWiFt configurations are 4 and 5 parameter fit function for a window-half-width (wHW) range of 10 to 16.

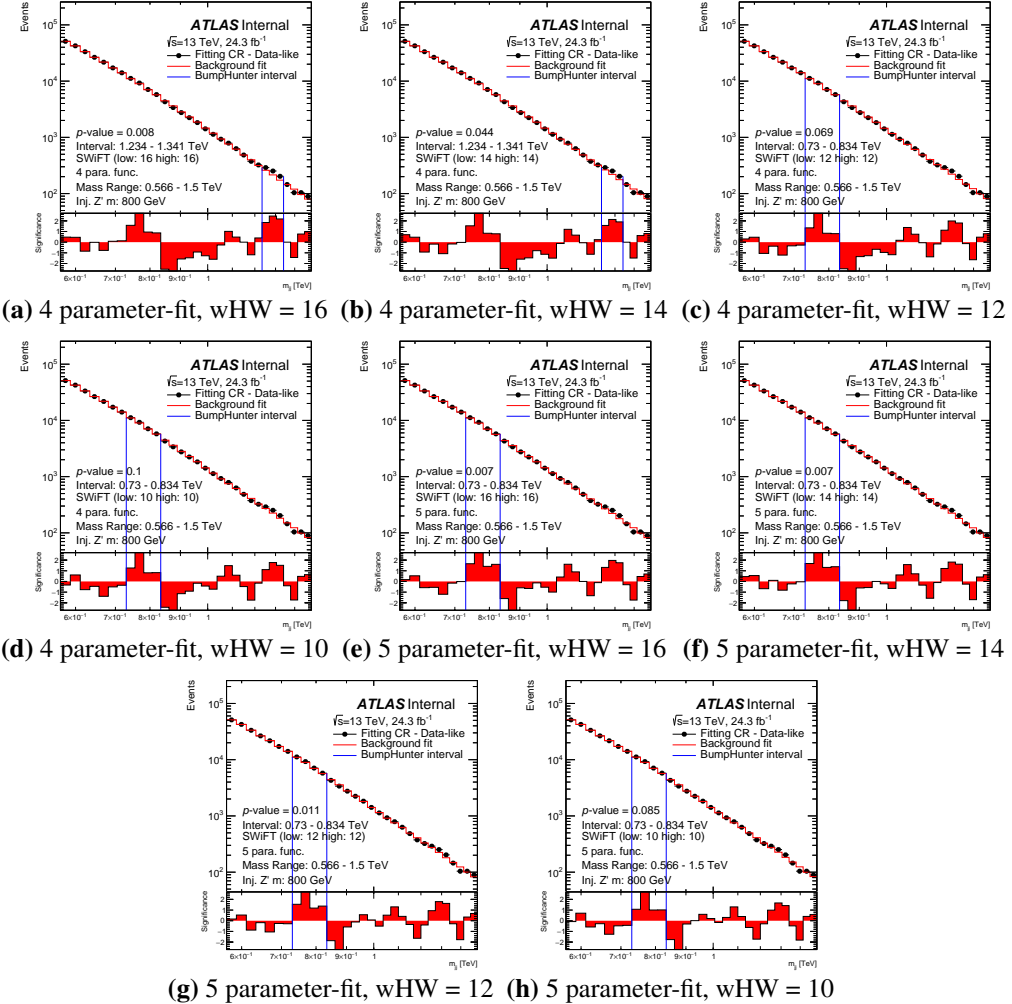


**Figure C.4:** The SWiFt search phase procedure run on a data-like distribution from the fitting control region with a Pythia8 SSM  $Z'$  of mass 800 GeV injected. The SWiFt procedure has been run for the 4 and 5 parameter fit function for a window-half-width (wHW) range of 10 to 16.

## **Appendix D**

# **Colophon**

*This is a description of the tools you used to make your thesis. It helps people make future documents, reminds you, and looks good.*

(example) This document was set in the Times Roman typeface using L<sup>A</sup>T<sub>E</sub>X and BibL<sup>A</sup>T<sub>E</sub>X, composed with a text editor.

## **Appendix E**

# **Contents Plan**

- **Introduction**

*Status: First Draft Done*

- **Theoretical Background**

*Status: First Draft Done*

Comments

- **ATLAS Detector**

*Status: First Draft Done*

Still needs cleaning and response to comments

I want to add pile-up and calo noise here.

- **Object Reconstruction And Calibration**

**Status : First Draft Done**

Needs editing

Want to add primary vertexing

Add in some discussion of high pT b-tagging

Cut down on bJES

- **Trigger**

**Status : First draft done**

Move trigger description here.

Needs a bit more cleaning and a bit of upmarketing.

- **Event Selection**

Need to cut high mass

*Status: 2nd Draft with full 16 done* Need to add: Full 16 + 15 data-set

- **Background Estimation and Search Phase**

*Status: 2nd Draft with full done* Few comments

- **Systematics and Limits Setting**

*Status: 2nd draft with summer16 done* Check on limits for 2016 as they develop.

- **Looking Forward - What more can be done?**

*Status: First Draft Done*

# Bibliography

- [1] Robert M. Harris and Konstantinos Kousouris. Searches for Dijet Resonances at Hadron Colliders. *Int. J. Mod. Phys.*, A26:5005–5055, 2011.
- [2] ATLAS Collaboration. Search for new phenomena in dijet mass and angular distributions from  $pp$  collisions at  $\sqrt{s} = 13$  TeV with the ATLAS detector. *Phys. Lett.*, B754:302–322, 2016.
- [3] Search for new phenomena in dijet events using  $37\text{ fb}^{-1}$  of  $pp$  collision data collected at  $\sqrt{s}=13$  TeV with the ATLAS detector. *Phys. Rev.*, D96(5):052004, 2017.
- [4] Albert M Sirunyan et al. Search for dijet resonances in protonproton collisions at  $\sqrt{s} = 13$  TeV and constraints on dark matter and other models. *Phys. Lett.*, B769:520–542, 2017. [Erratum: *Phys. Lett.*B772,882(2017)].
- [5] The ATLAS collaboration. Search for new light resonances decaying to jet pairs and produced in association with a photon or a jet in proton-proton collisions at  $\sqrt{s} = 13$  TeV with the ATLAS detector. 2016.
- [6] The ATLAS collaboration. Search for light dijet resonances with the ATLAS detector using a Trigger-Level Analysis in LHC pp collisions at  $\sqrt{s} = 13$  TeV. 2016.
- [7] Albert M Sirunyan et al. Search for Low Mass Vector Resonances Decaying to Quark-Antiquark Pairs in Proton-Proton Collisions at  $\sqrt{s} = 13$  TeV. *Phys. Rev. Lett.*, 119(11):111802, 2017.
- [8] F. Abe and et al. Search for New Particles Decaying to  $b\bar{b}$  in  $pp$  Collisions at  $\sqrt{s} = 1.8$  TeV. *Physical Review Letters*, 82:2038–2043, March 1999.
- [9] Search for Heavy Resonances Decaying into  $bb$  and  $bg$  Final States in  $pp$  Collisions at  $\text{sqrt}(s) = 8$  TeV. Technical Report CMS-PAS-EXO-12-023, CERN, Geneva, 2013.
- [10] Search for resonances in the mass distribution of jet pairs with one or two jets identified as  $b$ -jets with the ATLAS detector with 2015 and 2016 data. Technical Report ATLAS-CONF-2016-060, CERN, Geneva, Aug 2016.

- [11] ATLAS Collaboration. Search for resonances in the mass distribution of jet pairs with one or two jets identified as  $b$ -jets in proton–proton collisions at  $\sqrt{s} = 13$  TeV with the ATLAS detector. *Phys. Lett.*, B759:229–246, 2016.
- [12] Search for resonances below 1.2 TeV from the mass distribution of  $b$ -jet pairs in proton-proton collisions at  $\sqrt{s}=13$  TeV with the ATLAS detector. Technical Report ATLAS-CONF-2016-031, CERN, Geneva, Jun 2016.
- [13] John Alison, Francesco Armando Di Bello, Sergei Chekanov, Andrea Coccaro, Tobias Golling, Gabriel Facini, Andreas Korn, Marie Christine Lanfermann, Thomas LeCompte, Bingxuan Liu, Jeremy Love, Laurie McClymont, Olaf Nackenhorst, Nishu Nishu, James Proudfoot, Soo Ryu, Rui Wang, Ning Zhou, Karishma Sekhon, Ryan Christopher Edgar, Dante Amidei, and Jinlong Zhang. Search for resonances in the di-jet mass distribution with one or two jets identified as  $b$ -jets in proton-proton collisions at  $\sqrt{s}=13$  TeV with the ATLAS detector. Technical Report ATL-COM-PHYS-2016-1561, CERN, Geneva, Nov 2016.
- [14] Guido Altarelli and Martin W. Grunewald. Precision electroweak tests of the standard model. *Phys. Rept.*, 403-404:189–201, 2004.
- [15] C. Patrignani et al. Review of Particle Physics. *Chin. Phys.*, C40(10):100001, 2016.
- [16] S. L. Glashow. Partial Symmetries of Weak Interactions. *Nucl. Phys.*, 22:579–588, 1961.
- [17] S. Bethke and G. Dissertori and G. P. Salam. Quantum Chromodynamics, 2015. <http://pdg.lbl.gov/2015/reviews/rpp2015-rev-qcd.pdf>.
- [18] F. Englert and R. Brout. Broken symmetry and the mass of gauge vector mesons. *Phys. Rev. Lett.*, 13:321–323, Aug 1964.
- [19] Peter W. Higgs. Broken symmetries and the masses of gauge bosons. *Phys. Rev. Lett.*, 13:508–509, Oct 1964.
- [20] ATLAS Collaboration. Observation of a new particle in the search for the standard model higgs boson with the atlas detector at the lhc. *Physics Letters B*, 716(1):1 – 29, 2012.
- [21] CMS Collaboration. Observation of a new boson at a mass of 125 GeV with the CMS experiment at the LHC. *Phys. Lett.*, B716:30–61, 2012.
- [22] Katherine Pachal. Search for new physics in the dijet invariant mass spectrum at 8 TeV, Jan 2015. Presented 01 Jun 2015.

- [23] Bo Andersson, G. Gustafson, G. Ingelman, and T. Sjstrand. Parton Fragmentation and String Dynamics. *Phys. Rept.*, 97:31–145, 1983.
- [24] B.R. Webber. A qcd model for jet fragmentation including soft gluon interference. *Nuclear Physics B*, 238(3):492 – 528, 1984.
- [25] John Butterworth. This is not a measurement, 2015. <https://www.theguardian.com/science/life-and-physics/2015/jan/10>this-is-not-a-measurement>.
- [26] Christine A. Aidala, Steven D. Bass, Delia Hasch, and Gerhard K. Mallot. The Spin Structure of the Nucleon. *Rev. Mod. Phys.*, 85:655–691, 2013.
- [27] Christopher C Tully. *Elementary particle physics in a nutshell*. Princeton Univ. Press, Princeton, NJ, 2011.
- [28] F. D. Aaron et al. Combined Measurement and QCD Analysis of the Inclusive e+- p Scattering Cross Sections at HERA. *JHEP*, 01:109, 2010.
- [29] L. A. Harland-Lang, A. D. Martin, P. Motylinski, and R. S. Thorne. Parton distributions in the lhc era: Mmht 2014 pdfs. *The European Physical Journal C*, 75(5):204, May 2015.
- [30] T. Aaltonen et al. Observation of Single Top Quark Production and Measurement of —Vtb— with CDF. *Phys. Rev.*, D82:112005, 2010.
- [31] Michael E. Peskin. Dark matter and particle physics. *J. Phys. Soc. Jap.*, 76:111017, 2007.
- [32] M. Roos. Dark Matter: The evidence from astronomy, astrophysics and cosmology. *ArXiv e-prints*, January 2010.
- [33] Jonathan L. Feng. Dark Matter Candidates from Particle Physics and Methods of Detection. *Ann. Rev. Astron. Astrophys.*, 48:495–545, 2010.
- [34] Csaba Csiki and Philip Tanedo. Beyond the Standard Model. In *Proceedings, 2013 European School of High-Energy Physics (ESHEP 2013): Paradfurdo, Hungary, June 5-18, 2013*, pages 169–268, 2015.
- [35] Stephen P. Martin. A Supersymmetry primer. 1997. [Adv. Ser. Direct. High Energy Phys.18,1(1998)].
- [36] C. P. Yuan. Top quark and electroweak symmetry breaking mechanism. In *Quarks. Proceedings, 10th International Seminar on High Energy Physics, QUARKS'98, Suzdal, Russia, May 18-24, 1998*, 1998.

- [37] Paul Langacker. The Physics of Heavy  $Z'$  Gauge Bosons. *Rev. Mod. Phys.*, 81:1199–1228, 2009.
- [38] Search for new high-mass phenomena in the dilepton final state using  $36.1 \text{ fb}^{-1}$  of proton-proton collision data at  $\sqrt{s} = 13 \text{ TeV}$  with the ATLAS detector. Technical Report ATLAS-CONF-2017-027, CERN, Geneva, Apr 2017.
- [39] Cheng-Wei Chiang, Takaaki Nomura, and Kei Yagyu. Phenomenology of  $E_6$ -Inspired Leptophobic  $Z'$  Boson at the LHC. *JHEP*, 05:106, 2014.
- [40] Andreas Albert et al. Recommendations of the LHC Dark Matter Working Group: Comparing LHC searches for heavy mediators of dark matter production in visible and invisible decay channels. 2017.
- [41] Durmus A. Demir, Gordon L. Kane, and Ting T. Wang. The Minimal  $U(1)'$  extension of the MSSM. *Phys. Rev.*, D72:015012, 2005.
- [42] U. Baur, I. Hinchliffe, and D. Zeppenfeld. Excited Quark Production at Hadron Colliders. *Int. J. Mod. Phys.*, A2:1285, 1987.
- [43] G. Arnison et al. Experimental Observation of Isolated Large Transverse Energy Electrons with Associated Missing Energy at  $s^{1/2} = 540 \text{ GeV}$ . *Phys. Lett.*, 122B:103–116, 1983. [,611(1983)].
- [44] G. Arnison et al. Experimental Observation of Lepton Pairs of Invariant Mass Around  $95\text{-GeV}/c^2$  at the CERN SPS Collider. *Phys. Lett.*, 126B:398–410, 1983.
- [45] M. Banner et al. Observation of Single Isolated Electrons of High Transverse Momentum in Events with Missing Transverse Energy at the CERN anti-p p Collider. *Phys. Lett.*, 122B:476–485, 1983.
- [46] P. Bagnaia et al. Evidence for  $Z_0 \rightarrow e^+e^-$  at the CERN anti-p p Collider. *Phys. Lett.*, 129B:130–140, 1983.
- [47] F. Abe et al. Observation of top quark production in  $\bar{p}p$  collisions with the collider detector at fermilab. *Phys. Rev. Lett.*, 74:2626–2631, Apr 1995.
- [48] S. Abachi et al. Observation of the top quark. *Phys. Rev. Lett.*, 74:2632–2637, Apr 1995.
- [49] Atlas public lumi results run-2. <https://twiki.cern.ch/twiki/bin/view/AtlasPublic/LuminosityPublicResultsRun2>.

- [50] G. Aad et al. The ATLAS Experiment at the CERN Large Hadron Collider. *JINST*, 3:S08003, 2008.
- [51] A. Airapetian et al. *ATLAS detector and physics performance: Technical Design Report, 1.* Technical Design Report ATLAS. CERN, Geneva, 1999.
- [52] G. Aad et al. Performance of the atlas detector using first collision data. *Journal of High Energy Physics*, 2010(9):56, Sep 2010.
- [53] C Gutschow. First observation of electroweak z boson plus two jet production, October 2014.
- [54] ATLAS Collaboration. Performance of the ATLAS Track Reconstruction Algorithms in Dense Environments in LHC run 2. 2017.
- [55] Giulia Ripellino. The alignment of the ATLAS Inner Detector in Run-2. *PoS*, LHCP2016:196, 2016.
- [56] B. Mindur and et. al. Gas gain stabilisation in the atlas trt detector. *Journal of Instrumentation*, 11(04):P04027, 2016.
- [57] Claude Leroy and Pier-Giorgio Rancoita. *Principles of Radiation Interaction in Matter and Detection*. World Scientific, 2016.
- [58] Michele Livan and Richard Wigmans. Misconceptions about Calorimetry. *Instruments*, 1(1):3, 2017.
- [59] Lene Bryngemark, Torsten AKESSON, Else LYTKEN, and Johan RATHSMAN. Search for new phenomena in dijet angular distributions at  $s = 8$  and 13 TeV, Feb 2016. Presented 18 Mar 2016.
- [60] J.J. Goodson. *Search for Supersymmetry in States with Large Missing Transverse Momentum and Three Leptons including a Z-Boson*. PhD thesis, Stony Brook University, May 2012. Presented 17 Apr 2012.
- [61] R. Frhwirth. Application of kalman filtering to track and vertex fitting. *Nuclear Instruments and Methods in Physics Research Section A: Accelerators, Spectrometers, Detectors and Associated Equipment*, 262(2):444 – 450, 1987.
- [62] H. Kirschenmann. Jets at cms and the determination of their energy scale. <http://cms.web.cern.ch/news/jets-cms-and-determination-their-energy-scale>.

- [63] ATLAS Collaboration. Evidence for the  $H \rightarrow b\bar{b}$  decay with the ATLAS detector. 2017.
- [64] ATLAS Collaboration. Topological cell clustering in the atlas calorimeters and its performance in lhc run 1. *The European Physical Journal C*, 77(7):490, Jul 2017.
- [65] Gavin P. Salam. Towards jetography. *arXiv:0906.1833*, 2009.
- [66] G. Arnison et al. Hadronic Jet Production at the CERN Proton - anti-Proton Collider. *Phys. Lett.*, 132B:214, 1983.
- [67] Matteo Cacciari, Gavin P. Salam, and Gregory Soyez. The Anti-k(t) jet clustering algorithm. *JHEP*, 04:063, 2008.
- [68] ATLAS Collaboration. Jet Calibration and Systematic Uncertainties for Jets Reconstructed in the ATLAS Detector at  $\sqrt{s} = 13$  TeV. Technical Report ATL-PHYS-PUB-2015-015, CERN, Geneva, Jul 2015.
- [69] ATLAS Collaboration. Jet energy scale measurements and their systematic uncertainties in proton-proton collisions at  $\sqrt{s} = 13$  TeV with the ATLAS detector. 2017.
- [70] ATLAS Collaboration. Search for diboson resonances with boson-tagged jets in  $pp$  collisions at  $\sqrt{s} = 13$  TeV with the ATLAS detector. 2017.
- [71] ATLAS Collaboration. Data-driven determination of the energy scale and resolution of jets reconstructed in the atlas calorimeters using dijet and multijet events at  $\sqrt{s} = 8$  tev. Technical Report ATLAS-CONF-2015-017, CERN, Geneva, Apr 2015.
- [72] ATLAS Collaboration. Measurements of top-quark pair differential cross-sections in the  $e\mu$  channel in  $pp$  collisions at  $\sqrt{s} = 13$  TeV using the ATLAS detector. *Eur. Phys. J.*, C77(5):292, 2017.
- [73] Expected performance of the ATLAS  $b$ -tagging algorithms in Run-2. Technical Report ATL-PHYS-PUB-2015-022, CERN, Geneva, Jul 2015.
- [74] Optimisation of the ATLAS  $b$ -tagging performance for the 2016 LHC Run. Technical Report ATL-PHYS-PUB-2016-012, CERN, Geneva, Jun 2016.
- [75] Calibration of  $b$ -tagging using dileptonic top pair events in a combinatorial likelihood approach with the ATLAS experiment. Technical Report ATLAS-CONF-2014-004, CERN, Geneva, Feb 2014.
- [76] ATLAS Collaboration.  $b$ -tagging calibration plots using dileptonic  $t\bar{t}$  events produced in  $pp$  collisions at  $s=13$  tev and a combinatorial likelihood approach, 2016.

- [77] Gordon Watts, Frank Filthaut, and Giacinto Piacquadio. Extrapolating Errors for b-tagging. Technical Report ATL-COM-PHYS-2015-711, CERN, Geneva, Jul 2015.  
This is for internal information only, no approval to ever be seen outside of ATLAS.
- [78] Jeremy Love, Andrea Coccaro, Andreas Korn, Sergei Chekanov, Jeffrey Rogers Dandoy, Francesco Gescini, Thomas LeCompte, Laurie McClymont, James Proudfoot, Soo Ryu, Rui Wang, Ning Zhou, Gabriel Facini, Tobias Golling, and Nishu Nishu. Search for Resonances in the Mass Spectrum of  $b$ -Tagged Jets with the ATLAS Detector. Technical Report ATL-PHYS-INT-2016-022, CERN, Geneva, Oct 2016.
- [79] ATLAS Collaboration. Electron efficiency measurements with the ATLAS detector using the 2015 LHC proton-proton collision data. Technical Report ATLAS-CONF-2016-024, CERN, Geneva, Jun 2016.
- [80] ATLAS Collaboration. Muon reconstruction performance of the ATLAS detector in protonproton collision data at  $\sqrt{s} = 13$  TeV. *Eur. Phys. J.*, C76(5):292, 2016.
- [81] ATLAS Collaboration. Measurement of the photon identification efficiencies with the ATLAS detector using LHC Run-1 data. 2016.
- [82] ATLAS Collaboration. Reconstruction, Energy Calibration, and Identification of Hadronically Decaying Tau Leptons in the ATLAS Experiment for Run-2 of the LHC . 2015.
- [83] ATLAS Collaboration. Performance of missing transverse momentum reconstruction for the ATLAS detector in the first proton-proton collisions at at  $\sqrt{s}= 13$  TeV. Technical Report ATL-PHYS-PUB-2015-027, CERN, Geneva, Jul 2015.
- [84] Search for dark matter and other new phenomena in events with an energetic jet and large missing transverse momentum using the ATLAS detector. Technical Report ATLAS-CONF-2017-060, CERN, Geneva, Jul 2017.
- [85] Yu Nakahama. The atlas trigger system: Ready for run-2. *Journal of Physics: Conference Series*, 664(8):082037, 2015.
- [86] M. Aaboud et al. Search for pair production of higgs bosons in the  $b\bar{b}b\bar{b}$  final state using proton-proton collisions at  $\sqrt{s} = 13$  TeV with the atlas detector. *Phys. Rev. D*, 94:052002, Sep 2016.
- [87] 2015 start-up trigger menu and initial performance assessment of the ATLAS trigger using Run-2 data. Technical Report ATL-DAQ-PUB-2016-001, CERN, Geneva, Mar 2016.

- [88] Simone Alioli, Paolo Nason, Carlo Oleari, and Emanuele Re. A general framework for implementing NLO calculations in shower Monte Carlo programs: the POWHEG BOX. *JHEP*, 06:043, 2010.
- [89] Torbjorn Sjostrand, Stephen Mrenna, and Peter Z. Skands. PYTHIA 6.4 Physics and Manual. *JHEP*, 05:026, 2006.
- [90] J. Pumplin, D. R. Stump, J. Huston, H. L. Lai, Pavel M. Nadolsky, and W. K. Tung. New generation of parton distributions with uncertainties from global QCD analysis. *JHEP*, 07:012, 2002.
- [91] Peter Zeiler Skands. Tuning Monte Carlo Generators: The Perugia Tunes. *Phys. Rev. D*, 82:074018, 2010.
- [92] D. J. Lange. The EvtGen particle decay simulation package. *Nucl. Instrum. Meth. A*, 462:152, 2001.
- [93] Georgios Choudalakis. On hypothesis testing, trials factor, hypertests and the BumpHunter. In *Proceedings, PHYSTAT 2011 Workshop on Statistical Issues Related to Discovery Claims in Search Experiments and Unfolding, CERN, Geneva, Switzerland 17-20 January 2011*, 2011.
- [94] Torbjorn Sjostrand, Stephen Mrenna, and Peter Z. Skands. A Brief Introduction to PYTHIA 8.1. *Comput. Phys. Commun.*, 178:852, 2008.
- [95] ATLAS Run 1 Pythia8 tunes. Technical Report ATL-PHYS-PUB-2014-021, CERN, Geneva, Nov 2014.
- [96] Richard D. Ball et al. Parton distributions with LHC data. *Nucl. Phys.*, B867:244–289, 2013.
- [97] G. Aad et al. The ATLAS Simulation Infrastructure. *Eur. Phys. J.*, C70:823–874, 2010.
- [98] Jun Gao, Chong Sheng Li, Bo Hua Li, C.-P. Yuan, and Hua Xing Zhu. Next-to-leading order QCD corrections to the heavy resonance production and decay into top quark pair at the LHC. *Phys.Rev.*, D82:014020, 2010.
- [99] Johan Alwall, Michel Herquet, Fabio Maltoni, Olivier Mattelaer, and Tim Stelzer. MadGraph 5 : Going Beyond. *JHEP*, 06:128, 2011.
- [100] J. Alwall, R. Frederix, S. Frixione, V. Hirschi, F. Maltoni, O. Mattelaer, H. S. Shao, T. Stelzer, P. Torrielli, and M. Zaro. The automated computation of tree-level and

- next-to-leading order differential cross sections, and their matching to parton shower simulations. *JHEP*, 07:079, 2014.
- [101] Selection of jets produced in 13TeV proton-proton collisions with the ATLAS detector. Technical Report ATLAS-CONF-2015-029, CERN, Geneva, Jul 2015.
- [102] Tagging and suppression of pileup jets with the ATLAS detector. Technical Report ATLAS-CONF-2014-018, CERN, Geneva, May 2014.
- [103] Thomas Kittelmann, Vakhtang Tsulaia, Joseph Boudreau, and Edward Moyse. The virtual point 1 event display for the atlas experiment. *Journal of Physics: Conference Series*, 219(3):032012, 2010.
- [104] ATLAS Collaboration. Observation of a new particle in the search for the Standard Model Higgs boson with the ATLAS detector at the LHC. *Phys. Lett.*, B716:1–29, 2012.
- [105] F. Abe et al. Search for new particles decaying to dijets in  $p\bar{p}$  collisions at  $\sqrt{s} = 1.8$  TeV. *Phys. Rev. Lett.*, 74:3538–3543, 1995.
- [106] T. Aaltonen et al. Search for new particles decaying into dijets in proton-antiproton collisions at  $s^{**}(1/2) = 1.96$ -TeV. *Phys. Rev.*, D79:112002, 2009.
- [107] S. S. Wilks. The Large-Sample Distribution of the Likelihood Ratio for Testing Composite Hypotheses. *Annals Math. Statist.*, 9(1):60–62, 1938.
- [108] J. Heinrich, C. Blocker, J. Conway, L. Demortier, L. Lyons, G. Punzi, and P. K. Sinervo. Interval estimation in the presence of nuisance parameters. 1. Bayesian approach. *ArXiv Physics e-prints*, September 2004.
- [109] Glen Cowan, Kyle Cranmer, Eilam Gross, and Ofer Vitells. Asymptotic formulae for likelihood-based tests of new physics. *The European Physical Journal C*, 71(2):1554, Feb 2011.
- [110] ATLAS Collaboration. Luminosity determination in pp collisions at  $\sqrt{s} = 8$  TeV using the ATLAS detector at the LHC. *Eur. Phys. J. C*, 76(arXiv:1608.03953. CERN-EP-2016-117. 12):653. 71 p, Aug 2016. Comments: 53 pages plus author list + cover pages (71 pages total), 19 figures, 9 tables, submitted to EPJC, All figures including auxiliary figures are available at <http://atlas.web.cern.ch/Atlas/GROUPS/PHYS-ICS/PAPERS/DAPR-2013-01>.
- [111] Lev Davidovich Landau. On the energy loss of fast particles by ionization. *J. Phys.*, 8(4):201–205, 1944.

- [112] G Apollinari, I Bjar Alonso, O Brning, M Lamont, and L Rossi. *High-Luminosity Large Hadron Collider (HL-LHC): Preliminary Design Report*. CERN Yellow Reports: Monographs. CERN, Geneva, 2015.
- [113] Morad Aaboud et al. Search for new phenomena in high-mass diphoton final states using  $37 \text{ fb}^{-1}$  of proton–proton collisions collected at  $\sqrt{s} = 13 \text{ TeV}$  with the ATLAS detector. *Phys. Lett.*, B775:105–125, 2017.
- [114] Olaf Nackenhorst. Personal Communication.